Relations between seismic signals and reservoir properties of deep gas reservoirs in Northwest-Germany - Wustrow member, Rotliegend

Dissertation

Zur Erlangung des akademischen Grades doctor rerum naturalium
(Dr. rer. nat.)

Vorgelegt dem Rat der Chemisch-Geowissenschaftlichen Fakultät der
Friedrich-Schiller-Universität Jena

Von Dipl.-Ing. Peter Abram
Geboren am 28. Dezember 1974 in Bozen (Südtirol, Italien)

Gutachter:

1. Prof. Dr. Reinhard Gaupp

2. Prof. Dr. Michael Weber

Tag der öffentlichen Verteidigung: 18. April 2007

Abstract

This study tries to find the petrophysical basis for correlations between reservoir properties and seismic signals calibrated with geological information for Wustrow-sediments of the Rotliegend in NW-Germany. A secondary objective consists in explaining the large scatter of permeability for Wustrow reservoir rocks of comparable properties.
The correlations were ascertained in the DGMK-project 593-8, for instance to authigenic clay mineral types and permeability.

The investigations demonstrate that the differences in seismic signals (amplitude, shape and lateral coherency of seismic traces) are a product of distinct compressional field velocities (from wireline logs) and attenuation processes as in-situ bulk densities are barely varying within the investigated horizon.
The regions of different clay mineral authigenesis (illite and chlorite) diverge by their average compressional in-situ speeds. The differences suffice to provoke relevant variations in seismic signals. Total porosity appears not to affect the field wave characteristics distinctly as *high* void volumes are encountered in the province of *high* compressional speed. The distinct velocities for rocks of different authigenesis and the subsidiary effect of void volume are ascertained also at plug dimensions. Other rock properties affecting wave characteristics than porosity become thus relevant.
Plugs of comparable properties but largely varying compressional ultrasonic velocity are analyzed for textural features which certainly or potentially influence wave characteristics. These features represent, affect or indicate also reservoir quality. Consequently, the potential is tested to extend the relevant influence of the identified properties from the plug to the field scale.
clay minerals in positions important to the rigidity of the rock framework strongly reduce the stiffness and hence the compressional velocity. The investigations show that sand/siltstones of illite authigenesis demonstrate by far larger amounts of clay minerals between particle contacts than reservoir rocks of chlorite authigenesis. Further, rocks with different amounts of non-load bearing minerals but comparable porosity should differ by compressional velocity. The illitized plugs feature larger amounts of solid components, particularly illite fibres (IM), which do not contribute to rigidity. These textural properties appear to be laterally and vertically consistent throughout the reservoir due to the distinct evolutionary conditions of load bearing illite and chlorite minerals, their distinct relative proportions, the limited occurrence of IM-fibres to illitized regions and the continuous core documentation of corresponding clay mineral types. Hence, the characteristic textural distinctions could be co-responsible for the dissimilar field velocities of the regions of illite and chlorite authigenesis.
The average transmissivity is severely reduced by the presence of illite fibres (IM). The correlation to major permeability trends could thus be a product of the characteristic textural properties in the illitized sandstones affecting velocity and the limited occurrence of the IM-morphotype to illitized regions. Likewise, the predictability of seismic facies classes for intense bituminisation could be based on the elastic features of illitized reservoir rocks as the organic matter impregnation is widely restricted to the provinces of illite alteration.
The ascertained effects of particle contact conditions and pore geometrical attributes at the plug scale could co-determine both velocities and transmissivities of the Wustrow rocks too. Although in contrast for the other textural properties, evidences for such characteristic distinctions at the field scale could not be identified, their influence, also if possibly not prevailing, remains still plausible.
The reservoir rocks of the Wustrow horizon, whose cores were investigated for the concerning textural features, affect volumetrically the seismic signals to the largest extent. Furthermore, seismic signal modifications by other lithological units, internal reverberations, reflections on

thin shaly or saline strata intercalating the reservoir and shale layers not resolved by GR-logs are demonstrably not relevant.
Several features regarding geologic structure, gas contents in pores, seismic and logging acquisition, etc. are discussed which could hamper the extension of petrophysical features co-regulating wave characteristics at the plug scale to the field scale. Seismic energy loss could be caused by eventual characteristic variations in reservoir temperature, particle contact conditions and the relative motion of pore fluids and illite fibres (IM). The calculated maximal modification of the seismic amplitude by potential distinct gas saturations appears to be negligible. However, eventual characteristic fluid saturations could affect field velocities significantly.
The pore geometrical studies and the modelling of permeability evidence that the strongly diverging permeability for Wustrow-plugs of similar porosity and equal clay mineral type is attributable to characteristic variations in pore throat size and distribution, degree of interconnectivity, fractions of intragranular porosity and pore wall roughness. The void geometrical differences are a result of dissimilar secondary dissolution and mechanical and chemical consolidation, apparent at the micro scale.

Kurzfassung

Die vorliegende Studie versucht die petrophysikalische Basis für Beziehungen zwischen geologisch-kalibrierten seismischen Signalen und Reservoireigenschaften zu finden für Wustrow-Sedimente des Rotliegenden in NW-Deutschland. Ein Ziel sekundärer Bedeutung besteht darin, die starke Schwankung von Permeabilitäten bei den Wustrow-Lagerstättengesteinen mit vergleichbaren lithologischen Eigenschaften zu erklären.
Die Korrelationen wurden festgestellt im DGMK-Forschungsprojekt (593-8) und zwar zu wichtigen Charakteristika wie u.a. durchschnittliche Permeabilität und Vorkommen von authigenen Tonmineraltypen.

Die Unterschiede in den analysierten seismischen Signalen (Amplitude, Form und laterale Verfolgbarkeit von seismischen Spuren) des Wustrow-Horizontes sind ein Produkt von bedeutenden Divergenzen in der longitudinalen in-situ Geschwindigkeit (aus Bohrlochlogs) und in Dämpfungsprozessen, da die in-situ Rohdichte im untersuchten Horizont kaum schwankt.
Die Provinzen der Illit- und Chlorit-Authigenesen divergieren in deren durchschnittlichen longitudinalen in-situ Geschwindigkeiten. Die Unterschiede reichen aus um die seismischen Signale signifikant zu verändern.
Die durchschnittliche Gesamtporosität kann die Kontraste in den Laufzeiten nicht bedingen, da die *höheren* Geschwindigkeiten in den Provinzen *höherer* Porosität gemessen wurden. Die klaren Unterschiede in der Geschwindigkeit und die fehlende Dominanz der Porosität sind auch im Proben-Maßstab offensichtlich. Diese Tatsachen heben die Relevanz anderer textureller Gesteinseigenschaften für die Ursache der Korrelationen hervor.
Ausgewählte Kernproben vergleichbarer Eigenschaften aber von stark abweichender Kompressionsgeschwindigkeit und Permeabilität werden eingehendst analysiert in Bezug auf Gefügemerkmale, welche die Wellencharakteristika sicher oder potentiell mitbestimmen. Diese Gesteinsmerkmale sind, beeinflussen oder indizieren auch Lagerstätteneigenschaften. Anschließend wird untersucht, ob ein maßgeblicher Einfluß der identifizierten Eigenschaften auch im Feld-Maßstab besteht.
Tonminerale welche sich in einer texturellen Position befinden, in denen sie die Festigkeit des Gefüges beeinflussen, verringern die Kompressionsgeschwindigkeiten drastisch. Die Untersuchungen zeigen, dass Sand- und Siltsteine von Illit-Authigenese bedeutend mehr

solcher kornstützenden Tonminerale aufweisen als chloritisierte Gesteine. Weiters unterscheiden sich Gesteine mit unterschiedlicher Menge an nicht kornstützenden Mineralen aber gleicher Porosität in den Geschwindigkeiten. Die illitisierten Proben besitzen größere Mengen dieser Komponenten, wozu vor allem die Illit-Fasern des IM-Typs gehören. Diese beiden texturellen Unterschiede scheinen lateral und vertikal konsistent im untersuchten Lagerstättenbereich gegeben zu sein aufgrund der deutlichen Unterschiede in der Entstehung der authigenen Illit- und Chloritminerale, deren klar voneinander abgegrenzten Vorkommen im Untersuchungsbereich, deren stark divergierenden Mengenverhältnissen, die Beschränkung des Auftretens der IM-Fasern auf illitisierte Bereiche und der steten Präsenz von entsprechenden Tonmineraltypen in allen Kernabschnitten des Wustrow-Reservoirintervalles. Infolgedessen könnten diese texturellen Eigenschaften die unterschiedlichen in-situ Geschwindigkeiten der illitisierten und chloritisierten Bereiche zumindest mitbestimmt haben.

Die Permeabilität wird stark reduziert bei Anwesenheit von IM-Fasern. Die Korrelation zur Permeabilität könnte auf den charakteristischen texturellen Eigenschaften der illitisierten Sand- und Siltsteine und der Einschränkung der IM- Vorkommen auf illitisierte Provinzen im untersuchten Bereich basieren. Genauso könnte die Vorhersagbarkeit einer Bitumenimprägnierung auf die elastischen Besonderheiten der illitisierten Reservoirgesteinen zurückzuführen sein, da das Bitumen fast ausschließlich auf illitisierte Regionen im Untersuchungsgebiet beschränkt ist.

Die festgestellten Effekte aus den Unterschieden der Kornkontaktbedingungen und der Porengeometrie welche im Probenmaßstab bestehen, könnten die Kompressionsgeschwindigkeiten und Permeabilitäten im Feldes-Maßstab beeinflussen. Auch wenn im Gegensatz zu den anderen texturellen Eigenschaften keine direkten Beweise für charakteristische Unterschiede nachgewiesen werden konnten, bleibt deren Einfluss, auch wenn vielleicht nicht bestimmend, dennoch bestehen.

Der Wustrow Reservoirabschnitt, in dessen Kernen die betreffenden texturellen Eigenschaften untersucht wurden, beeinflusst die seismischen Signale volumetrisch am stärksten. Weiters sind andere lithologische Abschnitte, interne Reflexionen, Reflektionen an geringmächtigen tonigen oder salinen Einschaltungen und Tonlagen, welche nicht vom GR-Log aufgelöst wurden, für Modifikationen der seismischen Signale nachweislich nicht relevant.

Eigenschaften, welche die Bedeutung der texturellen Eigenschaften für das elastische und anelastische Verhalten im Feld-Maßstab reduzieren oder gar maskieren, werden diskutiert. Seismische Dämpfung könnte hervorgerufen werden durch eventuelle charakteristische Variationen in der Lagerstättentemperatur, den Kornkontakt-Bedingungen und der relativen Bewegung von Porenfluiden und IM-Fasern. Die berechnete maximale Modifikation der seismischen Amplitude durch die möglichen charakteristischen Gas-Saturationsunterschiede ist vernachlässigbar. Allerdings könnten diese Unterschiede relevante Geschwindigkeitskontraste verursachen.

Die porengeometrischen Studien und die Modellierung der Permeabilität beweisen, dass die weit gestreute Permeabilität von Wustrow-Reservoirgesteinen ähnlicher Porosität und identischer Tonmineral-Authigenese zurückgeführt werden kann auf charakteristische Unterschiede in Bezug auf Porenhalsweite, -verteilung, Porenverbindungsgrad, intragranularer Porosität und Porenoberflächenrauhigkeit. Diese porengeometrischen Differenzen resultieren aus unterschiedlichen Intensitäten von sekundärer Lösung und mechanischer und chemischer Kompaktion.

Acknowledgements

First of all, my cordial thanks go to Prof. Dr. R. Gaupp. He sparked my interest with the idea to this study. During the working progress he was steadily curiously committed to the development of the theories and supported me with valuable discussions and some important encouraging. This study was facilitated by his decisive aid to gain for me a financially secure coverage.

I am appreciative to Dr. R. Möller (Labor Wietze, RWE-Dea) who provided the necessary plug set and crucial petrophysical information. The Society for Petroleum and Coal Science and Technology (DGMK) and RWE-Dea is recognised for supplying the data of the DGMK-project 593-8, digital log files and the possibility to release all the results of the present study to publication.

Several working groups conducted measurements and permitted to utilize their tools:
Prof. Dr. P. G. Malischewsky and A. Ziegert are gratefully acknowledged for allowing me to determine the compressional speeds on their equipment and for valuable arguments on the results.
Dr. T. Wonik at the Institute GGA in Hannover enabled charge free NMR-measurements. R. Haifa and R. Kappes conducted the expensive analyses and discussed with me the outcome. Additionally the opportunity was given to present my investigations in their research establishment to a broad audience. I am grateful for their work and their friendly support.
A. Caron at the IzFP in Saarbrücken carried out the SAM-measurements on a sometimes fractious apparatus. I am thankful for his long-term and gratuitous engagement.

My work benefited from many consultations with experienced workers of petroleum exploration industry on scientific conferences and presentations in their research departments. My special thanks in this regard go to the research staff of EXXONMobil, who furnished some relevant details which are not retrievable from literature.
Dr. R. Samiee (TEEC, at that time) is sincerely thanked for aiding me in evaluating the applications and limitations of neural network techniques.
I am very grateful to Prof. Dr. J. Kley who read my preliminary script and discussed with me valuable modifications.

The study profited from a pleasant and calm atmosphere in the institute. My colleagues are thanked for their unhurried and very friendly mentality.

The Friedrich-Schiller-University of Jena is kindly acknowledged for providing a position as scientific associate in the public service.

My deep thanks go also to my fiancé Elena who backed me all the time.

Contents

Abstract
Kurzfassung
Acknowledgements
Contents

1 Introduction 1

1.1 Objective 1
1.2 Geological information on the investigated Wustrow member 2
1.2.1 Location and stratigraphy 2
1.2.2 Lithology, depth and tectonics 3
1.2.3 Porosities and permeabilties 5
1.2.4 Clay mineral morphotypes and diagenesis model 7
1.2.4.1 Clay mineral morphotypes 7
1.2.4.2 Diagenesis model 11
1.2.5 Gas accumulations within the investigated volumes 11
1.3 Seismic signal interpretation for the Wustrow member 13
1.3.1 Introduction 13
1.3.2 Generation of seismic signals 13
1.3.3 Neural network technique 15
1.3.3.1 Type of neural network 15
1.3.3.2 Results of the classification 16
1.3.3.3 Explanation of the parameters compared to neural network output and comments 18
1.3.4 Further techniques of seismic signal interpretation 19
1.3.5 Weak points of the techniques 19

2 Approach and Methodology 21

2.1 Introduction 21
2.2 Approach 24
2.3 Methodology 25
2.3.1 Utilized data 25
2.3.2 Methods 26
2.3.2.1 Measurement of ultrasonic compressional velocity 26
2.3.2.2 Optical microscopy 27
Mineralogical composition 27
Grain size analyses 27
2.3.3 Samples 27

3 Parameters affecting compressional velocity and attenuation at the plug scale 31

3.1 Effects of clay minerals between particle contacts on compressional velocity 31
3.1.1 Relation of seismic facies classes to clay mineral morphotypes and average reservoir permeability 31
3.1.2 Elastic influence of clay minerals 33
3.1.2.1 Introduction 34
3.1.2.2 Method 35
3.1.2.3 Results 39

3.1.2.4 Discussion 39
Remark on the potential elastic influence of bitumen 41
3.2 Effects of particle contacts on compressional velocity and permeability 43
3.2.1 Introduction 43
3.2.2 Method 44
3.2.3 Results 45
3.2.4 Discussion 46
3.2.4.1 Particle contacts and compressional velocity 46
Compressional velocity and the proportion of blocky cements 46
3.2.4.2 Particle contacts and permeability 47
Permeability of Wustrow reservoir rocks 47
Grain size sorting 47
Mechanical and chemical compaction 49
3.3 Effects of pore geometry on compressional velocity and permeability 50
3.3.1 Introduction 50
3.3.1.1 Effects of pore geometry on compressional velocity 50
3.3.1.2 Effects of pore geometry on permeability 52
3.3.2 Aim 52
3.3.3 Pore geometry from image analysis on thin sections 53
3.3.3.1 Method 53
Pore parameters 55
Resolution 59
Accuracy and precision 60
Analysis and presentation of data 61
Additional comments 62
3.3.3.2 Results 63
Tables 63
Frequency scales 69
Microscopic observations on pore geometry 69
3.3.3.3 Discussion 73
Effects of outcome on permeability 73
Modelling of permeability with pore geometrical attributes 74
Summing up 77
Effects of outcome on compressional velocity 77
Effects on some pore geometrical attributes when coding illite fibres as solid or as void volume - case study 78 78
3.3.4 Pore geometry from Nuclear Magnetic Resonance (NMR) 81
3.3.4.1 Method 81
Apparatus and parameters 81
3.3.4.2 Samples 81
3.3.4.3 Results and discussion 82
Effects of outcome on permeabilty 82
Effects of outcome on compressional velocity 85
3.3.5 Pore geometry from Mercury Capillary Pressure Porosimetry 86
3.3.5.1 Method 86
3.3.5.2 Samples 87
3.3.5.3 Results and discussion 87
Summing up 89

3.4 Solid components with no influence on rigidity 90
3.4.1 Introduction 90
3.4.2 Method 91
3.4.3 Results and discussion 92
3.5 Effects of compressional micro impedances of IC and CT-minerals on compressional velocities - Scanning Acoustic Microscopy (SAM) 95
3.5.1 Introduction 95
3.5.2 Method 95
3.5.3 Samples 97
3.5.4 Results and discussion 99
3.6 Effects of total petrographic clay content on compressional velocity 101
3.7 Seismic signal modifications by anelastic processes 103
3.7.1 Introduction 103
3.7.2 Effects of parameters 103
3.7.3 Relevance for seismic volume 106
Calculation of amplitude attenuation due to diffferences in water saturation 107
Summing up 109
3.8 Additional rock parameters affecting compressional velocity 110
3.8.1 Introduction 110
3.8.2 Effects of parameters 110
3.8.3 Relevance for seismic volume 111

4 Extension to seismic dimensions 112

4.1 Compressional velocities of lithological sections at the seismic scale 112
4.1.1 Introduction 113
Lithofacies Upscaling 113
4.1.2 Eolian dry section 114
4.1.3 Eolian damp section 115
4.1.4 Wustrow member without hanging wall 116
4.1.5 Non-reservoir section 117
4.1.6 Thin shale-reservoir rocks-interbeddings not resolved by GR-logs 118
4.1.7 Shale beds of different compressional velocity 119
Summing up 119
4.2 Relevance of velocity contrast for seismic signals 122
4.3 Influences of differences in stratigraphic structure on compressional velocity at the seismic scale 122
4.3.1 Introduction 122
4.3.2 Seismic resolution of intercalated shaly beds and shale 123
4.3.3 Interior reflections by shaly bedsand shale 123
4.4 Thicknesses of reservoir sections and relevance for seismic signals 124
4.5 Comparability of ultrasonic, sonic and seismic velocities 125
4.6 Indications for distinct textural properties at the seismic scale 126
4.6.1 Introduction 126
4.6.2 Particle contact conditions 126
4.6.2.1 Degree of compaction and cementation 126
Method 127
Results 127
4.6.2.2 Packing indices by different sedimentary facies 129

4.6.2.3 Packing indices by different grain sorting 129
4.6.2.4 Blocky cements 129
Summing up 130
4.6.3 Proportions of clay minerals between particle contacts and of not load bearing components - Consistency of petrological and textural features 131
4.6.4 Pore geometry 131
4.7 General aguments against or hampering the extension to seismic dimensions 132

5 Conclusions 134

6 References 138

Appendix

Curriculum vitae

Selbständigkeitserklärung (Declaration)

1. Introduction

1.1 Objective

Seismic attributes are commonly used in petroleum exploration to derive reservoir properties since the mid 1960's. However, the usefulness of seismic attribute interpretation has always been contentious. On the one hand strong criticism persists as many of the meanwhile innumerable attributes appear to lack a comprehensible background. On the other hand the advancements in computer capacity, seismic processing and interpretation techniques have brought about substantial improvements in the potential forecast of reservoir properties over the last two decades.

A recently finished study (DGMK 593-8, Gaupp et al. 2005) gained and integrated sedimentological, petrological and geophysical data on a section within the North German basin featuring permeable and tight gas deposits. The combined work of industry and research institutes consisted in calibrating three-dimensional seismic data with core and log information based on a geological model in order to predict reservoir characteristics in zones without any well information. The forecast features comprise crucial attributes like average reservoir permeability and diagenetic products affecting and indicating reservoir performance.

Naturally, petroleum industry is keenly interested in examining the reliability of such forecasts.
Therefore, the purpose of the present study is to identify the rock features which control these relations.
A secondary goal is to find the reasons for the large scatter of permeability in samples of comparable lithology and porosity present in the investigated horizon.

1.2 Geological information on the investigated Wustrow member

1.2.1 Location and stratigraphy

The investigated Wustrow member is located in the North of Germany and forms part of a 200 km wide belt with 160 German Rotliegend gas accumulations (Burri 1993). These partly economic deposits extend from the Salzwedel reservoir in the East to the Groningen field in the West (fig. 1.1).

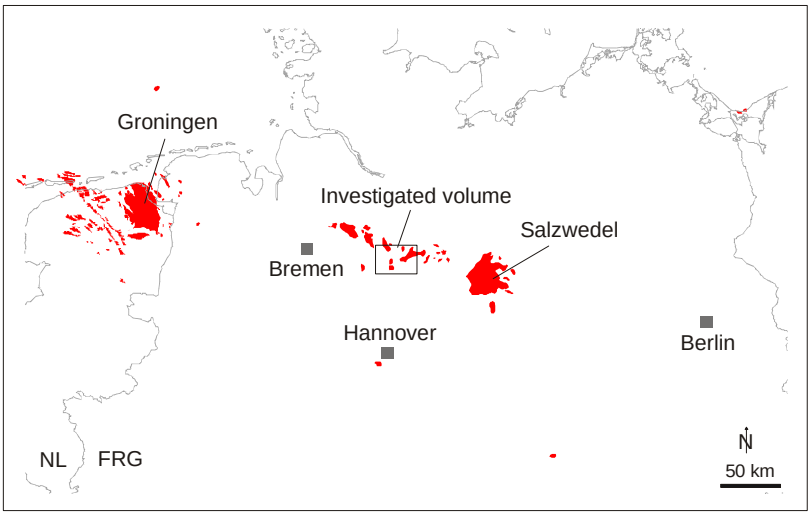

Fig. 1.1: Occurrence of major Rotliegend gas accumulations in Northern Germany shown in red. The small rectangle delineates location and extension of investigated volume. The map is based on charts from Lokhorst (1998).

Plugs and data from cores and logs derive from a horizon of 30 km × 40 km with a total of 42 wells (fig. 1.3). This region of the Wustrow member is referred in the present study as “large investigation volume” or “large sector”. The Wustrow volume, where the seismic signals and seismic facies classes were produced, extends over 10 km × 22 km with 11 wells (fig. 1.3). This part is included in the large sector and is denoted in the following as “seismic volume“, or “seismic sector”.
Most of the reservoir attribute maps presented in this work are based on data from the large sector.
The investigated Wustrow member appertains stratigraphically to the basal part of the Hannover Formation and was formed during the Rotliegend (Plein 1995, Schöder et al. 1995) (fig. 1.2).

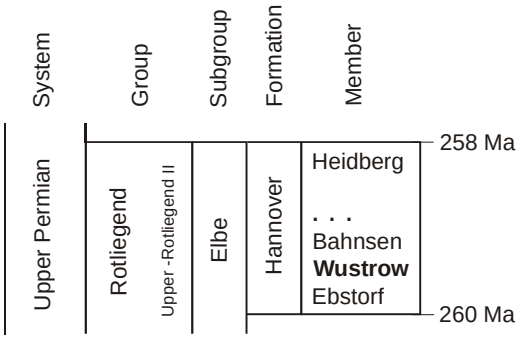

Fig. 1.2: Stratigraphic position of the Wustrow horizon. Based on Plein (1995) and German Stratigraphic Commission (2002).

The Rotliegend sediments of Northwest-Germany were deposited on the slightly north-dipping southern flank of the Southern Permian Basin and cover Autunian volcanics and Carboniferous series. Initially molasse-type sediments were deposited, followed by eolian sediments and salts. The Southern Permian Basin represents the southern part of an intracontinental basin complex in Northwest Europe. The Southern Permian basin is partly segregated in horst and graben structures which developed during the Autunian in response to East-West directed rift and wrench tectonics (based on Plein 1990, Ziegler et al. 1997).

The data in this study represent industrial property and is subject to restrictions of confidentiality. Therefore the geographical positions of the well bores is not included the charts and the well names are encoded as in the DGMK (German Society for Petroleum and Coal Science and Technology) - report 593-8 (Gaupp et al. 2005).

1.2.2 Lithology, depth and tectonics

The Wustrow member consists mainly of sandstones, siltstones and shale of eolian and lacustrine origin (Gaupp & Solms 2005). The generally well sorted and fine grained quartz silt and sandstones evolved parallel to the coastline of a perennial salt lake and compose the massive reservoir rocks of the Wustrow interval (Plein 1995). The deposition of the eolian sediments was affected by cyclic changes of groundwater levels and periodical floodings from the adjacent northern salt lake which caused pelitic and evaporitic deposition (Gast 1991, Gaupp et al. 1993). Repetitive tectonic activities at the basis of the interval facilitated the eruption of alkaline basalts and resulted in local unconformities (Plein 1995, Helmuth & Süssmuth 1993).
The Wustrow member is deeply buried at 4380-4600 m (top of horizon) and arranged in a horst and graben structure (pers. comm., R. Gaupp, 2005, coordinator of the DGMK-project). Generally its depth increases basinward to the northeast. The thickness rises likewise from the southwest to the northeast; from 11 m to to 42 m in the large sector and from 26 to 37 m in the seismic sector (fig. 1.3).

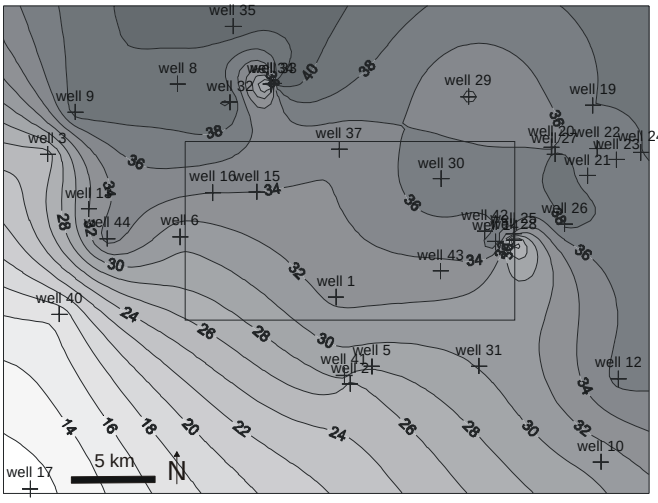

Fig. 1.3: True vertical thickness of the Wustrow member in meters. The small rectangle confines the seismic section. The chart is based on 32 wells (appendix A-7). The thickness increases basinward to the Northeast from 11 to 42 m within the large volume by approximately 10 m in the seismic volume.

Three generations of NS, NW-SE and NE-SW striking faults fractured the reservoir and provoked vertical tectonical offsets of up to 150 m (based on data of Tanner et al. 2005).

The top and the base of the Wustrow member consist of 1 m thick shale and 7-12 m thick sand-shale interbeddings. Massive sand- and siltstones of 5-28 m thickness form the actual reservoir in the middle part of the member and constitute with 50 to 95 % the bulk of the Wustrow horizon (fig. 1.4). The reservoir section comprises locally one to three 0,5 to 1m thin shale layers.
The total shaliness in the large sector rises in general opposition to the reservoir volume towards the West with 8 % and to the East with 40 % (fig. 1.5).
The internal geological stratification remains laterally traceable, particularly within the seismic sector.
The Wustrow member features principally three types of GR-logs according to the presence of shaly beds above, below and/or within the reservoir. The distribution of these types in the large survey is presented in figure 1.6.

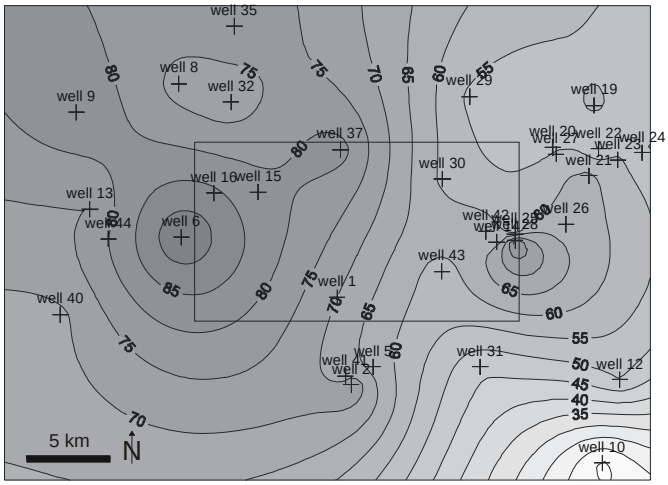

Fig. 1.4: Thickness of the Wustrow reservoir as percentage of the Wustrow member. The chart is based on the evaluation of 32 wells (appendix A-7). The eolian deposition is affected by lake level fluctuations and the morphology of the horst and graben structure. The seismic volume features a reservoir unit increase of 35 absolute %.

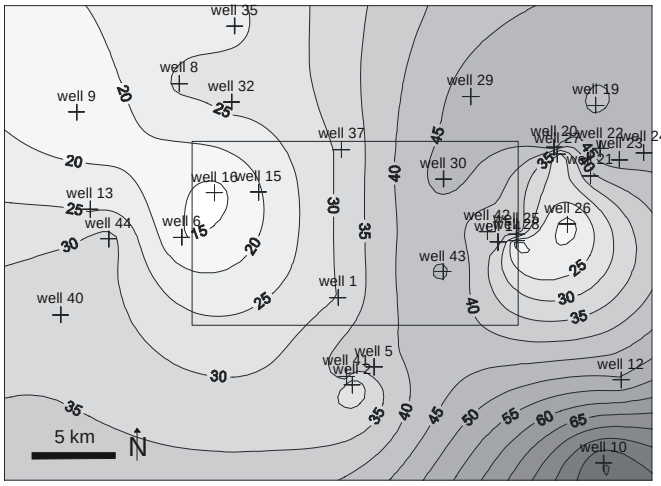

Fig. 1.5: Distribution of shale content as percentage of the Wustrow member. The smaller rectangle delineates the position of the seismic volume. The shaliness is based on the examination of GR-logs from 32 wells. The shale content increases from West with 8 % to the East with 40 % and to the South with a maximum of 75 %. The shaliness of the seismic volume increases likewise to the East from 15 to 37 % approximately. The distribution is a function of the periodical floodings of the northern playa lake and the morphology of the horst and graben structure.

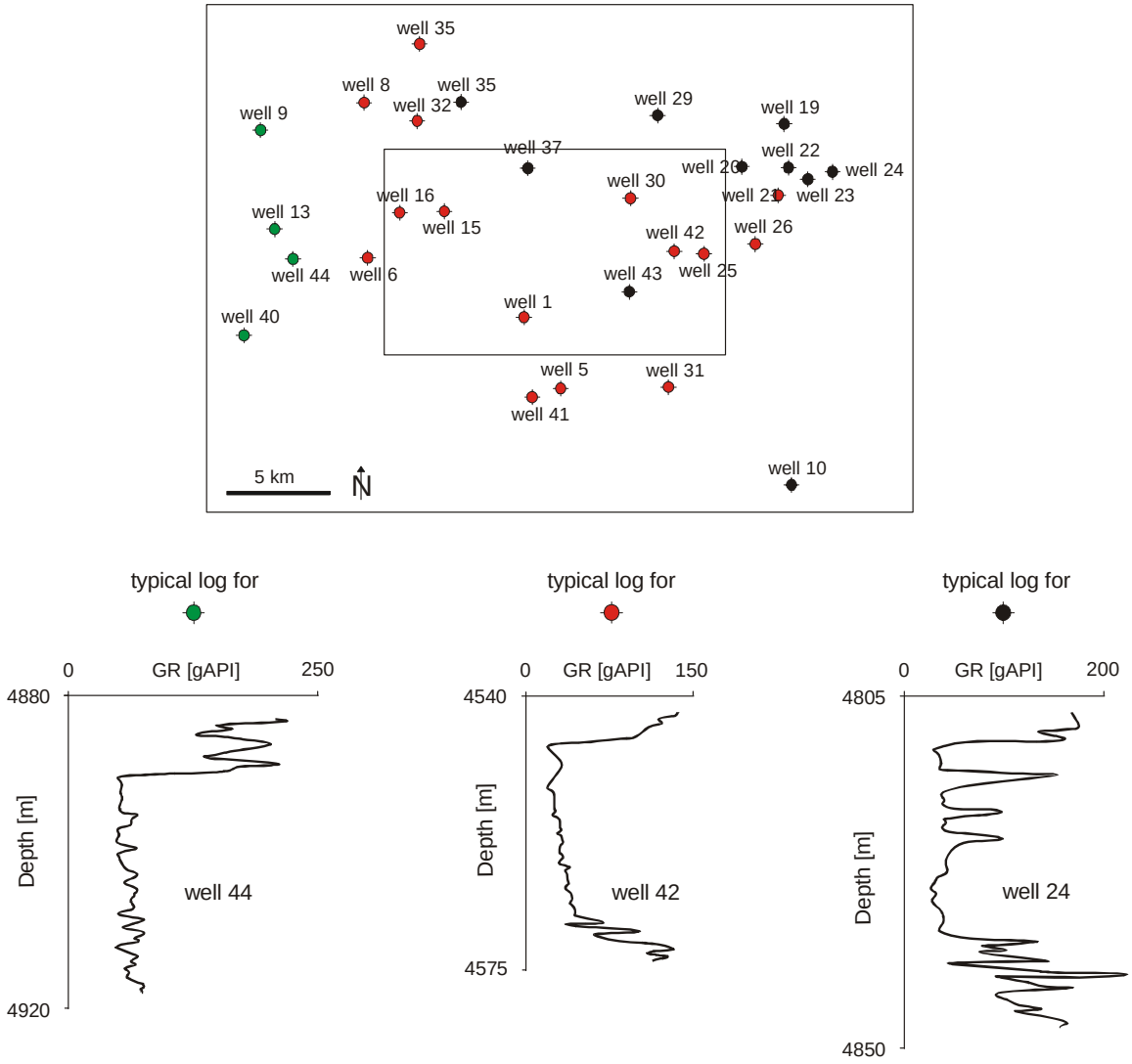

Fig. 1.6: Distribution of typical GR-logs for the Wustrow horizon. The presented logs start and end at the top and base of the Wustrow member. The large rectangle delineates the large survey; the small rectangle confines the seismic volume. Three characteristic logs are discernible according to the position of shaly and saline beds above, below and/or within the reservoir. The amount of intercalations within the reservoir can vary. The shown GR-curves represent original logs.

1.2.3 Porosities and permeabilities

According to petroleum companies (in Trappe et al. 2005) the average total porosities within the seismic volume present small variations and range between 9,1 and 11,7 %. According to own calculations total void volumes of the sand- and siltstone units within the seismic volume vary within 8,2 and 10,5 %, while the porosities of the shale layers range from 1 to 5 % (fig. 1.7).

The porosities derived in the present study were calculated from sonic log data by means of the Raymer and Hunt equation (Raymer et al. 1980) for water saturated samples with constant speeds for mineral and pore content. Therefore the porosities do not account for changes in pore content, lithology or texture. However, the computed porosities correspond well to sonic derived porosities, which were delivered for a few wells from petroleum companies.

Average void volumes from dry cores of the seismic section, which were taken predominantly within the reservoir, vary between 7 and 13,5 %.
The mean total porosities of the reservoir sediments within the large sector differ distinctly. The core data from the DGMK-database (appendix A-9) vary within 2,0 and 16,2 %, the sonic log derived porosities between 1,6 and 13,7%.

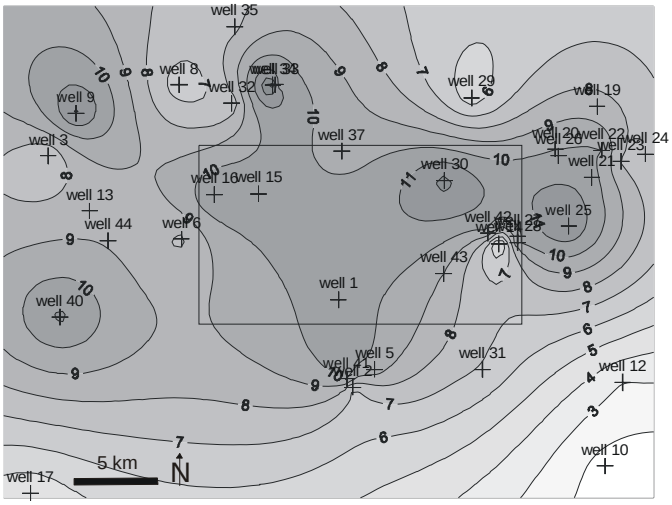

Fig. 1.7: Distribution of average total porosity in % quantified on sonic logs by means of the Raymer and Hunt equation (Raymer et al. 1980) for the reservoir intervals. The presented reservoir porosities comprise the porosities of intercalated shale beds. Small rectangle demarks the location of the seismic volume. The void volumes vary largely within the large section between 1,6 and 13,8 %, whereas the porosities within the seismic survey are roughly consistent.

Average permeabilities from reservoir sections are highly variable and range between 0,02 and 232 mD for the large section. The seismic volume features mean permeabilities within 0,1 and 55 mD. Minimum and maximum values in this sector constitute to 0,01 and 200 mD.
The distribution of permeability is presented in figure 1.8 and depicts a rough separation in reservoir quality in western and northeastern regions. This division of the reservoir is evident for both the large and the seismic volumes.

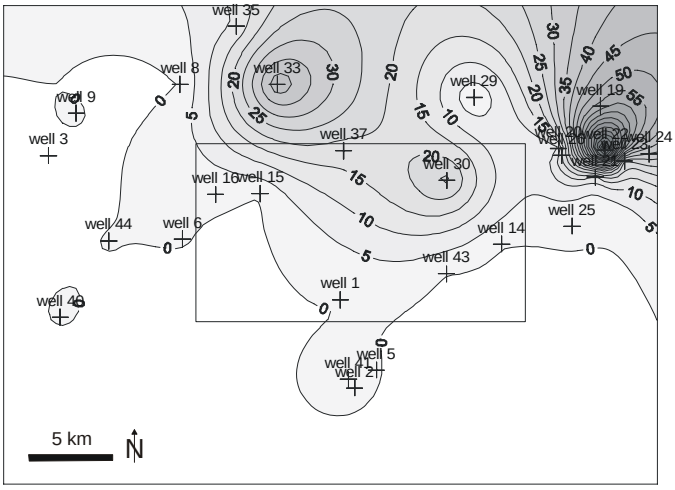

Fig. 1.8: Distribution of average permeability in mD; based on cores from the reservoir intervals of 25 wells. Small rectangle delineates the extension of the seismic volume. The average permeabilities vary widely within 0,01 and 117 mD for the large survey. Within the seismic volume the range

constitutes to 0,1 and 55 mD. The distribution presents a separation in western and northeastern sections.

Unfortunately no information on an eventual anisotropy of permeability is attainable from petroleum companies. As sedimentological structures are evident for the available plugs a directional dependence is plausible.

The sections of the Wustrow reservoir, which feature low permeabilities, are commonly referred to in literature as tight gas reservoirs (Gaupp et al. 2005). A tight gas setting is often defined as a gas bearing sandstone or carbonate which exhibits an in-situ permeability to gas of less than 0,10 mD (Law & Curtis 2002). Additional petrophysical features reducing fluid conductivity of low permeable sandstones represent low to moderate porosities, solid fluid interactions and effects of multiphase saturations related to capillary pores (Arastoopout & Chen 1987, Byrnes 1997, Dullien 1992, Shanley et al. 2004, Cluff et al. 2005).

1.2.4 Clay mineral morphotypes and diagenesis model

The here presented information on the clay mineral morphotypes and the diagenesis model comprises only characteristics which are relevant to this study.
For an extended overview of diagenesis in the large sector refer to Gaupp et al. (2005), for additional diagenesis types and diagenesis in general of the Rotliegend sediments to Platt (1991, 1993), Deutrich (1993, 1996), Gaupp (1993, 1996), Liewig & Clauer (2000), Schöner (2006).

1.2.4.1 Clay mineral morphotypes

Gaupp et al. (2005) differentiated the types of occurring clay minerals according to their chemistry and morphology. The classification is based on several former categorizations of precipitates in the Rotliegend from Gaupp (1996), Gaupp et al. (1993) and Deutrich (1993). The following descriptions for illite (I~) and chlorite (C~) minerals are based on the cited literature and where not specified on own microscopic observations.

The **IC-type** (plate 1.1) in the Wustrow reservoir forms illite fibres and filaments mostly parallel to the grain surface with varying mean thicknesses of <2 µm (Gaupp & Solms 2005). It generally occurs on the bare surface of the detrital component (Deutrich 1993) and resides also between the particle bonds. Often this illite type encases the whole particle and is affected by later diagenetical processes, like IM-overgrowth (Deutrich 1993).
The IC-type is generated by alteration of smectites originating from pedogenetic processes, detrital influx and/or post depositional infiltration of clay suspensions (Rossel 1982, Gaupp et al. 1993). According to Deutrich (1993) its syndepositional and early diagenetic evolvement is linked to an arid to semiarid depositional setting within the phreatic zone which is exposed to episodical floodings of suspension currents.
Due to the pore lining habit, its influence on porosity and permeability is supposed to be small (Gaupp 1996).

The **IM-type** is found as illite platelets and fibres on every kind of pore surface. Its “very thin and thread like crystals” (Rossel 1982) form a dense and sometimes pore bridging meshwork structure (Deutrich 1993). The illites are generated at intermediate burial (Gaupp et al. 1993) as they cover early diagenetic products and occupy intragranular voids of corroded components. This morphotype is impregnated with remnants from hydrocarbon migration and is often associated with intense feldspar dissolution (Gaupp & Solms 2005). The

occurrence of IM – fibres is restricted within the seismic volume to IC-altered sandstones. The permeabilities of the IM-cemented sandstones are severely reduced by the high specific surface of the fibres and its dense grid to average values below 1 mD even though mean porosities are moderate with 8-12 % (Gaupp 1996, Deutrich 1993, Rossel 1982).

The **CR-type** plasters grain surfaces as radially grown and ca. 0,5 µm thick platelets of chlorite (Deutrich 1993). The Mg-rich variety (Gaupp & Solms 2005) is formed at an early stage of diagenesis in texturally mature sandstones of high intergranular volume deposited at the margins of the salt lake (Deutrich 1993). Due to the habitus and the small dimensions its influence on permeability is regarded to be minor (Gaupp & Solms 2005).

The **CT-type** forms 2-4 µm thick chlorite plates on grain surfaces which are arranged dominantly parallel to the grain surface (Gaupp & Solms 2005). This morphotype of high Mg-content evolved at an early to intermediate diagenetic stage and hampers fluid flow barely due to its pore lining habit (Gaupp & Solms 2005).

The **CS-type** comprises thin plates and fan like chlorite crystals of 5-15 µm length grown sub-parallel on grain surfaces (Deutrich 1993). Its presence on intergranular corners implies an intermediate stage of diagenesis (Deutrich 1993) when already some compaction occurred. Chemically this variety features lower Mg-contents than the other morphotypes (Gaupp & Solms 2005). Sandstones with high contents of this chlorite morphotype produce low but still higher permeability values than IM-dominated samples (Gaupp & Solms 2005).

The distinct effects of clay mineral morphotypes on the fluid mobility are evidenced in a porosity-permeability plot of eolian dry sandstones (fig. 1.9). Plugs of IM- and IC alteration exhibit drastically lower permeabilities than comparable chlorite altered specimens. However the reducing effect of illite fibres appears to diminish for porosities exceeding 14-15%.

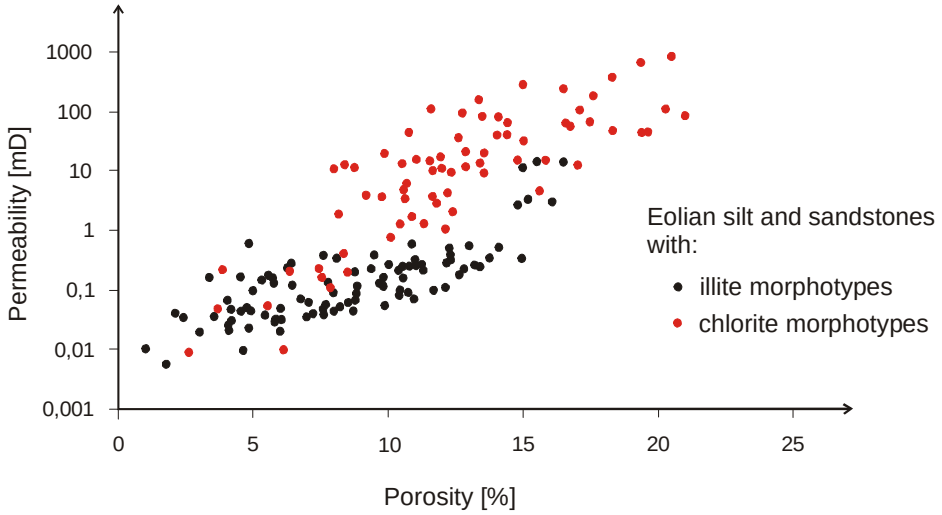

Fig. 1.9: Permeability versus porosity of eolian dry Wustrow reservoir rocks. The data points scatter according to the occurring clay mineral type. At porosities above 14-15 % the deteriorating effect of illite fibres on fluid mobility seems to decline. The data are from the DGMK-database measured on samples of the seismic volume (see appendix A-9).

Besides to deterioration of fluid flow by diffuse clay fibres in pore space (Deutrich 1993) and their large hydrophilic specific surface (Gaupp et al. 2004), Tanner et al. (2005) postulate a

permeability enhancement close to fault zones, where the deformation due to the high strain provoked increased secondary porosity.

Plate 1.1 illustrates the morphology of the diagenesis types as images of Raster Electron Microscopy (REM) and optical microscopy.

Plate 1.1: Optical (left) and REM images (right) recorded on thin sections for morphotypes of illite coating (IC), illite meshwork (IM), chlorite tangential (CT) and chlorite radial (CR).
A: Envelop of illite minerals around particles. The coating thickness varies within a few µm. Illite is encountered also within adjacent particle interfaces. The coatings are impregnated by brown hematite. Dark particles within the blue impregnated pore volume are remnants from grinding powder.
B: Dense aggregate of illite plates (IC) coating a primary grain. Image from Deutrich (1993).
C (crossed nicols): Flakes of illite sprouting on the particle surface into the pore space forming meshwork structure (IM). The network increases vorticity in migrating fluids and enhances fluid-solid processes which reduce flow efficiency.
D: Plates and fibres of illite, building networks within the pore space (IM). The reducing effect on permeability is palpably observable. Image from Deutrich (1993).
E: Coatings of chlorite (CT) with varying thickness. Dark particles within the blue impregnated pore volume represent particles from grinding powder.
F: Thin carpet of chlorite plates (CT) on primary quartz-grain (Qz). Image with courtesy of Robert Schöner.
G: Rims of chlorite fibres growing roughly perpendicular to particle surface (CR) appearing as faint crystals.
H: Compact rims of chlorite fibres (CR) covering the open particle surface entirely. Image with courtesy of Robert Schöner.

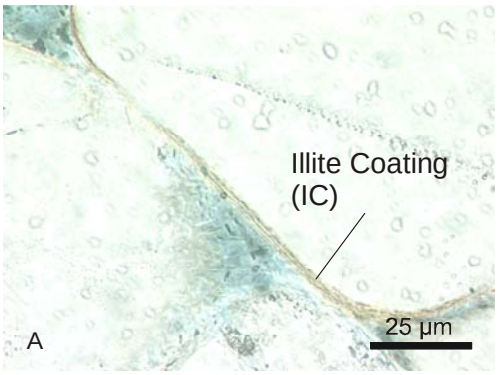
Illite Coating
(IC)
25 µm
A

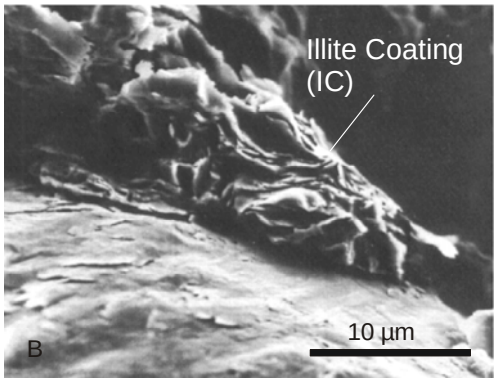
Illite Coating
(IC)
10 µm
B

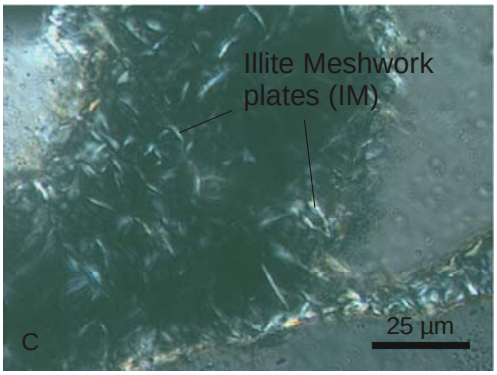
Illite Meshwork
plates (IM)
25 µm
C

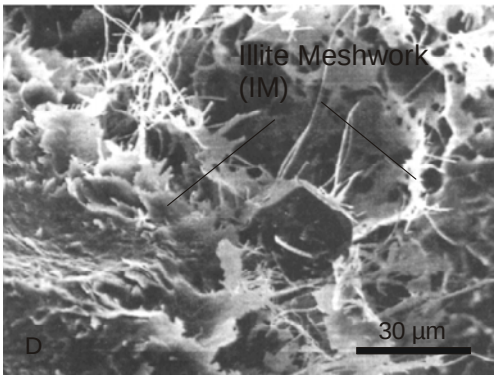
Illite Meshwork
(IM)
30 µm
D

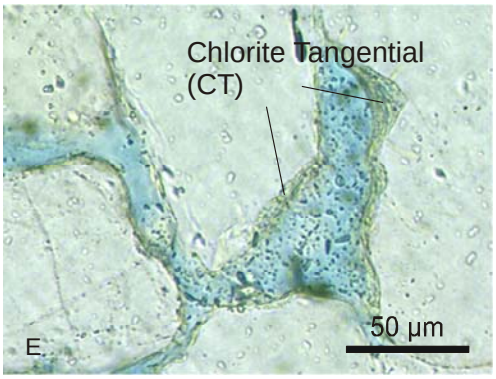
Chlorite Tangential
(CT)
50 µm
E

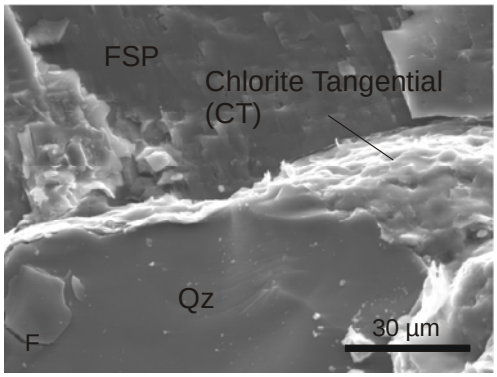
FSP
Chlorite Tangential
(CT)
Qz
30 µm
F

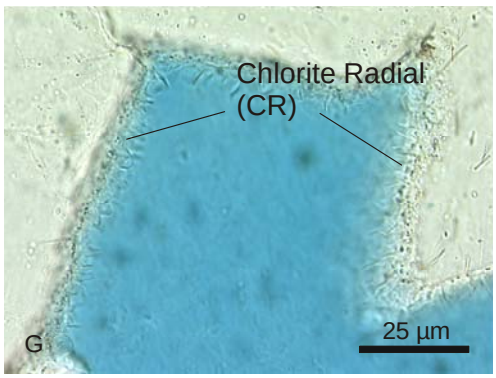
Chlorite Radial
(CR)
25 µm
G

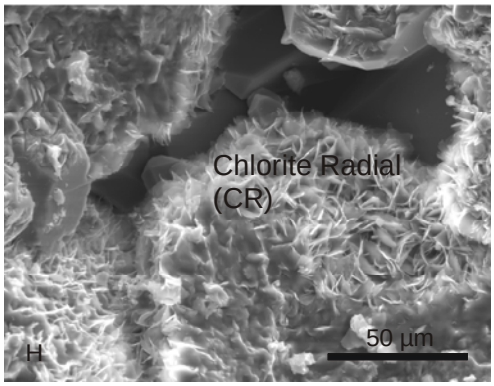
Chlorite Radial
(CR)
50 µm
H

1.2.4.2 Diagenesis model

The occurrence of the different diagenesis types in the Rotliegend and in the investigated horizon (fig. 3.1, bottom) is believed to be confined by major fault lines, the sedimentary facies, paleo-permeabilities, hydrocarbon emplacement, the distance to the Carboniferous and the presence of acid fluids and solvable components (based on Deutrich 1993, Gaupp et al. 2005, 1993).
According to the DGMK-project, NW- and NNW- striking lineaments acted as conduits for migrating hydrocarbons and confined compartments with specific diagenetical characteristics. The seismic volume is segregated into south western region with strong illitization and a north eastern region of chlorite authigenesis.
The southern and western parts were infiltrated by carboxylic fluids due to their close vicinity to the Carboniferous source rocks and their high paleo permeabilities. These acids increased the K^+-supply in the pore fluids by dissolving feldspars and volcanic lithoclasts deriving from volcanic and crystalline paleo highs and an alluvial-fluviatil setting in the South, and enhanced the precipitation of illite (Gaupp et al. 1993). The infiltration of the fluids towards the Northeast diminished due to the increasing distance to the Carboniferous (Tanner et al. 2005), the low paleo porosities in the Northeast and the impermeable NW-trending lineaments (Gaupp & Solms 2005).
In contrast, the northeastern region contained small amounts of feldspars and unstable components and was early cemented by anhydrite and calcite. These blocky cements enforced the grain framework during burial and were later dissolved by CO_2 deriving from the interaction of organic fluids and oxides (Gaupp 2005). The CR-rims of intermediate stage of diagenesis hindered the precipitation of quartz cement. These processes resulted in high primary and secondary porosity for this region of the reservoir (Gaupp & Solms 2005, Schwarzer & Littke 2005, Strauß & Solms 2000).
In this regard Gaupp (2005) designates an inversion of reservoir quality for the large survey as diagenetic processes inverted the initially porosity-permeability conditions in the north western and southern, and the north eastern part.
These diagenetic processes and the influences of the diagenesis types on fluid mobility explain the high permeabilities for the chloritized parts and the low permeabilities for the illitized sections of the reservoir.

1.2.5 Gas accumulations within the investigated volumes

The Wustrow interval represents the economical focus of the Rotliegend gas production (Plein 1995). The investigated seismic volume is part of several gasfields. Figure 1.10 delineates the western part of the large field in the East and some wells with gas discoveries, whose gas-water contacts are uncertain.
The migration of hydrocarbons occurred at several stages before the Triassic, in the Triassic, late Jurassic and is still ongoing in the present. Shale layers and the diagenetically altered sediments form the trap rocks for the investigated interval (based on log data from DGMK-database, see appendix A-7; and Burri et al. 1993). The extent of the gas reservoir in the East is codetermined by the tectonic structures. This region together with the wells 30 and 33-37 features the maximum permeabilities throughout the large volume. The remaining horizon demonstrates drastically poorer reservoir qualities and tight conditions.

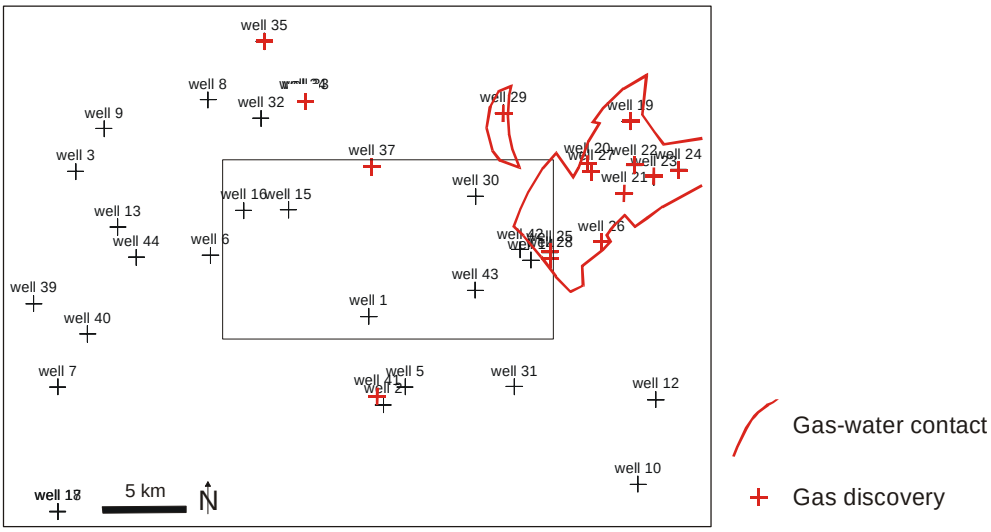

Fig. 1.10: Gas discoveries and gas water contacts in the large section and surroundings based on maps from Plein (1994), Gast (1988) and Philipp & Reinicke (1982). Large rectangle delineates the extensions of the large sector, small rectangle confines the seismic volume. The gas deposits are confined by tectonic lineaments. For a tectonic map please refer to figure 3.1 and Gaupp & Solms (2005).

The gas distribution is based on maps published in Plein (1994), Gast (1988) and Philipp & Reinicke (1982). The accumulations consist of dry gas with 20 % N_2 and no H_2S (based on maps of Plein 1994).
The Rotliegend in Germany is estimated to store 300-500 billion m³ of dry gas resources, the gas reserves amount to 300 billion m³ (Pasternak et al. 2001).

For further reading on the Wustrow member and the Hannover formation in general please refer to Gaupp et al. (2005), Gralla (1988), Gast (1991), Plein (1994, 1995), Helmuth & Süssmuth (1993), Schöder et al. (1995), Ziegler (1990), Ziegler et al. (1997), Hoffmann et al. (1989), Verdier (1996).

1.3 Seismic signal interpretation for the Wustrow member

1.3.1 Introduction

Several studies showed the utility of seismic attributes to investigate reservoir characteristics (e.g. Brown 1996, Russell et al. 2002, Rummerfield 1954, Lindseth 1982). The most successful attempts were achieved when interpreting rapid amplitude change as an alteration in reservoir quality particularly regarding porosity and gas content (Brown 1996). Brown (1996) demonstrated the benefits and limitations of seismic attribute analysis in his standard work “Interpretation of three dimensional seismic data” based on representative case studies.
Reservoir quality prediction based on the examination of seismic attributes was also carried out for the Rotliegend in Germany. Mathisen & Budny (1990) regarded void volume of the Lower Permian reservoir to be an important factor affecting the seismic signals at the interface with the Upper Permian Zechstein carbonates. The distinct ranges in porosity for both units cause substantial impedance contrasts and provide an opportunity to map reservoir quality from seismic amplitudes. An example for a change in the wavelets with increasing reservoir quality is illustrated in figure 1.11: increasing void volume in the Rotliegend sandstone section enhances the impedance contrasts at the contact to the dense evaporitic layers and provokes more intense deflections (Budny 1991).

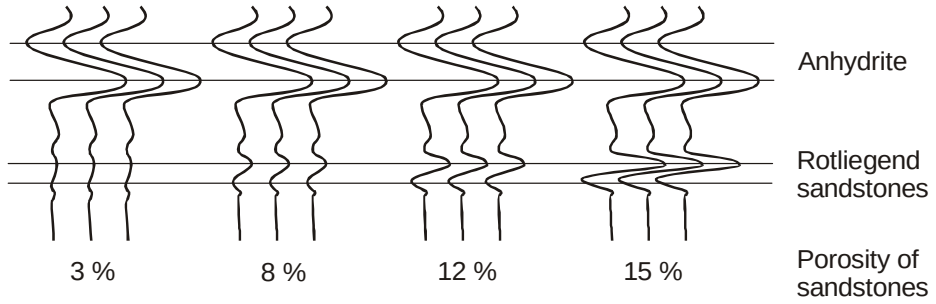

Fig. 1.11: Example for the sensitivity of reflection amplitudes to porosity presented on synthetic seismograms. Increasing void volumes in the Rotliegend sandstones generate intense augmenting deflections. Modified after Budny (1991).

Burri et al. (1993) regard seismic attribute mapping as a powerful tool in identifying “sweet spots” in the Rotliegend group based on their long-term working experience.
Despite the significant effect of porosity on seismic wave characteristics three dimensional data of low porosity and low permeability reservoirs still hold considerable potential for identifying commercial plays (Hart et al. 2003).

1.3.2 Generation of seismic signals

In the present study the term “seismic signals” refers to the seismic features of wavelets which were analyzed in the DGMK-project (see 1.3.3.1).
The near overburden of the Wustrow reservoir consists of shale with some intercalated thin saline and sandy strata (based on 40 GR-logs from the large area and on Plein 1995)). According to Dr. R. Samiee it can be regarded as a layer of uniform seismic properties (pers. comm., R. Samiee, 2005, geophysicist at TEEC at that time). This lithology forms also the top of the stratigraphic Wustrow member (fig. 1.12). Below this unit the Wustrow member is built up by a sandy and silty reservoir of higher porosities with some intercalated shaly layers. The resulting differences in the reflection coefficients generate the analyzed seismic

amplitude at the contact region and modify the reflection character of the seismic wave traces.

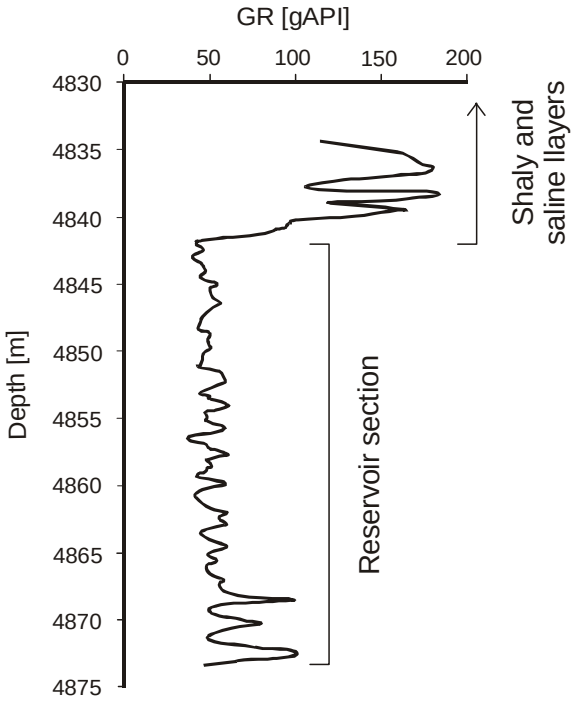

Fig. 1.12: GR-log of the Wustrow interval from well 9. The Wustrow member comprises the porous shaly reservoir section and its dense overburden composed of shale and some saline and sandy intercalations. The differences in lithological parameters at the interface of these units generate the analyzed seismic signal contrasts.

It is important to note that the analyzed signals were generated at the interface of the reservoir section and its dense overburden. The generated facies classes cover thus not the whole interval within the stratigraphic top and base of the Wustrow member but only its reservoir section and some underlying shaly, saline and sandy strata (fig. 1.13).

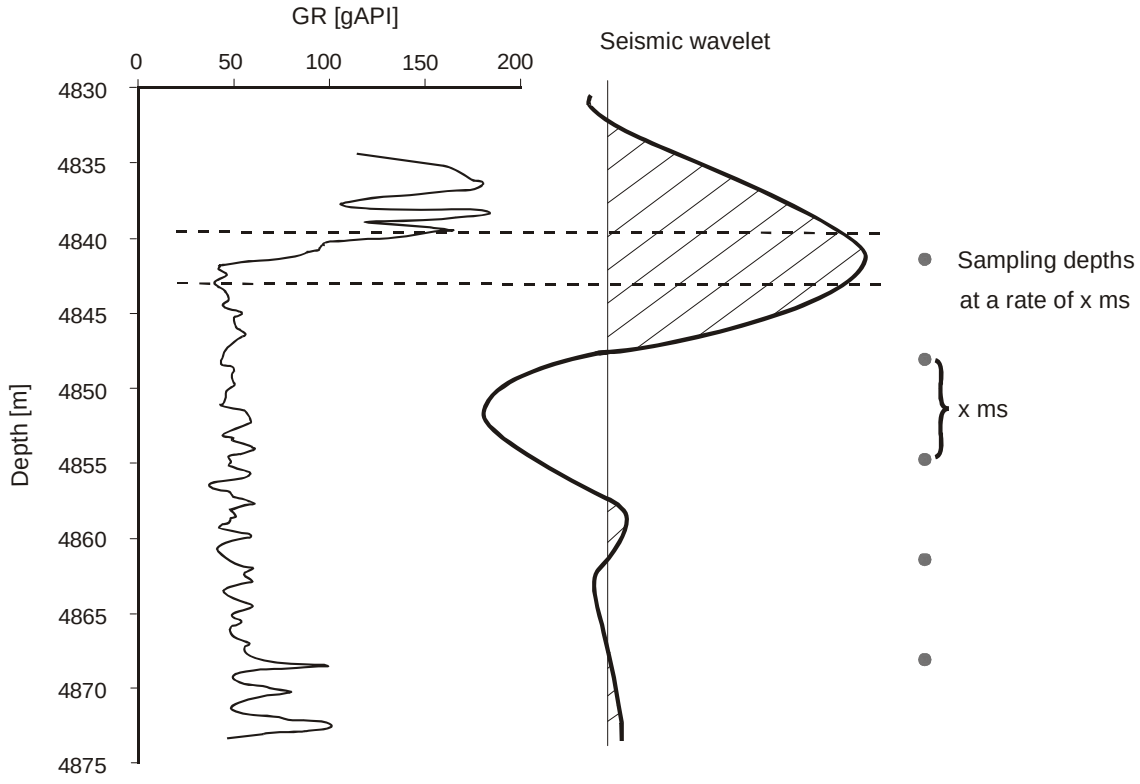

Fig. 1.13: Illustration for the position of the seismic amplitude within the Wustrow interval. The deflection is generated at the interface of the dense top layers and the underlying porous reservoir. The analyzed signals cover thus not the whole interval within the stratigraphic top and base of the

member. Five sampling points of constant time steps were chosen for the neural network classification to describe the overall wavelet character. The shown seismic wavelet does not represent a trace from the seismic volume.

1.3.3 Neural network technique

According to Trappe et al. (technical note) it was tried to reveal the reservoir quality by a conventional amplitude approach. While this technique resulted successful in other parts of the North-German basin (Trappe & Hellmich 1998, Hartung et al. 1993), the amplitude-anomalies for the investigated Wustrow horizon did not correlate to the reservoir parameters at the well locations. The seismic signals at reservoir depths presented a complex variation (Trappe et al., technical note) despite the similar porosities in the seismic volume.
So far it is not feasible to identify and quantify all the effects of lithological parameters and fluid type and -content on wave characteristics (Brown 1996). The combined effects of these parameters on seismic signals are occasionally intricate to resolve. However, it can be safely assumed that specific rock properties influence seismic signals distinctly and to different extents.
Therefore the DGMK-project used neural network techniques in order to reveal characteristic features in the wave signals.
The neural network classified the wavelets into groups of specific wave qualities, which are as distinct from each other as possible. These classes reflect differences in seismic signal characteristics which could have arisen from variations in reservoir properties.
After the categorization the output was tested with regard to relationships to known horizon attributes. Since valuable correlations were found, the seismic classes were used to derive reservoir properties qualitatively and quantitatively in zones without any well information.

1.3.3.1 Type of neural network

The following outline is based on published works from Trappe & Hellmich (2000), Callan (1999), Trappe & Schubarth Engelschall (2005), Arbib (1995) and discussions with Dr. R. Samiee (2005, geophysicist at TEEC, at that time).
The chosen neural network technique produces unsupervised classifications based on a self organizing feature map (SOFM) (Kohonen 1988). It consists of a two-dimensional, single layer of 8×8 neurons, which are all interconnected (Ritter et al. 1991).
The SOFM weakens and strengthens the connections in a manner that similar inputs are sent to neighbouring neurons. This learning process is carried out with a limited number of seismic patterns. These seismic patterns are extracted from random locations in order to minimize the influence of geological interpretations on the neural network output.
The input data represent amplitude, shape and lateral coherency of the seismic traces, which are found to describe best the characteristics of the different wavelets. The amplitude refers to the height of seismic deflection, the feature shape denotes particularly the breadths and numbers of deflections and the lateral coherency describes features of regularity in the seismic trace. More information especially regarding the used algorithm and the weighting of the signals was not attainable due to proprietary reasons. In order to reduce the input data the seismic traces were averaged within a window of 11×11 traces laterally and five samples vertically.
After the training process is completed (10.000 training steps), all the remaining seismic signals at the reservoir level are presented to the neural network and are classified.
The result is tested for stability by repeating the process with changed input parameters and by eliminating some training wavelets and predicting their outcome.

The defined classes of seismic signals and the forecast reservoir attributes are consequently charted against known attributes at the well locations to identify possible relationships. Additionally the distribution of the seismic classes was compared to the maps of petrophysical, petrological and sedimentological features to reveal further dependencies.

1.3.3.2 Results of the classification

The seven seismic classes defined by the neural network technique are presented in rainbow colours in figure 1.14. The map contains also the location of the 10 wells and the tectonic lineaments. The position and extension of the fractures and faults were derived by means of the coherency processing technique, which is explicated afterwards.

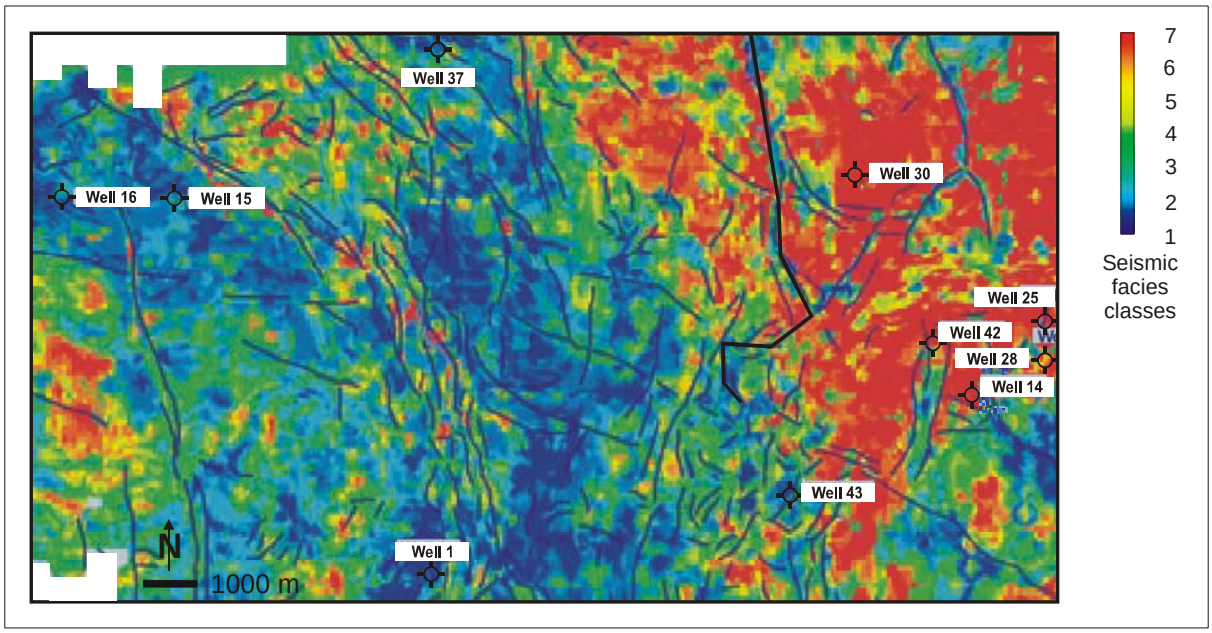

Fig. 1.14: Output of the neural network for the Wustrow horizon level. The classes are presented in rainbow colours. The black lines delineate the fractures and faults occurring in the Wustrow member. The red and yellow classes are predominantly encountered in the Eastern region the blue in the middle and western parts of the reservoir.

Relationships were identified to the average permeability, average density, diagenesis type, thickness, thickness × average porosity (tab. 1.1). No correlations were ascertained to average porosity, amount of eolian facies and cementation. These parameters are explained in the following section.

Reservoir attribute	Data source	Correlation to seimics	No correlation to seismics
Net thickness	Log data	X	
Average porosity			X
Porosity * thickness		X	
Average porosity	Core data		X
Average permeability		X	
Average density		X	
Eolian facies			X
Cementation			X
Diagenesis type		X	
Bituminisation		X	

Tab. 1.1: List of parameters exhibiting a dependence or independence on the seismic facies classification. The analysis was carried out by two methods: comparing the parameter at the well location with the corresponding facies class and confronting the attribute maps with the distribution of the seismic classes.

Figure 1.15 represents an example for a linear dependence between seismic facies classes and the parameter porosity × thickness at well locations.

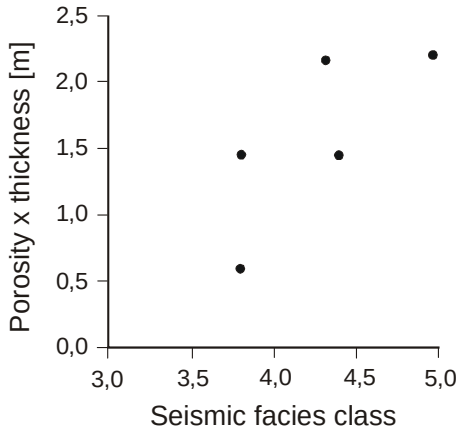

Fig. 1.15: Diagram of porosity × thickness of a well location versus corresponding facies class. A linear relation is observable. This type of plot represents one method to reveal possible dependencies. Modified after Trappe & Hellmich (2000).

An example regarding the graphical correlation of seismic classes to the distribution of a reservoir characteristic is illustrated in the overlay in figure 1.16. This relation to the major occurrence of diagenesis types and the consequent relation to average permeability is discussed in detail in chapter 3.1.1.

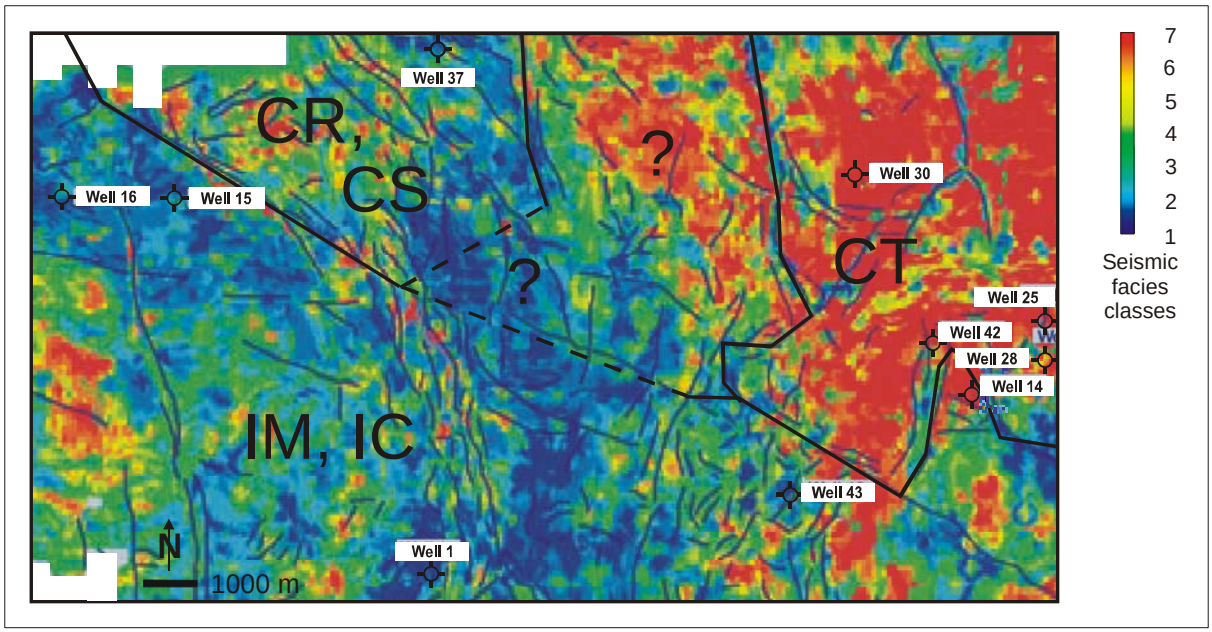

Fig. 1.16: Overlay of seismic facies classes and distribution of major diagenesis types. CR, CS, CT abbreviations refer to chlorite morphtyes, IC, IM abbreviations to illite morphotypes (chapter 1.2.4.1). The relationship is treated in detail in chapter 3.1.1. This overlay of an attribute map and the seismic classes represents one of the two utilized methods to reveal dependencies. Modified after Gaupp et al. (2005).

1.3.3.3 Explanation of the parameters compared to the neural network output and comments

All parameters represent average values mainly from the reservoir section of the Wustrow-member except for the feature total thickness.
Porosity and permeability were quantified on samples from the reservoir interval. The diagenesis types refer to the type and morphology of authigenic clay minerals in pore space. The bituminisation denotes the type and quantity of organic matter in pore space. The cementation is defined by the volumetric percentage of all authigenic minerals. The amount of eolian facies was derived by calibrating the GR curve with the sedimentary facies from core investigations and by extending the facies to uncored intervals based on the GR-log ("lithofacies upscaling" in Gaupp & Solms 2005).

Although seismic characteristics are strongly affected by the void space (Reynolds 1997) of the rocks no relation to average porosity was observed. This is remarkable and most probably due to the similar porosity within the reservoir, which consequently affects impedance uniformly. The correlation to total thickness × porosity is thus dependent on changes in thickness rather than on porosity. The parameter thickness was determined erroneously as that of the whole Wustrow member instead of the well section below its dense top layers (fig. 1.13). Unfortunately the DGMK-project used densities of the solid components and not of the whole rock. Therefore bulk densities were calculated in the present study from matrix-densities and porosities and compared to the seismic classes. In contrast to the DGMK-project, no correlation was found for the slightly changing values. This is conforming to the result that porosity does not correlate to the distribution of seismic classes as bulk density in sandstones is primarily dependent on porosity.

1.3.4 Further techniques of seismic signal interpretation

In the course of the DGMK-project additional methods were applied to investigate the seismic signals within the Wustrow reservoir:
The “reference pattern recognition” extracts seismic signatures at well locations with known properties and compares them to wavelets in the 3D-seismic volume. Correspondences to the reference trace could imply similar reservoir properties as the qualities encountered at the selected wells. The aim of this approach was to reveal reservoir characteristics in undrilled areas. This method was also used to test the output of the neural network. The reference pattern recognition delivered indeed a similar distribution of good and poor reservoir qualities as the seismic facies classification.
The “coherency processing technique” calculates the similarity of neighbouring wavelets. Generally zones of comparable lithology produce similar seismic responses, while seismic signals change strongly in the vicinity of fractures and faults. This method is used to track and map lineaments. Consequently the neural network output was assessed for seismic contrasts deriving from tectonic structures. This resulted in excluding the blue seismic class and the horizon information at the well 37 for the reservoir interpretation as the borehole was found to be too close to multiple faults. In some other areas the seismic classes could not be related either to reservoir properties or to effects from tectonical structures.

1.3.5 Weak points of the techniques

Principally the main advantage of the utilized techniques as compared to conventional methods consists in combining many attributes into classes and detecting also weak dependencies within a multivariate database. In contrast to geostatistical approaches and the mapping of single attributes the interrelationships of the variables do not need to be considered. It represents generally a competitive tool when single variable plots fail (compare studies in Porwall et al. 2003, Helle & Bhatt 2002, Harris & Pan 1993).
However, several weak points still exist, particularly with regard to the usability of neural network techniques:

- The lateral resolutions of the maps with the seismic classes and the reservoir properties differ strongly which leads to uncertainties when examining parameters by means of the overlay method.
- The investigated reservoir and its overburden are segmented by a dense system of fractures. These inhomogeneities can provoke a complex and poor seismic signal, which renders the interpretation ambiguous in some parts of the reservoir (pers. comm., R. Samiee, 2005, geophysicist at TEEC at that time).
- The seismic wavelets could be co-determined by parameters not considered so far, like internal reverberations of seismic waves or water saturation. These features, which do not indicate reservoir quality, could likewise affect the neural network output and will be discussed in the following chapters.
- A dome of the Zechstein salt extends over the seismic volume and can influence the distribution of seismic classes through its dampening effect on seismic wave energy.
  Figure 1.17 presents an isohypse map of the Zechstein top based on the Geotectonic Atlas of northwest-Germany (Baldschuhn et al. 1997). The base of the structure is essentially horizontal (based on maps in Tanner et al. 2005). The position of the diapir is also illustrated in Tanner et al. (2005), however, the extent of the salt dome shown there is erroneous due to mistakes in the determination of the geographic position of the seismic volume.

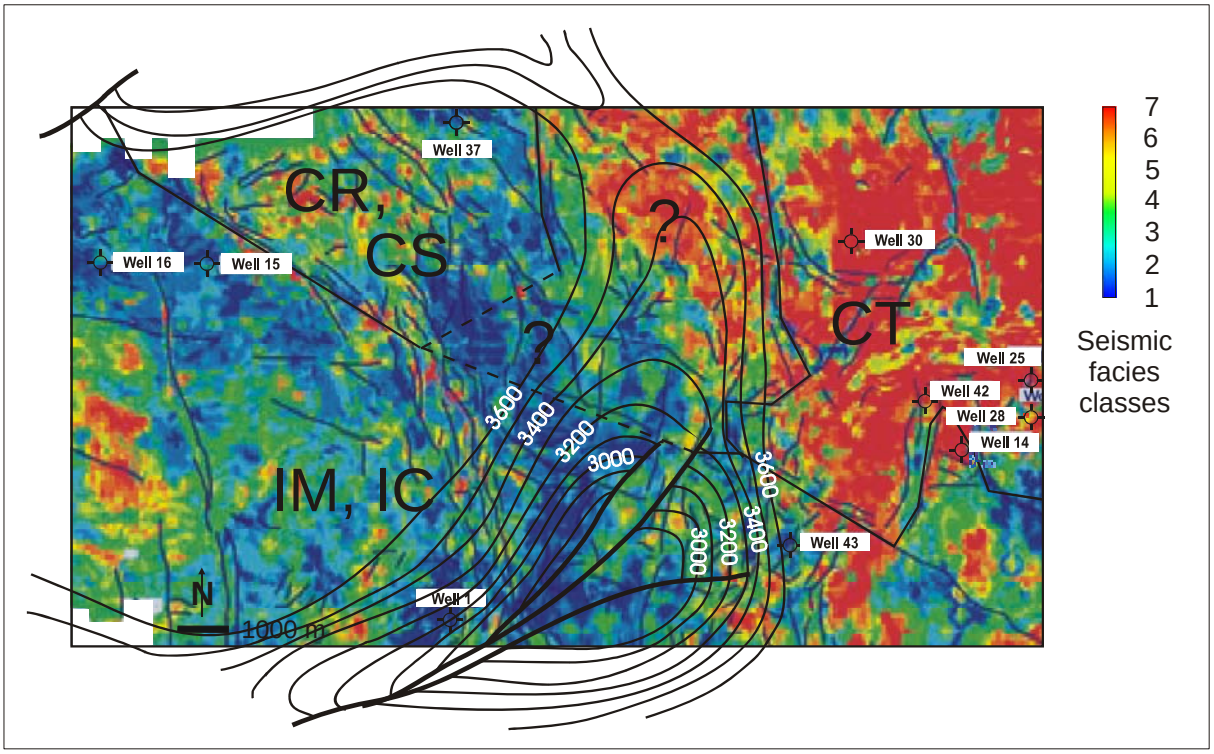

Fig. 1.17: Overlay of seismic facies classification and isopach map of the Zechstein salt dome. The magnitudes refer to the depth of the tops structure in meters, the lower boundary of the diapir is horizontal. The data for the salt dome are derived from Baldschuhn et al. (1997). No prevailing impact of the dampening effect on the seismic facies classification is observable due to the extension of the structure above reservoir parts with red and blue classes. This map is not conform to the overlay presented in Tanner et al. (2005) due to their erroneous determination of the geographic position of the seismic volume.

According to the overlay in figure 1.17 the salt dome covers a considerable part of the Wustrow interval and will thus assuredly induce dissimilar wave energy loss in the upper waves. Nevertheless, a prevailing impact of the salt structure on the seismic classification is not evident as the dome overlies parts with red and blue seismic classes.

- The differences in seismic wavelets are supposed to be only a function of the properties of the reservoir section and intercalated and underlying shale and saline layers. This assumption is only valid as long as the dense layers and their overburden are indeed seismically uniform throughout the examined volume.
- There exists general criticism in regard to seismic attribute interpretation (e.g. Brown 1996) and the results from Neural Network techniques (e.g. Arbib 1995).

  Furthermore, many seismic features appear to lack clear geological significance (Lindseth 1982). To cite an example, a frequently utilized attribute represents the 'variation in instantaneous frequency', which was related to stratigraphy. According to Yilmaz (1987) it turned out repeatedly difficult to interpret all the variation. Furthermore, Dvorkin et al. 2002 state, based on their working experience, that the interpretation of seismic features misses often geological understanding. So, for instance, porosity from seismic slownesses are derived by ignoring the reducing effects on velocity from the presence of petrographic clay (Dvorkin et al. 2002, Avseth et al. 2000).

  The negative comments on the results of neural network techniques in hydrocarbon exploration concern, likewise to the seismic signal interpretation, the uncertainty of their geological sense (Brown 1996). Furthermore, it is often claimed that the pre- and post-processing is not bare of a subjective component (Swingler 2001).

2. Approach and Methodology

2.1 Introduction

The seismic facies classes reflect differences in seismic traces with respect to amplitude, shape and lateral coherency. According to basic theory on seismic wave propagation and discussions with Dr. R. Samiee (geophysicist at TEEC at that time, 2005) these seismic attributes are mainly a result of contrasts in compressional impedance, i.e. the product of longitudinal velocity and bulk density. Therefore these parameters were tested for dependencies on lithological properties. After a few investigations the main focus was directed on the compressional velocities for the following reasons:

The analyses on bulk density did not give evidence for any relevant dependence on reservoir properties except for porosity. The average densities of the seismic volume are very similar and range within 2,51 and 2,58 g/cm³. Table 2.1 illustrates the ranges and mean values of in-situ densities of the Wustrow member for the seismic volume.
The bulk densities of the eolian plugs from the seismic volume vary likewise barely. The average densities of wells range from 2,35-2,48 g/cm³ (see appendix A-9).

Well	Diagenesis type	Mean porosity [%]	In-situ bulk density [g/cm³] 2,00 – 2,80
Well 1	IC+IM	7,9	
Well 14	IC+IM	9,1	
Well 15	IC+IM	8,2	
Well 16	IC+IM	8,0	
Well 43	IC+IM	7,0	
Well 28	CT	11,2	
Well 30	CT	11,2	
Well 37	CT,CR, CS	11,7	n.a.
Well 42	CT	9,7	

Tab. 2.1: In-situ bulk densities for the Wustrow member within the seismic volume. Densities derive from wireline measurements. The ranges are presented by the mean magnitude as vertical line and by the 25 and 75 % percentiles as ends of the boxes. The interval from 2,00 to 2,80 g/cm³ represents the range of densities for shale and shaly sandstones within these depths (Wohlenberg 1982, Schön 1998). Porosities represent mean values determined on cores. The bulk densities are very similar and range around 2,55 g/cm³.

Furthermore the DGMK-project and own investigations ascertained no correlation between the distribution of bulk density and seismic facies classes.
On the contrary the initial research on compressional velocity looked very promising. So the velocities of comparable eolian plugs vary according to the type of authigenic clay mineral in pore space. A velocity-porosity plot (fig. 2.1) illustrates the distinct ranges in dry plug speeds for eolian sandstones of illite and chlorite alteration. At 11 % void volume, for instance, chloritized samples differ approximately between 1700 till 2100 m/s and illitized plugs from 2300 till 2900 m/s. Porosity thus appears not to control the variability in compressional

velocity of these eolian samples. In addition, the travel times of plugs presented, in contrast to density, a large variability of up to 100%.

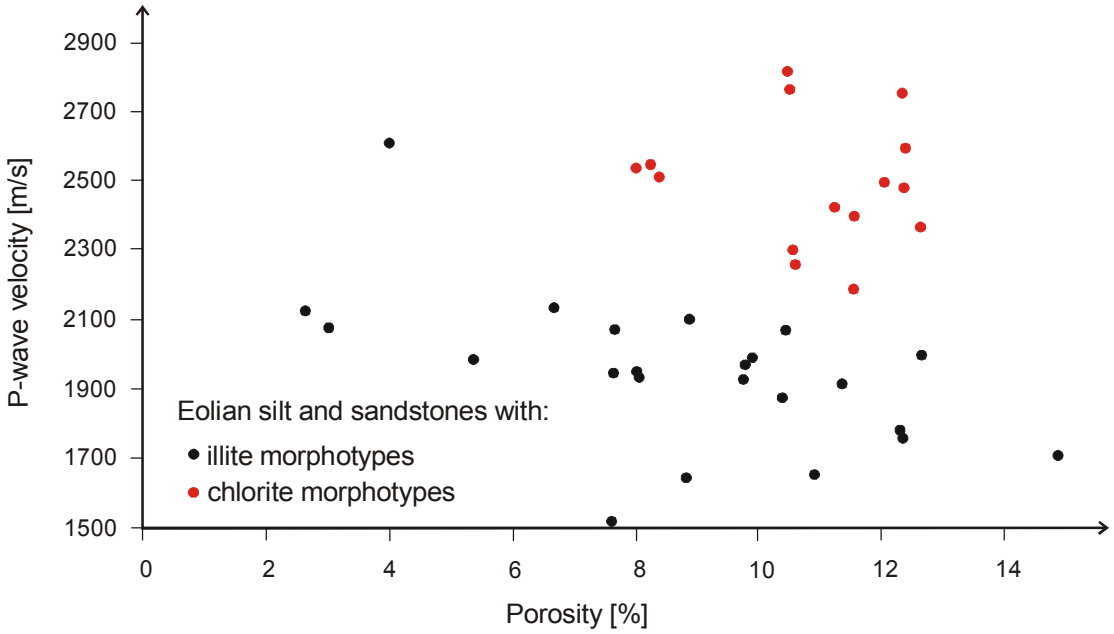

Fig. 2.1: Chart of compressional velocity and porosity for illitized and chloritized eolian sandstones. Velocities determined on cores. Velocities plotted against porosity due to their negative interdependence (compare Wyllie 1956). Velocity distinction is clearly visible according to occurring diagenesis type. At 11% porosity, for instance, illitized plugs vary from 1700 to 2100, chloritized plugs from 2200 to 2700 m/s.

During the investigations it was found that at the field scale the in situ-velocities from wireline logs manifest crucial relations to reservoir characteristics:
Table 2.2 lists the sonic speeds integrated over the Wustrow member without its top layers (see chapter 4.1.1) from wells within the seismic volume and its surroundings. The box illustrates the range of magnitudes within the 25 and 75 % percentiles and the vertical line represents the average velocity of the well. The boreholes are differentiated according to the occurring diagenesis type.
It is palpably evident that the average sonic speeds vary distinctly according to the clay mineral type in pore space and permeability.
The correlations of in-situ velocity and plug speeds to these and additional properties are explicated in detail in the following chapters.
Furthermore, the void volumes in the seismic volume appear not to affect solely the in-situ rock speeds. The comparatively higher sonic velocities are namely encountered in the sections of higher porosities and vice versa.

The configuration of the wave traces could also be co-determined by the lithologic and seismic acquisition parameters which induce seismic energy loss. Variations in pore gas content, for instance, provoke heterogeneous signal dampening throughout the seismic volume which potentially modifies wave traces distinctly. Such inelastic processes are likewise examined on their potential influence on seismic attributes and hence on the distribution of seismic facies classes.

	Diagenesis type	Mean porosity [%]	In-situ velocity [m/s]
Well 1	IC+IM	7,9	
Well 5	IC+IM	7,4	
Well 9	IC+IM	11,0	
Well 15	IC+IM	8,2	
Well 16	IC+IM	8,0	
Well 26	IC+IM	12,7	
Well 40	IC+IM	9,6	
Well 41	IC+IM	7,8	
Well 43	IC+IM	7,0	
Well 19	CT	15,6	
Well 20	CT	7,8	
Well 25	CT	n.a.	
Well 27	CT	10,8	
Well 30	CT	11,2	
Well 32	CR,CS, CT	12,0	
Well 35	CR,CS, CT	12,8	

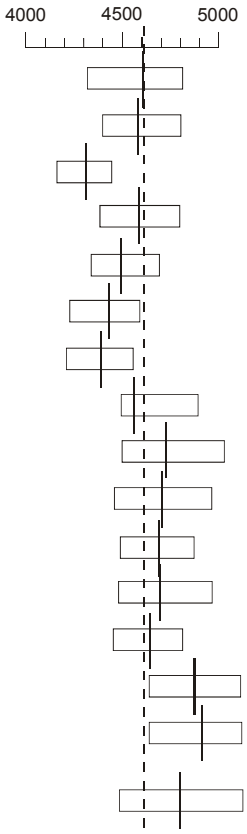

Tab. 2.2: Magnitudes of sonic log velocity as in-situ speed for wells differentiated according to the predominating diagenesis type. Data presented also from wells outside the seismic volume. The ranges are presented by the mean magnitude as vertical line and by the 25 and 75 % percentiles as ends of the boxes. The interval from 4000 to 5000 m/s represents the range of compressional velocity for shale and shaly sandstones within these depths (Schön 1998). Core porosities are given as mean values. The presented velocities are integrated over the Wustrow horizon. Wells of illite and chlorite alteration exhibit distinct ranges in compressional velocities. Well 43 deviates from this trend most probably due to its minimum void porosity. Wells with low void volume demonstrate comparatively high velocities and vice versa. This trend opposes the general behaviour of wave speed and porosity.

2.2 Approach

In order to individuate the petrophysical parameters affecting both compressional velocity and permeability the following approach was taken:

According to theory (Wilsom 2000) the compressional velocity of elastic waves is codetermined by the rigidity of the medium, which is represented in the formula for velocity by the elastic constants: compressional modulus K and shear modulus μ.

$$vp = \sqrt{\frac{K + 4/3 * \mu}{d}}$$

with vp compressional velocity in m/s; k compressional modulus and μ shear modulus in GPa; d density in kg/m³

Figure 2.2 demonstrates the dependence of longitudinal speed on the stiffness, presented as uniaxial compression strength (after McNally 1987).

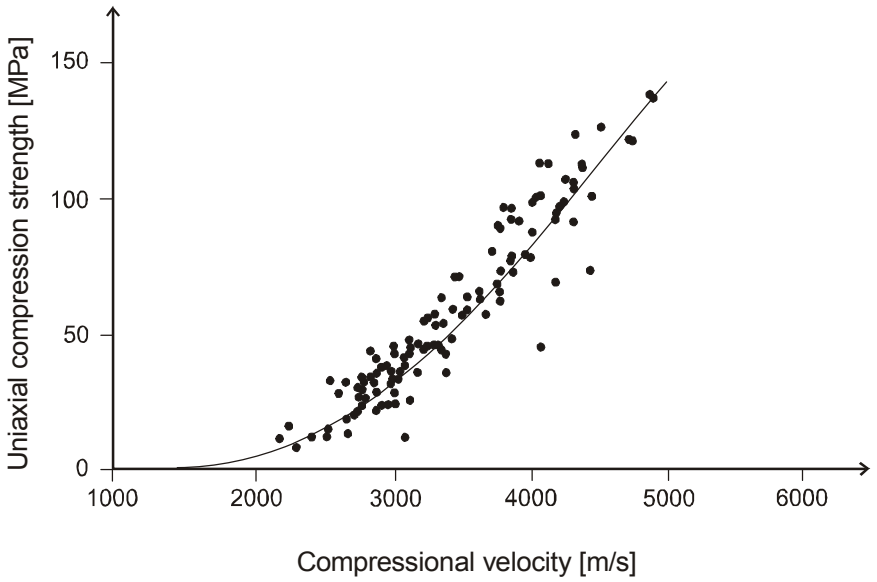

Fig. 2.2: Uniaxial compression strength and corresponding longitudinal velocities of sandstones (German Creek formation, Queensland). The speed increases exponentially with the compression strength and evidences its dependence on the rigidity of the rock framework. After McNally (1987).

The p-wave velocity of plugs is therefore tested on its dependence on several micro- and macro textural characteristics, e.g. types of grain contact and total petrographic clay content, which are believed to influence the rigidity of the porous medium. The investigated features represent or determine also reservoir characteristics of the Wustrow member. If pertinent relations are descried, the possibility is evaluated to extend those relations to seismic dimensions.
Other investigations focus on the question to what extent the seismic facies classes are a product of parameters evident at the field scale. So, for instance potential differences in stratigraphic features could provoke resonance effects and affect seismic wave traces distinctly.

Generally compressional velocities manifest a negative correlation to void volume (compare e.g. the classic paper of Wyllie et al. (1956). Many exploration studies evidenced a primary influence of seismic speed from average porosities (e.g. Brown 1996, Taner & Sheriff 1977, Rummerfield 1954; Mathisen & Budny 1990 and Trappe & Hellmich 2000 for Rotliegend reservoirs). Therefore variations in seismic attributes have been preliminary attributed to dissimilarities in average porosities.
It is important to note that the seismic facies classes do not reveal any correspondence to average porosity (Trappe et al. 2005 and chapter 1.3.3.2). This result is most probably caused by the small alterations in porosity within the seismic volume. Also when examining additional wells from the surroundings of the seismic survey no clear dependence on porosity becomes apparent (tab. 2.2). In opposition to the general velocity-porosity behaviour, the comparatively high porous well intervals exhibit even higher speeds and vice versa. The distinctions in sonic velocity for the regimes of different reservoir properties are hence not a function of variations in porosity.

This outcome demonstrates that other rock characteristics than porosity have determined the seismic wave speeds in this reservoir.
These features and their potential influence on compressional wave characteristics are analyzed in the following chapters. Thereby the investigative focus is set on the petrophysical

basis for the correlations to diagenesis types, average permeability and intensity of bituminisation.
In order to individuate relevant features influencing compressional velocity and attenuation and investigating their dependence on reservoir properties, some of the analyses were conducted on selected samples. These selected specimens are comparable regarding most of the lithologic properties but vary distinctly concerning compressional velocity and permeability.

2.3 Methodology

2.3.1 Utilized data

The present study utilizes information from:

- the DGMK-study 593-8, published by Gaupp et al. (2005), regarding:
  - sedimentological and petrological investigations (Gaupp & Solms 2005),
  - processing and interpretation of three-dimensional seismic data (Trappe & Schubarth-Engelschall 2005),
  - three-dimensional tectonic modelling (Tanner et al. 2005),
  - modelling of burial history, temperature evolution, and maturity, generation migration and accumulation of hydrocarbons (Schwarzer & Littke 2005),
  - findings derived by combining the single investigations,
  - and the raw data from core descriptions, wireline logs and standard analysis on thin sections;

- additional data gained on plugs by:
  - measurement of ultrasonic compressional velocities,
  - Nuclear Magnetic Resonance (NMR),
  - Scanning Acoustic Microscopy (SAM),
  - Mercury Capillary Pressure Curves,
  - micro-textural studies on thin sections to quantify
    - amount of load bearing clay minerals,
    - particle contact conditions,
    - pore geometrical attributes by image analysis,
    - volume of components not contributing to rigidity,
  - petrological data by optical microscopy,
  - and by combining the quoted data.

Scanning Acoustic Microscopy was performed by A. Caron at the ‘Fraunhofer Institute für Zerstörungsfreie Prüfverfahren (IzfP)’ in Saarbrücken. Nuclear Magnetic Resonance was carried out by R. Kappes at the ‘Institut der Geowissenschaftlichen Gemeinschaftsaufgaben (GGA)’ in Hannover.

2.3.2 Methods

Some of the studies utilize methods which represent own developments and are comprehensible in the context of their application. Therefore it was decided to explain these and other techniques in the according chapters. These methods comprise micro textural studies on thin sections, Nuclear Magnetic Resonance, Scanning Acoustic Microscopy and Mercury capillary pressure curves.
The ultrasonic velocity measurement, the determination of the mineralogical composition and grain size analyses by means of optical microscopy are described in the following.

2.3.2.1 Measurement of ultrasonic compressional velocity

The ultrasonic signals for velocity measurements were generated by a pulse generator (US-generator, Geotron USG 11) and sent into the plugs through a piezoelectric transducer. A high viscosity rubber was used for acoustic coupling. The received signal was amplified (RFT 3205) and digitized (TRB 4000, Krenz). The compressional velocities were determined with software for first arrival picking (TRS 2000, Krenz). The setup of the measurement is illustrated in figure 2.3. For further information on the equipment please refer to Malischewsky & Schnapp (2003).

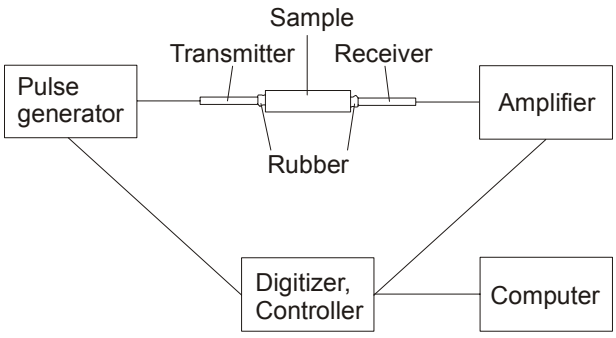

Fig. 2.3: Main units of ultrasonic measurement.

Velocity measurements are conducted in x, y, z - directions under atmospheric conditions on samples in a room dry state.
The cylindrical plugs feature dimensions of 3 cm × 3 cm. The end surfaces and the side lengths of the plugs are ground parallel to within 0,05 mm. The lengths of the travelling paths were measured with a micrometer screw to within 0,01 mm.
The samples did not undergo any treatments (e.g. mercury injection) before the ultrasonic recordings except for desalination and drying at 80°C for 8 hours.
For velocity measurements on granular assemblies the wavelength must exceed the mean grain size by at least a factor of 5 (e.g. Han et al. 1986). The frequency (f) of the p-wave is around 800 kHz in the sample. By applying a low plug velocity (c) of 1600 m and an average grain size of 0,1-0,2 mm for the formula $\lambda = v / f$ the wavelength (λ) results approximately 10-20 times larger than the dimension of an average grain.
The accuracy was determined by the comparison between actual travel time in Lucite and calibrated result and amounted to 0,8 %. The repeatability constituted to approximately 1% (see appendix A-12) except for some plugs with rough surfaces.
The determination of the device-specific delay time, caused by the generation and registration of the signals, and the calibration were conducted on Lucite prisms of different lengths and known velocity.
Most of the plugs contain laminations caused by alterations in grain sizes. P-wave velocities crossing these structures were 2%-42% (average 14%) lower than velocities parallel to the laminations. If laminations were present, only those velocities crossing the layers were used for the investigations. The specimens presented barely any fissures.
The velocity measurements were performed on all available plugs.
The attained p-wave velocities vary within the typical range of velocities for dry, consolidated sandstones (compare e.g. Fricke & Schön 1999).

2.3.2.2 Optical microscopy

Optical microscopy was used to derive basic mineralogical composition and to produce digital images for grain geometrical studies. Microphotographs were also applied for rigidity and pore geometrical studies.
The examinations were performed by means of a binocular microscope (Axioplan 2©, Carl Zeiss Micro Imaging GmbH), a digital colour camera (HV C20© , Hitachi) and a software programme for real time photo assessment and post-processing (Matrox Intellicam Interactive©, Matrox Electronic Systems).

Mineralogical composition

The mineralogical composition was quantified for detrital quartz, feldspar, lithoclasts, for authigenic calcite, anhydrite, feldspar, hematite illite and chlorite, and pores. Additionally, the relative amounts of etched to non etched feldspars were determined for comparative conclusions on the intensity of secondary solution. The quantification was restricted to all occurring minerals, however, without distinguishing further properties like the origin of quartz or lithoclasts as these features barely affect elastic wave characteristics (Wang 2001) or permeabilities.
The five thin sections of samples A-E were analyzed by point-counting 400 points per sample (automatic point-counter, Model G, Prior Scientific Instruments Ltd). The analyses were repeated and their results examined for accuracy with the graphs of uncertainty compiled by Howarth (1998). The outcomes fell within and at the borders of 95 % confidence.
It is important to mention that the proportions of voids could result underestimated and the abundances of especially illite fibres overrated. This is due to the fact that the quantification was performed with transmitted light where all visible minerals throughout the thickness of the thin sections are counted.
The mineralogical composition is listed in the appendix (A-9) and described shortly in the following.

Grain size analyses

Grain sizes were quantified on enlarged printed microphotographs. The procedure for producing these images is explained in chapter 3.1.2.2. The dimensions of a particle were determined with a ruler to a precision of 0,015 mm of real length. The lengths comprise the maximum and its perpendicular minimum diameter. All the quantitative grain-size analyses were based on the maximum diameters except for the aspect ratio which was calculated as the ratio of the two spans. The quantification was restricted to detrital components; however, syntaxial quartz cements could be included in the analyses. The raw data is listed in the appendix (A-3). The cumulative grain size distribution and calculated parameters (according to Füchtbauer 1988 and Pettijohn 1975) are presented in the following.

2.3.3 Samples

The available plugs represent Wustrow sand- and siltstones of the eolian dry, eolian damp and mudflat/lake environment (see appendix A-13). The samples were taken from cores by the petroleum companies. The sample set constitutes to 60 + 87 specimens from two wells of illite authigenesis and to 15 samples from one well featuring chlorite morphotypes. The cores underwent no treatments except for desalination and dehydration by 80° for 8 hours. The specimens were provided by RWE-Dea.

The mineralogical, petrophysical and sedimentological data for these specimens were gained in the course of the DGMK-project and this study. The mineralogical information was acquired by pointcounting analyses; porosity, permeability and density were determined by means of different standard techniques (e.g. He-injection, N_2-injection, Mercury Capillary Porosimetry).

The rigidity studies were performed on five samples that were chosen for their suited properties. The samples A, B, C, D, E represent core plugs taken from two wells at the same depth in the Wustrow member. The boreholes are located within the seismic volume and appertain to either the red or the blue seismic facies classes. The specimens derive from the "eolian dry" (see appendix A-13) environment.
The samples are rich in detrital quartz and bare of matrix and can be classified as sublitharenite and subarkose (Pettijohn et al. 1973) (fig. 2.4). The proportions of lithoclasts are slightly elevated for the illitized samples. In correspondence to the seismic facies class samples A-C are characterized by chlorite (CT) and specimens D and E by illite alteration (IM+IC). These morphotypes are the sole authigenic clay minerals in their samples (the term authigenic minerals in this study includes the illite morphotype IC despite its probable allochthonous origin). The chloritized samples exhibit comparatively larger proportions of blocky precipitates due to their more intense anhydrite cementation.
The maximum and minimum particle diameters amount to 0,21-0,28 and 0,13 mm, respectively, and are similar among the specimens. The aspect ratio of the subrounded constituents is likewise comparable and reflects an intermediate sphericity. The very good sorting and the skewness of these fine grained sandstones (Folk & Ward 1957) result rather congruent and comply with the core interpretation of the DGMK-project for an eolian facies (Füchtbauer 1988, Tucker 1993).
The results of the grain size and shape analysis are summarized in table 2.3 and figure 2.5. The complete database is adjoined in the appendix (A-3).

Samples	Mean diameter [µm]	Aspect ratio [ ]	Sorting [ ]	Skewness [ ]
A	217	0,58	-0,60	-0,19
B	216	0,59	-0,49	0,08
C	281	0,53	-0,50	-0,25
D	247	0,61	-0,53	0,07
E	210	0,67	-0,46	-0,03

Tab. 2.3: Particle geometrical aspects of the five sample determined on thin sections. The five samples present very good sorting according to the criteria of Folk & Ward (1957), the aspect ratio indicates resembling particle shapes.

The porosities and bulk densities are comparable and range from 10,0 to 11,5 % and 2,367 and 2,430 g/cm³, respectively. In contrast, the permeabilities vary very strongly despite the similar void volumes. The permeabilities differ from 0,05 to 118,8 mD, thus by a factor of 2400. The samples of chlorite alteration manifest the highest but still different fluid conductivities.
The compressional plug speeds result dissimilar and vary by a maximum of 47 %. The lowest velocities are measured for the illitized probes and vary far less (40 m/s) than the speeds of the chloritized sandstones (650 m/s).
The specimens contain subtle laminations due to variabilities in grain sizes. The inhomogeneities are orientated across the axis of the cylindrical plug. The chloritized samples comprise additionally some isolated, mm large and utterly cemented grain aggregates.

The epoxy impregnated thin sections were cut across the laminations and parallel to the axis of the cylindrical plugs. They provide a section parallel to the path of the ultrasonic wave and the fluid flow direction in the permeability measurement.
The velocities of the five samples exhibit a directional dependence of 1 to 4 % with the lowest speeds transverse to the laminations.
Permeabilities were measured parallel to the plug axis. An anisotropy of these samples is not ascertained (pers. comm., R. Möller, 2004, Laboratorium Wietze) but supposable.

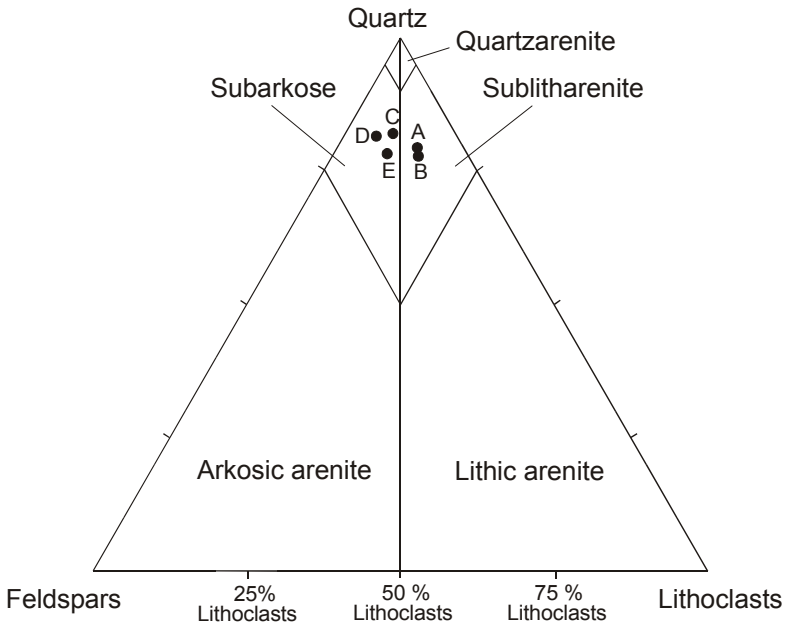

Fig. 2.4: Ternary diagram for sandstone classification (after Pettijohn et al. 1973). Proportions of detrital quartz, feldspars and lithoclasts were determined by means of pointcounting (400 counts). No matrix is present. Proportions are given in percent. The five samples present small variations in composition of accessory minerals and plot within the fields of subarkose and sublitharenite.

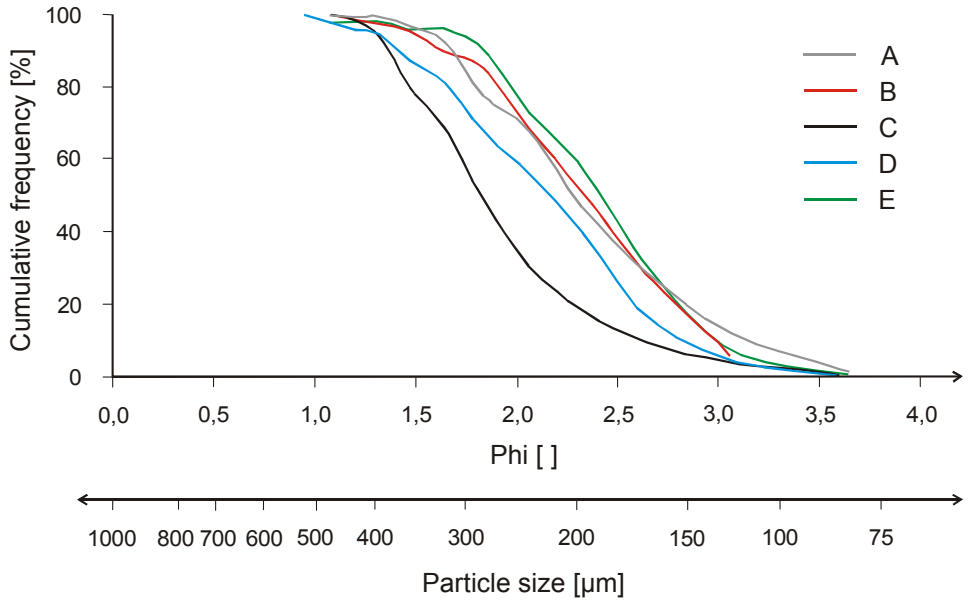

Fig. 2.5: Cumulative frequency and particle size determined on thin sections. The sizes are given as Phi (-log[diameter; 2]) and in µm. The five samples are composed of similar particle sizes and comparable sorting.

These five samples are similar in mineral composition, porosity, density, particle shape but diverge strongly in longitudinal velocity and permeability (tab. 2.4).
The investigations on abundances of load bearing clay, on particle contact conditions and on pore geometrical aspects were particularly conducted on these samples.

Samples	A	B	C	D	E
Diagenesis type	CT	CT	CT	IC + IM	IC + IM
Porosity [%]	10,47	11,56	11,52	11,30	10,10
Bulk density [g/cm³]	2,40	2,37	2,39	2,39	2,43
Facies	dry eolian	dry eolian	dry eolian	dry eolian	dry eolian
Grain size [µm]	217	216	281	247	210
Sorting, skewness	very good, equal	very good, equal	very good, equal	very good, equal	very good, equal
Mineralogic composition	similar	similar	similar	similar	similar
Point counted porosity	10,2	9,6	10,1	9,7	9,2
Sandstone type	sublitharenite	sublitharenite	subarkose	subarkose	subarkose
Permeability [mD]	1,40	16,47	118,8	0,213	0,053
P-wave velocity [m/s]	2814	2440	2160	1950	1990

Tab. 2.4: Petrological, sedimentological and petrophysical properties of samples A-E. Permeabilities and velocities were measured across the laminations. The complete database is given in the appendix (A-9). Samples A-C are of chlorite, samples D-E of illite alteration. The properties are similar except for the strongly varying permeabilities and compressional velocities.

3 Parameters affecting compressional velocity and attenuation at the plug scale

3.1 Effects of clay minerals between particle contacts on compressional velocity

3.1.1 Relation of seismic facies classes to clay mineral morphotypes and average reservoir permeability

The DGMK-project ascertained a graphical congruence between the distribution of different clay minerals and of seismic facies classes (Gaupp et al. 2005). As some of these diagenesis types strongly influence fluid mobility, the correlation is of fundamental interest.

Figure 3.1 presents the distribution of the 5 dominating diagenesis types of clay minerals in the seismic volume. The lines delimit the estimated occurrences of the morphotypes. This map is composed from an overlay published in Gaupp & Solms (2005). The original chart is a product from the integration of the coherency processing technique (Trappe & Schubarth-Engelschall 2005), three dimensional structural modelling (Tanner et al. 2005) and sedimentological and petrological investigations (Gaupp & Solms 2005). It must be noted that the boundaries represent a possible but not exclusive interpretation of the diagenesis model.
It is important to add that, according to own investigations on the petrographic data from the DGMK-project, the volumetric abundances of the described diagenesis types vary distinctly within the eolian Wustrow intervals. Illite morphotypes within the illitized sandstones of the large volume are at least 3 to 9 times more frequent than chlorite morphotypes in the chloritized sandstones. Their average abundances range within 2,4 and 8,1 %, and 0,3 and 1,2 %, respectively, in the well sections of the seismic volume. The provinces of chlorite authigenesis can contain illite morphotypes but their frequency in such parts of the seismic volume is evanescently small. The regions of illite diagenesis feature parageneses of both clay mineral types. However, the proportion of the chlorite morphotypes constitutes less than 0,5% in the illite altered regimes within the seismic volume.

Based on figure 3.1 illite meshwork appears to occur in the bulk of the seismic volume while the northeastern region is dominated by chlorite morphotypes. CR-, CS-, CT-minerals can form a paragenesis but with largely varying proportions in the reservoir. The red area within the large survey (bottom of figure 3.1) and outside of the seismic volume demarks the occurrence of the hematite type, which is known to favour good reservoir properties. According to the petrographic database of the DGMK-project (appendix A-9) the latter precipitate is barely present in the seismic volume and is hence not examined in the present study.

Trappe & Schubarth-Engelschall (2005) and Gaupp & Solms (2005) report that the distribution of the seismic facies classes coincides with the incidence of the diagenesis types.
Figure 3.1 illustrates the distribution of the clay morphotypes and the seismic facies classes. Table 3.1 lists the wells with the corresponding diagenesis type, average porosity and average permeability differentiated according to the seismic facies classes, based on data from the DGMK-project. Borehole 37 was placed apart due to its vicinity to a fault zone which is responsible for the poor seismic signal quality in that location (Trappe & Schubarth-Engelschall 2005).

	Porosity [%]	Permeab. [mD]	Diagenesis type	Seismic facies class
Well 1	9,9	0,12	IC, IM	Blue
Well 15	10,7	0,26	IC, IM	Blue / green
Well 16	10,5	0,28	IC, IM	Blue / green
Well 43	7,0	0,10	IC, IM	Blue
Well 42	9,7	n.a.	CT	Red
Well 14	9,1	0,20	IC, IM	Red
Well 28	11,2	n.a.	CT	Red / yellow
Well 30	11,2	49,15	CT	Red
Well 25	9,5	n.a.	CT	Red
Well 37	13,5	8,67	CR, CS	Blue / green (?)

Tab. 3.1: Diagenesis types, porosities and permeabilities from Wustrow well intervals within the seismic volume differentiated according to seismic facies classes. Well 37 is not considered due to its location within a fault zone, which provoked poor seismic data quality in that area. The table documents that, the blue and green seismic groups appear to correspond to well sections of illite alteration and reduced permeability. The red and yellow categories seem to reflect mostly chlorite diagenesis types, their predictability for reservoir permeability is not evident from the data in this table.

Table 3.1 and figure 3.1 suggest that especially the blue and green classes correspond to the illite cemented regions of the reservoir and to poor reservoir performance. The sensitivity for the red areas to reflect only chlorite facies is not obvious throughout the chlorite provinces and should be validated moderately indicative. However, the predominant distribution of red and yellow classes corresponds to the eastern part of a large region featuring high reservoir permeabilities (up to 250 mD). Unfortunately the red and yellow regions lack more boreholes of known permeabilities.

There exist a few exceptions in the general correlation:

- The reservoir interval in well 14 is located within a zone of a red seismic class although it was characterized by Gaupp & Solms (2005) as an IC and IM-cemented section.
- The region of illite authigenesis contains some smaller red fields.

Since these inconsistencies could be due to the different resolutions of the seismic and the attribute reservoir maps, the author suggests that the seismic facies groups correlate to the *major* occurrence of diagenesis facies. Furthermore, the emphasis for the forecast of reservoir properties should be placed on the blue and green seismic classes.

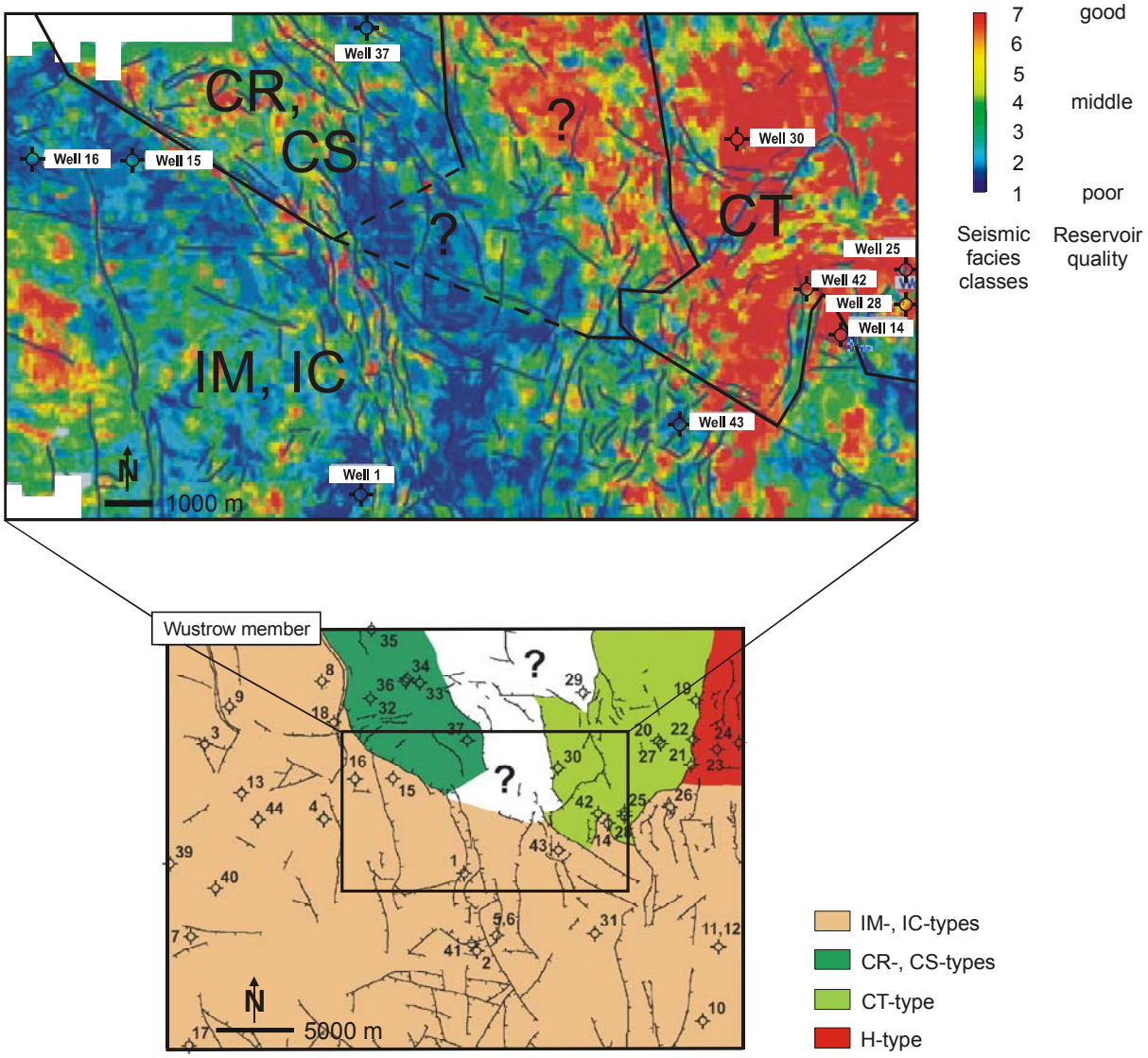

Fig. 3.1: Below: Large rectangle represents region with sedimentological and petrological data and occurrence of diagenesis types, smaller rectangle demarks the seismic volume for which seismic facies classes were generated. The location of well 30 is wrong in the map, its position should be shifted to the east (compare map above). The confining lines for diagenesis types are based on the diagenesis model and follow tectonic lineaments (after Gaupp & Solms 2005). These compartments separate the western and southern province with dominant illitization from the regime, where illite morphotypes are barely present.
Above: Occurrence of diagenesis types within the seismic volume and distribution of seismic facies classes. The distributions of red and yellow classes and of blue and green classes coincide largely with the major occurrence of chlorite and illite morphotypes, respectively. The red and yellow groups in the eastern part coincide furthermore with the eastern extension of a large field of high reservoir permeability.

3.1.2 Elastic influence of clay minerals

3.1.2.1 Introduction

As mentioned in chapter 2.2 the compressional velocity is positively correlated to the stiffness of the aggregate formed by grains, clays and blocky cements. The higher the rigidity of this compound the higher results the p-wave velocity.

Clay minerals are believed to deteriorate the rigidity and velocity of sandstones (e.g. Wang 2001, Klimentos 1991, Han et al. 1986, Minear 1982, Hamilton 1970). Their reducing effect on the stiffness results from their relatively low elastic constants ranging between 6-12 GPa for k and 4-6 GPa for μ. These magnitudes were determined on cold pressed clay mineral powders, aggregates and parallel to crystallographic c-axis on kaolinite, montmorillonite, dickite and smectite by Prasad et al. (2002) and Vanorio et al. (2003). The modules of main components like ά-quartz and anhydrite are higher and constitute to 38 GPa and 41,5 GPa (Alexandrov et al. 1966) and to 52 GPa and 23 GPa (Gebrande 1982), respectively.
Some studies reported a decreasing compressional velocity of consolidated sediments with increasing total clay content (Tutuncu et al. 1994 for tight gas sandstones, Tosaya & Nur 1982, Han et al. 1986, Eberhardt-Phillips et al. 1989, Klimentos 1990).
The dependence is demonstrated graphically based on the dataset of Han et al. (1986) in figure 3.2. The ultrasonic speeds were determined on water saturated sandstones of varying porosity and total clay content at a differential pressure of 49 MPa and at a frequency of 0,6 till 1 MHz (Han et al. 1986).

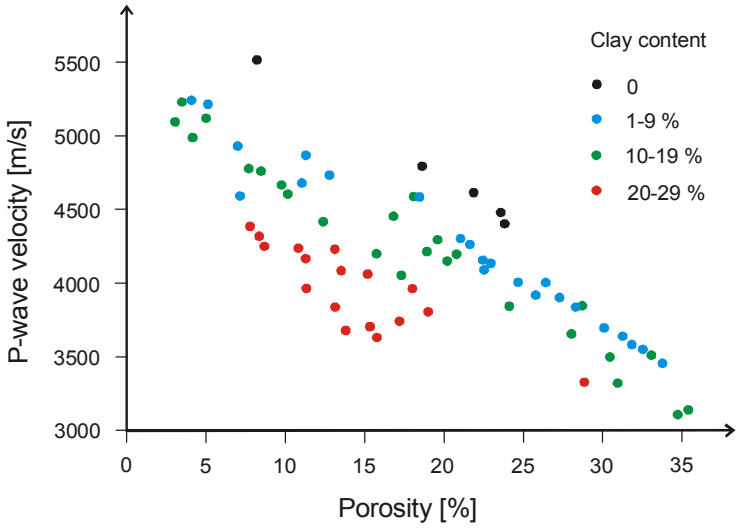

Fig. 3.2: P-wave velocity versus core porosity of 75 water saturated sandstones. Confining pressure amounts to 49 MPa and ultrasonic frequency ranges from 0,6 to 1 MHz. The variability of total clay content is presented in colours. The scatter in the p-wave velocity-porosity dependence is clearly attributable to differing total clay content. Chart modified after Schön (1998) and based on the dataset of Han et al. (1986).

Clay minerals should affect the rigidity of the grain-clay-cement compound as long as they reside between grain-to-grain contacts, thus in a micro textural position important to the stiffness. This type of clay minerals are deformed during the passage of the compressional wave and are thus “load bearing” constituents. An important and simple investigation in this regard was carried out by Bernard et al. (2003), who measured a significant signal dampening and velocity decrease for p-waves after inserting a clay mineral layer throughout the contact area of two glass cylinders. Diaz et al. (2003) investigated this effect on natural quartz sandstones containing glauconite, present as an iron rich variety of clay mineral (Weaver & Pollard 1972) and supporting the framework as pseudo matrix. They report that this clay mineral reduced the p-wave impedances substantially: at 12 % porosity, for instance, the glauconitic sandstone features a decrease by 15-20 % compared to the impedance of the sample free of glauconite. Gal et al. (1999) examined several datasets of sandstones which exhibit a non linear behaviour of compressional velocities and porosities. The study revealed palpable correlations when sandstones with load and not load bearing

clay minerals were differentiated. All cited authors attributed their findings to the diminution of stiffness by the presence of clay minerals.

Unfortunately so far literature does not report further studies in this regard. Furthermore, according to geophysicists from industry (pers. comm., 2005, geophysicists at URC-ExxonMobil and Shell Exploration and Production) a velocity effect of such a micro textural property has not been involved in any seismic modelling up to now.

Different amounts of load bearing clay minerals should affect the rigidity and hence the p-wave velocity of sandstones diversely. As shown in chapter 2.1 sonic velocities differ distinctly for the provinces of illite and chlorite alteration (tab. 2.2). This distinction is characteristic for the seismic volume and its surroundings. Similar to the reservoir scale plugs manifest divergent compressional speeds according to their diagenesis types (fig. 2.1).
In order to investigate this relationship the amounts of clay minerals between particle contacts were quantified for IM/IC-illitized and for CT-chloritized eolian sandstones.

3.1.2.2 Method

Eolian dry sandstones (for description of 'eolian dry' see appendix A-13) were chosen, which had similar porosity, mineral composition, grain sorting and grain sizes but differed strongly in permeability and velocity. The samples contained either CT-, or IM-/IC-cements. The properties of these samples A-E are described in chapter 2.3.3. Additionally to these 5 samples 16 thin sections were investigated from eolian dry sandstones of different porosity and grain size. These specimens derive from the same wells and differ by clay diagenesis type.
The amount of load bearing clay minerals was determined by estimating the ratio of the length of particle-to-particle contacts with clay minerals to the total length of contacts of one component (fig. 3.3).

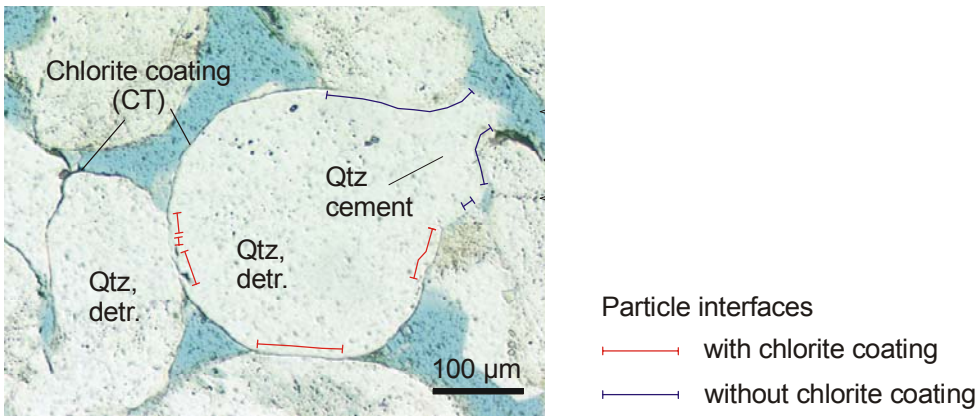

Fig. 3.3: Example of particle from CT-altered sandstone. Particle bonds are differentiated into interfaces containing and lacking clay minerals (here CT). The estimated ratio of contacts with clay content to whole contacts constitutes to 40 %.

Therefore thin sections were photographed at 200 fold magnification with approximately 50 neighbouring pictures. The images crossed the slight laminations of the plugs and overlapped to enable their correct fitting. Each sample was reproduced by two to three straight stretches of microphotographs consisting of approx. 3 × 15 recordings taken on representative locations within the thin section. The analysis was carried out on the photo

composites (fig. 3.4). In order to facilitate the quantification and enhance accuracy the compilations were plotted as enlarged pictures each of approximately 1,2 m × 0,2 m size.

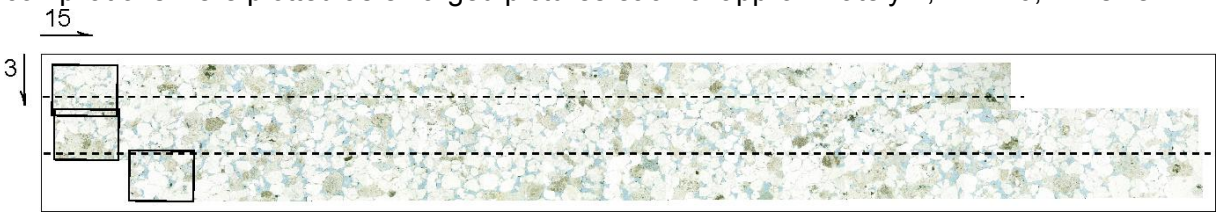

Fig. 3.4: Example of a photo composite from sample C. One stretch is presented of approx. 3 × 15 microphotographs. Dotted lines cross detrital particles which are subject to analysis. Small rectangle delineates size of a single microphotograph. The enlarged picture with measure is given in the appendix (A-14).

The ratios were determined by optical assessment of grains, which fell on straight lines through the composites. The measurements were carried out on 50 detrital particles for each sample. Initially the lengths were quantified by pacing off the interfaces with a thread and trimming the marked thread sections. However, this technique turned out to be exceedingly time consuming. It was hence chosen to quantify the ratio by visual estimation. Precision and accuracy resulted good with this method after some training on particles with exactly defined ratios.
The repeatability and representativity of this approach was controlled by repetitive measurements on identical and on different components. The accuracy amounted to 5 absolute %, the precision constituted to 15 relative %.

The differentiation of clay minerals at contacts from bare contacts was exercised by preceding scrutiny of bonds at larger magnification. Nevertheless it was not always feasible to discern particle surfaces from clay coatings, especially if chlorite envelopes appeared colourless. Such indeterminable interfaces in the samples of chlorite alteration were interpreted as chlorite rims. Hence the average percentages of CT-type sandstones represent maximum quantities. In contrast, coatings of illite were easily to identify due to their widespread impregnation by hematite or sometimes bitumen. During the analysis the interpretation of the boundaries was repeatedly tested by investigating the same bonds with the microscope at a larger magnification.
The bulk of the weight supporting chlorite and illite coatings resides between contacts of grains to later precipitated blocky cements of mainly quartz. Such bonds were only counted if the blocky cement acted as a sustainer within the compound. A constituent was regarded load supporting if it touched at least two framework particles. Figure 3.5 illustrates a blocky cement-grain interface, where the precipitate does not reinforce the particle fabric.
Plate 3.1 exemplifies interfaces covered by either chlorite or illite coatings of particle bonds to detrital grains and to blocky cements.

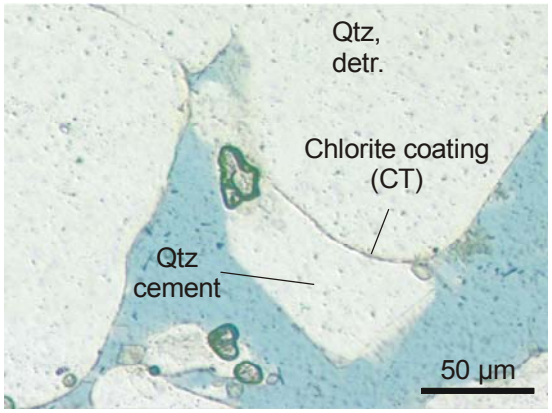

Fig. 3.5: Example of a particle cement interface featuring rims of CT-type. The length is not included when calculating the ratio as the cement is not load bearing.

Sometimes it was ambiguous whether IM-fibres or IC rims, enclosed in very thin interstices, were load supporting or not (fig. 3.6). However, the small number of such ambiguous bonds did probably not bias the clear-cut outcome. The enlarged images and microscopic observations allowed to detect coatings to a minimum thickness around 1 µm and 0,5 µm, respectively. Clay coatings which were not microscopically visible are thus not included in the quantifications.

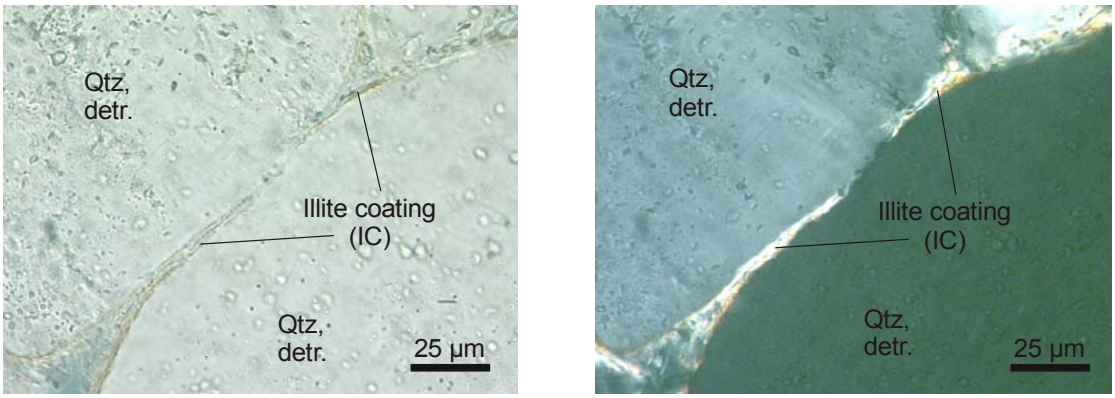

Fig. 3.6: Example of a particle transition with and without interstitial illite coating. Left plane polarized light, right crossed nicols. It is ambiguous whether the clay minerals line a pore or if the rims bear the framework load.

Plate 3.1: A: Interfaces of detrital grains within a sample of chlorite alteration (CT). The lower, lower left and lower right contacts bear coatings of chlorite. The upper and upper right bonds lack chlorite rims.
B: Enlarged segment of rectangle in picture A. Chlorite coatings appear predominantly as translucent faint and dark green minerals with plane polarized-light. With crossed nicols chlorite minerals appear black.
C: Example of load supporting interfaces constituted by quartz cements (Qtz cement) and detrital grains. Nearly the whole contact surface of the bonds feature chlorite coatings. Such configurations constitute the bulk part of all contacts with chlorite envelopes.
D: Example of contacts between primary quartz grains featuring persistent illite coatings (IC) of varying thickness. Picture is taken taken with parallel nicols.
E: Same particles as in image D recorded with crossed nicols. Illite coating is evident due to its characteristic high translumination.
F: Example of interfaces between quartz precipitates and detrital grains. The contacts feature approximately 5 µm thick illite envelopes.
G: Same particles as in image F photographed with crossed nicols.

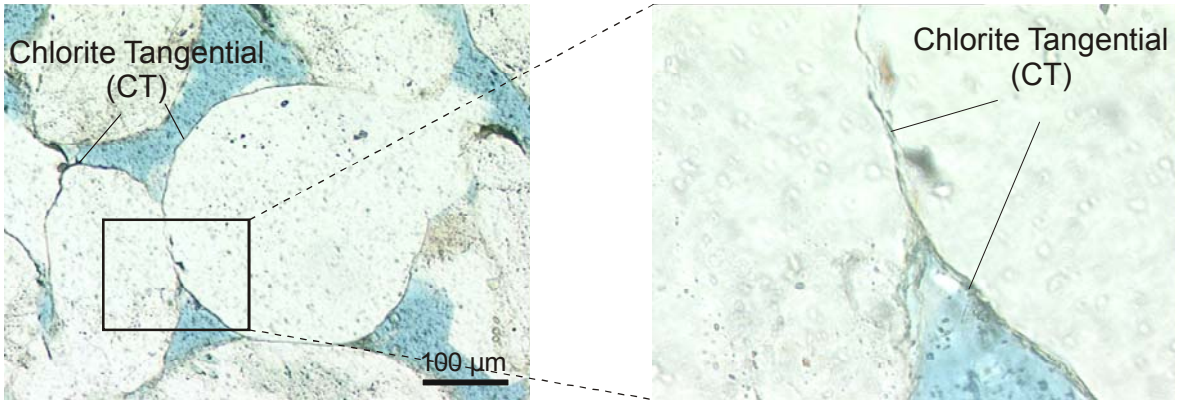
Chlorite Tangential
(CT)
100 µm
Chlorite Tangential
(CT)

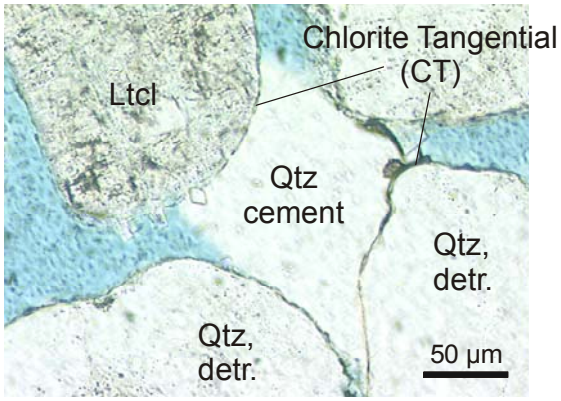
Chlorite Tangential
(CT)
Ltcl
Qtz
cement
Qtz,
detr.
Qtz,
detr.
50 µm

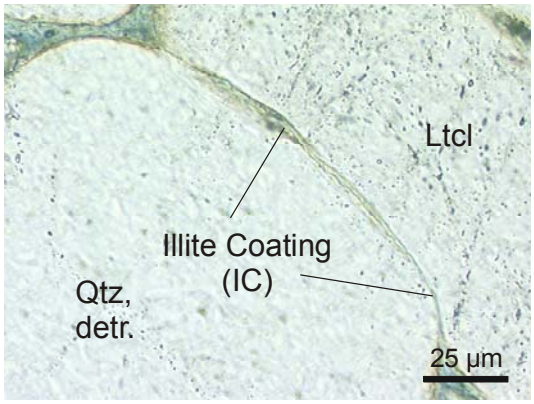
Ltcl
Illite Coating
(IC)
Qtz,
detr.
25 µm

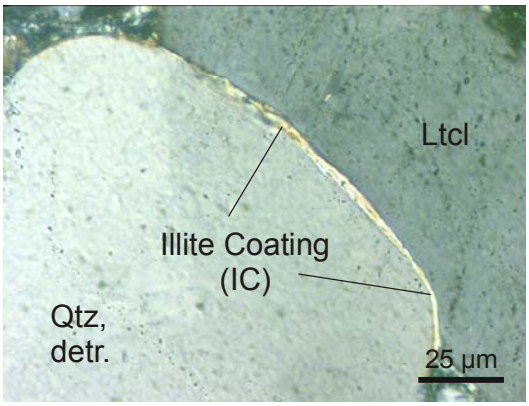
Ltcl
Illite Coating
(IC)
Qtz,
detr.
25 µm

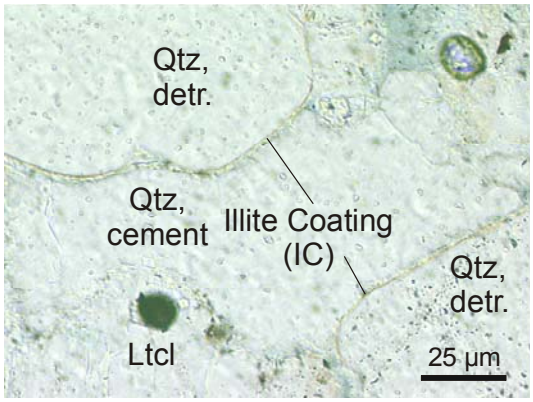
Qtz,
detr.
Qtz,
cement
Illite Coating
(IC)
Qtz,
detr.
Ltcl
25 µm

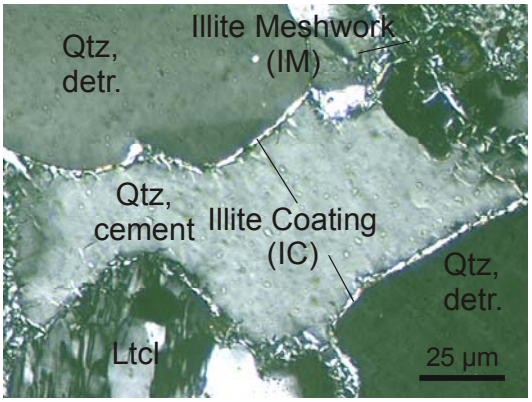
Qtz,
detr.
Illite Meshwork
(IM)
Qtz,
cement
Illite Coating
(IC)
Qtz,
detr.
Ltcl
25 µm

3.1.2.3 Results

As presented in chapter 2.3.3 samples A-E are comparable in most of the lithological parameters but exhibit widely dissimilar p-wave velocities. Table 3.2 lists the mean values and standard deviations of the ratios determined for these probes.
The amount of clay minerals between particle contacts results differently for the analyzed IM/IC- and the CT altered sandstones. The contact surfaces of the illitized samples are covered to an average quantity of 90% with illite minerals, whereas the interfaces for the CT-cemented samples contain less than 44 % chlorite (tab. 3.2).

As previously explained load bearing clay minerals reduce the rigidities and velocities of rocks drastically (e.g. Diaz et al. 2003, Gal et al. 1999). The analysis demonstrates that the contact surfaces of the particles in the illitized probes are mostly covered by clay coatings. This micro textural distinction could thus co-determine the significant lower velocity of these illitized plugs.

	Samples	A	B	C	D	E
	diagenesis type	CT	CT	CT	IC +IM	IC+IM
	p-wave velocity	⊢	high	⊣	⊢ low	⊣
Proportion of coated contact to total contact length	Mean value (%)	44	41	38	91	88
	Standard deviation (rel. %)	16	16	14	15	14

Tab. 3.2: Ratio of lengths of particle contacts containing clay mineral coatings to total particle contacts of an average grain given as mean values and standard deviations for the five eolian dry samples A-E. Samples of chlorite diagenesis feature comparatively high, specimens of illite authigenesis low p-wave speeds. The average ratios differ clearly for the groups of different diagenesis type. The particle bonds from these chloritized probes contain less than half of the coatings present in the interfaces of illitized samples. The amount of load bearing illite coatings is with approximately 90 % high and probably relevant in co-determining the distinct variations in plug velocity.

The quick microscopic revision of the 16 thin sections revealed a similar distinction in the presence of load bearing clay coatings according to the occurring clay morphotype. These differences were not quantified but appeared similarly large and as clearly ascertainable as in samples A-E.
Unfortunately no more plugs were available to verify this characteristic property for illitized sandstones from other wells.

3.1.2.4 Discussion

So far the textural difference in load bearing clay minerals for the two groups of sandstones was evidenced for the eolian sections of two wells. The following considerations and observations strongly indicate that the dissimilarity in the amount of clay minerals between particle contacts could characterize the whole eolian intervals within the seismic volume:
- According to the studies of Gaupp et al. (1993) and Deutrich (1993) the clay mineral IC evolved syndepositionally and at an early stage of burial. Hence, during compaction it resided within the grain fabric in a future weight supporting position. Tangential chlorite coatings formed at a later, intermediate stage of diagenesis when some mechanical consolidation had already occurred. This morphotype is thus not as abundant as the IC-morphotypes at micro textural locations affecting rigidity.
- The seismic volume additionally contains sandstones of late stage CR- and CS-type alterations. However these morphotypes do not reside in structural positions influencing the stiffness of the sandstones and were thus not examined. As evidenced by the petrographic

database of the DGMK-project (appendix A-9), these chloritized sandstones exhibit similar and smaller amounts of the load bearing chlorite morphotype CT.
- Different parts of the reservoir underwent different diagenetical processes, which could have dissolved morphotypes to various degrees. However, according to the petrographic dataset of the DGMK-project and own observations (appendix A-9), IC-types alone are at least 3-7 times more abundant in illitized samples than the sum of all chlorite types in chloritized sandstones (see appendix A-9). Schöner (2006) investigated the diagenetical processes in several Rotliegend reservoirs of varying porosity and sedimentary facies from the northern and southern flank of the Southern Permian Basin. He encountered similar differences in the abundances of illite and chlorite morphotypes (pers. comm., R. Schöner, 2006).

The velocity-permeability plot (fig. 3.7) demonstrates the clear separation of eolian samples into illitized- and chloritized sandstones. Their divergence in p-wave velocities could be due to their different amounts of load bearing clay minerals.

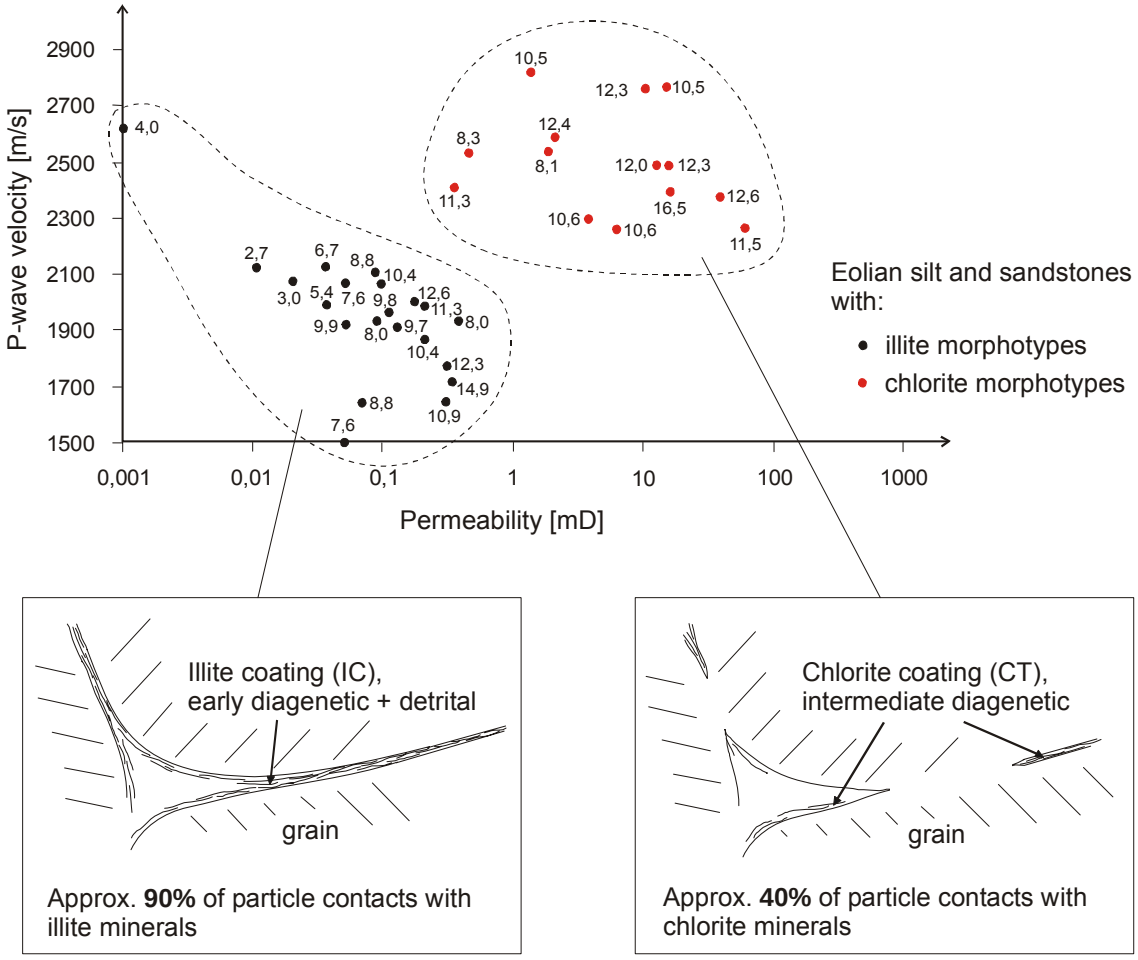

Fig. 3.7: Above: Permeability velocity plot for eolian sandstones of illite and chlorite alteration. Both sandstone groups vary distinctly regarding these petrophysical properties due to the presence of permeability reducing illite meshwork (IM), and probably due to the distinct abundances of load bearing clay minerals.
Below: Schematic illustration of textural difference for the investigated sandstone types in the amount of weight supporting clay minerals.

Some questions need to be settled in order to support a notable influence of load bearing clay minerals on elastic wave characteristics:

So far it has not been specified at which minimum thickness a load bearing clay layer affects remarkably the elastic characteristics of a rock. Bernard et al. (2003) utilized a 0,05 mm thin lamina within the glass cylinders, which is abut 5-10 times the thickness of the illite coatings occurring in the analyzed samples. Unfortunately, their paper did not specify if a slimmer sheet suffices to measure a significant change in the elastic signal. However, Prasad et al. (2002), who examined the elastic behaviour of clay bearing materials with Atomic Force Acoustic Microscopy (AFAM), state that clay minerals layers smaller 2 µm alter the elastic modules of the framework significantly. Therefore the thicknesses of the illite coatings could suffice to affect the rigidity of the framework.
Furthermore it is undisclosed to which extent minerals require to cover weight supporting interfaces in order to affect the overall elastic constants. So, for instance, the 10 % of bare contacts in the illitized sandstones could possibly bear the whole compressional load of a propagating wave.
However, the latter reservation can be partly invalidated: the datasets of Han et al. (1986), Klimentos & McCann (1990) and Best & McCann (1995) feature total clay proportions between 2 and 35 %, 1 and 30% and 2 and 23 %, respectively. They document a conspicuous decrease of velocity with already small contents of clay minerals. Unfortunately they did not differentiate the clay minerals into load and non-load bearing components. According to the DGMK-database and own quantifications (appendix A-9) the total clay contents in the reservoir rocks of the seismic volume vary within comparable 2 and 28 %, the proportion of illite coatings within 2 and 18 %. These facts could indicate that illite coatings are sufficiently abundant in particle contacts effectively reduce velocities.

The following chapters discuss additional textural properties potentially provoking the distinctions in primary velocity for the sandstones of different diagenesis type and permeability.

Remark on the potential elastic influence of bitumen

As fields of intense organic matter impregnation coincide with the presence of illite morphotypes for this reservoir (Gaupp et al. 2005), the amount of load bearing clay minerals could be answerable indirectly for the petrophysical basis of the relation between seismic classes and bituminisation.
A direct effect from organic matter on the compressional velocity was not investigated and cannot be excluded. Bitumen occasionally occupies micro textural positions between grain overgrowths and structure supporting, late stage quartz and calcite cements. However due to its late formation in burial diagenesis (Gaupp et al. 1993), its abundance results much lower than for load bearing clay minerals. Organic matter is also present macroscopically as mm-dm thin streaks and veins parallel to the bedding plane. This was observed on cores of the underlying Ebstorf member and on photos of Wustrow cores. Therefore the elastic constants of bitumen could contribute to the overall elastic properties.
Literature does not report elastic behaviour of solid organic matter except for caustobioliths (e.g. Schön 1998). Also no comparable velocity measurements were feasible on bitumen free and bitumen rich Wustrow cores due to the lack of suited plugs. Nevertheless, the presence of load bearing bitumen should intensify the velocity contrast of illitized and chloritized domains as to the following reasons:
Compressional velocities decline generally with decreasing bulk density for mineral compounds lower than 4,0 g/cm³ (Tiab & Erle 2004). As solid organic substances, even if diagenetically altered, do not exceed 2 g/cm³ (Schön 1998), the low density of bitumen would correspond to relatively low velocities. Likewise the elastic constants of bitumen are supposed to result substantially low compared to those of main mineral constituents due to

its composition of resins, asphaltenes and hydrocarbons (Killops & Killops 1993). A low hardness for bitumen was observed when handling organic matter impregnations (Kerogen types I+II; 0,5 R0) from unweathered organic rich dolomites for geochemical analyses (Abram et al. 2001).

3.2 Effects of particle contacts on compressional velocity and permeability

This chapter describes the approach to relate distinct p-wave velocities and permeabilities to differences in particle contact conditions.

3.2.1 Introduction

The intensity and velocity of a mechanical vibration front seizing a particle composite should be co-determined by the shape and abundance of particle bonds.
It is supposable that broad contact areas refract elastic deformation faster and to a higher degree than point-shaped connections. Likewise indenting component surfaces should improve transfer of mechanical impulses compared to plain junctions.
Differences in these micro textural features and their relative abundances could affect the stiffness of particle composites and therefore the velocity of transmigrating elastic waves.

According to Bernard et al. (2003) and own inquiries evidence is sparse for direct relations between compressional impedances or velocities and specific particle bonds. So far, the literature reports dependencies based only on the position of cement in pore space. According to Dvorkin & Nur (1996) cements located at the particle contacts increase the stiffness of the rocks by reinforcing the contacts. They investigated two groups of North Sea sandstones which differed by velocity despite similar mineral composition and porosity. They attributed the speed contrasts to the presence or absence of such blocky precipitates. Avseth et al. (2000) likewise ascribed variable compressional velocities of a reservoir to the rigidity enhancing effect of cements: the part of the sandstone layer with elevated velocities contains sandstones with cemented particle contacts, while in the other part with lower speeds the sandstone framework is completely uncemented and friable.
More thorough investigations regarding the influence of particle contacts on velocity were conducted on artificial granular assemblies.
Dvorkin et al. (1991, 1994) evidenced both theoretically and experimentally such dependencies for a system of spherical glass beads whose interparticle contact surfaces contained epoxy cement. These authors report a steep rise of elastic constants and wave velocities when increasing the amount of epoxy. For instance, a rise in epoxy saturation from 0 to 5 % results in a velocity increment from 1800 to 2500 m/s (fig. 3.8).

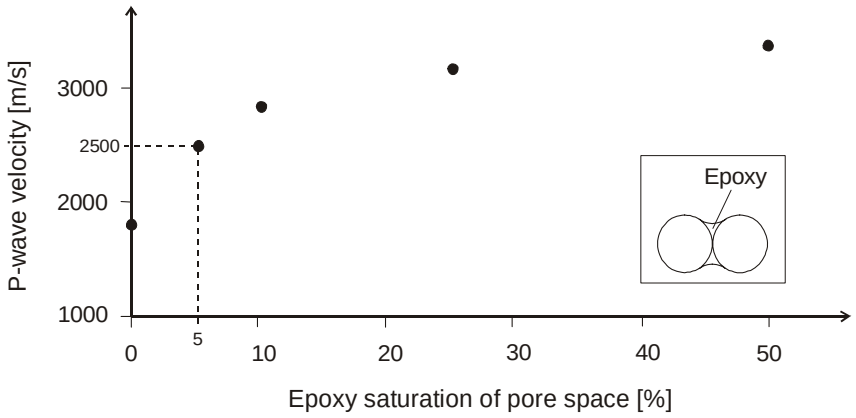

Fig. 3.8: Compressional velocity plotted against epoxy saturation for a glass bead assembly. Epoxy is located at the interface of the bead contacts. The speed rises with the abundance of the resin. The velocity contrasts are evident particularly at low saturation when the bond surfaces are magnified by addition of small amounts; modified after Dvorkin et al.(1994).

Qualitively similar trends for velocities were found when enlarging the particle bonds of glass beads by freezing water accumulated at the bead contacts (Liu et al. 1991).
These dependencies for particulate assemblies were also reproduced by numerical simulation (Trent 1991, Trent & Margolin 1992).
Several other studies describe a general increase of velocity and elastic constants with effective pressure for consolidated sediments (e.g. Wyllie et al. (1956), and Tutuncu et al. (1994) for tight gas sandstones). This correlation is due to the enlargements of contact area (Schön 1998) by grain sliding (Schopper 1982) and closure of compliant micro voids (Prasad & Manghnani 1997).

3.2.2 Method

The apposite plugs for the comparative studies were selected from CT-altered sample A-C to exclude rigidity differences from dissimilar amounts of load bearing clay minerals. Similar amounts of weight supporting intergranular clay minerals were already verified. The illitized sample D was considered separately
The investigated types of particle surfaces are differentiated into point- and long shaped tangencies, sutured and concavo-convex bonds, contact to blocky cement and exposure to open pore space (fig. 3.9).

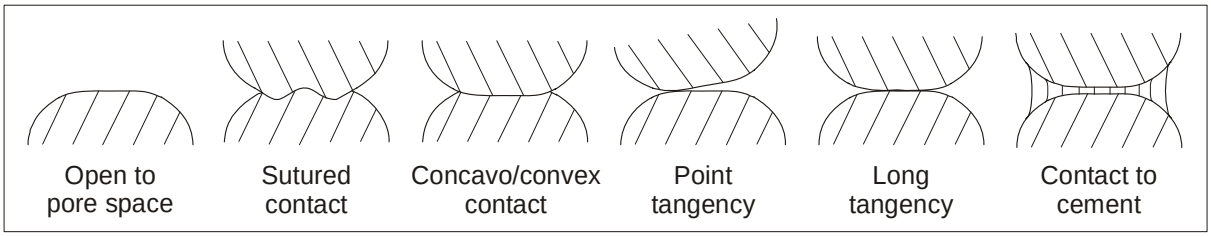

Fig. 3.9: Types of differentiated particle bonds.

Contacts to blocky cement can be attributed to long tangencies and were only considered for precipitates affecting rigidity. Concavo-convex junctions can evolve by dissolution processes and by grain rearrangement during compaction, whereas sutured contacts solely arise from pressure dissolution (Wilson & McBride 1988). However, both bonds were grouped together as the emphasis was set only on the effect of the contact.
Taylor (1950), Füchtbauer (1967) and Dillon et al. (2004) characterized grain structures by enumerating the types of grain junctions and weighting their lengths by factors. However, those methods are deemed to insufficiently reflect the measure between point-shaped to extended contacts. Therefore the specific grain bonds were not tallied but quantified as relative lengths of each particle perimeter.
The types of component contacts were quantified on composites of enlarged microphotographs similar to the investigations on the amounts of load bearing clay minerals. Each sample was analyzed by 150 grains, which fell along straight lines, in order to exclude any subjective filtering and to support representativity. The analysis was restricted to surfaces of detrital components.
After exercising on precisely measured particle surfaces, which were determined by utilizing trimmed threads, the analysis based on visual estimation achieved satisfying accuracy. The repeatability and representativity was tested by comparing outcomes of repetitive measurements on identical and on different grains.

3.2.3 Results

The relative abundances of component contacts are summarized in table 3.3 and demonstrate characteristic distributions for each specimen.
The average grain in sample A with the highest velocity features the lowest exposure to open pore space and the largest contact areas to solid components. Its high amount of sutured and concavo-convex junctions indicates a relative tighter packing. The particles in sample C with the lowest speed are the most isolated ones with bare surfaces and comparatively rare bonds, and form the least consolidated composite. The contact to blocky cement features the highest variability for the four samples.

Samples	A	B	C
	chloritized	chloritized	chloritized
porosity			
p-wave velocity			
permeability			
Open to pore space	17	29	56
Sutured & concavo/convex	43	48	31
Tangential (point & long)	<1	1	5
Blocky cement	40	22	8

Tab. 3.3: Proportions of types of contact for an average grain. Quantities are quoted in % for specimens of eolian dry facies and CT-alteration. The samples differ markedly in the spectrum of particle contacts; the framework of sample C with minimum velocity and maximum permeability features the most isolated pores, whereas sample A with converse permeability and plug speed demonstrates the most dense compound.

Additionally to the CT-altered sandstones an illitized plug was analyzed regarding its particle contact conditions. Its low permeability and p-wave velocity results from the permeability reducing illite fibres in pore space and presumably from the large abundances of illite coatings within particle interfaces. The spectrum of particle bonds is listed in table 3.4.

Sample	D
	illitized
porosity	similar
p-wave velocity	lowest
permeability	lowest
Open to pore space	14
Sutured & concavo/convex	19
Tangential (point & long)	56
Blocky cement	11

Tab. 3.4: Proportions of types of contact for an average grain examined on a eolian dry of IC/IM-alteration. The quantities are quoted in %. The spectrum of particle contacts indicates a consolidated framework. Compared to the samples A and B this sandstone features more tangential bonds.

The average particle surface within the illitized framework features the lowest contact to open pore space. Most of the particle interfaces are long and point shaped tangencies and feature comparatively low indenting surfaces.

3.2.4 Discussion

3.2.4.1 Particle contacts and compressional velocity

The variability in grain bonds conforms to the diverging velocities. The more intense the cementation and chemical and mechanical compaction the higher results the velocity.
It is supposable that sample D, despite of its differences in the shape of the particle bonds, would exhibit similar compressional velocities as samples A and B in case it underwent chlorite alteration.
The implications on velocity concerning the micro textural position of cement are covered in section x.

Compressional velocity and the proportion of blocky cements

As previously explained cements located at particle bonds augment the rigidity and velocity of sandstones. Table 3.3 demonstrates likewise an increasing tendency of plug speed with the abundance of contacts to load bearing blocky precipitates.
Therefore plug velocity was tested on a larger set of samples for a dependence on the proportion of blocky cements. The latter comprises quartz, anhydrite, calcite and barite precipitates whose quantities derive from the DGMK-database and own analyses (Appendix A-9). Unfortunately the examined specimens represent only illite altered eolian dry sandstones due to the lack of additional appropriate chlorite samples.
The diagram (fig. 3.10) charts plug velocities versus the corresponding quantities of blocky cements. The dotted lines confine data points of a single well. Both clouds demonstrate a palpable positive interrelation of the parameters. However, by involving the corresponding core porosities a fair influence of void volume on velocity is even perceptible, particularly for the upper region. The low porosity samples feature exclusively maximum velocities. On the other hand samples of comparable void volumes demonstrate different plug speeds.
In summary, this approach yields an ambiguous outcome and cannot demonstrate a causal relation. The reasons for the distinct distribution of the data points according to the wells could be based on textural features like particle contact conditions and were not investigated in this study.

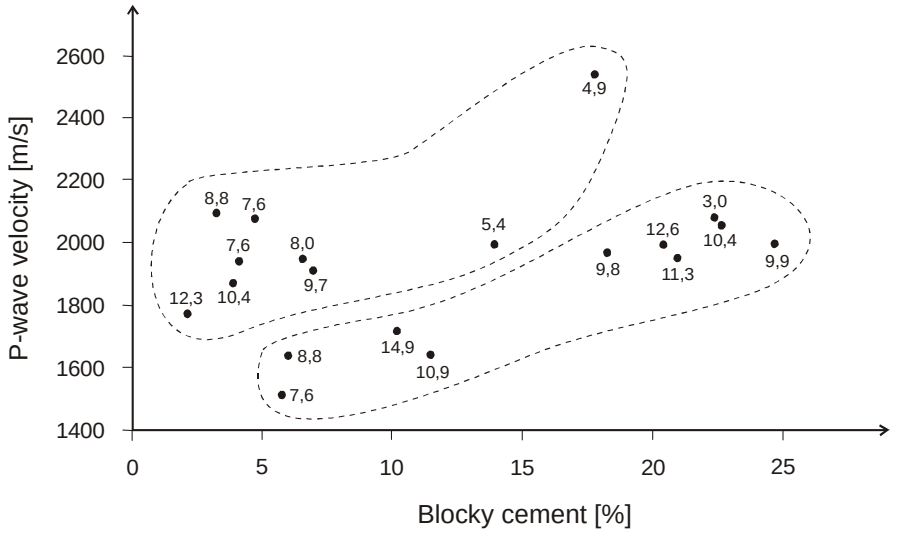

Fig. 3.10: P-wave speeds of plugs against the point counted proportion of blocky cements. A clear positive tendency between the parameters is visible. Core porosities also demonstrate an influence on velocity.

It must be noted that this example illustrates the encountered complicacies when deriving two-dimensional trends from a multidependent database. An unambiguous derivation of petrophysical interrelations is thus feasible only on appropriate thoroughly analyzed specimens, which differ only by the corresponding petrophysical parameters. As these conditions restrict the examinations to a reduced plug set an extension to a wider range of specimens of specific properties was not viable in this work.
However, the distinctions in the spectrum of particle bonds represent the only conceivable feature inducing the contrasts in p-wave velocity and permeability for the three chloritized plugs.

3.2.4.2 Particle contacts and permeability

Permeability of Wustrow reservoir rocks

According to Gaupp & Solms (2005) varying permeability for eolian samples of similar porosity are due to the presence of certain morphotypes of illite and chlorite. As covered in chapter 1.2.4.1, the fibrous and diffusive distribution of illite meshwork in pore space and its hydrophilic specific surface reduce fluid mobility drastically. The chlorite morphotypes barely affect permeability either because of their grain lining habit or their rather small amount. However after differentiating chloritized (CR, CS, CT) and illitized (IM) reservoir rocks in a permeability-porosity-plot (fig. 3.11), there is still a large spread of permeability, particularly for chloritized plugs: at 12% void space, permeability ranges in between 0,4 and 118 mD.

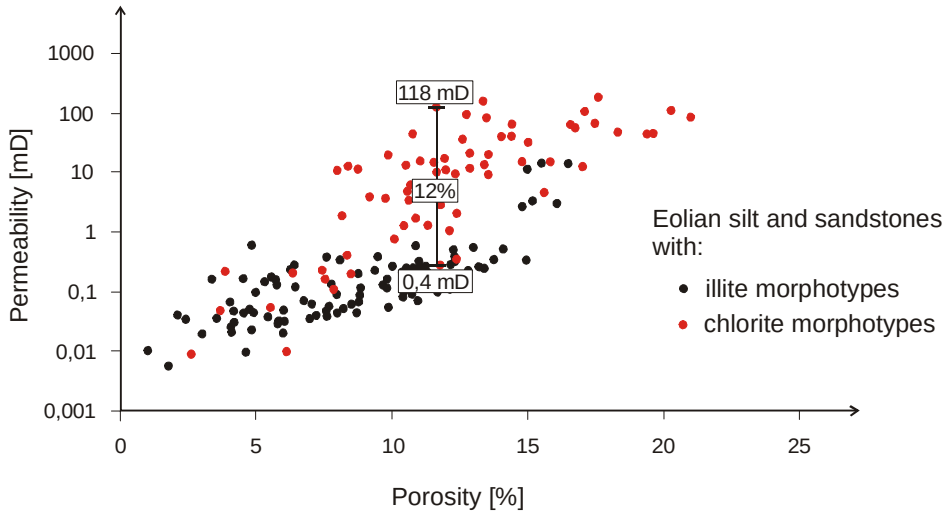

Fig. 3.11: Permeability versus porosity of eolian dry reservoir rocks of the seismic volume. The data points are differentiated according to clay mineral morphotype. Main permeability trends are attributable to the occurrence of illite fibres in pore space. The chloritized specimens still feature a wide scatter in permeabilities: at 12 % void volume the permeability varies by a factor of 300. The illitized plugs exhibit less scatter in permeability for comparable samples. Based on the DGMK-database (appendix A-9).

Grain size sorting

Generally permeability increases with a narrower grain size distribution (e.g. Terzaghi 1955, Schön 1998). Therefore grain sorting is added in the diagrams for only chloritized (fig. 3.12) and only illitized plugs (fig. 3.13). This parameter was determined on thin sections in the DGMK-project with 5 good and 1 poorly sorting. Samples without values for sorting are not included in these charts.

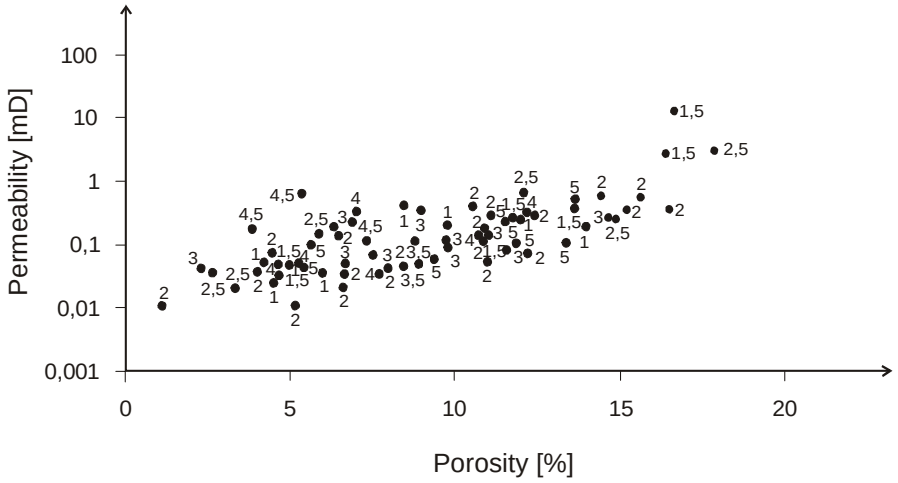

Fig. 3.12: Porosity-permeability plot for illitized samples only. Grain sorting added next to data points with 1 denoting poorly and 5 well sorted. Well sorted plugs present elevated permeabilities. However many less sorted samples feature also high permeabilities. Based on DGMK-database (appendix A-9).

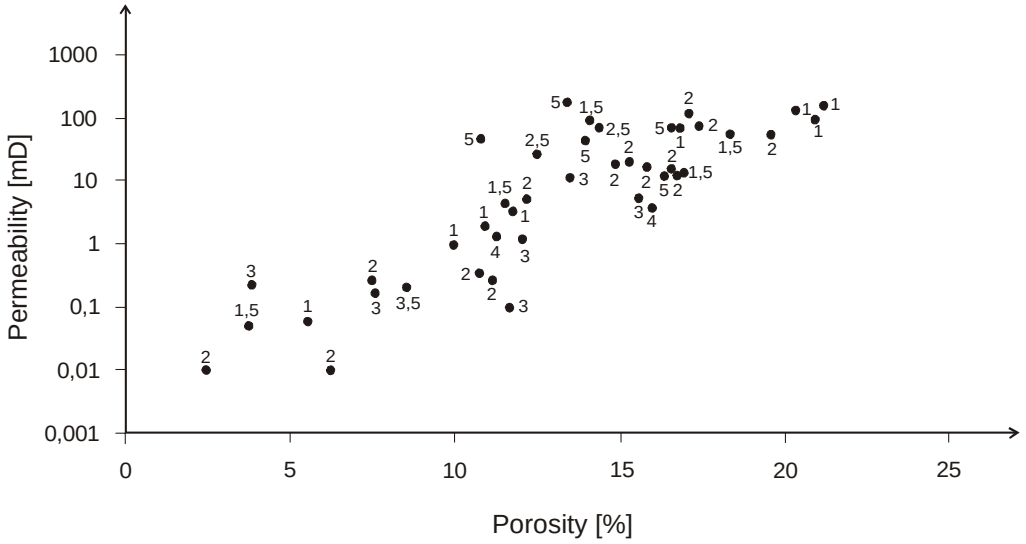

Fig. 3.13: Chart of porosity versus permeability for chloritized samples only. Grain sorting is added next to data points with 1 denoting poor and 5 well sorted. Better sorted sandstones exhibit the higher permeabilities. However, poorly sorted plugs likewise produce elevated permeabilities. Based on DGMK-database (see appendix A-9).

According to the two diagrams the better sorted sandstones show relatively moderate and high permeabilities. However, a large amount of poorly sorted sandstones, which represent the bulk part of the samples, still generate comparatively high transmissivities. This is valid for both the chloritized and illitized sandstones.
Furthermore, the permeabilities of samples A, B, C, whose grain size distribution results similar, vary by a factor of 80 (tab. 2.4).
Therefore grain sorting does not provoke the transmissivity contrasts for eolian Wustrow sandstones of chlorite or illite alteration.

Mechanical and chemical compaction

The degree of mechanical and chemical consolidation could also co-determine permeabilities too. Generally it is believed that the prevalent reason for the deterioration of flow properties in tight but porous sandstones consists in the presence of authigenic clay minerals and blocky cements. These features restrict and plug pores and pore throats (Soeder & Randolph 1987 and Dutton et al. 1993, based on tight gas reservoirs). Furthermore, Tutuncu et al. (1994) states that the grains of tight gas sandstones "interlock with each other" forming denser packings compared to medium permeability sandstones. Such interstitial "slot pores" (Soeder & Chowdiah 1990) and the frequent particle contacts (Tutuncu et al. 1994) narrow effective pore radii and preclude fluid flow drastically.
Therefore different grain contact conditions could explain the large divergence in permeabilities for the three investigated samples. Differences in particle bond configuration could also provoke the wide permeability range for Wustrow sandstones of similar porosity and lithology.

3.2.4.3 Dependence of compressional velocity on permeability based on particle contacts

As quoted before, tight packing of particles should result in elevated velocities and reduced permeabilities. Only limited studies exist on elastic properties of low permeable rocks (e.g. Gregory 1976, Han et al. 1986, Murphy 1982, Murphy 1984, Tutuncu et al. 1994). Furthermore literature does not report any empirical permeability and velocity dependencies based on particle contacts. However, Tutuncu et al. (1994) postulates a proportional trend of elastic travel times and permeability due to the enhanced acoustic coupling in low permeable structures.

Table 3.3 presents indeed an increasing tendency of transmissivity with declining speed for the three CT-altered samples. This tendency is though not ascertainable for further samples due to lack of sufficiently available plugs with comparable lithological properties. Nevertheless, an interrelation of these parameters based on particle contact conditions results very plausible.

3.3 Effects of pore geometry on compressional velocity and permeability

3.3.1 Introduction

3.3.1.1 Effects of pore geometry on compressional velocity

Every gas- or water filled porosity decreases the elastic and anelastic compressibility of the rock framework. Generally compressional velocities manifest a rough correlation to total porosities (Wyllie et al. 1956). However, for rocks of comparable lithology, porosity and saturation conditions compressional speeds can differ by 2000 m/s as a result of differences in pore structure (e.g. Wang et al. 1991, Anselmetti & Eberli 1993, Basan et al. 1997). Voids are namely believed to affect the response to a mechanical impulse depending on their size, shape and interconnectedness, and their orientation to the direction of deformation (Guéguen & Boutéca 2004, Prasad et al.1999):

Principally, the velocity of primary waves should depend on the deformability of the porous body. Spherelike or ellipsoidal voids should thus exhibit a larger resistance to compression than large thin apertures perpendicular to the direction of compression (Committee on Fracture Characterization and Fluid Flow 1996, O'Connell & Budiansky 1974, Wang 2001) as round pores are less compressible. Furthermore, very small pores like capillaries should be more deformable than larger pores (Wang 2001). So far, studies (e.g. Anselmetti & Eberli 1997) are very sparse which demonstrate velocity changes at constant pressures based only on the shape of the voids. Natural rocks probably feature high variability regarding the configuration of the pore network. It results hence challenging to relate travel times empirically to individual pore shapes. However, a dependency of primary velocity on pore sphericity is "existent with certainty" for rather homogeneous pore systems in rocks (pers. comm., H. Yin, 2005, petrophysicist at research department URC, ExxonMobil).
Prasad et al. (1999) found pore interconnectedness to be an important factor governing wave velocity of sandstones and furthermore suggest a directional dependence of interconnectedness on travel times. They investigated velocities in various directions of sandstones and observed lowest speeds vertically to the size of mean pore throats.
Akbar et al. (1993) demonstrated that elastic properties depend strongly on pore alignment. Attenuation results namely minor for waves propagating perpendicular to the long axis of elliptical pores than for waves migrating parallel to the axis. Likewise Prasad & Manghnani (1997) related experimentally directional dependencies of compressional velocities with pressure to the mean pore axis orientation of sandstones.
All the above quoted effects on p-wave characteristics according to the shape, arrangement and interconnections of voids are outlined schematically in figure 3.14.

Furthermore, elastic properties of saturated rocks depend on the fluid type and fluid distribution in the pore system (e.g. Toksöz et al. 1976, Akbar et al. 1994, Biot 1956 a & b). Pore contents of high rigidity increase velocities, e.g. water saturated rocks feature comparatively higher compressional speeds than gas saturated rocks (Wyllie et al. 1956). Due to the distinct elastic properties of various fluid types (Batzle & Wang 1992), it results important which phase resides in the compliant voids. Toksöz et al. (1976) and Mavko & Nur (1979) modelled seismic properties of sandstones for cases where two immiscible fluids selectively occupy voids of distinct sizes. They showed that the compressional velocities are strongly dependent on the properties of the phase filling the voids of small aspect ratio, i.e. the ratio of long to short pore axis (Dullien 1992). Furthermore, compressional speeds for sandstones with round pores turn out higher and for sandstones with flat pores lower in the

gas saturated case, compared to sandstones saturated with liquid fluids like oil or brine (Toksöz et al. 1976, Endres & Knight 1991).

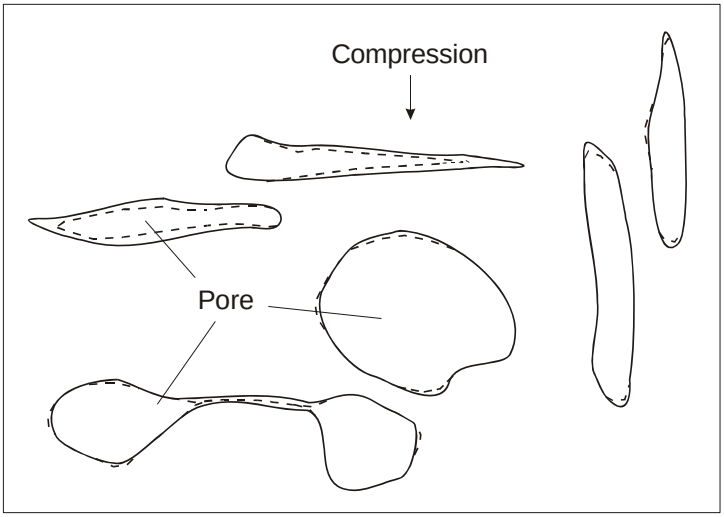

Fig. 3.14: Response to elastic compression of pores with varying shape and mean axis orientation, contour of deformation in dotted lines. Voids of large aspect ratio exhibit higher opposition to deformation than thin apertures. Pores with main orientation perpendicular to deformation are more affected by compression than voids parallel to compaction. Interconnections represent generally thin pores. The closure of compliant pores augments particle contact area and increase the rigidity of the framework, which rises velocity (based on Akbar et al. 1993, Guèguen & Boutèca 2004, Anselmetti & Eberli 1997).

Several other studies relate the elastic behaviour of fluid bearing rocks to pore fluid movement. The mobility of a fluid in a porous system is amongst other material properties a function of pore geometry:
Important mechanisms affecting the elastic behaviour represent the inter- and intra pore flows of viscous fluids during the passage of the wave (Murphy et al. 1984, 1986, O´Connell 1984). This squirting (Mavko & Nur 1979, Palmer & Traviolia 1981) of fluids is induced by the deformation of the voids. As the intensity of the pressure variation in large pores is much smaller than that in thin apertures, the liquid is squeezed from thin cracks into gas containing neighbouring large pores or adjacent cracks of different orientation (Mavko & Nur 1975, Pointer et al. 2000). Squirt flow occurs at a microscopic scale through thin conduits to larger apertures and macroscopically, where interconnected regions of the porous material feature different fluid concentrations (“patchy saturation”) (Akbar et al. 1994). The degree of pressure equilibration by fluid drift is thus intimately related to pore geometry (e.g. Dvorkin et al. 1994, Mavko & Nur 1979). Generally fluid bearing porous systems with insufficient possibilities for fluid movement and pressure release exhibit major opposition to deformation. This state of unrelaxation causes a stiffening of the compliant cracks and therefore elevated rigidities and velocities. The local elasticity of larger voids remains unaffected. Partial saturated rocks with a wide range of void sizes and high degree of interconnection exhibit hence lower velocities as rocks with a high fraction of isolated compliant cracks (Mavko & Nolen Hoeksema 1994).
Squirt flow is furthermore frequency dependent: When the deformation oscillates at low frequencies the pore fluid can easily flow from the thin voids to larger and less compressed pores; at higher frequencies the liquid cannot achieve pressure equilibration. This effect manifests itself in a considerable frequency dependent raise of longitudinal velocity (Cadoret et al. 1995). So far no microstructural theory is capable to predict the behaviour at intermediate frequencies (Pham et al. 2002).

The resulting viscoelastic response of a fluid bearing rock is thus related to fluid saturation, wave frequency, and the microscopic details of the fractions and compressibilities of the thin conduits and the stiff pores.

3.3.1.2 Effects of pore geometry on permeability

As explicated before, pore structure is an important rock feature controlling compressional wave propagation. Some authors believe it to be the most dominant textural property determining the elastic and inelastic behaviour of rocks (e.g. Kuster & Toksöz 1974, Wang 2001, Sun 2004).
Pore geometry is also known to codetermine permeability, the ease of a fluid to pass through a porous medium. Clayfree sandstones can exhibit large scatter in permeability although of similar porosities due to relevant distinctions in the shape, arrangement and interconnections of voids (Schön 1998, Doyen 1988). According to Dullien (1992) the specific hydraulic permeability is a function of only a few pore aspects: pore throat diameter and distribution, and degree of pore interconnectedness. Other parameters like the dimension of the pores result far less crucial in determining flow rates. Pore throats represent namely physical restrictions to fluid flow, and the interconnectedness of pores enables fluid migration, while pores act only as voids for fluid storage (Dullien 1992, Bourbié et al. 1987). Other authors regard also pore roughness, i.e the pore surface area in relation to the pore volume, as important feature affecting permeability (Schopper 1982, Brunauer et al. 1938). Some mineral surfaces bind namely dissolved ions, e.g. negatively loaded layers of SiO_4-Tetraeder in clays adsorb anions like hydroxyl-groups. These processes build viscous layers which narrow fluid conduits (Crain, 2000) and reduce thus the fluid conductivity in fine capillaries.

Wustrow sandstones of similar porosity and lithology show a wide range in permeability (fig. 1.9 and Gaupp et al. 2005). As demonstrated in chapter 3.2.4.2, grain sorting and the presence of authigenic clay morphotypes explain not sufficiently the differences in fluid mobility. At 12% void volume permeabilities of plugs with solely chlorite alteration vary by a factor of 300 (fig. 3.11). Furthermore, fibres of illite meshwork seem not to dominate flow properties of eolian samples with void volumes exceeding 12-13% (fig. 3.11).
As indicated in chapter 3.2.4.2 and as alleged in former studies on tight gas sandstones (Tutuncu et al. 1994, Soeder & Chowdiah 1990), permeability in comparable samples differs due to different particle contact conditions. It is namely plausible that the types and the frequency of various mineral bonds, besides to mineral solution, cause distinctions in pore geometry and permeability. A tighter packing and a more intense cementation, could narrow and eliminate conduits, isolate pores and impede thus fluid flow severely.

3.3.2 Aim

Pore geometry seems thus to influence both the viscoelastic behaviour and permeability of rocks.
Relations of compressional velocity to pore geometrical features could potentially be responsible for the rough correlation of average permeability to seismic facies classes (Gaupp & Solms 2005) and the ascertained distinct in-situ speeds of reservoir provinces with different diagenetic alteration (this work, chapter 2.1).
Therefore samples of comparable properties except for permeability and extensional speed are tested for eventual differences regarding the above mentioned pore parameters.
The applied methods comprise Image analysis of pores detected on thin sections, Nuclear Magnetic Resonance (NMR) and Mercury Capillary Pressure Curves.

3.3.3 Pore geometry from image analysis on thin sections

3.3.3.1 Method

The chosen samples for the image analysis represent the specimens A-D.
The quantification of pore parameters was conducted on microphotographs by means of image analysis techniques. Generally thin sections through porous rocks are believed to provide enough information about the geometry of the whole network (Dullien 1992, Fauzi 1997, Ehrlich et al. 1984, Doyen 1988). So, for instance, Ehrlich et al. (1984) demonstrated that significant correlation exists for parameters of the three-dimensional pore structure. They succeeded in predicting macroscopic transport processes by analyzing microscopic images.

The whole setup consists of a binocular polarizing microscope (Axioplan 2© Carl Zeiss MicroImaging GmbH), a digital colour camera (Hitachi HV-C20©) connected to the beam path, and a computer unit with several software programmes. The later are utilized for real time photo assessment (Matrox Intellicam Interactive© Matrox Electronic Systems), for preprocessing (Corel PhotoPaint© Corel Corporation), for compiling the photos (CorelDraw© Corel Corporation), and for earmarking mineralogical features, transformation to bicolor images and consequent object analysis (ImageC© Aquinto AG).
The digital pictures were taken with plane polarized light at a magnification of 50. The stretches of photos crossed the slight laminations. The position of each photo was defined by the aid of a sample holder for fine-tuning adjustment in x- and y direction to allocate pictures for future revisions. The photos slightly overlapped by approximately 5-10% to enable a precise compilation.

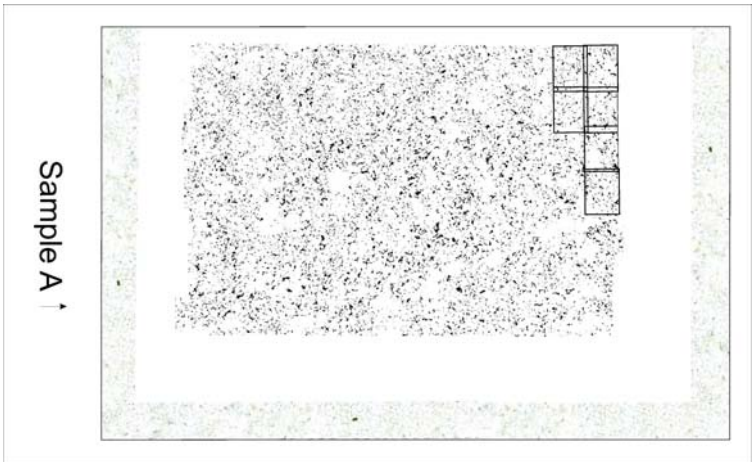

Fig. 3.15: Thin section of sample C to illustrate the method and to exemplify the degree of coverage. The overlay consists of the composed original microphotographs and the images with the digitized pores in black. Small rectangles delineate size of a single microphotograph; the images are approximately in measure. The long side of the large rectangle corresponds to 27 mm.

Each thin section was recorded with 55-84 pictures which reproduced approximately 50-80 % of the sample areas (fig. 3.15). The surveys were arranged according to several patterns in order to reproduce any inhomogeneity in texture, e.g. variation in the intensity of cementation.

Before manufacturing the thin sections, the samples were impregnated with blue epoxy resin (Araldite 2020 XW 396/XW397 © Huntsman LLC) to let voids appear as blue areas. The pores are mapped by the presence of this blue-dyed epoxy impregnation. The

transillumination was intensified which cross-faded minerals and enhanced correct colour coding. However a direct digital earmarking of the bluish colour on the original photographs was not realizable. The sometimes inhomogeneous light focus provoked namely a shift in the colour scale within the same image. Furthermore appear some solid components in the same bluish colour which rendered a fast identification of voids difficult.
Therefore each image was preprocessed in Corel Photo-Paint. The colours except for blue tints were replaced by white with the option “colour substitution” after appropriate definition of limiting grey scales. The remaining colours, which were not attributable to voids, were erased by hand. During these steps the products were continuously revised meticulously with the original photos to avoid wrong coding. Where needed, objects were redrawn. Figure 3.16 exemplifies the elaboration steps on a microphotograph of sample C. Consequently the images were composed in CorelDraw according to their survey patterns.
The image analyzing software transformed the photo compilations into binary figures by defining the grey scale interval for the blue colour. The voids were marked black, the solid components were obliterated white.
Many working steps offered the option to erode and dilate objects in order to decrease data volume, to cancel small isolated objects possibly deriving from solid components and to intensify dimly appearing pore connections. These editing was omitted in order to conserve all porosity and particularly thin conduits which are crucial to permeability.

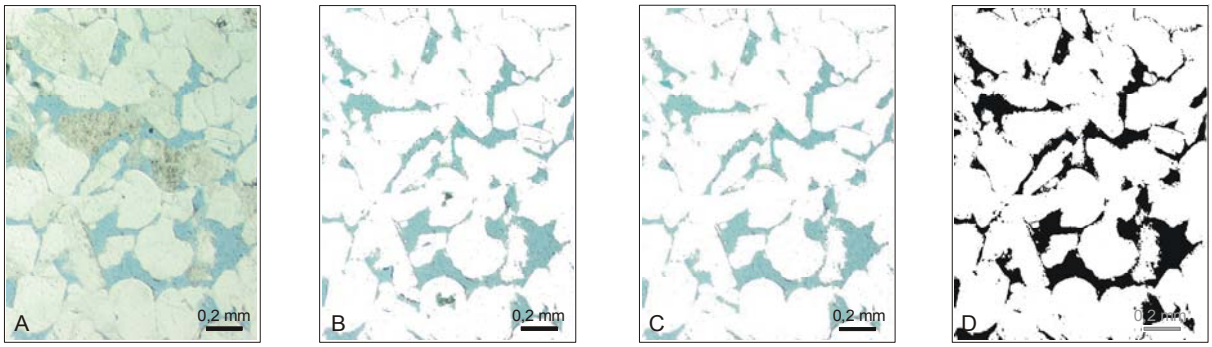

Fig. 3.16: Processing steps illustrated on a microphotograph.
A: Original digital micro photograph at plane polarized light. Voids were impregnated by blue epoxy.
B: Colour substitution with Corel PhotoPaint© . Tints from minerals are replaced by white.
C: Erasure and redrawing of objects by hand in Corel PhotoPaint© and Paint© by continuous comparison to original picture.
D: Colour substitution by means of ImageC© . Black reproduces voids, white maps solid constituents.

The morphotype of illite meshwork (IM) appears in the microphotographs as dull, blue cover of 1- 4 µm (fig. 3.17). The colour coding could not delineate the tiny fibres and map them as solid components. The analyzed voids in the illitized samples comprise thus the IM-crystals. In consequence the pore aspects of specimen D represent a network without the presence of these illite rims. Nevertheless is the influence of this clay mineral on pore characteristics assessed on specially elaborated images and discussed at the end of this chapter.

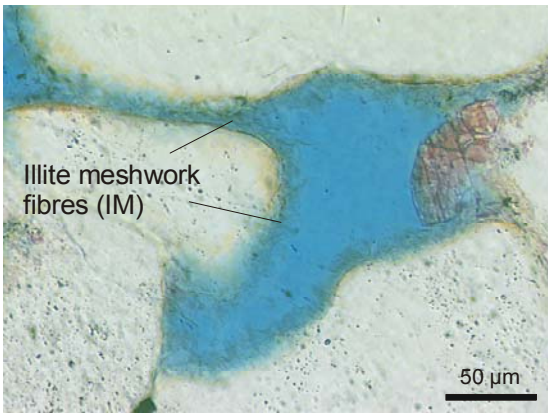

Fig. 3.17: Microphotograph of pore with fibres of illite meshwork (IM). IM-crystals appear as faint blue and grey covers over pore walls. Due to their tiny shape and bluish colour coding these precipitates are classified as voids. Consequences for the analysis are discussed at the end of the chapter.

Fig. 3.18 (next two pages): Pore networks of samples A-D. Voids are depicted black, solid constituents plotted white. The small rectangle in network of sample B delineates size of a microphotograph.

Pore parameters

Pores could be defined as local enlargements in a pore system which are linked by smaller connecting spaces referred to as throats (Wardlaw & Taylor 1976). Micro fractures are the record of anelastic deformation, i.e. the volume change, which remains after removal of a stress field, and includes microcracks, microfaults and deformation bands (Blenkinsop 2000). In the following comments the term 'pore' denotes all microscopic apertures without differentiating micro fractures, throats or larger voids for simplicity reasons. This stands in accordance to literature on pore parameters.

The ImageC© programme analyzed all pores with regard to the following attributes (ImageC© handbook):
Size F: The size refers to the areal extent of a pore.
Perimeter U: The perimeter refers to the outer length of a pore and is approximated indirectly with the parameter projection: $U = \pi / 4 * (\Pr o0° + \Pr o45° + \Pr o90° + \Pr o135°)$. According to own tests and ImageC© deviate the established perimeter barely from the real values.
Convex perimeter V: This parameter quantifies the length of a convex coating around the object in form of an elastic band (fig. 3.19).
Position in x- and y-direction: This feature denotes the two-dimensional position of the balance point of a pore.
Feret projection: This parameter designates the length of projection at angles incrementing by 5° (5°, 10°, 15°, etc.) (fig. 3.19).
Orientation: This attribute represents the direction of the longest Feret projection.
Projection: This characteristic determines the extension of an object in various directions of 5° and differs from the Feret projection as shown schematically in figure 3.19. It is used for the calculation of the perimeter and the chord length.
Chord length: This attribute refers to the length of test lines slicing the object in various directions (0°,45°, 90°, 135°) and is calculated by: $chordlength(x°) = \frac{area}{\Pr oj(x+90)°}$.
Genus: This topological quality quantifies the number of holes in the object with 1 describing a complete object, 0 one hole, -1 two holes etc.

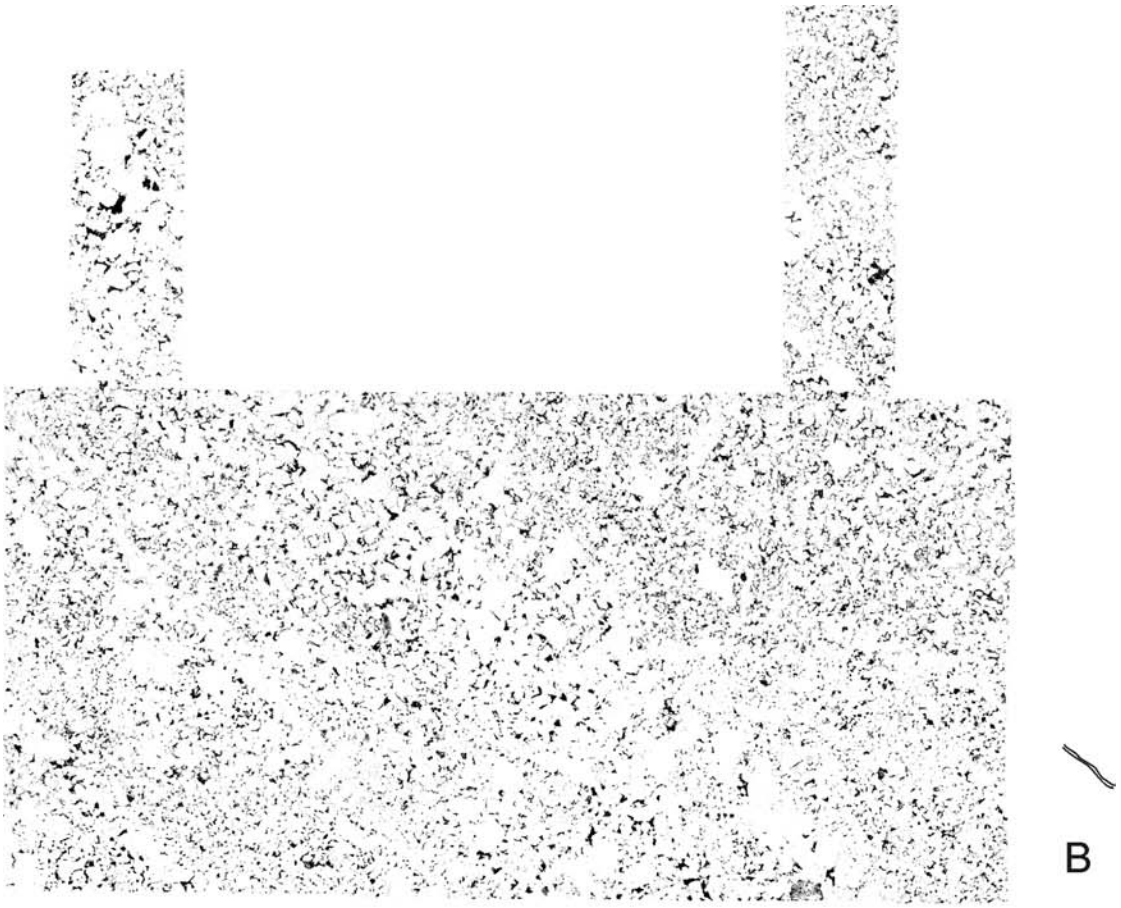
B
A
5 x 1mm
5 x 100 µm

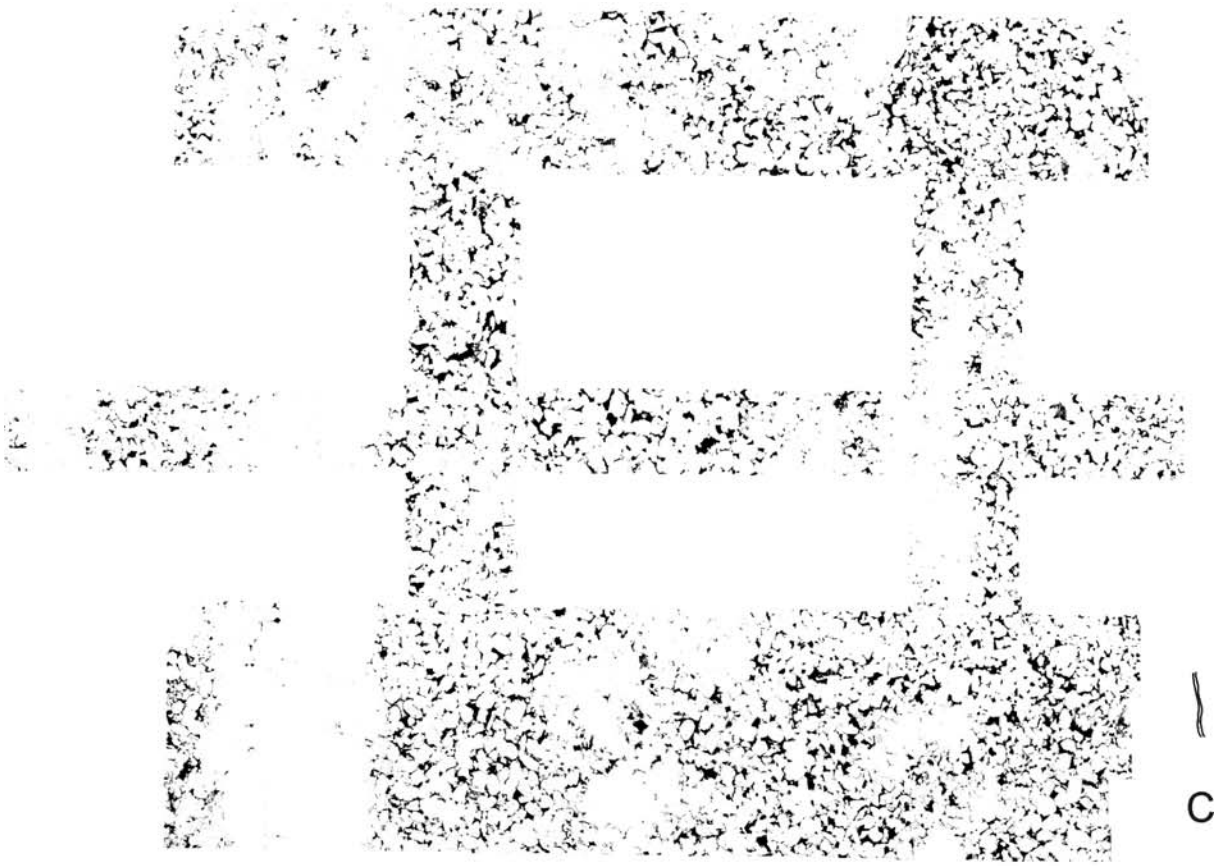

C

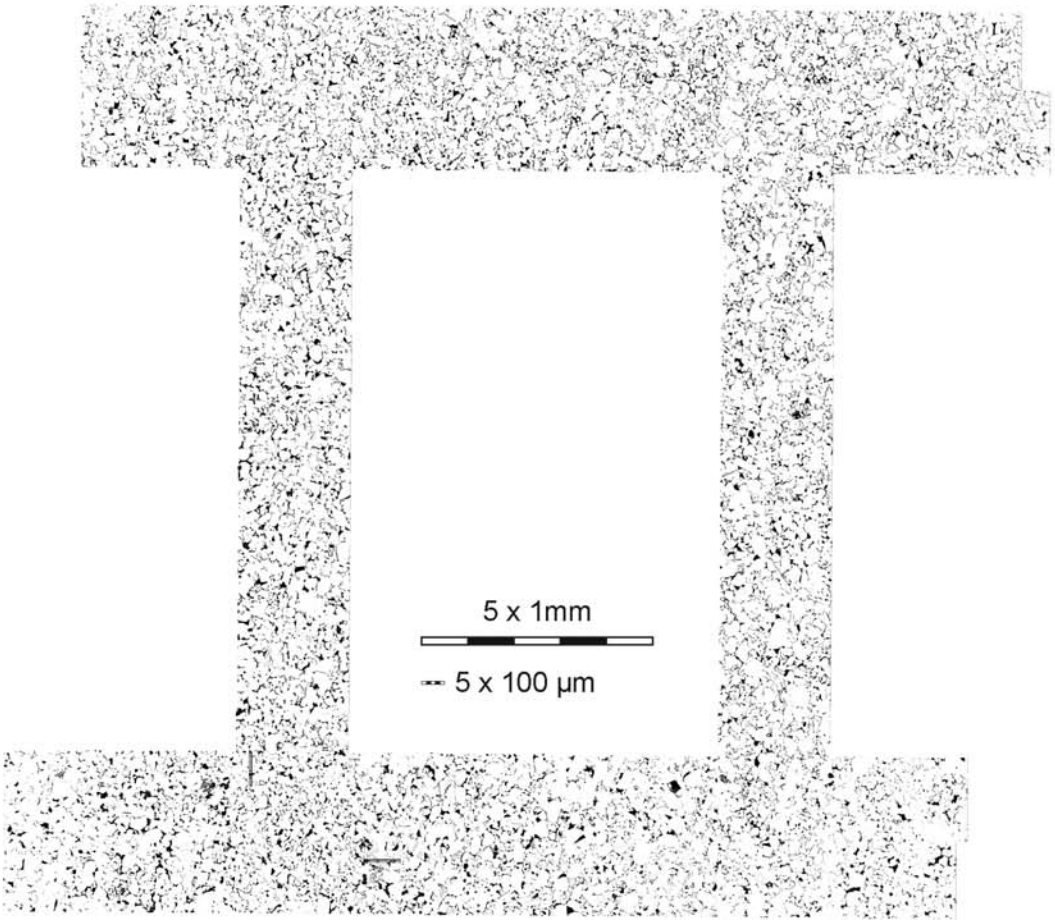

D

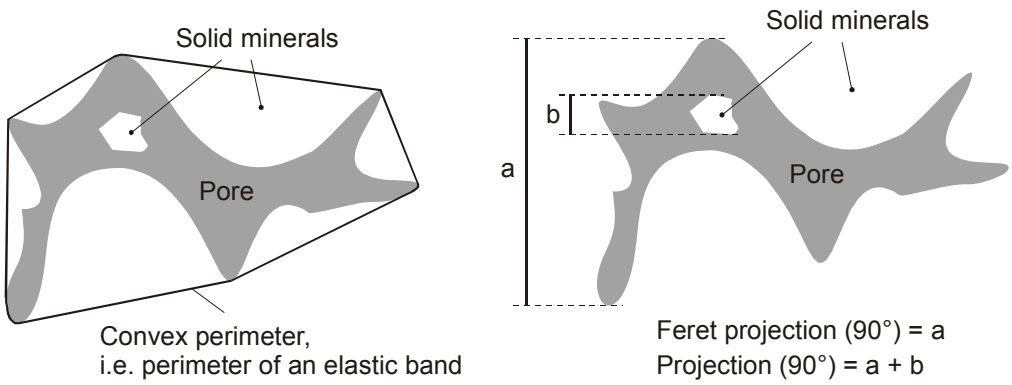

Fig 3.19: Illustration of the pore parameters convex perimeter, Feret projection and projection according to the ImageC© handbook.

Additional pore parameters were derived by combining the attributes from the software output and using spreadsheet analysis. The attributes distance of objects, effective pore diameter and anisotropy represent own derivations, the remaining parameters were taken from literature (Mowers & Budd 1996, Dullien 1992, Kendall & Moran 1963).

Aspect ratio: It refers to the ratio of short to long axis based on Feret projections or chord lengths, ranges from 1 to 0, and indicates a degree of circularity with 1 denoting perfectly circular.

Effective pore diameter: This parameter refers to the diameter of a pore throat and represents a basic outcome of mercury capillary pressure curves (see chapter 3.3.5). This crucial attribute for estimating permeability (Carman 1956, Engelhardt 1960) is approximated by the minimum chord length.

Average distance of pores to a fix point: It denotes the average offset between voids exceeding two dots to a fix point. 10-20 appropriate pores were chosen as fix points within the image composite. Those points were distributed in 3-7 horizontal lines across the investigation area. The software delivered x, y coordinates of the balance point of each void (fig. 3.20). The distances of the fix points to each pore were calculated by means of the Pythagoras theorem. The analysis of average distance was consequently restricted to circular areas of two diameters around the fixed points.

Number of objects per area: It quantifies the number of pores per unit area. The areas of investigation correspond to the circles utilized to determine the mean offset between apertures to fix points.

Fractions of porosity: This attribute defines the proportion of pores smaller than specific benchmarks of pore size.

Convex perimeter / perimeter: This characteristic measures the degree of divergence of the convex envelope from the perimeter and varies within 0 and 1.

Anisotropy: This parameter quantifies the directional dependence of pore geometry. Therefore pore sizes are examined within 5-12 sections located orthogonal to each other throughout the image composite. One direction of the investigation bands aligns to the axis of the plug. The pore dimensions are averaged within the sections and consequently for each of the two directions. Anisotropy is determined by the relative divergences of the mean values of these orientations.

Orientation: This characteristic approximates an eventual pore alignment by calculating the mean orientation and the standard deviation of the maximum Feret projection or maximum chord length.

Perimeter / pore size: This ratio is directly proportional to pore surface area per unit volume (Kendall & Moran 1963) and can provide information regarding the pore roughness or

tortuosity (Rink 1976). However the quotient does not deliver like the aspect ratio magnitudes from which direct information is inferable. Only comparative conclusions are feasible. Furthermore this parameter determined by image analysis is poorly utilized so far. Its usability is thus restricted to a qualitative difference of the four analyzed pore geometries.

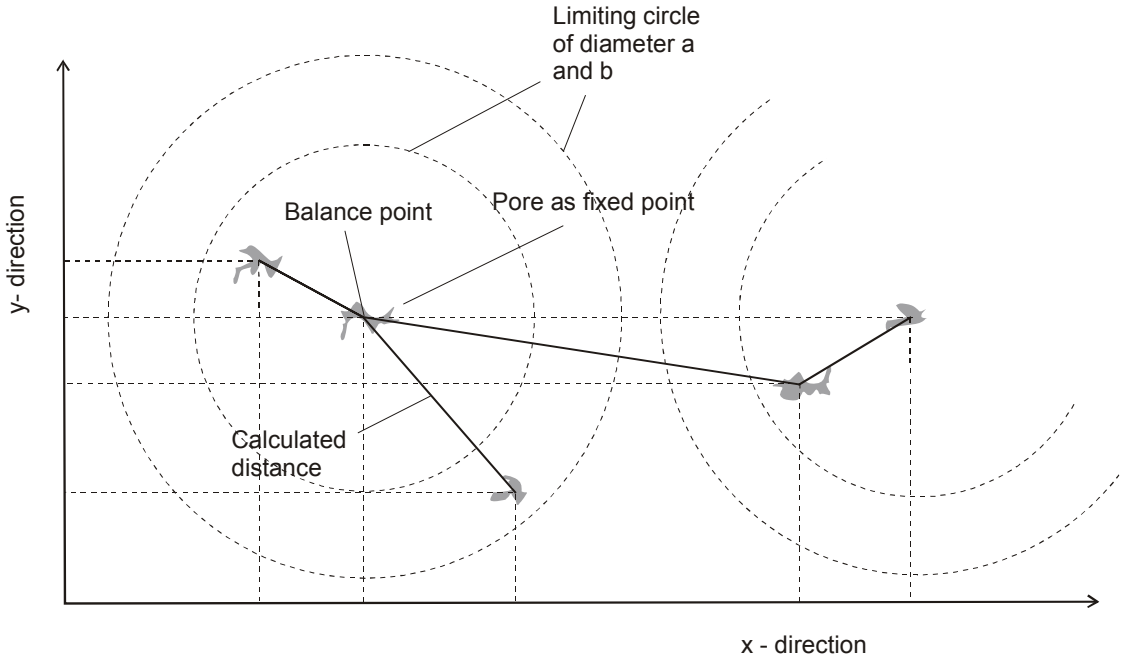

Fig. 3.20: Illustrative explanation of the parameter 'distances of pores to a fix point' and 'density of pores per are'. The ImageC© software outputs balance points of pores in x, y coordinates. The balance points of appropriate pores chosen as fix points and distances from fix points to each pore are determined by the Pythagoras-theorem. The parameter distance to pore refers to the average offset of pores within a circle. The attribute density of pores per area defines the number of objects within a circle. Both parameters are calculated for several fix points in the image composite and determined for circles of two diameters.

The ImageC© software is not capable to quantify the degree of interconnections for each pore, and the tortuosity (twistedness or crookedness) of a pore network. These important features enabling flow and determining the flow rate of pore fluids (Dullien 1992) were assessed by microscopic appraisal.

Resolution

The minimum resolution refers to the pixel size. The size of a dot amounts to 3,13 µm in side length and 9,76 µm² in area. Following the proposal of Pittman (1971) that micro pores feature diameters less than one micrometer in at least one direction, the analyzed voids comprise no micro porosity.
The image analysis was restricted to objects starting with a size of three pixels due to the subsequent considerations:
- During the elaboration of the raw data it turned out that including voids of small sizes provoked an erroneous bias in the trends. The pore parameters for objects filled out with only one pixel do not characterize namely the morphology of the void. For instance, no information on the real area of such a pore is deducible from the size of the squarish dot.
- The mercury capillary pressure curves document for chloritized samples effective pore radii of 4-7 µm, thus 8-14 µm of pore diameter. Table 3.5 lists the possible extensions of objects with three pixels and the extension of voids with corresponding effective pore radii by

considering circular and squarish shapes. It follows that the geometry of these conduits is included in the analysis. Unfortunately range the low effective pore dimensions of illitized plugs with 0,2 till 1 µm below and at the limit of resolution by means of optic microscopy.

Linear extensions [µm]		
Effect. pore diameter (NMR)	Circular shape	Rectangular shape
8	8	5,7 - 8
14	14	9,9 - 14
For objects of three dots	3,1 - 9,9	

Tab. 3.5: Possible linear extensions of effective diameters by NMR exemplified for circular and rectangular voids, and for pores of three pixels determined by image analysis. Effective pore diameters refer only to chloritized samples: pore geometrical analysis includes thus effective pore restrictions for these specimens.

It is important to note that the imbibition process with epoxy resin reaches only interconnected apertures and restricts the injection of pores to the applied pressure difference of 1 bar and the viscosity of the resin. Furthermore small voids could be overlaid by solid components. A lower threshold of the dimension, above which all objects are definitely detected, conforms hence to the thickness of the thin section, to 27 µm ± 2µm.

Accuracy and precision

Accuracy was determined by comparing the diameter of a circle calculated by the software (after correction of measure) with its true value. The dimension of the analyzed figure corresponded to the span of an average pore. Accuracy for a mean pore size amounted to 2 % The divergence results from the fact, that the objects are analyzed with squarish pixels. The accuracy diminuishes hence with increasing pore or declining pixel dimensions. The precision of the ImageC©-software constituted to 0 %.
Objects which exceeded the border of the image composites were excluded from analysis by limiting the window of examination to the inner 90 % of the area.
The representativity of the analyzed area was verified by the similar outcomes for the whole area and for several smaller sections.
Some inaccuracies could have occurred for instance:

- By wrong colour coding as some objects were not attributable to pores, components, light breaking effects at boundaries or grinding powder from thin section preparation;
- By handling the huge quantity of raw data which amounted to in total 16 million values, 2-5 million for each thin section. This necessitated to divide the whole dataset into equal sets and multiplied calculation steps as the storage limits of the programme for spreadsheet analysis (60.000) did not suffice. Furthermore, the data volume and the partitioning of the data record required to use statistics statistics extensively when deriving representative parameters for each sample.

Analysis and presentation of data

The pore parameters of the samples were analyzed for distinctions by comparing their mean values, percentiles, standard deviations and graphical distributions. The percentiles and {graphs allowed testing the independence of characteristic pore geometrical distinctions from scaling effects.
The results of the pore geometrical analysis are summarized predominantly in tables. Each spreadsheet lists the ranges of the three chloritized samples and the single illitized specimen for a specific range of void sizes: table 3.11, 3.12 and 3.13 for all objects equal and larger 3, 17 and 440 pixels, respectively. This differentiation was conducted in order to discern eventual distinctions in pore geometry based on the dimensions of the voids. As explicated above the lower benchmark was established to minimize wrong colour coding and a distortion of the results due to improper reproduction of morphology for very small objects. The middle boundary includes approximately two thirds of the occurring dimensions, while the highest threshold restricts the analyses to the very large voids. The two higher limits needed to be set rather straightforward as the voids feature varying sizes for the four samples.
The average values represent arithmetic means, the percentiles refer to the values at the borders of 95 and 5 % occurrence.
The distribution of pore geometrical parameters is additionally illustrated as frequency scales. Unfortunately not all attributes could be displayed as graphs. Some parameters exhibit namely very high scatter. In order to reduce the spread and render curves comparative, classes were defined in which the corresponding percentages were accumulated. As this procedure resulted exceedingly labour-intensive, the graphs were not elaborated for all intervals of object sizes.
given
Unfortunately the standard parameter perimeter output by the software can only be used with reservation. The ImageC programme includes in the quantification of the parameter perimeter additionally the circumferences of holes within the object, i.e. solid components within the pores. Two voids of equal circumference exhibit dissimilar perimeters if one pore contains inner components (see fig. 3.19). In place of the form factor, which derives from the perimeter, the feature aspect ratio was thus utilized. The attribute convex perimeter/perimeter was restricted to objects of genus=1.

Regrettably delivered the software not values true to scale despite of correct handling. When the fault was detected a major part of spreadsheet calculation was already completed. Hence the processing was continued and only the results were amended. The correct dimensions resulted by comparing the software output for a line by its real length. Consequently correction factors for one and two-dimensional parameters were determined and applied to the attributes. The raw and calculated data presented in the appendix (A-4) are thus not corrected to real dimensions.

Some basic figures are analyzed with the ImageC© software for a better understanding of several pore parameters (fig. 3.21). The output for these circle, polygons and pore shapes is summarized in table 3.6. The parameters for the objects 5-14 were normalized by defining the side length of the small square (object 5) as 1.

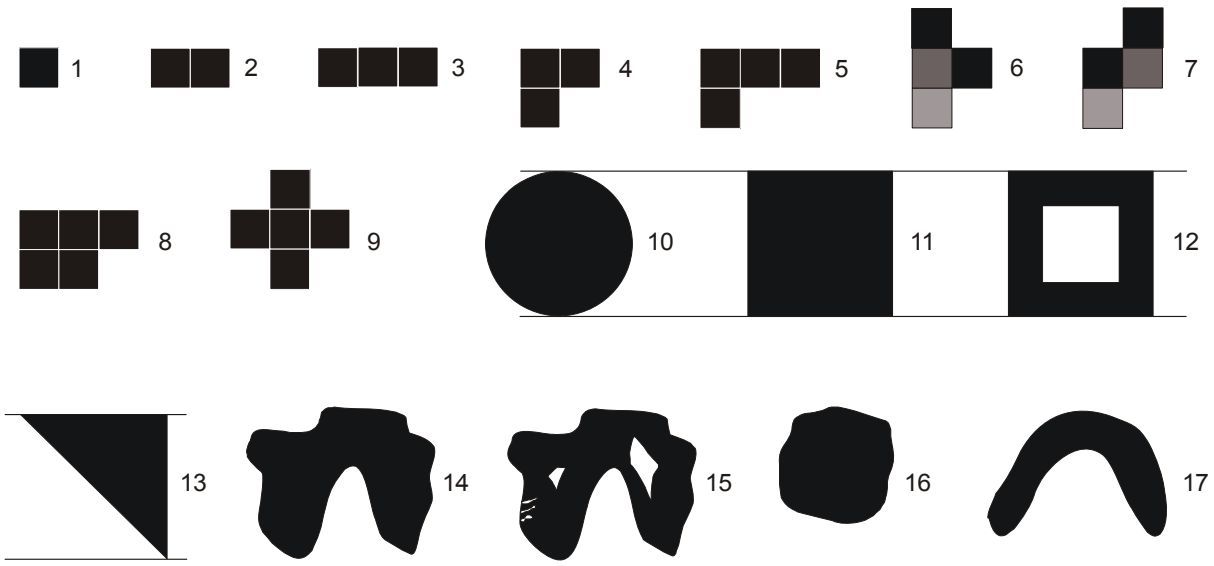

Fig. 3.21: Basic geometrical shapes and sketches of pores. Pore geometrical results are shown below (tab.3.6). 1-9 denote objects consisting of squarish dots, 10-13 represent some geometrical objects of equal vertical extensions, 14-17 mark sketches of pores.

Objects	Area	Perimeter	Convex Perimeter	Minimum Feret	Maximum Feret	Maximum Feret Pr.	Aspect ratio	Orientation
1	1,0	4,0	3,8	1,0	1,41	1,41	1,00	/
2	2,0	6,0	5,7	1,0	1,73	1,73	1,00	0
3	3,0	8,0	7,6	1,0	3,16	1,85	0,59	0
4	3,0	8,0	7,1	2,0	2,11	2,11	1,00	135
5	4,0	10,0	8,7	2,0	3,60	2,5	0,69	160
6	4,0	10,0	8,8	2,0	3,60	2,82	0,78	90
7	4,0	10,0	8,8	2,0	3,60	2,23	0,62	120
8	5,0	10,0	9,4	2,0	3,60	2,82	0,78	160
9	5,0	12,0	9,6	2,82	4,20	4,20	1,00	/
10	355	67	67	67	67	67	1,00	/
11	452	85	85	21	30	30	1,00	/
12	326	123	85	21	30	30	1,00	/
13	226	69	69	15	30	15	0,50	45
14	371	148	83	22	30	27	0,91	12
15	394	104	83	22	30	27	0,90	12
16	236	56	56	17	19	18	0,95	127
17	217	89	74	18	26	20	0,77	172

Tab. 3.6: Some pore parameters for illustration. Analysis is carried out on objects presented in figure 3.21. The attributes of objects 1-9 are normalized to the square 1 with a side length of 1 [ ]. No dimensions exist for the presented magnitudes. The parameter chord length would have identical till similar values as minimum Feret projection. The bulk part of the parameters reflects the shape of the objects truthfully, except for some inconsistencies like for the aspect ratios of objects 2, 11, 12 which turns out 1 despite of their non spherical shape. The forms 11 and 12, and 14 and 15 differ in perimeter due to the holes in object 12 and 15, their convex perimeters are identical.

Additional comments

The parameter aspect ratio is represented by the ratio of the maximum feret projection and the length of the projection perpendicular to the to the maximum Feret extension. This

quotient yields a better measure for circularity than the ratio of minimum and maximum feret projections or chord lengths, which are not necessarily inclined orthographically to each other.
The parameter chord length quantifies the length of lines slicing the objects in various directions. The software outputs the minimum, maximum and mean stretches for each object. The minimum magnitude of this attribute was utilized to approximate the effective pore diameter. However as the determination of chord length is restricted to a few directions the minimum chord length will not equal the effective void restriction and turn out elevated for most of the analyzed pores. Despite of this inconsistency this feature was utilized as it represented the only possibility to quantify at least estimatively the crucial parameter pore throat.
The x, y coordinates delivered by ImageC© are not true to scale. The software is capable only to utilize fixed grids and hence does not modify the grid according to the defined measure. However as the samples were analyzed by the same lattice comparative studies on the two parameters “distance between pores” and “concentration of pores” per unit area are feasible.
Particular attention was set to maintain the pixel size equal on the original and processed pictures. The resolution of the images could be altered due to transforming and exporting data files, for instance, by converting CorelDraw data into jpeg-files the pixel size increases by a minimum of 20% and resolution is thus severely reduced.
In the search of appropriate techniques for reproduction also a diascanner was taken into consideration. This apparatus offers the advantage to register the whole thin section in one scan without having to survey the sample with single photos and to compile them consequently. The achieved resolution (2270 DPI) turned out 7 times lower than with the optical microscope. Unfortunately resulted this feature too low for pore geometrical examinations as especially the thin conduits affect the permeability of porous media rigorously (Dullien 1992).
The derivation and processing of all pore parameters (16, 2 million values) extended over 6,5 months particularly due to extensive elaboration of microphotographs and spreadsheet analysis.

3.3.3.2 Results

According to the results summarized in the tables 3.7-3.13 and the frequency scales 3.23 A-E the bulk of the pore parameters varies for all samples and for all the analyzed ranges of pore size.

Tables

A straightforward distinction turns out when examining the proportions of objects larger than certain sizes (tab. 3.11-3.13). For instance, the quantity of objects greater than two dots is lowest for sample C with 39 % and highest for sample A with 76 %.
Most of the pore attributes show an increase from the chloritized specimen A to C. The average pore size in table 3.11 for sample C is with 1511 µm² 3,1 and 3,6 times larger than for plugs B and A respectively, and the 95% quantile 3,3 and 4,5 fold greater, respectively. The low percentile yields constant values as it corresponds in this case to the minimum analyzed pixel area of 3 µm × 9,8 µm = 29,4 µm².
Increasing tendencies from specimen A to C are observable also for the one-dimensional parameters like feret projection and chord length. The perimeter and convex circumference exhibit similar large differences like the pore sizes.

No clear distinctions present the average magnitudes and percentiles of the latter parameters. The derivated ratios demonstrate likewise no palpable trend for the chloritized plugs except for the quotients of Feret projections.
The illitized specimen features similar magnitudes to those of the chlorite altered sandstones. Except for the attribute perimeter and convex perimeter range the so far discussed parameters for sample D around the values for the chloritized samples A and B.

The parameter distance of pores from fixed points shows only small variability for the four specimens for both circles of investigation (table 3.7).

	Diameter = a		Diameter = a*2/3	
	mean	st. dev.	mean	st. dev.
A	115	32	77	44
B	115	44	65	28
C	122	40	82	27
D	118	42	80	28

Tab. 3.7: Average distances of pores from fixed points for the two diameters of investigation. No unit is given due to the dimensionless x-y grid of the ImageC software. 'a' corresponds approximately to 2 mm. The mean offsets between voids turns out rather resembling for all the samples. The standard deviations differ more pronouncedly.

	Amount of objects				Density [n / area]	
	Diameter = a		Diameter = a*2/3		Diameter = a	Diameter = a*2/3
	mean	st. dev.	mean	st. dev.		
A	374	163	157	20	2192	2058
B	839	48	356	41	4918	4680
C	488	39	237	26	2858	3096
D	773	136	358	32	4533	4679

Tab. 3.8: Amount of objects within circles of diameter a and a × 2/3. Density refers to the number of objects related to the circle areas. 'a' corresponds approximately to 2 mm. The concentration of pores varies substantially: the network of sample A is built up by the smallest amount of voids, whereas the pore structures of specimens B and D feature most frequently apertures.

However the networks of the samples are composed by dissimilar amounts of pores per area (tab. 3.8). The concentrations of voids differ for sample A with the lowest magnitude by 58, 28 and 55 % for specimens B, C and D, respectively.

It must be noted that although the average offsets between voids resulted similar, the concentrations can still vary. The perimeter offset between pores is namely determined by averaging all the spacings to the fixed points. Incrementing the number of pores in a homogeneous distribution does hence not change the average offset to the fixed point. This fact is illustrated schematically in figure 3.22. The resembling results for this parameter indicate hence a rather homogeneous distribution of apertures within the networks of all four samples.

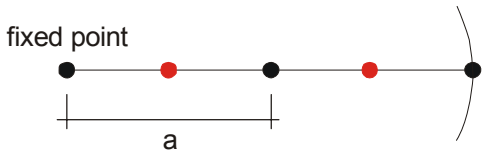

Fig. 3.22: Circles represent the pores, left circle is the fixed point and right circle is the outer pore located here at the boundary of the investigation area. The mean distance from the fixed point for the system with only black circles is 'a', adding the red circles does not alter the outcome.

Table 3.9 lists the anisotropy of the parameter pore size. The magnitudes represent the divergence in percent for the averages and the standard deviations of the parameter pore size in both directions.

	Anisotropy [%]
A	2,6
B	2,9
C	6,4
D	1,9

Tab. 3.9: Directional dependence of pore geometry quantified by the relative divergence of average pore size in two orthogonal orientations. Anisotropy turns out low and resembling for the four pore geometries. Although slight laminations by particle size variations are optically apparent, these inhomogeneities seem not to induce a substantial directional dependence on the overall pore geometry.

The anisotropy results similar and low for all samples. The pore geometry of sample C features the highest directional dependence with a maximum of 6,4 %. The laminations in the plugs appear not to induce an orientational trend on the overall void structure. However,. the standard deviations of the pore sizes for sample B differ remarkably for some sections. The pore sizes of an individual specimen however turn out similar for all its sections.
Most probably the pore geometrical distinctions by the particle size variations are attenuated by the integration of the investigation bands.

The parameter orientation of pores demonstrates resembling alignments for all samples. The bulk amount of voids seems to be arranged in angles of 0, 45, 90, and 135°. However the same result was attained when rotating the image composite by 10°. This conspicuous result renders the parameter orientation unreliable.

The porosity determined by image analysis turns out similar for the three chloritized samples and ranges from 9,4 to 10,0 % (tab. 3.10). The porosity for sample D results elevated with 14,1 as IM-fibres were analyzed as void volume.

	Porosity [%]
A	9,4
B	10,0
C	9,7
D	14,2

Tab. 3.10: Porosity of the digitized networks by aid of image analysis. The void volumes turn out similar for samples A-C; the network of sample D features elevated magnitude as IM-fibres were coded as voids.

	Diag.	Por. [%]	Perm. [mD]	Dens. [g/cm³]	Veloc. [m/s]	Total objects	Analyzed objects	%	Size			Perimeter			Convex perimeter		
									5%	Mean	95%	5%	Mean	95%	5%	Mean	95%
A	CT	10,47	1,40	2,40	2814	102.290	77.740	76	29	418	1.621	26	80	340	26	45	218
B	CT	11,56	16,47	2,37	2450	58.631	30.376	52	29	474	2.218	26	107	406	26	81	284
C	CT	11,52	118,80	2,39	2164	19.943	7.712	39	29	1.511	7.293	26	188	783	26	135	542
D	IC/IM	11,30	0,21	2,39	1950	29.387	20.116	68	29	602	2.729	26	134	500	26	105	358

Conv. Per / Per

	Minimum			Mean		
	5%	Mean	95%	5%	Mean	95%
A	0,60	0,95	0,98	3	12	50
B	0,81	0,96	1	10	24	81
C	0,82	0,96	1	7	39	152
D	0,78	0,95	1	8	23	75

Feret projections

	Minimum			Mean			Maximum			Feret orthog. / Max Feret		
	5%	Mean	95%	5%	Mean	95%	5%	Mean	95%	5%	Mean	95%
A	3	4	15	15	18	218	6	22	87	0,44	0,75	1
B	5	7	27	12	34	118	15	42	145	0,42	0,60	1
C	5	15	47	11	58	232	14	73	291	0,38	0,57	1
D	4	6	21	12	44	147	10	43	144	0,39	0,58	0,94

Chord lengths

	Minimum			Mean			Maximum			Min / Max		
	5%	Mean	95%	5%	Mean	95%	5%	Mean	95%	5%	Mean	95%
A	3	4	15	3	6	19	7	9	22	0,40	0,59	0,76
B	5	7	27	6	12	24	7	15	35	0,46	0,68	0,88
C	5	15	47	6	17	39	7	22	59	0,34	0,67	0,90
D	4	6	21	5	15	24	7	14	29	0,46	0,67	0,88

Tab. 3.11: Pore geometrical parameters for objects equal and equal and larger 3 dots. The parameters are quoted in averages and 5 % and 95 % percentiles.

	Diag.	Por. [%]	Perm. [mD]	Dens. [g/cm³]	Veloc. [m/s]	Total objects	Analyzed objects	%	Size 5%	Size Mean	Size 95%	Perimeter 5%	Perimeter Mean	Perimeter 95%	Convex perimeter 5%	Convex perimeter Mean	Convex perimeter 95%
A	CT	10,47	1,40	2,40	2814	102.290	21.481	21	191	1.471	6.831	74	232	833	74	145	436
B	CT	11,56	16,47	2,37	2450	58.631	9.793	17	121	1.515	5.669	74	288	870	74	194	490
C	CT	11,52	118,80	2,39	2164	19.943	3.133	16	121	3.619	17.028	74	405	1.536	74	280	922
D	IC/IM	11,30	0,21	2,39	1950	29.387	8.623	29	191	1.309	4.809	74	261	780	74	188	491

Conv. Per / Per

	Minimum 5%	Minimum Mean	Minimum 95%
A	0,60	0,95	0,98
B	0,70	0,87	1
C	0,74	0,90	1
D	0,70	0,74	1

Feret projections

	Minimum 5%	Minimum Mean	Minimum 95%	Mean 5%	Mean Mean	Mean 95%	Maximum 5%	Maximum Mean	Maximum 95%	Feret orthog. / Max Feret 5%	Feret orthog. / Max Feret Mean	Feret orthog. / Max Feret 95%
A	10	37	153	23	47	141	29	67	267	0,44	0,75	1
B	14	41	107	25	63	156	30	78	193	0,31	0,65	0,90
C	15	59	198	25	90	294	29	110	363	0,35	0,70	0,89
D	15	29	105	24	59	145	29	78	199	0,34	0,62	0,89

Chord lengths

	Minimum 5%	Minimum Mean	Minimum 95%	Mean 5%	Mean Mean	Mean 95%	Maximum 5%	Maximum Mean	Maximum 95%	Min / Max 5%	Min / Max Mean	Min / Max 95%
A	7	11	25	10	13	28	7	16	34	0,47	0,67	0,79
B	8	15	28	10	18	32	11	20	35	0,54	0,75	0,92
C	8	21	47	10	23	50	12	23	56	0,51	0,73	0,93
D	8	15	26	11	17	30	13	21	35	0,48	0,71	0,91

Tab. 3.12: Pore geometrical parameters for objects equal and larger 17 dots. The parameters are quoted in averages and 5 % and 95 % percentiles.

	Diag.	Por. [%]	Perm. [mD]	Dens. [g/cm³]	Velocity [m/s]	Total objects	Analyzed objects	%	Size 5%	Size Mean	Size 95%	Perimeter 5%	Perimeter Mean	Perimeter 95%	Convex perimeter 5%	Convex perimeter Mean	Convex perimeter 95%
A	CT	10,47	1,40	2,40	2814	102.290	1.804	3	2.243	6.632	20.225	330	792	2.434	230	405	775
B	CT	11,56	16,47	2,37	2450	58.631	581	1	4.852	8.766	18.026	587	1.239	2.529	396	604	992
C	CT	11,52	118,80	2,39	2164	19.943	565	3	5.095	15.190	42.380	474	1.357	3.373	383	786	1.602
D	IC/IM	11,30	0,21	2,39	1950	29.387	446	2	4.820	7.850	15.627	566	1.157	2.108	416	635	988

Conv. Per / Per

	5%	Mean	95%
A	not available as large pores contain many holes		
B			
C			
D			

Feret projections

	Minimum 5%	Minimum Mean	Minimum 95%	Mean 5%	Mean Mean	Mean 95%	Maximum 5%	Maximum Mean	Maximum 95%	Feret orthog. / Max Feret 5%	Feret orthog. / Max Feret Mean	Feret orthog. / Max Feret 95%
A	66	100	303	88	161	315	87	178	536	0,37	0,64	0,93
B	85	134	214	127	193	318	149	240	403	0,15	0,61	0,92
C	82	168	350	122	251	502	152	313	660	0,38	0,62	0,84
D	87	139	229	134	203	313	161	254	389	0,38	0,60	0,90

Chord lengths

	Minimum 5%	Minimum Mean	Minimum 95%	Mean 5%	Mean Mean	Mean 95%	Maximum 5%	Maximum Mean	Maximum 95%	Min / Max 5%	Min / Max Mean	Min / Max 95%
A	13	22	35	15	25	41	17	30	49	0,65	0,74	0,81
B	19	27	41	20	30	45	23	33	51	0,73	0,84	0,93
C	26	40	61	28	44	65	32	49	73	0,69	0,83	0,95
D	18	26	42	20	29	46	22	33	52	0,68	0,82	0,94

Tab. 3.13: Pore geometrical parameters for objects equal and larger 440 dots. The parameters are quoted in averages and 5 % and 95 % percentiles.

Frequency scales

The frequency scales of parameters manifest perceptible distinctions for the four specimens. In order to keep track of the following comments only a smaller proportion of frequency diagrams are shown in this chapter. The complete charts are adjoined in the appendix (A-4).
Samples A and D present the narrowest peaks for most of the attributes, while the parameters of sample C display the widest scatter. For instance, the minimum chord lengths for objects starting with three dots vary for sandstone A within an interval of 52 µm with a pronounced deflection at 5 µm. In contrast this attribute for sample C differs by 104 µm and generates a slightly declining amplitude. Similar graphical separations are evident for the parameter pore size (fig. 3.23 D).
However, most of the quotients illustrate rather congruent distributions. So, for instance, shows the attribute convex perimeter/perimeter similar values for pores larger two dots. Only the graphs of the ratio of Feret projection (fig. 3.23 E), representing the aspect ratio, vary by featuring dissimilar numbers of crests of various heights.
Distinctions in frequency are also verifiable by examining the percentiles plotted in tables 3.11-3.13. So, for instance, demonstrates sample A the lowest 5 % but also a relative high 95 % rank for the attribute maximum chord length for objects larger 16 dots.
Most of these distinct characteristics are observable for all the three differentiated intervals of pore sizes (appendix A-4, fig. 3.23).

Fig. 3.23 (A-E) (next two pages): Selected frequency scales of pore attributes. These charts demonstrate amongst other things the independence of geometrical distinctions in pore geometry from scaling effects.
A-C: Minimum chord lengths of objects from 3, 17 and 440 dots ongoing. Graph A enlarged for better appraisal, abscissas in graphs B and C coincide. The distinctions in graphical distribution are evident for the three intervals of pore sizes. The differences demonstrate the distinct pore geometries of the four samples.
D: Pore size of objects exceeding two dots. The four samples differ palpably in their spectra of void sizes. Sample C prescinds mostly from the samples and features the largest and most scattering pore dimensions. The other curves are less distinct but their differences in pore geometries are still prominent.
E: Ratio of Feret orthogonal and maximum Feret. This quotient approximates best the aspect ratio. The pore geometry of sample A features the most circular shapes whereas the voids in specimens C and D appear to be in sum the less spherical pores.

Microscopic observations on pore geometry

The pore network of sample C exhibits a wide scatter of pore sizes with by far the largest voids of all samples (fig. 3.18). The degree of interconnections between pores appears to be higher compared to samples A and B and lower compared to specimen D. The apertures reach sometimes extensions similar to the adjacent minerals and surround wide parts of the components. These areas of low tortuosity and high porosity contain regions, where primary voids are pervasively occluded by quartz, anhydrite and calcite precipitation (fig. 3.18). The dense aggregates of mm-size are dispersed within the thin section and seldom conjoint. Intragranular porosity is present in feldspars and lithoclasts and contributes with 20 % (tab. 16 in appendix A-9:) to a high extent to total porosity, compared to the other three samples. The pore surfaces appear rounded and angular, and are except for cement surfaces predominantly a function of the primary mineral morphology. Sample C demonstrates the most significant evidences for secondary solution:
- The amount of etched lithoclasts results highest with 41% for all four samples (see appendix A-9).

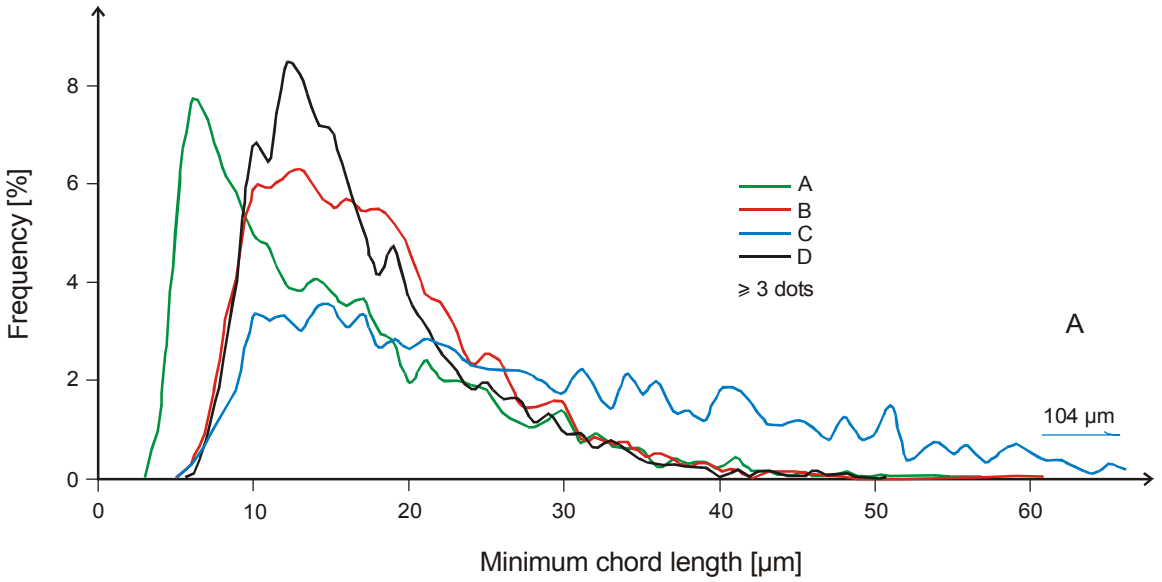
Frequency [%]
Minimum chord length [µm]
A
B
C
D
⩾ 3 dots
A
104 µm

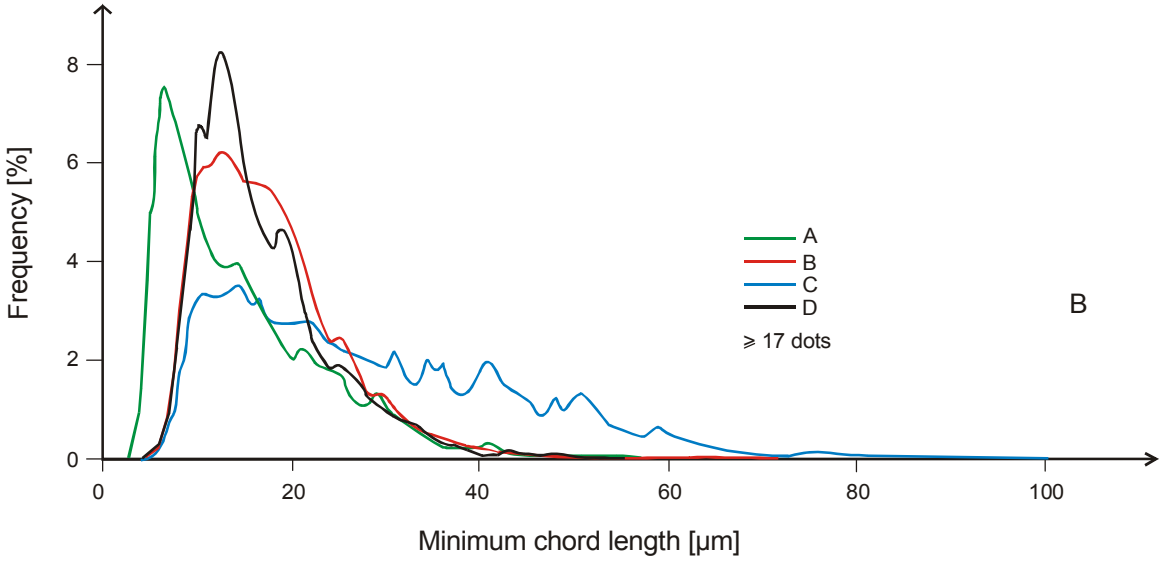
Frequency [%]
Minimum chord length [µm]
A
B
C
D
⩾ 17 dots
B

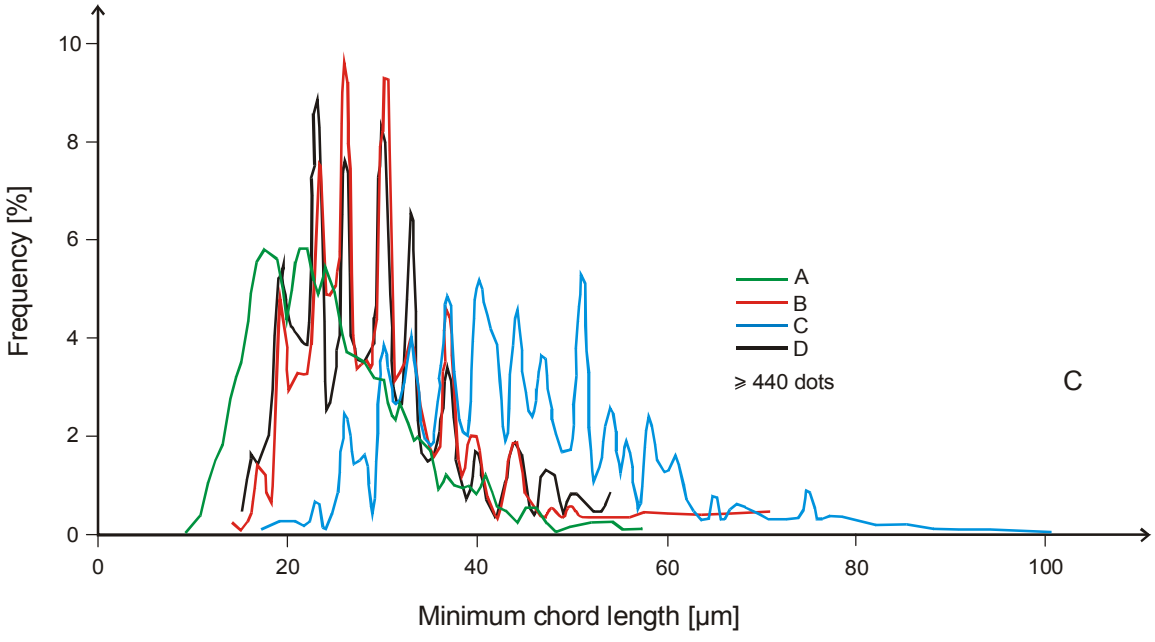
Frequency [%]
Minimum chord length [µm]
A
B
C
D
⩾ 440 dots
C

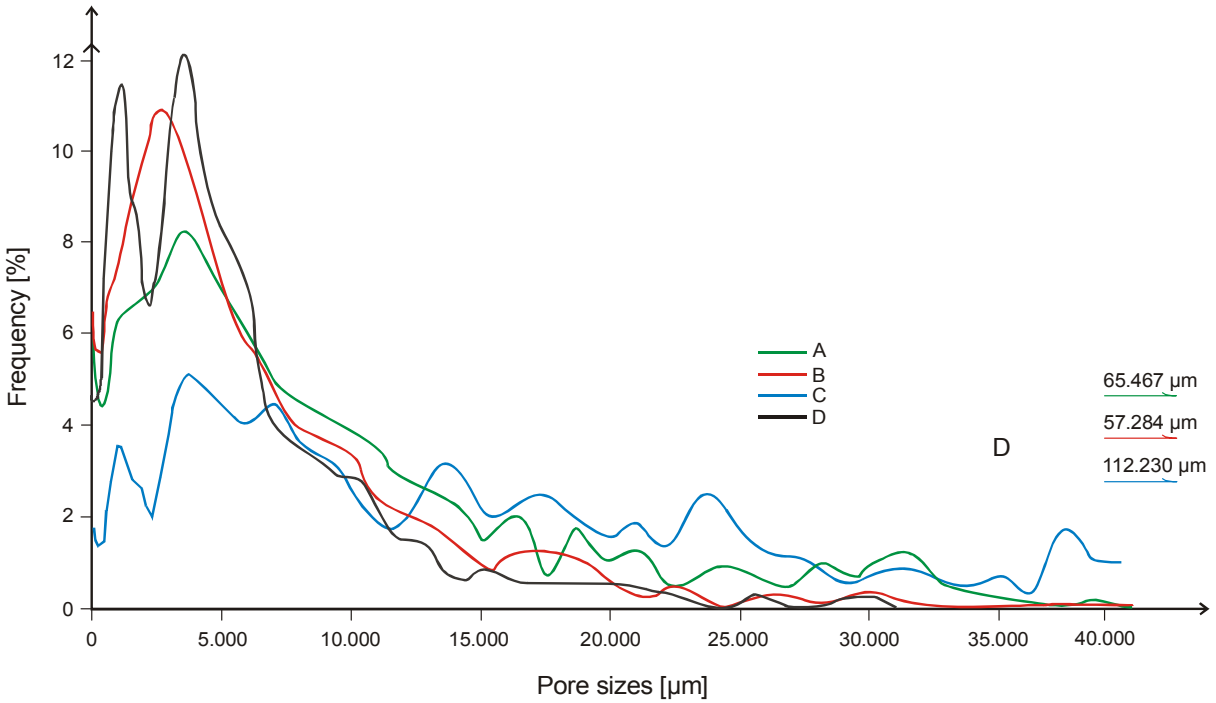

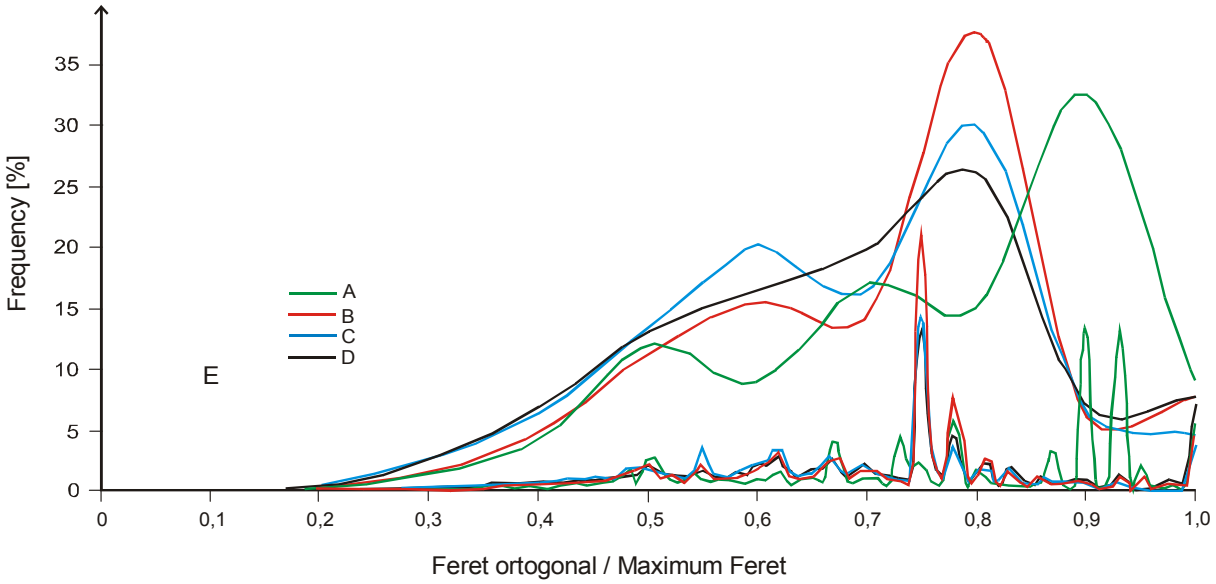

- The pore body contains large voids which in all likelihood can be associated to the dissolution of minerals, particularly feldspars and lithoclasts.
- The fraction of intragranular porosity is comparatively highest.
- The occurrence of isolated and dense clusters indicate a dissolution of blocky precipitates which had occluded large parts of the sandstone framework.

The dissolution comprised substantially authigenic minerals as the highest fraction of void volume represents primary intergranular porosity.

Sample D demonstrates the most homogeneous pore network composed of small voids well interconnected by thin and remarkably long conduits (fig. 3.18). The bulk part of the apertures is formed by intergranular gussets while the pore throats represent thin conduits between neighbouring mineral surfaces. The fraction of intragranular porosity resembles to

sample B. Although the fabric of sandstone D is characterized by a more compacted texture than for plug C it seems to feature a significant higher amount of interlinked voids and less tortuosity. The intensity of cementation is lowest for all samples. Regions of complete cement occlusion, like observed for the chloritized plugs, are absent. The proportion of etched lithoclasts and the fraction of intragranular porosity turned out lowest with 17 % and 4 %, respectively, compared to the chloritized specimens. The pore network barely embodies large pores and features almost primary porosity. The morphology of pore surfaces is rounded till angular and appears to be a function of grain- and cement shape and not of secondary solution.

The pore structure of sample A consists of isolated voids of more spherical shape than for sample D (fig. 3.18). Pore interconnections are barely existent due to the intense sandstone consolidation. Some apertures are completely occluded by authigenic precipitation. These cements form with adjacent minerals dense agglutinations which are smaller than in sample C and likewise isolated. The fraction of intragranular void volume on total porosity results with 16 % comparatively high (see appendix A-9). The voids contain often several µm large authigenic calcites, which are mapped as white spots in the black objects. The pore geometry is especially a product of cementation and is mainly composed of primary intergranular porosity. Some pore systems are generated by cement dissolution and are locally confined. Sample A manifests far less substantial modifications by secondary solution compared to specimen C.

Sample B contains laminations of preponderantly small and large void dimensions which are generated by an alteration of grain size within the thin section (fig. 3.18). The pores are smaller than for sample C but still exhibit a wide range. The interlinkage of pores seems to be better developed than for sample A especially for the beddings of larger particle diameter. However reach the pore throats by far not the frequency and diameters of those in sample C. The long and thin conduits between mineral surfaces observed in the illitized thin section are absent. The clusters with complete cement occlusion are also isolated and of small dimension. Intragranular porosity amounts to 13% and represents the lowest fraction within the chloritized samples but is still substantially larger than in sample D. Large voids are present but with far less abundance than for sample C. The pore geometry of this plug resembles rather the network structure of specimen A.

Figure 3.24 illustrates characteristic pores and pore geometries found in the four samples.

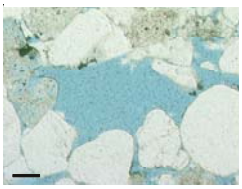


Large pore associated to secondary dissolution of mainly lithoclasts and feldspars. This type present is particularly in specimen C.

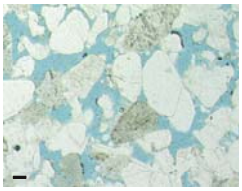
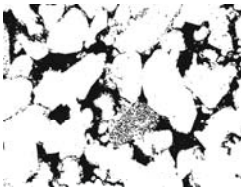

Loose particle texture with pores surrounding components forming large scale void networks with high degree of interconnectedness. This type is present particularly in specimen C and less frequent in B. The lower middle etched lithoclasts features intragranular voids.

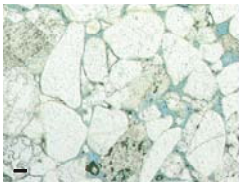
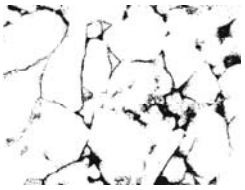

Long and thin conduits between adjacent particle surfaces with high degree of interconnections between small voids. This type is only developed in sample D building homogeneous and mostly primary networks.


Cement occluding voids and forming large scale dense aggregates of block precipitates and other particles. This type is present only in chloritized samples; particularly abundant in specimen C.

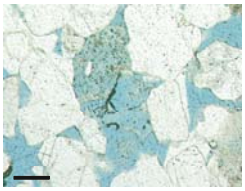
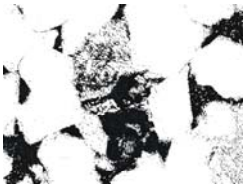

Intragranular porosity formed by particle dilution, here lithoclast. This type represents substantial porosity in all samples especially in the chloritized specimens.


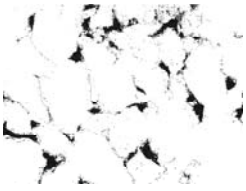

Small primary voids of low interconnection; geometry principally formed by detrital mineral walls and blocky precipitates; no indications of secondary solution discernible with optical microscopy; composes large parts of samples A and B.

Fig. 3.24: Pore types observed in four samples. Microscopic images are recorded with plane polarized light and after void decoding. Pores appear black, solid constituents white. Small black bar at the corner of the microscopic images represents 50 µm.

3.3.3.3 Discussion

Effects of outcome on permeability

As mentioned before, permeability is a function of a few pore geometrical aspects: frequency and dimension of pore throats, degree of interconnectedness and pore roughness.

The diameter pore throat, which was approximated by the minimum chord length, varies in accordance to the permeability of the chloritized specimens. Sample C with the highest permeability of 118,8 mD exhibits a 3 fold larger size of pore restriction than sample A with 1,4 mD. Furthermore appear the pores in specimen C to be connected by a wider range of throat diameters compared to the narrow distributions of minimum chord lengths for the samples A, B, and D.
Solid-fluid interface processes like bounding of water molecules can narrow fluid conduits in capillaries severely. Hence the large proportions of small void sizes and the lower aspect ratios for samples A and B could intensify the permeability contrasts.
The 5 fold larger fraction of intragranular porosity of sample C compared to the illitized specimen could also reduce flow rates distinctly. The isolated regions of complete cement occlusion are believed to elongate potential migration paths but should not impede fluid flow.
Permeabilities are generally a strong function of grain size distributions and particle contact conditions which could vary within individual and across laminations.
The average pore sizes result comparable parallel and perpendicular to the plug axis. However, the attribute shows a pronounced variability within some individual sections in both x- and y-direction. As a liquid will follow the path of least resistance it is plausible that regions of diverse pore structures could cause anisotropic behaviour. The similar average offsets of the pores for all specimens indicate an assimilable network. This conformity between the samples is most probably a result of their resembling grain size distributions and the fact that their pore network is composed of a large fraction of primary intergranular porosity.
It is plausible that principally with a declining number of pores the permeability of a porous system should decrease. Sample A with the lowest concentration of voids hence features the minimum permeability for the three chloritized sandstones. The framework of plug C contains likewise comparatively low number of pores. However, the larger throats and higher degree of interconnectedness present in sample C enhance pore efficiency to fluid transport strongly.
Generally, the pore parameters of the illitized sample reflect a similar pore geometry as the chloritized sandstones and range predominantly within the magnitudes of attributes of samples A and B. This result indicates that without the presence of illite fibres in pore space the plug D would exhibit higher permeabilities, potentially between 1 and 15 mD.

Modelling of permeability with pore geometrical attributes

The individual effects of pore throat and pore roughness on permeability can be quantified by means of the Kozeny-Carman equation. This relation is based on a simple model, ‘the capillary tube model’ and was derived by Kozeny (1927) and later reworked by Carman (1956). The pore is ideally modelled as a cylindrical channel of radius r and length l within a cube of side length L (fig. 3.25).

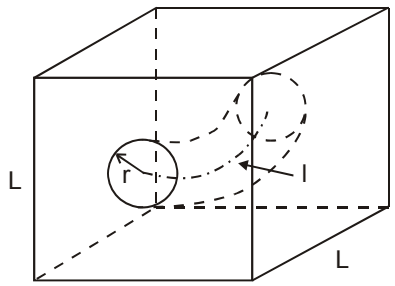

Fig. 3.25: Simplified model of a pore assumed as cylindrical channel. Modified after Schön (1998).

The permeability results from the Darcy equation by assuming that the flow rate follows the Hagen-Poiseulle law, as:

$k = \frac{\Phi * r^2}{4 * T^2 * \chi}$ with k as permeability and Φ as porosity.

For non circular tubes the factor 2 is replaced by the cross section shape factor χ accordingly (e.g. Engelhardt 1960, Georgi & Menger 1994).

Although this equation derives from a simple approximation of a pore network and may be used with caution for sandstones of high tortuosity (Carman 1956) it has widely been recognized directly (e.g. Collins 1961, Ruzyla 1986, Chilingarian et al. 1992) and after modifications (e.g. Pape et al. 1985) as a useful method to estimate permeability.

For the following calculations the minimum chord lengths and the image derived porosity are utilized for objects larger two dots from table 3.11. For simplicity reasons the capillaries are assumed to be equal and the unknown variables were supposed to be constant. The modelled permeabilities result as follows (tab. 3.14):

	A chloritized	B chloritized	C chloritized	D illitized
Core permeability (mD)	1,4	16,5	118,8	0,21
Proportions	1	11,8	85	0,15
Permeability by Kozeny-Carman, r variable	A*2,5²	A*5²	A*7,5²	A*4,5²
Proportions	1	4	9	3,2
Permeability by Kozeny-Carman, χ & r variable	B*2,5²/3,0	/	B*7,5²/1,67	/
Proportions	1	/	16	/

Tab. 3.14: Permeabilities from cores and from modelling by means of the Kozeny-Carman equation (Carman 1956). Permeabilities are calculated by varying the channel radius r and the cross section shape factor χ. To ease interpretation the relative factors of permeabilities are added, with 1 representing the permeability of sample A.

These results demonstrate that the ascertained variation in pore throats can not solely provoke the differences in core permeability, also when maximizing the differences by assuming an ellipsoid shape factor for sample A and a triangular cross section for sample C (cross section shape values from Schön 1998).

In order to quantify the effect of pore roughness on the core permeability the Kozeny-Carman equation is modified into:

$k = \frac{\Phi^3}{\chi * (1-\phi)^2 * SS^2 * T^2}$, with SS denoting the specific internal surface.

For use with thin section data the specific surface is replaced by the ratio of pore perimeter and pore size (Mowers & Budd 1996):

$$k = \frac{\Phi^3}{\chi * (1-\phi)^2 * T^2 * 16 * U^2 / (\pi * F)^2}$$

This introduced quotient of two dimensional parameters is directly proportional to the three dimensional ratio of pore surface area per unit volume (Kendall & Moran 1963). By applying the ratios shown in table 3.16 from image analysis and the average pore sizes for objects larger two dots the calculated permeabilities constitute to (tab. 3.15):

	A chloritized	B chloritized	C chloritized	D illitized
Core permeability (mD)	1,4	16,5	118,8	0,21
Proportions	1	11,8	85	0,15
Permeability by Kozeny-Carman, U/F variable	C/0,19²	C/0,13²	C/0,07²	C/0,22²
Proportions	1	2,1	7,4	0,7

Tab. 3.15: Permeabilities from cores and from modelling by means of the modified Kozeny- Carman equation (Carman 1956). Permeabilities are calculated by varying only the pore roughness U/F. This variable substitutes the three dimensional ratio of pore surface per unit volume. To ease interpretation the relative factors of permeabilities are added, with 1 representing the permeability of sample A.

	Perimeter / area [m^{-1}]
A	0,19
B	0,23
C	0,12
D	0,22

Tab. 3.16: Attribute perimeter per area for pores exceeding two pixels which was used for calculation of modelled permeabilities.

The results evidence that pore roughness solely can likewise not cause the variances in core permeability.

Permeabilities could be modelled also by introducing the electrical formation factor into the Kozeny-Carman equation (Pape et al. 1985). This factor is a purely geometric parameter and describes to which extent a porous body allows transport processes (Pape et al.1999) and replaces the tortuosity. The latter results often tricky to quantify. Unfortunately no data on electrical measurements on Wustrow core plugs were attained from the Petroleum Companies due to proprietary reasons.

More models and theories which include pore geometrical effects like pore wall morphology or pore connectivity in a more sophistically manner, were presented e.g. by Gueguen and Dienes (1989), Schopper (1972) and Pape et al. (1987). However estimations of permeability with those relationships were not conducted due to lack of corresponding data and as some of these complex approximations go beyond the scope of this chapter.

Summing up

The pore geometrical features determining permeability (see e.g. Dullien 1992) differ distinctly for the three chloritized sandstones. It is assumable that pore throat size and -range, degree of interconnectedness, fraction of intragranular porosity and pore wall roughness provoke jointly and to a substantial extent the variances in core permeability. The permeability of the chloritized sandstones is furthermore a function of the framework compaction and locally extensive dissolution.
The similarity of pore geometry for sample D to the structures in specimens A and B suggest that without illite meshwork (IM) in pore space the illitized sandstone D would permit considerably higher permeabilities. This assumption does not consider any diagenetic modifications becoming potentially effective if illite types are absent.

Effects of outcome on compressional velocity

The above quoted attributes relevant to velocity differ for the four samples in accordance to their plug travel times. The trends of these parameters are outlined in table 3.17 and integrate the three investigated intervals of pore sizes.

	Sample A chloritized	Sample B chloritized	Sample C chloritized	Sample D illitized
Porosity				
Permeability	→	→	→	lowest
P-wave velocity	←	←	←	lowest
Density				
Pore interconnectedness	low	medium	high	high
Sphericity	high	low	low	low
Orientation			n.a.	
Range of pore size	narrow	narrow/ medium	wide	narrow

Tab. 3.17: Trends of parameters affecting rigidity of pores. No magnitudes are presented as the parameters are integrated over the three intervals of pore sizes. Range of pore size is set apart as its squirting effect is only existent by presence of pore liquids.

The attribute pore interconnectedness, which is believed to reduce ultrasonic and seismic speeds (e.g. Prasad et al. 1999), is highest for samples C and D. These sandstones exhibit the lowest velocities. In correspondence thereto, sandstone A with the highest speed manifests the lowest degree of interlinkage of pores.
The magnitude of sphericity is believed to increase elastic modules and velocities (e.g. Anselmetti & Eberli 1997). Sandstones C and D contain the most deformable voids as their apertures feature significantly lower aspect ratios. The pore network of specimen A presents the most spherical voids which enhances the rigidity of the framework.
Unfortunately the data on the orientation of the pore axis were not utilizable to verify a velocity dependence on the alignment of pores and pore throats.
The effects of partial fluid saturation affecting wave characteristics by building viscous skins (Biot 1956 a & b) and inducing fluid squeezing mechanisms (Murphy et al. 1984) are not verifiable empirically on these plugs as no experiments with varying gas content and frequency were conducted. However, partially saturated sandstones with a large range of pore sizes and high degree of pore interlinkage demonstrate low velocities due to enhanced fluid mobility (Mavko & Nolen Hoeksema 1994). Therefore the pore network of sample C

should comparatively improve squirting phenomena and exhibit minor plug speeds. As mentioned before, the velocities are particularly affected by the properties of the fluids occupying the voids with low aspect ratio (Toksöz et al. 1976, Mavko and Nur 1979). In case of similar fluid distribution the velocity of specimen C should hence be dominated by its pore contents. Despite of the resembling low aspect ratio for sample D a similar effect would probably be not ascertainable for the water bearing case. The illite rims will retard namely the fluid movement in the conduits and hence reduce pressure equilibration and increase the velocity.

Effects on some pore geometrical parameters when coding illite fibres as solid or as void volume – case study

As previously explained, the coats of illite meshwork are mapped as pore volume. The colour analysis could namely not delimit the tiny fibres and mark them as solid components. However coding the illite rims as dense solid pore material results likewise not realistic as within the fibres significant interstitial void volume is present (plate 1.1. C, D). In order to quantify the range of variation in pore geometry, when typing the IM-overgrowths as either void or solid components, microscopic pictures were especially elaborated. Figures 3.26 and 3.27 illustrate figuratively the significant differences in pore geometry for both cases. Figure 3.26 displays the void network when mapping the illite meshwork fibres as pore volume and when classifying them as solid material. The geometric differences are exemplified in detail on a pore in figure 3.27, where the IM-fibres appear clearly within the black objects as thin white stripes. The pictures are not recorded on sample D but on an illitized, finer grained eolian (mean grain size <0,1mm) sandstone with 9,8 % porosity. The analyzed section of this sample reproduces the total pore network not representatively.

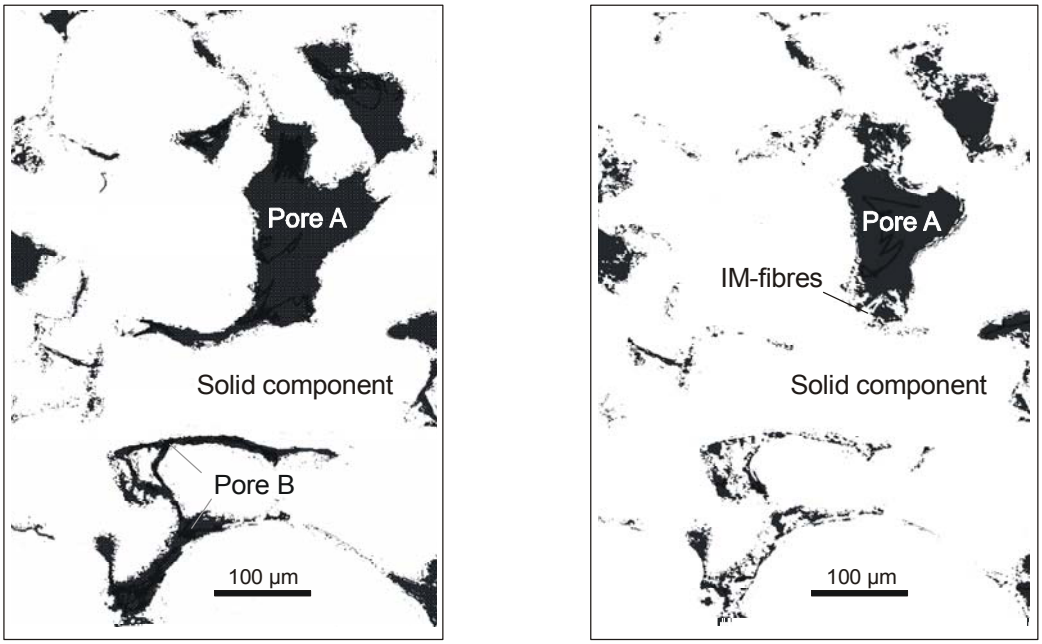

Fig. 3.26: Pore system of an illitized sandstone containing illite fibres of the IM-type. Left pore system when classifying illite crystals as void volume; right network when coding the precipitates as solid constituents. Black areas represent pores, white areas solid constituents. Distinctions are palpably evident when comparing the alteration of the digitized pores A and B in the two networks

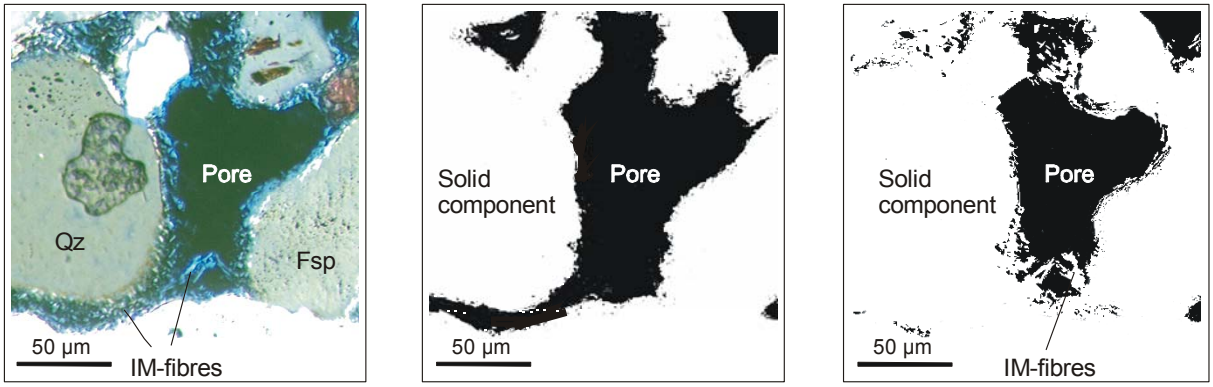

Fig. 3.27: Variations in reproduced network exemplified on a pore in detail. Voids are coded black, solid constituents white.

The network with illite coded as voids presents comparatively larger and more interlinked pores. For instance, the void region marked as 'pore B' in figure 3.26 appears as an interconnected pore structure while in the other version of the network it is dissected in multitudinous isolated apertures. The pores in the right network delineate these fibres and result thus more corrugated in the corresponding pictures. The image derived porosities vary significantly with 15,8 % and 10,2 % for figure 3.26.

Table 3.18 lists some pore geometrical attributes quantified on both figures for objects larger than two dots with the image analysis technique.
The magnitudes for the average pore size and its percentiles vary distinctly according to the larger size of voids when incrementing the pores by the volume of the fibres. The aspect ratios demonstrate a slightly more spherical shape for the average pore. The minimum chord lengths result akin for both cases and do not reflect the deductions on interlinkage drawn by eye.

Area	**mean** [µm]	divergence [%]	**95%** [µm]	divergence [%]	**5%** [µm]	divergence [%]
IM as void volume	32		47		0,4	
IM as solid constituent	23	**29**	34	**7**	0,4	**0**
Min. chord length	**mean** [µm]	divergence [%]	**95%** [µm]	divergence [%]	**5%** [µm]	divergence [%]
IM as void volume	1		3		0,4	
IM as solid constituent	2	**7**	4	**57**	0,5	**10**
Aspect ratio	**mean** [µm]	divergence [%]	**95%** [µm]	divergence [%]	**5%** [µm]	divergence [%]
IM as void volume	0,75		0,94		0,44	
IM as solid constituent	0,82	**9**	0,96	**57**	0,44	**0**

Tab. 3.18: Pore geometrical attributed determined with image analysis technique for the networks in fig. 3.26; palpable difference in pore size. The analyzed network is not representative for the whole pore structure.

Table 3.19 lists also the pore features of the comparatively large void marked as ‘pore A’ in the figure 3.27. For this individual void the geometric attributes differ markedly for both cases of coding: the pore sizes and the minimum chord length by 39 and 36 %, respectively.

	A chloritized	B chloritized	C chloritized	D illitized
Core permeability (mD)	1,4	16,5	118,8	0,21
Proportions	1	11,8	85	0,15
Permeability by Kozeny-Carman, U/F variable	C/0,19²	C/0,13²	C/0,07²	C/0,22²
Proportions	1	2,1	7,4	0,7

Tab. 3.19: Pore geometrical parameters derived with image analysis technique for pore A in figure 3.27. Clear distinctions are manifested in pore size and minimum chord lengths.

In summary should an image of a pore system composed of voids and interstitial fibres should feature comparatively larger apertures, more interlinkage and less tortuosity. The variations in pore geometry for both cases depend on the abundance and textural position of the fibres.
This case study illustrates the possible differences in pore geometry which are encountered when mapping the fibres either as solid rims or as void volume. Both networks do not reflect the real conditions but would provide maximum and minimum limits for the attributes.
It is not feasible to determine the range of attributes accurately for both cases with the available data. However in this work the pore geometric information of sample D was principally interpreted concerning conclusions on permeability and velocity by the absence of the IM-fibres.

3.3.4 Pore geometry from Nuclear Magnetic Resonance (NMR)

3.3.4.1 Method

Nuclear Magnetic Resonance (NMR) techniques are applied in the petroleum industry to derive pore size distributions and the fraction of moveable fluid in order to estimate formation permeability (Arns et al. 2005). Although the retrievable information represents important aspects of reservoir characterisation NMR applications are so far not sufficiently embraced in geological studies (Basan et al. 2003).
The following outlines on the working principles of the NMR measurement are based on literature published by Fukushima & Roeder (1981), Kleinberg & Horsfield (1990), Kenyon (1992) and Stapf & Han (2005).
The NMR penetrates water filled porous rocks with electromagnetic fields. The magnetic moments of the atoms tend to align to the direction of the artificial energy. The orientation of the field is changed repeatedly which provokes a continuous re-arrangement of the excited particles. This reorientation produces a radio signal itself, which can be detected. Most of this energy is released by the hydrogen nucleus. The magnitude of the returning signal is thus a measure for the water and hydrocarbon filled porosity. The decay rate of the radio waves is a function of the interactions between fluids and pore walls. Long relaxation times derive from fluids in large pores, which are predominantly moveable due to reduced attraction from solid surfaces. Below certain time cutoffs fluids are considered immobile either due to capillary forces in smaller pores or by coulomb forces in the clay minerals. By studying the curve of the decline in magnetization, NMR-relaxation rates deliver the proportions of pore water: the two volumes adsorbed to clay and capillary surfaces, and the mobile fraction.
The theory to the NMR-magnetisation decay is largely based on relatively simple pore geometries (Arns et al. 2005). The interpretation of signals can result erroneous as internal magnetic fields (Øren et al. 2002) and heterogeneities in surface relaxivity are ignored in the NMR-model (Hürlimann 1998, Appel et al. 2001). Such eventual improper assumptions could render the use of default time cutoffs for different rock types disputable (Dunn et al. 2002, Basan et al. 2003).

Apparatus and parameters

The measurements were carried out in the ‘Institut der Geowissenschaftlichen Gemeinschaftsaufgaben (GGA)’ in Hannover by R. Kappes. Relaxometry was conducted on a ‘Maran Ultra 5’ manufactured by Resonance Instruments. The ‘pulse echo’-spectrometer is optimized for analyses on porous rocks. The relaxation times were set according to the recommendations in literature for shaly sandstones (e.g. Howard et al. 1991, Kenyon 1992, Straley et al. 1991). The results deviate significantly for a few samples due to the difficulties encountered when determining the decay curves (pers. comm., R. Kappes, 2004, Institute GGA, Dunn et al. 2002). For more information on equipment and procedure please refer to Rifai et al. (2005).

3.3.4.2 Samples

The NMR-measurement was conducted on eolian dry sandstones of the Wustrow interval from two wells within the blue and one well within the red seismic facies classes. The specimens feature variable porosities and permeabilities and are either IM- and IC- or only CT-altered. Their fluid conductivities differ clearly according to the occurring diagenesis type. In total, 37 specimens were examined, the samples B, C and D were included in the analyses.

The relaxation diagrams and the absolute and relative magnitudes of the water fractions for each sample are alleged in the appendix (A-10).

3.3.4.3 Results & discussion

Effects of outcome on permeability

Figure 3.28 presents two relaxation graphs for specimens of illite and chlorite authigenesis. These graphs are representative for both groups of reservoir rocks.
The intensity of the radio signal decays earliest for the illitized probe. The signal exhibits two large peaks within the time regions reflecting clay bound and capillary water. The magnetization from mobile molecules turns out comparatively small. In contrast, the decay spectrum of the chloritized sample manifests a considerable large free water fraction. These characteristic distinctions for illitized and chloritized sandstones are observable for most of the analyzed samples.

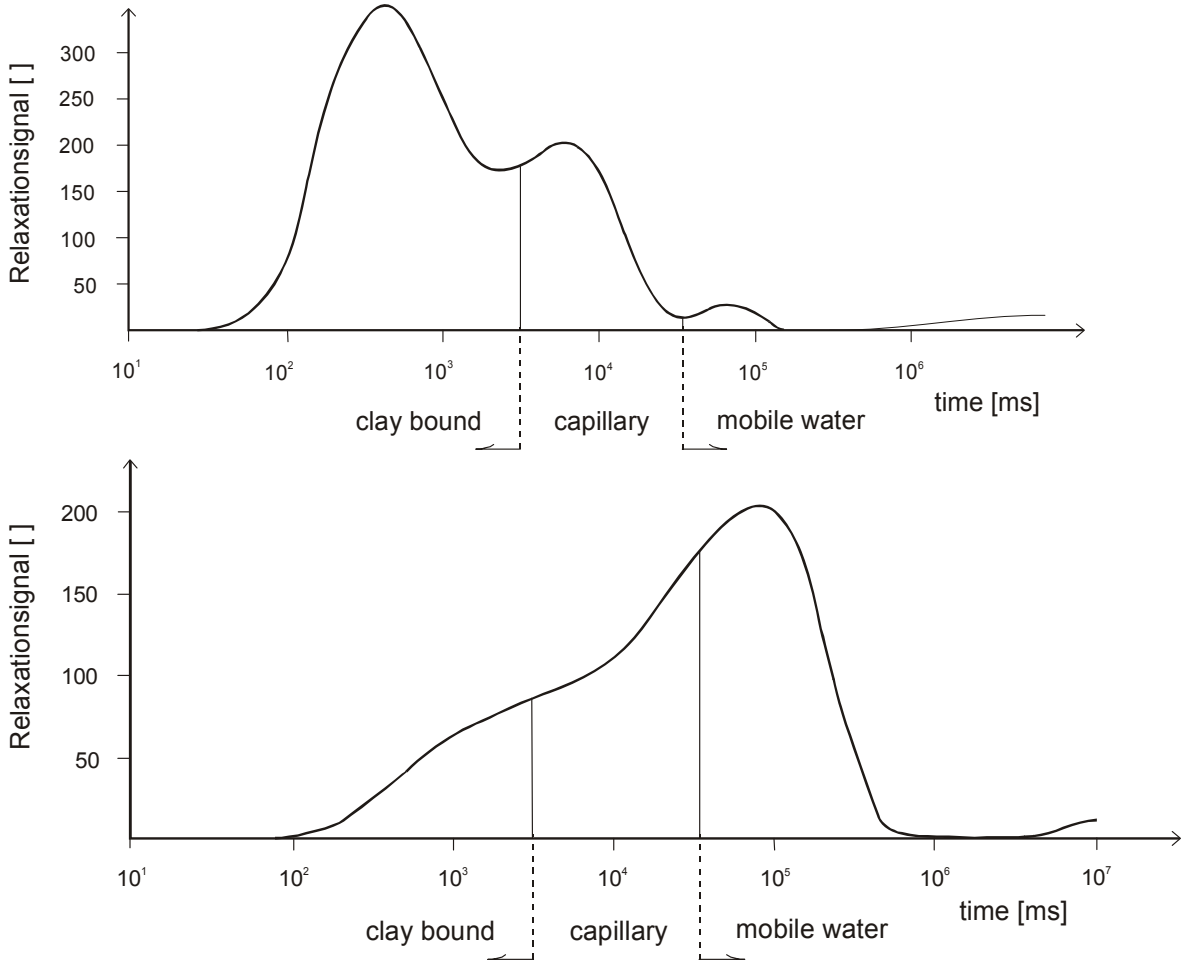

Fig. 3.28: Representative decay spectra for illitized and chloritized sandstones.
Above: Decay spectrum of an illitized sandstone of 4,1 % porosity and 0,004 mD. The vertical lines within the graph demark 4 and 33 ms as time cutoffs of relaxation for clay bound and capillary water fractions respectively. Most of the pore water is immobilized; the clay bound water represents the bulk volume of pore water.
Below: Decay spectrum of a chloritized sandstone of 11,5 % porosity and 16,5 mD. Time cutoffs as are chosen above: The lowest fraction of relaxation derives from the clay bound water, the largest from the mobile water.

Table 3.20 lists average values, maxima and minima differentiated by the occurring diagenesis type.
The average illitized reservoir rock presents the largest fraction of water bound to the clay minerals. This porosity is significantly lower for the mean chloritized sample. The immobile water fractions comprise the bulk part of the water volume for both groups. The most pronounced distinction represents the proportion of mobile fluid which turned out more than twice as large for the chloritized category than for the illitized group.

Eolian sandstones of:	illite alteration (n=25)	chlorite alteration (n=12)
Water type		
clay bound	47	34
capillary bound	36	25
mobile	17	40
immobile	83	59

Tab. 3.20: Average water proportions for reservoir rocks of illite and chlorite alteration. The immobile water type represents the sum of capillary and clay bound fluids. A clear distinction is existent in mobile and immobile water fractions.

Figure 3.29 presents the volume of clay bound water and the corresponding illite contents. The illite content is determined by point counting (DGMK-database, appendix A-9) and represents the total authigenic clay content as other secondary clay minerals are barely present in these reservoir rocks. The samples of chlorite diagenesis type are not included in the chart. Their point-counted amount of authigenic chlorite constituted to less than 1,5 % and was hence too erroneous (according to tht estimations of uncertainty in Howarth 1998).
The data points are distributed in two regions. These clouds confine samples of an individual well. The specimens of the two boreholes differ by illite content. The diagram evidences that in both clouds the bound water fraction rises clearly with increasing illite abundance.

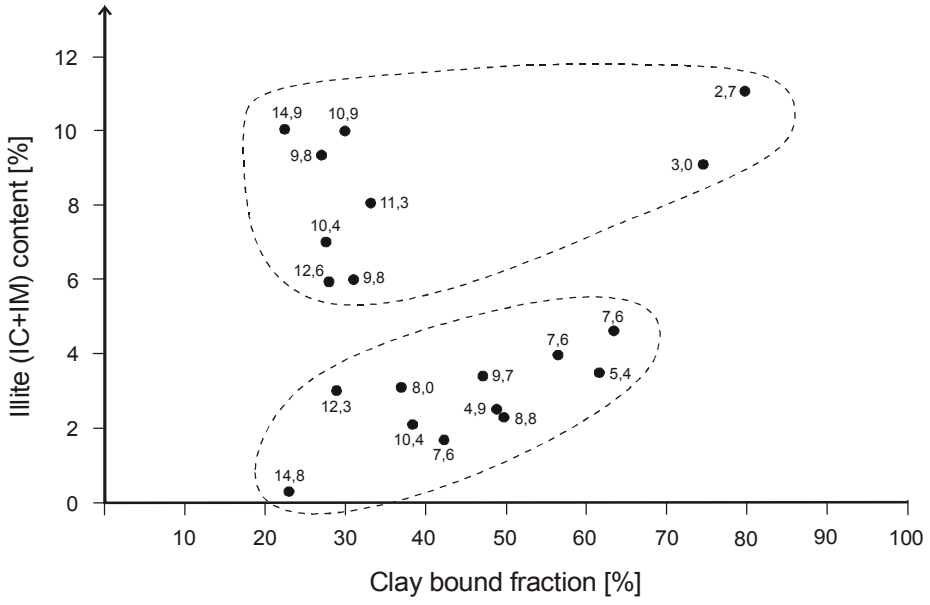

Fig. 3.29: Proportion of water bound to clay mineral surface and point-counted illite content. The illite content represents total authigenic clay content in these illitized sandstones. The two data clouds include exclusively samples of one individual well. The water fraction is given as percentage of pore water. The porosities are added next to the data points. A trend of increasing clay bound water fraction with augmenting illite abundance is palpable.

The graphs in figure 3.30 show furthermore an increasing tendency for the volume of free water with permeability for both low and high permeable samples.

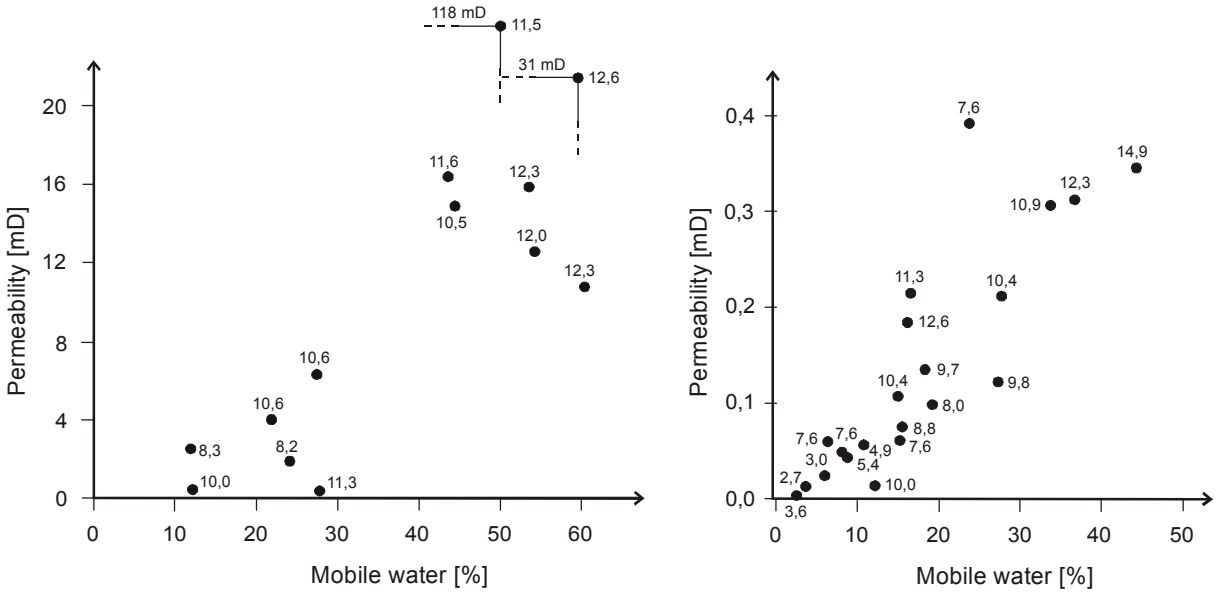

Fig. 3.30: Permeability and free water fractions. Mobile water is given as percentage of total pore water. The porosities are next to data points. A clear interdependence for both parameters for high (chloritized, left) and low (illitized, right) sandstones is visible.

Table 3.21 lists the fractions of water and fluid fractions for the samples B, C and D. The proportions of free water vary significantly in accordance to the permeabilities. This distinction is mainly a function of the amount of fluid entrapped in capillaries. The water adsorbed to clays is slightly distinct for the three samples and results low for sample D compared to the average magnitude of illitized sandstones. The NMR-results comply with the findings attained by the image analysis technique. So, for instance, the maximum pore sizes for sample C are reflected in its largest abundance of mobile fluid.

	Sample C chloritized 118,8 mD	Sample B chloritized 16,5 mD	Sample D illitized 0,2 mD
Water type			
clay bound	29	32	37
capillary bound	20	28	46
mobile	51	40	18
immobile	49	60	83

Tab. 3.21: Water fractions of the samples B, C and D. Clear distinction is visible in the proportion of mobile water content according to their permeability. Sample D features a comparatively slightly elevated clay bound water fraction.

In summary, the analyzed illitized and chloritized specimens differ clearly according to the water fractions in their pore system. The silt and sandstone groups are characterized by distinct pore size distribution: The void networks in the illitized reservoir rocks comprise comparatively larger proportions of capillaries and far less apertures of larger aspect ratio which reduce the interface area for solid-fluid interactions. Furthermore, the data document that the influence of clay minerals impeding fluid flow is distinctly more pronounced for reservoir rocks of illite alteration than for samples with chlorite morphotypes. Most probably

the exposed surfaces of illite meshwork fibres, which gather into pore space, favour the immobilization of water molecules.
In contrast the rims of tangential chlorite should provide minor accessible surface to enable the generation of viscous skins. This precipitate is namely less exposed to the fluid due to its pore lining habit and further far less abundant than illite meshwork crystals (chapter 3.1.1).
These data support the finding of Gaupp & Solms (2005) who attributed the reduced flow properties in illitized sandstones to the presence of illite fibres in pore space. The apparent influence deriving from pores of capillary size on permeability alludes to an additional significant source determining flow properties of these Wustrow sandstones. The deteriorating effect of fine pores on fluid conductivity became clearly evident in the analyses regarding the pore geometry of the three chloritized sandstone samples.

Effects of outcome on velocity

As explicated in chapter 3.3.1.1 pore geometry co-determines the firmness and velocity of porous rocks. The feature pore size represents one crucial attribute affecting elastic wave speed (e.g. Anselmetti & Eberli 1997, Guéguen & Boutéca 2004, Prasad et al. 2003). The NMR- derived pore size distribution could thus manifest a relation to the plug speeds.

Figure 3.31 charts the sample velocities and fractions of free water which approximate the quantity of large voids.
The data points are arranged in two clouds: the upper region represents exclusively samples with chlorite precipitation, whereas the lower section contains only data from samples with illite alteration. The lower cloud exhibits a clear dependence of velocity on the proportion of large pores. This trend is slightly noticeable for the chloritized samples.
The corresponding core porosities were plotted next to the data points as velocity of elastic waves diminuishes heavily with increasing void volume (Wyllie at al. 1956). It appears that the distribution of the values could be additionally a function of this property. When examining the results of samples from resembling porosities (same figure) the graphical correlation still persists and becomes more trustworthy.

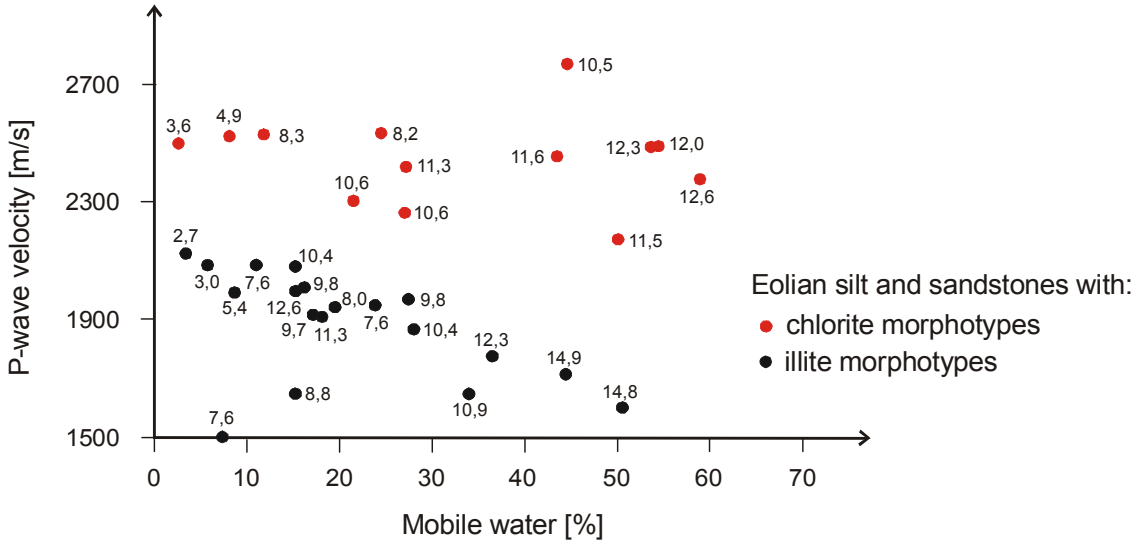

Fig. 3.31: P-wave velocity against fraction of mobile water for sandstones of both diagenesis types. Mobile water is given as percentage of total pore water The porosities are added next to the data points. A clear negative correlation for both parameters for samples of illite alteration is existent. Only a slight indication of interdependence for chloritized sandstones is visible.

However, this seeming dependency could also be caused by distinctions in micro textural features like variations in the type and frequency of particle contacts, in the abundance of clay minerals within particle contacts or in pore geometrical characteristics like void interconnectedness and void axis alignment.
This latter result exemplifies like in chapter 3.2.4.1 the need for conducting the textural studies on appropriate specimens in order to reduce the sum of the relevant factors affecting compressional velocities and permeabilities.

3.3.5 Pore geometry from Mercury Capillary Porosimetry

3.3.5.1 Method

Mercury Capillary Porosimetry represents an experimental method to derive petrophysical properties regarding fluid transport efficiency like effective porosity, pore throat sizes and displacement pressure (Jennings 1987). This information provides an aid in evaluating formation quality, especially regarding net pay criteria like reservoir pressure limits for economic hydrocarbon recovery (Schowalter 1979).
Mercury, acting as a non-wetting fluid is injected into a porous rock. As surface forces resulting from the interaction within and between liquids and bounding minerals (Vavra et al. 1992), will oppose the entrance of mercury (Purcell 1949), confining pressure is applied and stepwise increased. The volume of penetrated fluid, which displaces the wetting air, is recorded at each corresponding pressure level (Melas & Friedman 1992).
The applied capillary pressure is given by the Washburn equation (Washburn 1921):
$P_c = \frac{2 * \delta \cos\theta}{r_c}$ with σ as interfacial tension (480 dynes/cm, for mercury), θ as contact angle (for mercury in air 140°) and radius r as radius of a cylindrical pore (Pittman 1992).

Thus the capillary radius can be attained through the fraction of the pore system which is accessible at the corresponding pressure stage. The volume of penetrated fluid approximates the abundance of the actual pore radius. The calculated pore dimensions represent pore throat sizes as the penetration rate is limited by the minimal constrictions in the fluid pathways. With these data frequency scales of pore throat sizes and semilog plots of pressure against imbibed mercury volume are compiled.
However, these mercury capillary curves do not deliver the size of the pores themselves but rather the largest aperture through which the pore volume can be accessed. The calculated values represent thus only the effective size of the throats, which may not equal the real dimensions (Vavra et al. 1992). In addition, a shielding effect exists in which small pore connections could prevent mercury intrusion of pore volumes with large throats until sufficient pressure is applied to intrude this porosity (Wardlaw 1976).
A number of parameters can be extracted from Mercury Capillary Porosimetry. The most utilized ones are effective porosity, pore throat sorting (Thomeer 1960, modified by Jennings 1987), reservoir grade (Jennings 1987), accessibility ratio (Wardlaw & Taylor 1976), withdrawal efficiency (Wardlaw & Taylor 1976), pore throat to pore size ratio (Yuan & Swanson 1989), relative permeabilities (Amyx et al. 1960) and height of the hydrocarbon column to guarantee production (Smith 1966).
To produce most of these factors data on residual mercury saturation are needed and special techniques of mercury injection are conducted. However, the petroleum companies provided only raw data on standard mercury injection and no information on residual saturation.

The interpretation in this study is hence restricted to effective pore radius, effective porosity and pore throat sorting:
Effective pore radius quantifies the radius of the void restriction in two connected pores (Dullien 1992).
Effective porosity refers to the proportion of total porosity accessible for mercury at certain thermodynamic conditions (Melas & Friedman 1992).
Pore throat sorting is defined as the ratio of pressures at the first and third quartiles of mercury saturation:

$$PTS = \left(\frac{3rd\ quartile\ pressure}{1st\ quartile\ pressure}\right)^{1/2}$$

It quantifies the sorting of pore throats and ranges from 1,0 indicating perfect sorting to 8,0 signifying essentially no sorting (Melas & Friedman 1992). Most rocks fall into the range of 1,2 and 5,0 (Jennings 1987).

3.3.5.2 Samples

The analyzed Wustrow sandstones derive from wells of the low and high permeability regions. The specimens are either CT or IC/IM-altered. The permeabilities of these eolian dry plugs range below 1 mD and between 1 and 198 mD, respectively. Unfortunately no more data were available from other wells as these tests are expensive and hence not abundant (pers. comm., R. Möller, 2004, Laboratorium Wietze). In total 22 specimens were examined, however, samples A-E could not be included.
The pore throats were calculated by means of the Washburn equation and the previously quoted parameters for mercury. All curves and data of the samples are alleged in the appendix (A-8).

3.3.5.3 Results and discussion

Table 3.22 lists the mean values and minimum and maximum magnitudes of the average pore throats, effective porosities and pore throat sorting. The maximum applied pressure constituted for all samples to 150 bar.

		Porosity [%]	Permeability [mD]	Effective pore radius, [µm]		
				min	mean	max
CT-altered samples	n=7	9,24-17,59	4,12-198,07	1,65	3,16	5,32
IC/IM-altered samples	n=9	6,33-15,45	0,04-1,07	0,22	0,37	0,56

	Effect. porosity, [%]			Pore throat sorting, [ ]		
	min	mean	max	min	mean	max
CT-altered samples	95,68	97,43	99,13	1,84	2,21	2,47
IC/IM-altered samples	56,20	74,24	86,00	2,66	2,91	3,16

Tab. 3.22: Parameters quantified by means of Mercury Capillary Porosimetry given in mean, minimum and maximum magnitudes. The data are differentiated into high and low permeability samples which correspond to CT and IC/IM altered specimens. The samples represent sandstones of the eolian dry facies. Effective porosity and effective pore radius differ distinctly for the two sandstone groups according to their permeability. Pore throat sorting evidences a narrow distribution of pore throats for all samples with a slightly better sorting for the samples of higher fluid conductivity.

The high permeability plugs differ distinctly from the low permeability samples by the first two parameters: the fraction of accessible pore volume is highest for the plugs of CT-alteration; their pore throats result on the average nine fold larger. Pore throat sorting indicates for all pore systems a narrow distribution and turns out slightly better for the high permeability plugs. These distinctions result evident for these samples regardless of their porosities.
Figure 3.32 graphically illustrates the distinctions by means of the representative pore throat distributions of the chloritized and illitized samples.

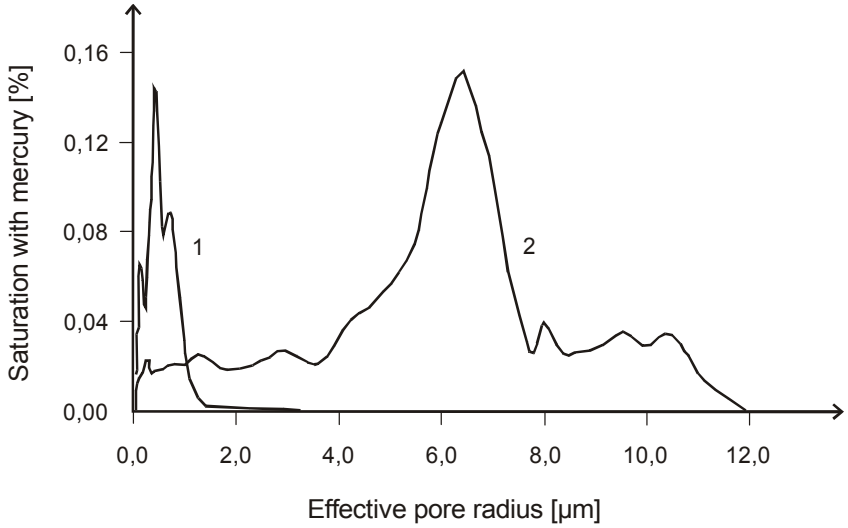

Fig. 3.32: Frequency scales of effective pore radius as function of the saturation with mercury. The graphs derive from sandstones of similar porosity but strongly varying permeability. The properties of the two samples and the determined parameters are listed in the lower table 3.23. The graphs differ distinctly in the range of effective pore radius according to their fluid conductivities.

	Porosity [%]	Permeability [mD]	Alteration	Eff. pore radius [%]	Eff. porosity [%]	PTS [ ]
1	11,13	0,24	IC/IM	0,38	79,2	2,94
2	12,73	104,88	CT	5,32	98,4	2,17

Tab. 3.23: Properties of the two samples for the graphs in figure3.32.

Figure 3.33 demonstrates the clear dependence of permeability on effective pore radius for both groups of reservoir rocks. It should be noted that the calculated pore throats in the illitized pore systems represent the void constrictions left by the framework and the illite overgrowths.

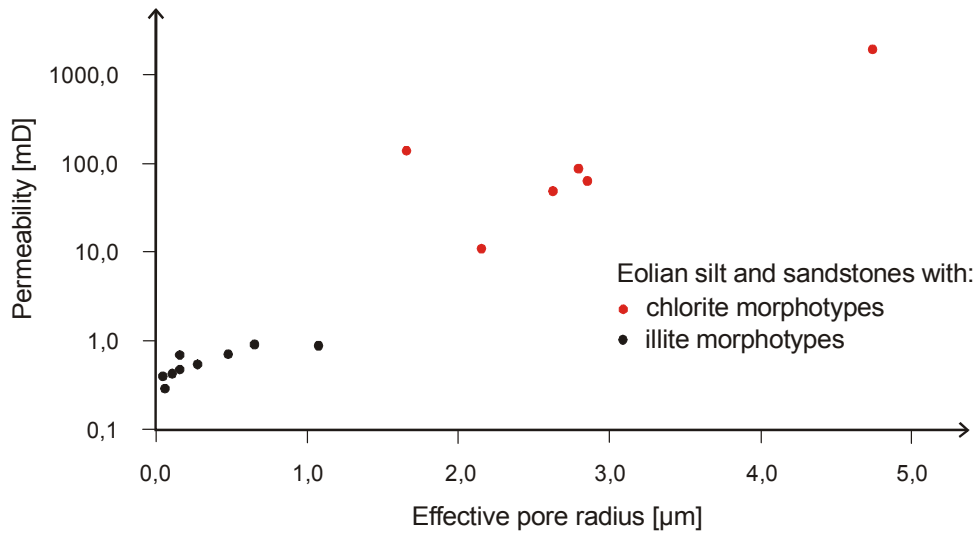

Fig. 3.33: Effective pore radius versus permeability. Clear dependence is visible between these parameters for both sandstone groups. The pore radius for the illitized samples represents the void restrictions formed by the pore wall and the irregular IM-fibres in pore space.

Table 3.24 lists minimum chord lengths from image analysis technique determined on samples A, B and C and the effective pore diameters from Mercury Capillary Porosimetry of sandstones, with equal diagenesis type and comparable porosities and permeabilities. As explicated in chapter 3.3.3.1, the minimum chord length approximates the restrictions in the pore system.

	Eff. pore throats in [µm] from:	
	Image analysis	Merc. Poros.
A	6	4,3
B	12	8,1
C	17	10,6

Tab. 3.24: Effective pore throats from image analysis and Mercury Porosimetry. The samples A, B, C were not analyzed with Mercury Porosimetry.

The values derived by the two techniques are the same order of magnitude and comparable. The minimum chord lengths result for all three plugs slightly higher. This parameter represents namely the minimum magnitude of the average chord lengths in various directions which do not necessarily measure the restriction in the pore system (see chapter x).

Summing up

The results of the Mercury Capillary Pressure Curves evidence that the pore geometries of the two sandstone groups differ distinctly regarding their effective pore throats and the proportions of accessible void volume. The characteristic distinctions in the latter parameters co-determine the differences in permeabilities.
No compressional velocities could be determined on the analyzed samples. However, pore throats and pore throat distributions are not regarded to affect rigidity of porous rocks significantly as differences in these characteristics do not necessarily imply different pore shapes or degrees of interconnectedness.

3.4 Solid components with no influence on rigidity

3.4.1 Introduction

The abundance of interstitial load bearing clay minerals has been evidenced to affect the velocity of comparable sandstones at the plug scale due to its softening effect on the particle composite (e.g. Diaz et al. 2003, Gal et al. 1999). The fact that the grain contact surfaces of illitized sandstones are nearly fully coated with clay minerals could be answerable for the predominantly diverging velocities for samples of different diagenesis type. Furthermore the shape and relative quantities of grain bonds and junctions to cement co-determine the primary speeds of comparable plugs.

As explained in chapters 3.1.2.1 and 3.2.1, constituents of clay-cement-particle structures reside at positions with dissimilar effects on the overall rigidity. Blocky precipitates at particle bonds corroborate the sandstones (e.g. Dvorkin & Brevik 1999, Avseth et al. 2000) as they enlarge the contact area. Cements in contact with only one load bearing component or occurring even isolated do not indurate the compound. Components within the particle contacts contribute fully with their elastic constants to the stiffness of the framework and augment or deteriorate the overall rigidity according to their properties.
These different effects on elastic behaviour according to the textural incidence of particles are outlined schematically in figure 3.34.

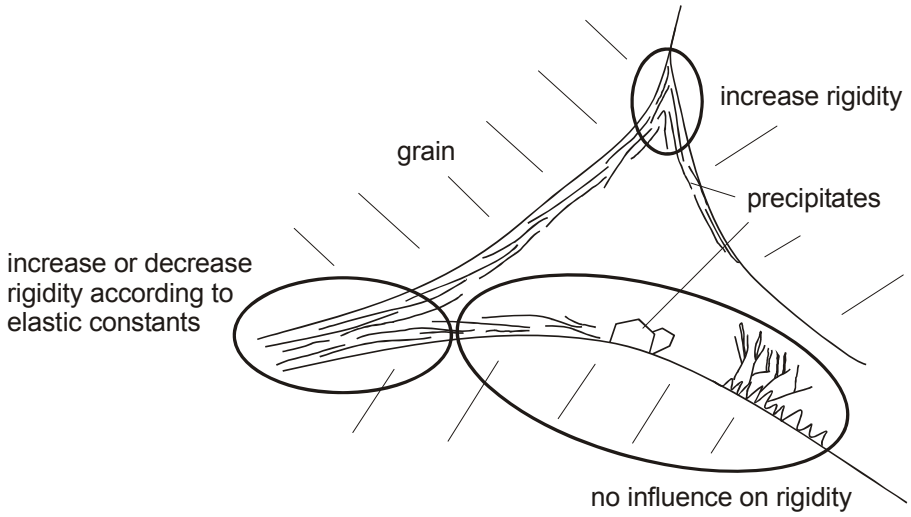

Fig. 3.34: Sketch of a pore with precipitates. Distinct effects on elastic behaviour exist from the textural position of precipitates. Minerals between particle contacts affect the overall elasticity according to their own elastic constants (left circle). At this position reside the load bearing illite coatings in the illitized sandstones (chapter 3.1.2.1). Precipitates at particle bonds enlarge the contact area and enforce the compound (upper circle) (e.g. Dvorkin & Brevik 1999 and chapter 3.2). Ccomponents with contact to only one load bearing constituent reduce porosity but will not affect the stiffness of the compound.

Wyllie et al. (1956) related velocity to the porosity of a rock by adding the specific travel times of the fluid and solid components weighted by their relative amounts. The time average equation, which represents one of the most important deliverables of petrophysics, is based on a simplified model of a water saturated porous medium (fig. 3.35).
The void volume yields from the following equation:
$\tau_{total} = \tau_{solid} * (1-\phi) + \tau_{fluid} * \phi$ with ø as porosity and τ as specific travel time of an elastic wave crossing both phases.

However, this model does not take into consideration the effect on rigidity from particle contact conditions, pore geometrical aspects or from the textural position of the components. For the following considerations the volume of a rock is additionally differentiated into mineral volumes affecting and not affecting the elastic behaviour (fig. 3.35).

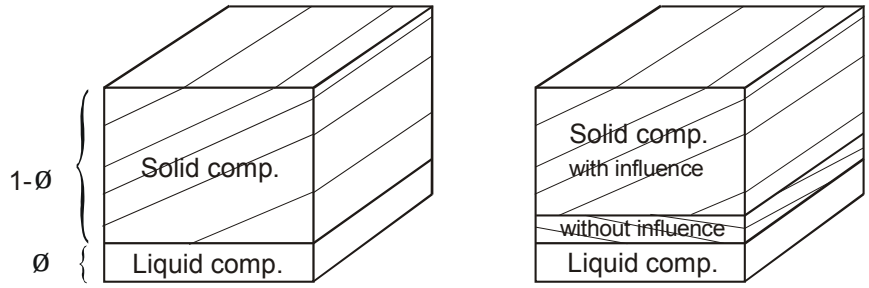

Fig. 3.35: Simplified models of a porous rock saturated with water. The rock volume is 1, ø as porosity quantifies the water volume, 1-ø the volume of the solid components. Left: cube without differentiating the solid components into volumes affecting and not affecting rigidities; right: non-load bearing components are presented as separate volume.

It is obvious that this modification reduces the proportion of the fast part. This has the crucial consequence of a decline in overall velocity. A sandstone containing non-load bearing components will thus demonstrate a lower elastic velocity than a specimen of equal porosity but featuring only weight supporting constituents. These non-load bearing components occupy pores and diminish porosity but keep stiffness and elastic velocities unchanged. The effect of bulk density on travel time is usually smaller than that of rigidity (Schön 1998) and remains unaltered provided the mechanical impulse deforms the entire mass of the solid particles.
Gal et al. (1999) uses similar considerations to explain non-linear relations of velocity on void volumes. They suggested that “pore clays located away from grain contacts” should not affect rigidities and hence velocities. Several datasets were investigated which presented such apparent independencies. A good fit between speed and porosity was revealed when adding to the void fraction the volume of the precipitates.

Chapter 1.2.4.1 describes the shape of the clay morphotypes occurring in the seismic volume. From the whole spectrum of authigenic generations and the importance by their abundance in pore space especially the fibres of the illite meshwork type arise as sandstone component with the minimum contribution to rigidity. Its fibres gather freely into pore space and are much more frequent than other particles which do not influence the stiffness like CR, CS-types or blocky cements in contact with just on weight supporting constituent (based on modal analyses from the DGMK-database and own observations, appendix A-9).

3.4.2 Method

Samples A-E were examined to test for eventual differences in their non-load bearing solid.
The analysis was conducted on printed enlarged composites of microphotographs, which were also utilized for the determination of clay mineral abundances within particle contacts. The procedure for producing the image composite is described in chapter 3.1.2.2.
An area was defined by connecting points of component-to-component contacts at positions affecting rigidity (fig. 3.36). This area confines precipitates and parts of the load bearing framework. The parameter which was determined represents the proportion of the enclosed solid components within that region.

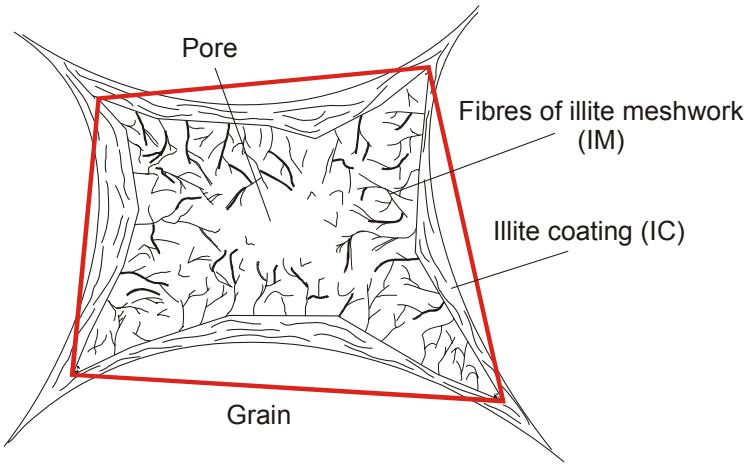

Fig. 3.36: Schematic of a pore, precipitates and surrounding grains. The clay minerals are illite morphotypes. The solid lines connect points at particle contacts important to rigidity of the particle composite. The enclosed area comprises the pores and all solid constituents which do not affect the elastic constants. The parameter determined is the amount of these components within the area.

The quantification was conducted on 100 pores within each sample. Those voids were analyzed which fell on a straight line through the photo composite to avoid subjective filtering. Consequentially the relative proportion of the area within the sample was calculated, utilizing void volumes determined by point counting. This computed volume is referred as V_{p+c} with p standing for pore and c for component. V_{p+c} is related to the whole rock volume and represents the proportion which should not affect stiffness and barely velocity. So for instance, if a sample features an average solid content of 20 % within these areas and 12 % porosity, V_{p+c} results in 14,4 %.
The determinations were carried out by eye after some training on precisely defined proportions. These proportions for training were determined by delineating the surfaces by the aid of CorelPhotoPaint© and utilizing the option 'colour substitution', which delivers amongst other information also area proportions. The analysis allowed only an accuracy and precision of 5 absolute %.
The morphology of the particles for the five samples is comparable based on the observations during the analyses and the particle shape properties presented in table 2.3. and in appendix A-3. Their shape should hence not influence the outcome.
The images project all minerals independently from their depth in the thin section. Therefore the determined volumes represent maximum values.

3.4.3 Results and discussion

Table 3.25 lists the proportion of non-load bearing components in relation to the confined area around the pore and to the whole rock volume. The magnitudes are given in percentages. The standard deviations for the volume of non-load bearing components within the area vary within 13 and 19 %. The complete database is presented in the appendix (A-15).
The illitized sandstones contain the largest volume of minerals without rigidity enforcing effects. This result is predominantly due to the presence of illite meshwork (IM). The variances for the chlorite sandstones A, B, C are attributed to different abundances of blocky cements with contact to only one weight supporting component.
Furthermore, the compressional plug velocities decline with augmenting non-load bearing minerals and with the parameter V_{p+c}. This finding is consistent with the above quoted deliberations.

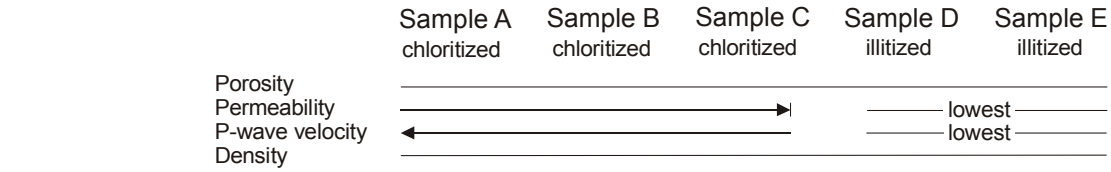

	Sample A	Sample B	Sample C	Sample D	Sample E
Comp. without infl. [%]	7	7	12	22	28
Vp+c [%]	11,5	12,5	13,0	14,5	14,0
Porosity [%]	10,5	11,6	11,5	11,3	10,1

Tab. 3.25: Amounts of non-load bearing components related to the area and to the whole rock volume. Porosities derive from cores. V_{p+c} is highest for the illitized samples due to the large amounts of IM-fibres in pore space. The variability for the chloritized samples is attributable to the different abundances of blocky cements not contributing to rigidity. The illitized samples with largest V_{p+c} feature the lowest velocities.

The analyses yield also a relevant distinction between porosity and V_{p+c}. So, for instance, the illitized sample D exhibits 11,3 % and 14,5 % respectively. This difference conforms to Deutrich's investigations on illitized Rotliegend sandstones (Deutrich 1993), who calculated paleo porosities and found remarkable increases when adding the space of the illite meshwork (IM) to total porosity. Furthermore, it emerges from the DGMK-petrographic database (appendix A-9) that, just as in the above analyzed samples, the quantity of illite meshwork, and the sum of illite meshwork and illite coating in the illitized samples are far more abundant than the sum of the chlorite morphotypes in chloritized samples.

Fig. 3.37 presents the velocities of the samples versus their core porosities and V_{p+c}.
It is palpably perceptible that the changes in longitudinal speeds are not attributable to the nearly constant porosities but they correlate well to V_{p+c}.

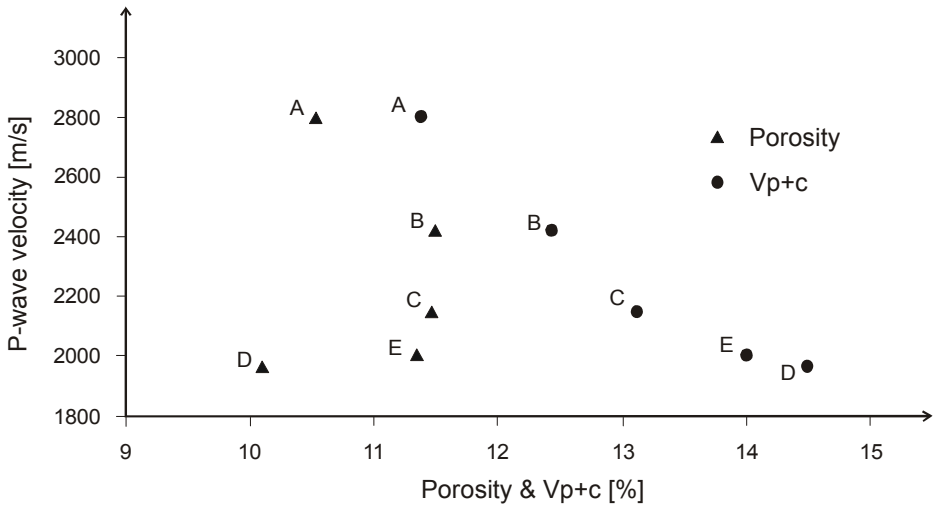

Fig. 3.37: Longitudinal plug velocities of the five samples against their core porosities and V_{p+c}. Velocity and porosity barely correlate; however, when plotting the volume of pores plus components not contributing to rigidity a correlation to velocity becomes apparent.

The findings here presented corroborate that the rigidity and velocity of a rock depend on the void volume of the weight supporting fabric and not on its porosity alone.

The comparatively larger abundances of minerals not contributing to the stiffness could thus represent an additional reason for the lower velocities encountered in the sandstones of illite alteration.

3.5 Compressional micro impedances of illite (IC) and chlorite coatings (CT) – Scanning Acoustic Microscopy (SAM)

3.5.1 Introduction

Some studies (Dvorkin & Nur 1996, Prasad et al. 1999, Avseth et al. 2000) evidence the rigorous increasing effect of cement on the rigidity and velocity of sediments, if the cement is located *at* the particle bonds. Further Yin & Dvorkin (1994), Dvorkin et al. (1994) document that the amount of this contact cement influences elastic constants to a much higher degree than its stiffness does. However, if the cement is located *within* the particle junctions, its elastic properties should fully affect the total stiffness and velocity of the framework.
As outlined in chapter 3.1.1 illitized and chloritized samples are characterized by different types and abundances of load bearing clays. The low plug velocities of illitized sandstones appear to be attributable to the large abundances of illite coatings within the particle bonds.
It is possible that potentially dissimilar elastic properties of illite and chlorite coatings co-determined the distinct speeds of both groups of reservoir rocks too. Therefore the impedances of these morphotypes are determined in order to inspect for any characteristic elastic influences.
Although the knowledge on the elastic behaviour of clay minerals is essential for the interpretation of elastic responses from clay bearing rocks, the studies regarding their effects remain sparse. So far, the bulk of the studies derived elastic constants of clays on a theoretical and empirical basis and showed little agreement (in Vanorio et al. 2003): The magnitudes for compression module ranges from 20 to 50 GPa (Alexandrov & Ryzhova 1961, Wang et al. 2001, Castagna et al. 1995). However, Berge & Berrryman (1995) have shown that he compression module of clay should be below 10-12 GPa (in Vanorio et al. 2003). Prasad et al. (2002) utilized Atomic Force Acoustic microscopy (AFAM) to accomplish first-ever quantitative measurements of Young's modulus on clay minerals. Vanorio et al. (2003) conducted p-and s-wave velocity measurements on clay mineral powders as functions of pressure and saturation and supported the AFAM-results. The determination of elastic behaviour of clay minerals remains a challenge as the complicacies consist in: the sheet like structure leads to strong anisotropic effects (Katahara 1996); their small grain sizes render it tricky to isolate individual crystals for acoustic measurements (Vanorio et al. 2003); their Ion Exchange Capacity when using polar molecules affects their structure (Theng 1974); their low permeabilities yields saturation difficult (Vanorio et al. 2003); their fluid saturations are only vaguely determinable.

3.5.2 Method

The following approach tries to ascertain impedances of the clay morphotypes at the micro scale by means of the Scanning Acoustic Microscopy (SAM).
The subsequent outlines on the working principles are based on discussions from Arnaud Caron at the Fraunhofer Institute in Saarbrücken, and reports from Prasad (2001), Grill et al. (1996), Zinin et al. (1997), Hillmann et al. (1994), Würz et al. (1995) and Lemmons & Quate (1974).
Scanning Acoustic Microscopy (SAM) represents a new technique to quantify and qualify microstructure as variations in acoustic impedance. Textural features of the surface and subsurface of the specimen are studied with the help of highly resolving ultrasonic waves analogue to the reflection seismology principle.

Scanning Acoustic Microscopy has been evolved for material science purposes to reveal non-destructively internal discontinuities like voids, cracks or laminations in material grades as molding compounds, electronic components or cement.
A block diagram of the SAM sketches the main parts of the setup (fig. 3.38). The Acoustic and Scanning Unit comprises the transducer, which emits and receives ultrasonic waves, the sapphire rod acting as a focusing lens and a sample stage movable in three dimensions. The Pulse Generator and Receiver Unit excite the electron pulses for the transducer and amplify the reflected signals. The Stage Control Unit accomplishes stage motion. The Image Handling Module converts the electrical pulses into a grey scale image according to the determined impedance contrasts in the specimen.

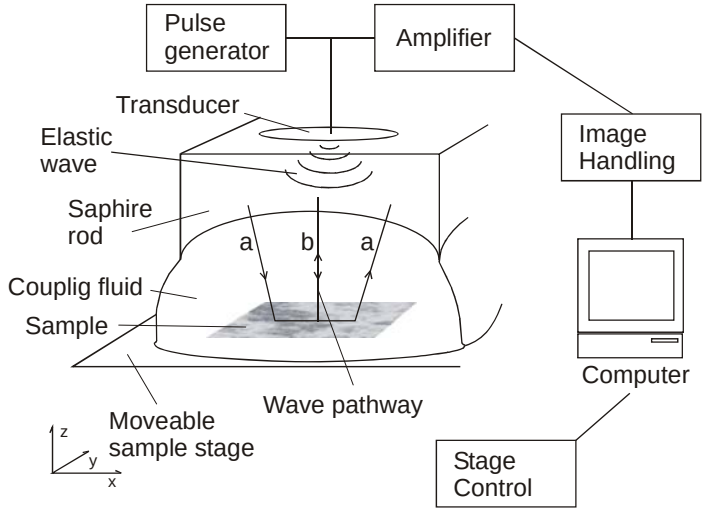

Fig. 3.38: Main units of SAM setup. Ultrasonic wave is emitted and registered in the Pulse generator, transducer and amplifier. The phases of waves of two pathways (a, b) are measured. The moveable sample stage enables three modes of scans. The image handling module generates image in grey scales according to impedance contrasts.

Three types of scans are accomplishable: An x-t scan depicts amplitude variation in time at a fixed stage position. It corresponds in reflection seismology to a seismic trace. An x-z recording is composed of several x-t scans as the lens moves along a line. The analogue in reflection seismology represents a seismic section. The x-y sampling measures x-t scans within a confined area. Its counterparts in reflection seismology are 3D seismic survey and side scan sonar.
The incident longitudinal waves generate Rayleigh waves, which travel along the surface of the sample and dissipate energy in form of longitudinal rays. The reradiated p-waves from path a and b (fig. 3.38) are detected and interfered. Additionally the distance z is reduced continuously which changes the phase of the rays at different rates. Due to the induced constructive and destructive interference a series of oscillations, A(z), is generated, which is a function of distance and represents a material characteristic.

The wavelength of the oscillation is calculated as follows (Briggs 1992):

$\Delta z = \frac{\lambda o}{2(1-\cos \theta r)}$ with λo as wave length in the coupling medium (water) and θr as Rayleigh angle.

V(z) of the Rayleigh wave (V(r)) is derived from

$Vr = Vo(1-(1-\frac{Vo}{2\,f\Delta z})^2)^{-0,5}$ with Vo as wave velocity in the coupling fluid and f as frequency of the oscillation.
The required variables f and λo are determined from Fourier analyses on the interference curve (Briggs 1992). Hirsekorn & Pangraz (1994) report additional methods to derive Vr.
Changes in Vr originate in alterations of density and elastic constants. Scanning Acoustic Microscopy hence detects impedance contrasts in the sample. As an example figure 3.39 depicts the relative micro impedances as grey scales for a quartz grain (left particle in figure 3.39) and interstitial cement overgrowth. The quartz particle exhibits intragranular zones of different micro impedance (Prasad 2001) probably generated during their forming or by burial stress. The intergranular cement shows relatively moderate impedance.
The grey scale output of SAM can additionally be calibrated with materials of known impedance to infer quantitatively micro impedances of the investigated particles.

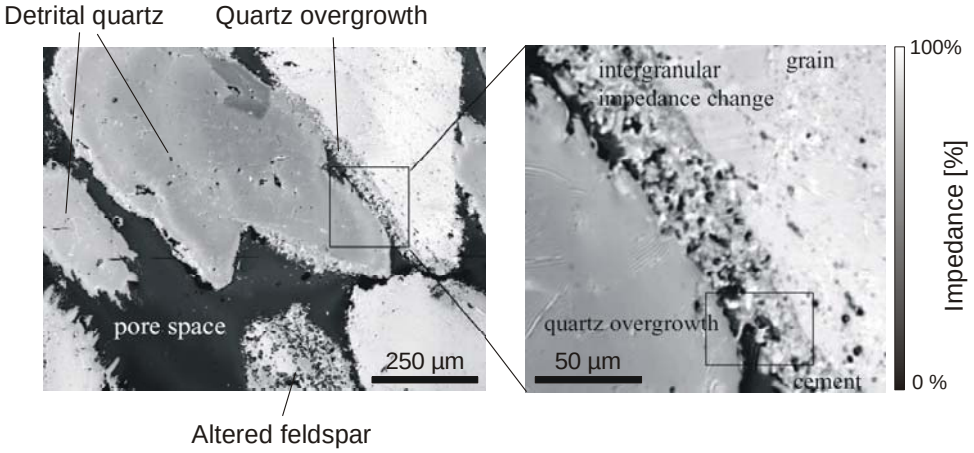

Fig 3.39: High resolution SAM x-y-image generated with 1 GHz frequency. Impedance is grey colour coded with white denoting high, dark grey low impedance. Impedance is given in % of grey levels. Black areas present pores. The rectangle in the right image presents pore bridging cements. The altered feldspar exhibits intragranular impedance change. The right image presents intergranular impedance contrasts of detrital quartz and cements. Modified after Prasad (2001).

Data of the Scanning Acoustic Microscopy can result erroneous due to difficulties especially encountered when:
- Selecting the transducer frequency that still provides a low signal-to-noise ratio for good imaging;
- Positioning the sample holder and transducer in a manner that the transducer is not normal to the plane of the sample and the scan path is not parallel to the plane of the stage;
- The surface of the sample is not plane parallel to the sample holder or features morphological irregularities.

3.5.3 Samples

For the purpose of comparative studies the investigated clay minerals need to be contained in a single specimen. The amplifying rates of the detected signal are instable when samples are changed due to the high temperature sensitivity of the amplifier (pers. comm., A. Caron, 2006, IzfP-Saarbrücken). Unfortunately, the mutual occurrence of illite and chlorite coatings in a single plug is rare for the investigated reservoir and such a sample was not available.
Therefore replacements for these clay minerals were utilized:

Deutrich (1993) investigated the chemical composition of chlorite and illite morphotypes in the Rotliegend sandstones. He denoted the occurring chlorites according to the classification of Tröger (1969) as Bavalite, Aphrosiderite, Fe-Rhipidolite and Pyknochlorite. Unfortunately the chlorite coatings were not included in his investigations. However, Gaupp & Solms (2005) report for this morphotype similar high MgO and FeO-contents as for the classified C-type in Deutrich (1993), which indicates a comparable mineralogy. For the SAM-measurements Fe-Rhipidolite was selected because it contains high Fe-contents and its mineral formula represents a mean chemical composition for the occurring chlorite minerals.
The illite morphotypes exhibit according to Deutrich (1993) variable compositions within the chemical compounds of muscovite and phengite. However, the illite substitute deviates from this mineralogy as it contains more Mg and Fe (Hower & Mowatt 1966) (fig. 3.40). A more appropriate replacement could not be selected due to time restrictions. Nevertheless its dioctahedral structure and the absence of mixed layer phases with smectite are consistent with the properties of the corresponding illites presented in Deutrich (1993). Further its 1Md polymorph type matches to the structure of the illite morphotypes (Deutrich 1993, Hower & Mowatt 1966).

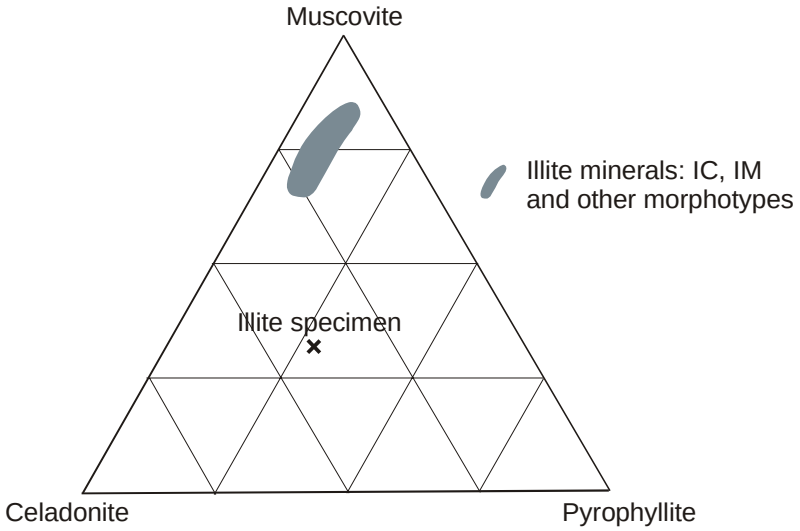

Fig. 3.40: Ternary diagram illustrating the composition of illite minerals in the Rotliegend sandstones of North Germany. The utilized illite specimen for SAM features a different composition as a more suited specimen could not be selected due to time restrictions. Based on Deutrich (1993), Hower & Mowatt (1966).

Both clay samples derive from argillaceous unweathered pure sediments of the equivalent mineral. They represent reference clays, acquired from the Clay Minerals Society Source Clay Repository of the University of Missouri. More information on the specimens is available in Hower & Mowatt (1966) and Post & Plummer (1972).
Several fragments of the untreated clay samples of cm-size were embedded in an epoxy plug so to render measurements accomplishable parallel and across their foliation. A quartz rich Rotliegend sandstone was included for eventual comparative studies based on the average impedance of several SAM-measurements on quartz components. The surface of the sample composite was polished to maintain a plain cross section. A picture of the sample composite is shown in figure 3.41. The investigated area of a single measurement constitutes to 550 µm × 512 µm.
Scanning Acoustic Microscopy was performed by A. Caron at the ‘Fraunhofer Institute für Zerstörungsfreie Prüfverfahren’ in Saarbrücken.

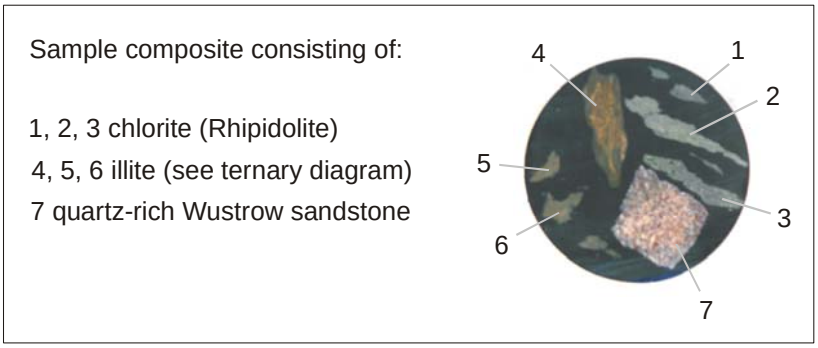

Fig. 3.41: Sample composite featuring fragments of illite and chlorite minerals and a quartz-rich Wustrow sandstone for comparative analyses.

Blocky precipitates are not included in the investigations. The modules of minerals like quartz or anhydrite are already good investigated and similar (e.g. Gebrande et al. 1982). Furthermore, the textural stiffness of clay minerals is drastically lower in comparison to other framework constituents (see chapter 3.1.2.1) and should hence affect the overall elastic behaviour more effectively.

3.5.4 Results and discussion

The measurements delivered not reliable magnitudes of impedances as observable in the high standard deviations (tab. 3.26).
Probably the instable amplification rate or the irregularities in the specimen surfaces generated the high scatter in the outcome. After a more intense polishment the specimen composite was analyzed again. Unfortunately, the electrode exciting the piezoelectric transducer on top of the sapphire rod lost electrical conductivity. As the reparation is not feasible in the foreseeable future a new run of analyzes can not be conducted by the end of this study.

However, the preliminary results are presented. The impedances in table 3.26 are not true magnitudes as the outcome was not calibrated with materials of known impedance. The three impedances of the chlorite fragments vary more strongly than those of the illite fragments maybe due to the orientation of foliation or the quoted reasons. The quartz components in the sandstone were not analyzed.

	Impedance [Rayl]			Impedance [Rayl]	
Sample (chlorite)		St. dev.	Sample (illite)		St. dev.
1	5691	5517	4	5518	5297
2	5259	5106	5	5667	5101
3	6616	6822	6	**5806**	5411
Average	**5855**	5815	**Average**	**5664**	5269
St. dev.	693	896	St. dev.	143	156

Tab. 3.26: Impedances of SAM-measurements. The impedances are not calibrated and represent thus not true magnitudes. True impedances would be approximately 1000 -2000 fold higher (compare Schön 1998). The average impedances of the illite and chlorite samples are similar. However, the standard deviations are too high for an accurate interpretation.

Figure 3.42 presents x-y scans for two chlorite and illite fragments. The variation in impedance is higher for the chlorite sample. According to A. Caron (pers. comm., 2006, IzfP Saarbrücken) the surface contrast turns out too high for an accurate interpretation.

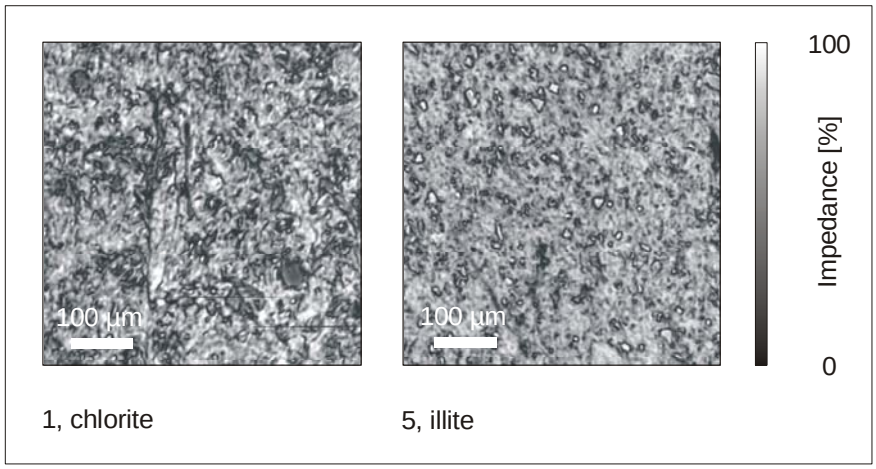

Fig. 3.42: Impedance in % of grey levels for chlorite and illite fragments 1 and 2. The x-y scan was taken with 1 GHz frequency. Both images present too high contrasts in grey levels.

3.6 Effects of total petrographic clay content on compressional velocity

Several studies report a systematic decrease of longitudinal velocity with increasing total clay content for both well and poorly consolidated sandstones (e.g. Tosaya & Nur 1982, Kowallis et al. 1984, Klimentos 1991, Best & McCann 1995, Diaz et al. 2003). This tendency has been attributed to the softening effect on the rock matrix (Tutuncu et al. 1994) especially by structural and laminal clays (Minear 1982, Han et al. 1986). For more information please refer to the above quoted literature and chapter 3.1.2.

The plug velocities of eolian dry samples were examined for a potential dependence on total petrographic clay content (fig. 3.43).
The data points exhibit no sensitivity to compressional speeds with increasing volume of detrital mica, illite and clay aggregates, and authigenic illite and chlorite. The petrographic data derive from the DGMK-database and own analyses (appendix A-9).
However, the plot includes four measurements for samples deriving from the damp sandsheet facies (see appendix A-13) which indicate a slight negative relation. Unfortunately, no more specimens from the damp dominated environment were attained from petroleum companies to inspect this apparent relation.
According to Han et al. (1986), Klimentos & McCann (1990) and Best & McCann (1995) extensional velocity declines already with a small proportion of clay minerals, for instance by 2-4 % total clay content (Han et al. 1986). The clay volumes of the Wustrow sandstones suffice thus to impact on the elastic constants.

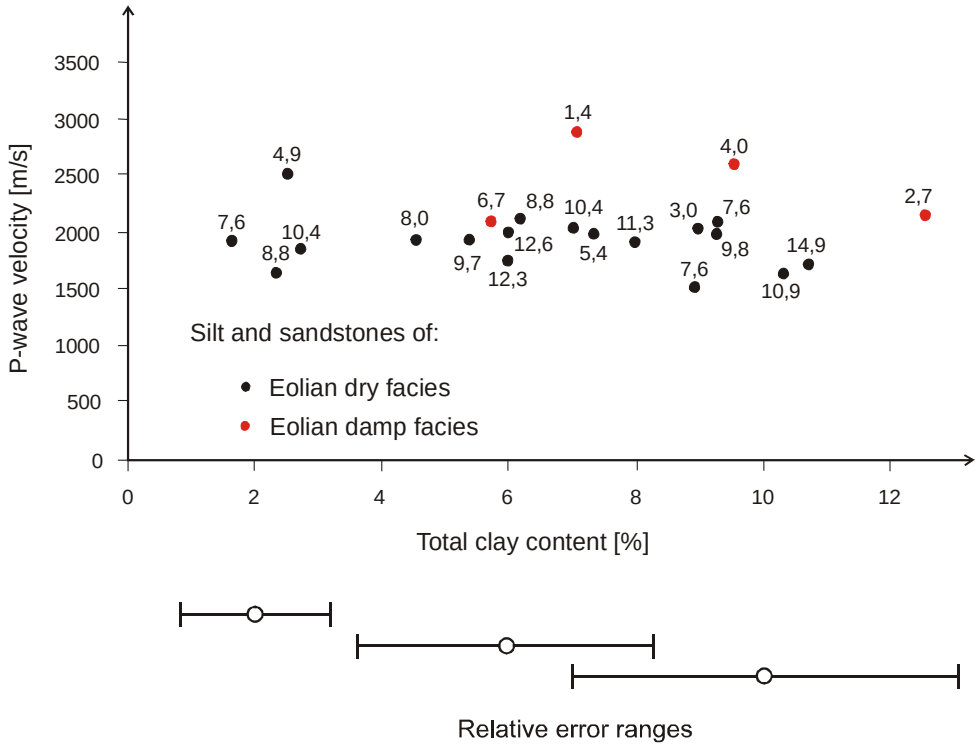

Fig. 3.43: Longitudinal plug velocity versus petrographic total clay content established by point counting. The data points are differentiated into damp and eolian dry sandstones. Porosities are added next to data points. The relative error ranges are added according to estimators of uncertainty by Van der Plas & Tobi (1965) and Howarth (1998). No dependence is visible of velocity on total clay content for eolian dry plugs. A slight indication of a negative correlation exists for eolian damp samples.

Generally the statistical uncertainty for low percentages of point-counting records is substantially large. The relative errors for the presented data vary within 65 and 23 relative % according to the modified chart of Van der Plas & Tobi (1965) (Howarth 1998). The range of inaccuracy is added in the velocity-plot for 2, 6 and 10 % mineral volumes determined for 300 counts.

The apparent impartiality of compressional plug velocities on petrographic total clay content for eolian dry sandstones could be attributable to several reasons:
- The total clay content does not differentiate between minerals affecting and not affecting elastic constants;
- Eventual differences in the particle contacts of the investigated samples could provoke likewise velocity contrasts;
- The variability in velocity shows a faint dependence on porosity.

These findings corroborate the need for discriminating micro-textural features into properties influencing and not influencing wave propagation characteristics.

3.7 Seismic signal modifications by anelastic processes

3.7.1 Introduction

All of the explications quoted before refer to the elastic deformation of particle composites. However, a fraction of the wave energy is converted into irreversible particle movement and frictional heat. These anelastic processes attenuate the wave amplitudes and modify the phase of the propagating waves (Schön 1998).

The Neural Network technique (Trappe et al. 2005) utilized attributes which characterize the configuration of seismic wavelets. Distinct features in the seismic wave traces could hence also be attributed to energy absorption besides to velocity changes. This chapter describes factors affecting energy dissipation and evaluates consequently whether and to which extent these parameters modified the investigated wavelets of the seismic volume.

The decline of an amplitude from a plane-wave single frequency sinus pulse is given by:
$A(x) = Ao * e\hat{}(-\alpha * x)$, where Ao refers to the original amplitude at x=0, x is the distance between source and measuring point and ά is the attenuation coefficient given in [Nepers/m] (Schön 1998, Klimentos & McCann 1990).
The coefficient ά increases with augmenting signal dampening and varies within 10^{-4} till 10^{-1} Nepers/m for consolidated sedimentary rocks (Schön 1998).
Alternative coefficients quantifying attenuation properties are the dimensionless quality factor Q and its inverse, the specific dissipation factor Q^{-1}(Knopoff 1964, 1965). Johnston & Toksöz (1981) defined Q as the ratio of the actual energy of the wave and the rate of energy loss:
$Q = \frac{\omega * E}{-dE/dt}$ with ώ as angular frequency, E as energy, t as time after excitation.
Q^{-1} results hence as a measure for the ratio of dissipated to stored energy and is defined through ά as
$Q^{-1} = \frac{\alpha * c}{\pi * f}$ with c as phase velocity and f as frequency (O'Connell & Budiansky 1977).
The quality factor Q ranges roughly within 5 and 100 for consolidated sedimentary rocks at various frequencies and saturation ranges (after Bradley & Fort 1966).

3.7.2 Effects of parameters

The various effects of parameters on the longitudinal attenuation of porous sediments are outlined in the following:

Differential pressure: Attenuation decreases with increasing differential pressure most presumably due to the closing of microcracks, fractures and other defects, till approx. 40 MPa (approx. 1500 m burial depth) (Toksöz et al. 1979, Klimentos & McCann 1990). The pressure dependence exceeding this benchmark is far less pronounced due to the lower rate of porosity decline (Schön 1998).
Strain amplitude: Attenuation increases rapidly with strains exceeding 10^{-6} (Winkler & Nur 1978) mostly due to frictional sliding at grain contacts (Winkler & Nur 1982) and is independent for lower strains typical for seismic surveys (Gordon & Davies 1968) and borehole sonic logs (Murphy 1982).
Frequency: Energy loss for dry rocks results nearly independent from frequency (e.g. Wyllie at al. 1962, Pandit & Savage 1973). For partially and fully saturated rocks viscous effects of the pore fluids cause dampening to be related on frequency (e.g. Winkler & Nur 1982,

Murphy 1982) (fig. 3.44). However, energy dissipation for low frequencies varies barely and such contrasts are negligible in the seismic frequency band (10-200 Hz, Wang 2001) at constant water saturations (based on data of Murphy 1982, Pham et al. 2002).

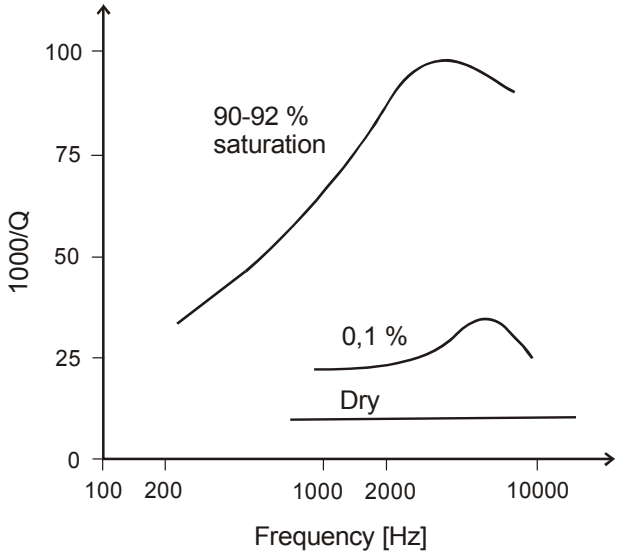

Fig. 3.44: Attenuation 1000/Q versus frequency for sandstone plugs with varying water saturation at ambient conditions. Energy loss varies distinctly according to saturation and frequency. After Murphy 1982.

Temperature: Temperature affects especially the attenuation properties of pore fluids due to viscous effects and phase changes (Batzle & Wang 1992, Burkhardt et al. 1990) and leaves solid rock constituents unchanged except for thermal cracking of minerals at high temperatures (Gordon & Davis 1968).
Fluid saturation: Attenuation for fluid saturated rocks shows a complex dependence on the saturation range, saturation conditions, fluid type and frequency (Johnston et al. 1979). The compressional attenuation is minimum in dry rock and greater in partially water containing sandstones, reaches its maximum around 80 % according to frequency and is substantially reduced at total water saturation (fig. 3.48) (based on Winkler and Nur 1979, Murphy 1982, Best and McCann 1995). This behaviour is due to complex and only partly proven fluid mechanisms caused by: viscous interaction between the *overall* motion of the pore fluid and the solid rock framework (Biot 1956 a & b, McCann & McCann 1985) and the *local* motion of fluid into and out of pores during the passage of the compressional wave (e.g. O`Connell & Budiansky 1977, Murphy et al. 1984, O'Connell 1984, Best et al. 1994) (fig. 3.45); different pore geometrical aspects, especially concerning aspect ratio (Mavko & Nur 1979); distinct absorption of energy by the alteration of phases (Spetzler & Anderson 1968); effects of fluid distribution (Mavko & Nur 1979); different gas distributions in the pore system (White 1975, Johnston et al. 1979).

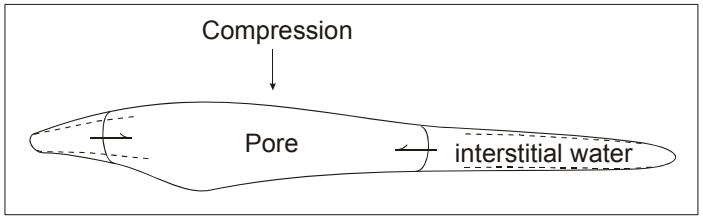

Fig. 3.45: Sketch of a pore with water located within the gussets, contour of deformation in dotted lines. During the passage of the compressional waves the compliant pore walls are compacted which

reduces pore volume and squeezes water into open pore sectors. After decompression the pore returns into its original shape. The returning interstitial water does not provoke any mechanic impulse on the framework. This local flow induces wave energy dissipation. Based on Winkler & Nur (1982), O'Connell & Budiansky (1977).

Pore fluid distribution: For samples of constant saturation, the distinctions regarding the distribution of pore fluids appear to shift the maxima of extensional attenuation but not to influence the general attenuation behaviour (Yin et al. 1992).
Particle contact conditions: Larger contact areas between particles should decrease signal dampening. This is indicated by the pressure dependence of attenuation for sandstones at low differential stress due to closure of micro-voids and thus enhanced energy transfer (Lockner et al. 1977, Johnston et al. 1979). Klimentos & McCann (1990) regard a directional dependence of attenuation according to the orientations of the bedding planes as possible but could not verify it.
Porosity: Bradley & Fort (1966) note an inversely proportional trend of quality factor and void volumes for sandstones and limestones. This is due to the weakening of the solid matrix by the presence of pores (Johnston et al. 1979).
Clay content: Klimentos & McCann (1990) show that clay content exerts a dominating effect on compressional attenuation with an effect on attenuation a magnitude greater than that from porosity. Their studies demonstrate a linear correlation of intra pore clays (kaolinite, illite-smectite, chlorite) to energy dissipation for water saturated sandstones at high pressures when microcracks are closed. Similar relations report Tutuncu et al. (1994) for tight gas sandstones, and Best et al. (1994) and Marks et al. (1992). The petrophysical basis for this dependence consists in absorption and dispersion mechanisms deriving from viscous and inertial interaction between pore fluid and the high specific internal surface of the clay particles (Klimentos 1991, Best et al. 1994). Figure 3.46 presents the attenuation coefficients of sandstones for varying clay content at 40 MPa confining pressure and 1 MHz frequency from the study of Klimentos & McCann (1990).

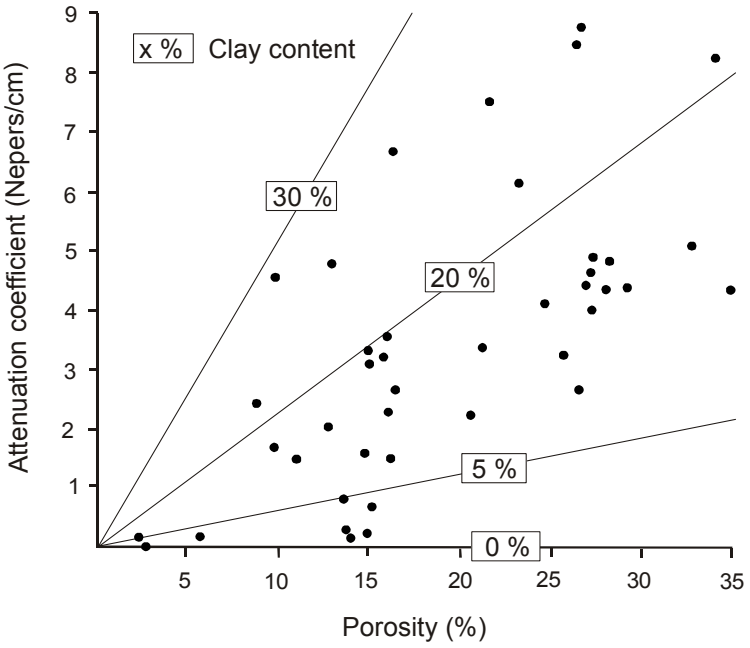

Fig. 3.46 : Attenuation coefficient ά versus porosity and clay content for sandstone samples. Solid lines separate probes with a certain clay content. With augmenting clay content energy dissipation increases. After Klimentos & McCann 1990.

Pore orientation: Akbar et al. (1993) demonstrated that attenuation is strongly affected by the orientation of the long pore axis. The extensional dissipation factor results elevated for wave propagation perpendicular to the long axes of the elliptic pores compared to the attenuation for vibrations migrating parallel to the axis (fig. 3.47).

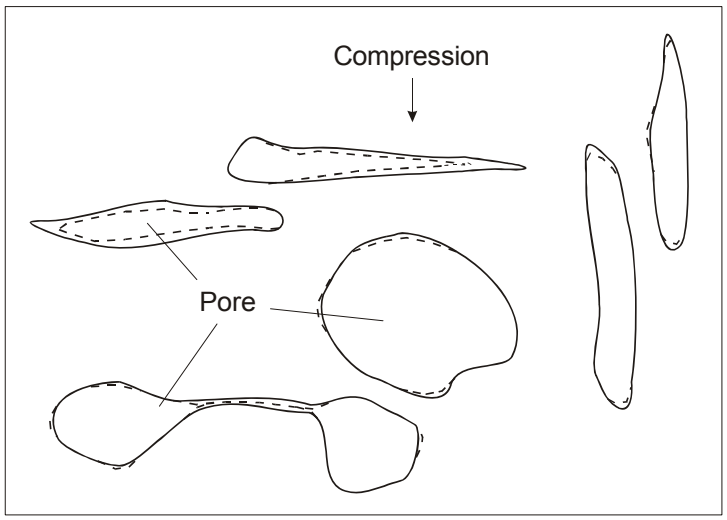

Fig. 3.47: Effects of pore geometry on compressional attenuation. The contour of deformation of pores with varying shape and mean axis orientation is shown in dotted lines. Voids of large aspect ratio exhibit higher resistance to compaction than thin apertures. Pores with main orientation perpendicular to deformation are more affected by compression than voids parallel to compaction. The partial closure of compliant pores augments particle contact area and enhances energy transfer which reduces energy loss (based on Akbar et al. 1993, Guèguen & Boutèca 2004, Anselmetti & Eberli 1997).

For extended overviews on the attenuation of elastic waves, which represents the most sophisticated topic in petrophysics (Schön 1998), please refer to Johnston et al. (1979), Schön (1998) and Pride et al. (2003).

3.7.3 Relevance for seismic volume

The above quoted lithological and seismic acquisition parameters could affect the shape of the seismic wavelets. The following paragraphs discuss whether and to which extent those factors co-determined the wave traces of the seismic volume:

In order to derive quantitatively the effects of water saturation at reservoir conditions, representative data are needed. However empirical attenuation-saturation graphs for the seismic bands are sparse at elevated pressure and temperature conditions (Pham et al. 2002). The reasons therefore are the limitations of spatial resolution imposed by seismic bandwidths (Best & Sams 1997). Murphy (1982) established graphs of dissipation factor as a function of frequency and water content. The measurements were conducted on clay-free, quartz-rich, high porosity sandstones with strain amplitudes less than 10^{-7} at ambient conditions. Its experimental setup does not necessarily correspond to the reservoir situation during seismic acquisition. The water content in Murphy's analyses was namely varied by draining. The fluid distribution in the experiment does hence not assuredly comply with the distribution in the reservoirs pore space. Additional inconsistencies could arise from eventual lithological differences in regard to clay content, particle contacts or microcracks and thermodynamic conditions.

Despite of these deficiencies his dependencies are utilized to draw at least approximate conclusions on the behaviour of attenuation in the seismic volume.
Figure 3.48 depicts the attenuation dependence on water saturation for seismic frequencies, extrapolated from the contour plot (Murphy 1982) for 80 Hz. The behaviour of attenuation agrees qualitatively with the theoretical investigations of Mavko and Nur (1979), Yin et al. (1992) and Pham et al. (2002).
According to the staff of the department for reservoir geology in RWE-Dea (pers. comm., 2005), the water content varies within 25 and 75 % for the Wustrow sandstones. Within that range the dissipation factor demonstrates a comparatively moderate decline (fig. 3.48). Unfortunately the available log data comprise no resistivity curves and no formation water conductance to derive water saturations within the seismic volume more accurately. Such calculations would have been executed with the dual water model for clay bearing formations (Schlumberger 1991).

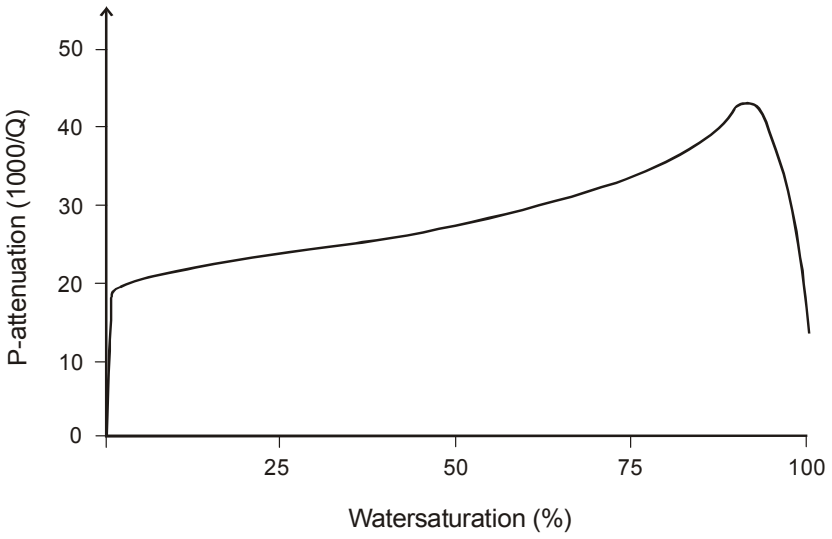

Fig. 3.48: Attenuation 1000/Q versus water saturation for sandstone plugs, frequency 80 Hz, measured at ambient conditions. Energy loss 1000/Q varies largely within 0 and 48 with a maximum at 90% water saturation. Note the dominantly linear and moderate increase within the saturation range of 3 and 75 % (after Murphy 1982).

Calculation of amplitude attenuation due to differences in water saturation

The change of seismic amplitudes is quantified for this saturation range. Eventual variations are maximized by assuming high gas content for the blue and green, and low gas content for the yellow and red classes. Such a reservoir filling is conceivable as gas reduces overall rock speeds (Serra 1984) and the low sonic velocities are encountered in the blue and green classes. Other petrophysical influences like micro textural differences are neglected. In order to attain a representative speed difference for the different Wustrow provinces, the sonic log speeds were applied due to the lack of seismic speed data. According to Schön (1998), De et al. (1994) and Pham et al. (2002) the deviation of the extensional travel times for wireline tools, which operate at sonic frequencies (1000-10000 Hz, Winkler 1986), is minor and negligible compared to travel times of the seismic band (10-200 Hz, Winkler 1986). The replacement of the seismic velocities is hence of no relevance for the outcome.
The amplitudes for the classes are attained by:

$$\alpha = \frac{\pi * f}{Q * v} \text{ and } A(x) = Ao * e\hat{}(-\alpha * x)$$

For wells within the classes 1-3: f as 80 Hz, Q as 43,5 from 1000/Q as 23 (dimensionless) (fig. 3.48), and v as 4550 m/s as the corresponding mean sonic velocity.
For wells within the classes 4-7 the parameters were chosen as follows: Q as 29,4 from 1000/ Q as 34 and v as 4760 m/s as the corresponding mean sonic velocity.
The amplitudes result as $A(x) = Ao * 0{,}9987$ for the blue and green facies and $A(x) = Ao * 0{,}9982$ for the red and yellow classes. The variation in the height of seismic deflections amounts thus to only 0,05 %. Even by applying the maximum and minimum attenuation factors (fig. 3.48) the divergence constitutes to 2,75 %. By considering additionally a minimum frequency of 10 Hz the difference amounts to solely 2,78 %.

Frequency and strain amplitude appear not to be relevant for the seismic facies classification as their effects at seismic survey conditions result either negligible or inexistent.

Temperature variations could potentially arise by the inconsistent thickness of saline layers within the Rotliegend (Plein 1995, Trusheim 1971) or the large-scale Zechstein salt anticline (Tanner at al. 2005) as salt strata enhance heat flow due to their high thermal conductivity (O'Brien & Lerche 1988).

Differences in reservoir pressure could for instance originate from varying paleo permeabilities during burial, which could have impeded fluid migration for pressure relief, or variations in pore fluid content (Hyne 1991). Unfortunately no information was attainable from petroleum companies and contractors regarding eventual distinctions in thermodynamical conditions. As previously mentioned the pressure dependency is a strong function of the closure of micro-voids (Toksöz et al. 1979). However, it is plausible that the high confining pressure at depths of 4300-4500 m closed most of the compliant thin discontinuities. Several pressure-attenuation studies document namely that the decline in attenuation levels off at 7000 psi (Toksöz et al. 1979), at 250 bar (Winkler & Nur 1982) and at 300 bar (Pham et al. 2002) for water saturated sandstones which corresponds to approx. 2000 m, 1000 m and 1200 m of geostatic load.
A further source for differences in pressure represents the degree of mechanical compaction in tectonic settings like fault zones (Byerlee 1990). Differences in tectonic stress could influence the development of porosity loss and pore pressure excess with burial (Guéguen & Boutéca 2004). Tanner et al. (2005) generated maps of tectonic deformation, which confine the areas of mechanical rock volume change along lineaments for the seismic volume. However, concentrations of tectonical compression appear to be existent rather regularly throughout the seismic volume. A more thorough investigation about the pressure effect on seismic attenuation is not feasible with the available sample- and data base.

It is plausible that no unique mean orientation of pores is existent for the regions of different seismic classes. The occurring depositional facies like eolian and lacustrine settings feature namely a wide variability in micro structures within the cm- and dm-scale (Füchtbauer 1988, Tucker 1993). Furthermore, grain contacts conditions which co-determine pore geometry intensively, vary as much within as between sedimentary facies (Atkins & McBride 1992). More information regarding distinct particle contact conditions and pore geometry at the field scale is covered in chapter 4.6.2 and 4.6.4, respectively. Hence, pore orientation could affect attenuation at the seismic scale uniformly within the reservoir and not contribute to the seismic facies classification.

Illite provinces contain large abundances of intrapore clay minerals (IM) compared to the chlorite domain in the seismic volume (based on petrographic DGMK-database and on own

observations, appendix A-9). The viscous and inertial dissipation processes postulated by Klimentos & McCann (1990) could hence alter seismic wave characteristics for the illitized and chloritized regions. Unfortunately, no attenuation measurements were conducted in this study to verify any relevant dissimilarity for sandstones of different diagenesis types.
However, when accomplishing attenuation analyses on plugs the following requirements should be fulfilled:

- Specimen should be fully water saturated in order to
  - enable viscous and inertial coupling by the pore fluid and the intrapore clay minerals;
  - reduce Bulk compressional losses as water saturated pores are barely compressible and attenuation by marginal fluid motion is negligible (Murphy 1982).
- Differential pressures should reach limits high enough to ensure complete closure of compliant micro voids. Such a benchmark is established by increasing stress until compressional velocities show constant values.
- Samples should be characterized by comparable mineral composition, porosity, grain size parameters, pore geometry and particle contact conditions.

These constraints render comparative analyses feasible as other attenuation mechanisms are precluded.

The remaining features affecting seismic energy loss like varying clay content have been examined and discussed in the velocity studies. As “velocity and attenuation behave anti-proportional” (Schön 1998) those findings are valid also for the anelastic behaviour of the Wustrow sandstones. So, for instance, distinctions in particle bonds could codetermine the shape of seismic wavelets for the regions of different diagenesis type.

Summing up

Most of the above explicated parameters inducing wave energy loss appear impertinent for the seismic frequency band. Solely the dissipation mechanisms resulting from eventual characteristic variations in reservoir temperature, particle contact conditions and the relative motion of pore fluids and intrapore illite meshwork fibres could speculatively modify the deflections of the investigated seismic traces. Depending on the characteristic wavelets of the seismic classes those features accentuate or moderate the amplitude dissimilarities. The calculated modification in amplitude deriving from different ranges in water saturation appears to be small and could result likewise negligible for other parameters.
These findings support the substantial importance of extensional velocity contrasts for their impact on the seismic signals and hence on the seismic facies classification in this reservoir.

3.8 Additional rock parameters affecting compressional velocity

3.8.1 Introduction

The subsequent chapter discusses the effects on compressional velocity by rock and acquisition parameters which have not been investigated in the antecedent sections.
Generally wave speed and attenuation exhibit a contrarious behaviour (Schön 1998). Therefore, for most of the following rock features, the compressional velocity exhibits an antithetic dependence compared to the behaviour of attenuation described in the previous chapter.

3.8.2 Effects of parameters

Differential pressure: The compressional velocity of a rock augments with the applied differential pressure. The non linear dependence is mainly an effect of decrease by porosity, the closure of compliant microcracks and improvement of contact conditions with burial (Wyllie et al. 1956, Avcan et al. 1968, Schön 1998, Wang 2001).
Strain amplitude: Extensional velocity remains constant with increasing strain amplitude until strain reaches $10^{-6,3}$. Then the speed declines slightly (based on dry sandstones at ambient conditions, Winkler & Nur 1982, Gordon & Davis 1968). As mentioned before deflections in seismic acquisition amount to 10^{-7}. Seismic velocity features hence no dependence on this parameter (Murphy 1982).
Frequency: Generally compressional velocity rises with frequency for wet sandstones of constant pore fluid saturation (Wang 2001). The increase proceeds monotonically from the seismic to the ultrasonic bands (10-10^6 Hz, Murphy 1982) (Winkler 1986). The slowness of dry rocks turns out independent of frequency (Winkler 1986, Pham et al. 2002). Based on the graphs presented in Pham et al. (2002) augment longitudinal speeds of sandstones barely from 1 to 200 Hz. Eventual distinct seismic frequencies within the reservoir should hence not provoke relevant velocity contrasts.
Temperature: The effect of temperature on the velocity of water saturated rock is proportionally very small compared to other influences of porosity or saturation (Hearst et al. 1989). Dependencies arise from the temperature dependence of pore fluids (Batzle & Wang 1992) particularly for oil bearing rocks (Wang 2001). However, seismic velocities decrease only slightly with increasing temperature for gas- or water saturated rocks (Timur 1977, Wang & Nur 1990). Any influence on wave velocity arising from probable heat anomalies affecting the seismic properties of the pore content can thus be excluded for the Wustrow member.
Fluid saturation: Compressional velocity shows a complex relation to water content. However, the complexity seems to disappear at seismic frequencies (Mavko & Nolen-Hoeksema 1994). Laboratory experiments on this dependence at seismic frequencies are sparse (Mavko & Nolen-Hoeksema 1994). Figure 3.49 represents an extrapolation from a velocity-frequency-water content plot for 80 Hz, established with theoretical models for sandstones at a differential pressure of 40 MPa by Pham et al. (2002).
Velocity drops rapidly when the water saturation diminuishes from 100 to approximately 90 % and increases steadily till complete drainage is achieved. This behaviour resembles to other experimental data in this regard (Mavko & Nolen-Hoeksema 1994, Lucet 1989, Murphy 1982). The velocity graph demonstrates further a roughly opposite behaviour to variations in water saturation as observed for the dissipation factor.
The responsible petrophysical processes are less various and complicated than for the attenuation - fluid content dependency: At full saturation the pore fluid module is the same order of magnitude as the framework module; the inbibition of a few percent of gas drops the

bulk modulus of the composite fluid to a value close to gas; the initial decline in velocity represents hence a consequence of the reduction in the overall bulk module of the sandstone, the following increase is a density effect (based on Murphy 1982, Toksöz et al. 1976).
According to the staff of the department for reservoir geology in RWE-Dea (pers. comm., 2005) the gas saturation varies within 25 and 75 %. Within that range the seismic velocity could change by 70 m/s (fig. 3.49) which corresponds approximately to 28 % of the variation in velocity for the well sections in the blue/green and red/yellow seismic classes (see chapter 4.2).

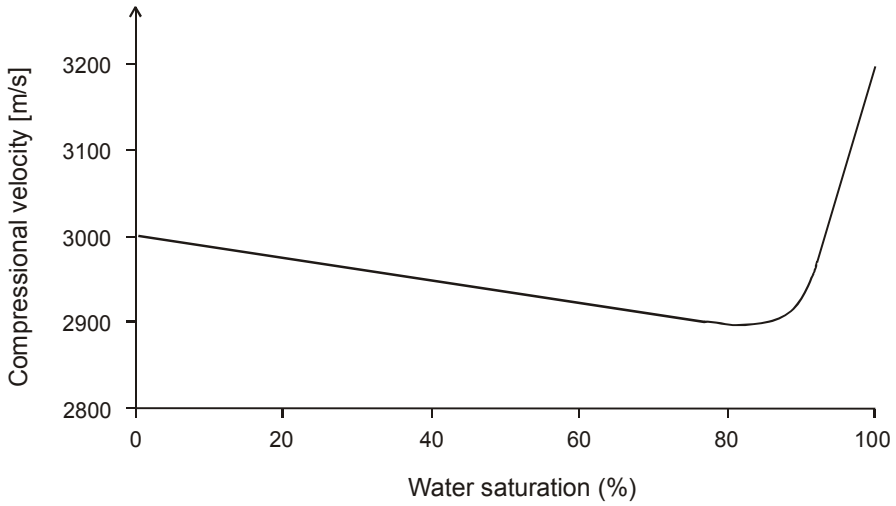

Fig. 3.49: Compressional velocity of a sandstone in dependence to water saturation for seismic frequency of 80 Hz at a differential pressure of 40 MPa. Within the range of saturation existent in the reservoir varies the velocity varies by 80m/s which corresponds to 28 % of the velocity difference encountered in the well sections of the blue/green and red/yellow seismic classes.

The modelled velocity-saturation dependencies (Pham et al. 2002) do not consider the hardly quantifiable effects of fluid distribution on velocity for sandstones at varying frequencies (e.g. Gist 1994, Knight et al. 1998). These vague and complex influences are not considered in this work.

3.8.3 Relevance for seismic volume

From the above discussed parameters variations in compressional seismic velocities could arise from eventual heterogeneities in differential pressure or fluid saturations at the reservoir scale. Overpressure could be created by changes in tectonical exposure, dehydration reactions of minerals or impeded fluid pressure relief during burial (Hyne 1991). Unfortunately, no information was obtained from industry on the thermodynamical conditions in the Wustrow member due to proprietary reasons.
As mechanical compaction is believed to play an important role especially in early and intermediate burial (Pettijohn 1975, James & Choquette 1986, Fisher et al. 1999) the pliable micro cracks should be closed and not contribute to any velocity contrasts in the deeply buried Wustrow silt and sandstones. Concentrations of tectonical deformation, representing an ulterior source for pore pressure and porosity alteration, are distributed rather evenly in the seismic volume (Tanner et al. 2005) and could be regarded as not decisive for the configuration of seismic wavelets.
Characteristic fluid saturations within the reservoir regions of blue/green and yellow/red classes can affect the seismic velocities dissimilarly. Depending on the distribution of the gas content within the reservoir contrasts in speed are either intensified or extenuated. An influence of this parameter on the seismic facies classification is thus probable.

4. Extension to seismic dimensions

The following chapter represents a comprehensive and multifaceted section of this work. It examines the possibility to extend the dependencies ascertained at the plug scale in the previous chapters to seismic dimensions.
In a first step it is tested whether the distinct velocities for reservoir rocks of different diagenetic authigenesis are also evident for the reservoir section and for the overall horizon. Subsequently it is evaluated, to which extents other lithologies than the reservoir affect the overall field velocity.
Then macro structural features, the reservoir thickness and the divergence in field velocity for provinces of illite and chlorite alteration are examined for their influence on seismic wave characteristics.
In order that the dependencies of the plug scale could be effective also at seismic dimensions indications are sought for distinctions regarding textural and petrophysical properties like particle contact conditions at the seismic scale.
Finally some additional general conditions follow which argue against or hamper the extension to seismic dimensions.

4.1 Compressional velocities of lithological sections at the seismic scale

4.1.1 Introduction

As explained in chapter 2.2 eolian Wustrow samples of comparable void volumes show characteristic ranges in velocities according to their clay mineral morphotypes (fig. 1.9, tab. 4.1). The provinces of different diagenetic alteration feature distinct reservoir properties and correlate to the seismic facies groups. As the velocities co-regulate the seismic facies classification it results thus crucial to test if the dissimilar speeds at the plug scale subsist also at seismic dimensions.
This chapter evaluates whether the well sections of the eolian dry intervals, the sections of the eolian dry and damp facies, which together constitute the reservoir part of the Wustrow member, and the entire horizon feature distinct travel times according to the corresponding diagenesis types.
However, speed contrasts at the seismic scale could be generated also by different lithologies in the Wustrow member. So, for instance, consolidated shale beds can exhibit largely varying and diverging velocities from porous sandstones (Castagna et al. 1985). This is due to their generally lower void volumes (Schön 1998) and their elastic anisotropy parallel and normal to the plane of bedding (e.g. Banik 1984, Tosaya et al. 1982).
A divergent velocity of the illitized and chloritized domains could thus be determined by potentially distinct velocities of the different lithologies in the Wustrow member.
Therefore, this chapter examines also the average in-situ speeds of the non-reservoir volume and the shale beds for eventual characteristic influences on velocities at the seismic scale and hence the seismic facies classification.

The following velocities of the entire Wustrow member and the volumetric proportions do not comprise the shaly and saline strata at the top of the horizon. As explicated in chapter 1.3.2 the seismic wave trace, utilized for the seismic facies classification (Trappe et al. 2005), does not start at the stratigraphic top of the Wustrow member, but at the interface region of its dense top and the actual reservoir. It was hence decided not to include the shaly overburden of the reservoir into the velocity analyses. All the below quoted parameters refer thus to well

sections of the silt and sandstone horizon and intercalated and underlying non- reservoir lithologies. The lower limit of the investigated interval was set close to the deepest sampling point of the seismic attribute analyses at the stratigraphic base of the Wustrow member. The thickness of the excluded section amounts to 0,3 till 3 m and corresponds to 1 till 16 % of the whole Wustrow interval. Besides, the average sonic speeds from the reservoir and its underlying strata, and from the whole stratigraphic member are substantially resembling. In this chapter the interval of the Wustrow member below its dense top layers is denoted as 'Wustrow member without top layers'.

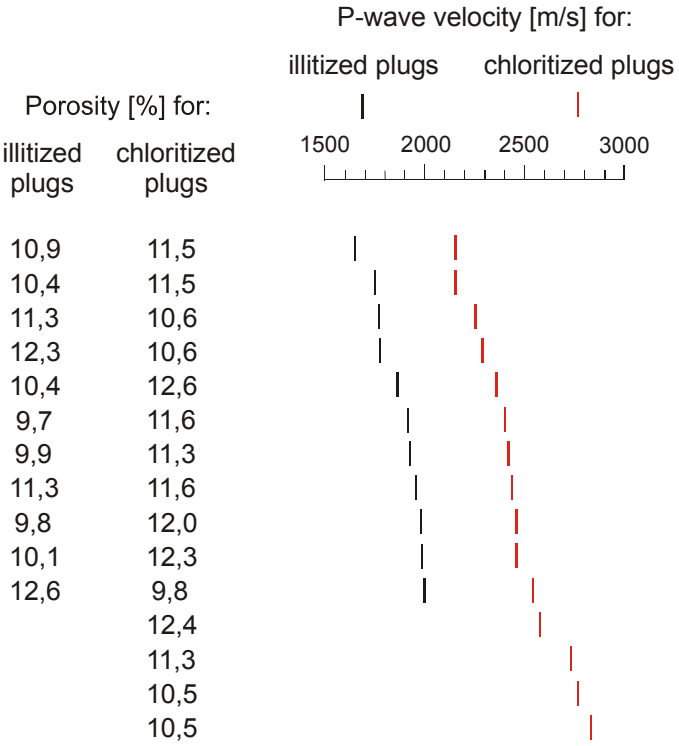

Tab. 4.1: Compressional speeds of plugs of eolian damp and dry facies with illite and chlorite alteration. The porosity of the selected samples varies slightly to enable the comparison of velocity. The interval from 1500 to 3000 m/s represents the typical range of compressional velocity for dry shaly sandstones of this porosity span at surface conditions (Schön 1998). All plugs differ distinctly by compressional speeds according to their clay mineral authigenesis. A limit for the reservoir rocks of this porosity span could be set around 2100 m/s.

Lithofacies Upscaling

The different sedimentary facies were identified in the GR-logs by lithofacies upscaling (Gaupp & Solms 2005). This technique is based on characteristic GR-cutoffs for major environments, which differ by shale and clay content. The benchmarks were established in the DGMK-project by comparing GR-records with core lithologies. The differentiated lithologies of eolian dry, eolian damp and non-reservoir facies are extrapolated from cored to the entire Wustrow interval except for its upper shaly and saline layers by the calibrated GR-log. The raw data are adjoined in the appendix (A-7).

4.1.2 Eolian dry section

As the analyzed samples represent merely silt and sandstones of the dry environment the sonic velocities taken into consideration must derive also exclusively from the same sedimentary facies. For this purpose the well intervals of the eolian dry facies need to be determined.
Figure 4.1 presents the distribution of the eolian dry sediments. The quantities increase principally from the East with 15 %, with a minimum of 5 % in the Southeast, to the West with a maximum of 68 %. Within the seismic volume the eolian dry sections amount to 30 till 55 with a resembling trend.

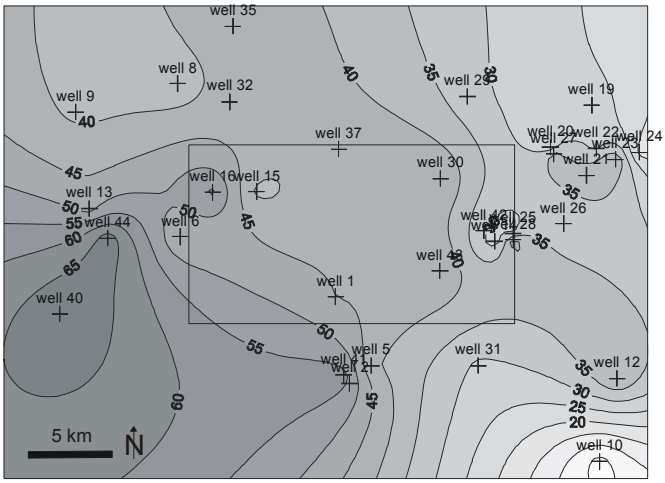

Fig. 4.1: Distribution of eolian dry intervals related to Wustrow member without top layers. Small rectangle delineates extension of seismic volume. The plot is based on lithofacies upscaling from 33 wells. Eolian dryenvironment constitutes the bulk of the Wustrow member without top layers in the West of the large survey with 68%. Towards the East and the Southeast the proportions decline strongly to 15% and 5%. Within the seismic volume eolian drysediments amount to 30 to 55 %.

This attribute map differs from the chart published in Gaupp et al. (2005) as the latter was based on the proportions to the whole Wustrow member.

Table 4.2 lists the wells and their in-situ velocities integrated over the sections of the dry sedimentary facies, other lithologies and the Wustrow member without top layers. The compressional speeds derive from sonic logs within the seismic volume and its surroundings. The table is differentiated according to the corresponding diagenesis types. The range of velocity is illustrated with the average value as a vertical line and the 25% and 75% quartiles as the ends of the box. Mean porosities are added for a better evaluation of the relationship between diagenetic type and velocity.
The investigation of sonic speeds was extended outside of the seismic volume to boreholes in the large survey. There the average porosities from cores vary significantly between 2% and 18%. As void volumes reduce velocities (Wyllie et al. 1958) strongly, wells with average porosities exceeding the range of 7% to 13,5% were excluded from the analyses. This limit was set in order to maintain the effect of the void volume as comparable as possible within the investigated volume.
It must be noted that the given porosities do not represent the averages of the Wustrow member without top layers but of the reservoir sections. The calculated porosities presented in chaper 1.2.3 are based on sonic logs and are thus not suited to examine for dependencies

of porosities to sonic velocities. Porosities from the density log were not computed due to the uncertain and usually large correction factor for gas for gas-bearing reservoirs (Crain 2000).
According to table 4.2, the sonic speeds for illitized well intervals of the dry facies turn out mostly lower than for the chloritized well sections. The turning point in velocity could be chosen around 4500-4550 m/s. Borehole 43 and 41 within the IC-group deviate from this trend with a high velocity, but presumably due to their comparatively low porosity of 7,0 and 7,8 %. It is remarkable that, although velocity and void volumes behave anti-proportional, the relatively higher sonic velocities are found in the intervals of higher porosities and vice versa (see well 35 with 12,4 % and 4722 m/s as an example).
When comparing the rise and decline of average speeds from well to well for the eolian dry section and the Wustrow member without top layers a significant analogy is observable. So, for instance, present the velocities of all the chloritized wells, except for borehole 35, identical changes.

It can thus be stated that the characteristic velocity ranges are evident also at a larger scale of a well interval of tens of metres for illitized and chloritized silt and sandstones of the dry facies.
The analogue change in velocity evidences that the volumetric proportion and the velocities of the eolian dry intervals could suffice to co-determine the travel times of the Wustrow member without top layers.
Further, the porosity seems not to control the separation in speed for the diagenetical types as high velocities must then be certainly faced in the illitized interval of the seismic volume and its near surroundings.

4.1.3 Eolian damp section

Besides the sediments of the eolian dry environment also the rocks of the damp facies constitute the reservoir section of the Wustrow member. Hence, the in-situ velocities of this facies contribute likewise to the overall velocities and are thus tested for distinct influences.

The eolian damp facies comprises sandy eolian bodies, interrupted by fine grained siltstone and mudstone lithologies, the latter exhibiting very low porosities and permeabilities. The intercalations evolved in response to the playa lake incursions and an oscillating capillary fringe within eolian dune units (based on Kocurek & Havholm 1993, Mountney & Thompson 2002).
Figure 4.2 illustrates the proportional occurrence of the eolian damp facies within the horizon. The magnitudes are likewise based on lithofacies upscaling. The magnitudes vary within 5 % in the South and 43 % in the North and reflect the sedimentary influence of the northern perennial lake (e.g. Gaupp 2005, Ziegler 1990). The attribute charts of the dry and damp facies evidence that the eolian intervals constitute mainly the bulk of the Wustrow member without top layers within the seismic volume (55 - 92 %).

The DGMK-project was mainly focused on the investigation on reservoir properties of the eolian dry facies. Unfortunately, no comparable plugs of the damp facies are available to test for characteristic amounts of load bearing clay minerals, particle contacts and plug velocity ranges. Nevertheless, similar micro textural positions and abundances of IC and CT-types should be expected for the moist dominated environment as the paragenetic sequence outlined in the diagenetic model applies for those silt and sandstones too (pers. comm., R. Gaupp, 2006, coordinator of DGMK-project).

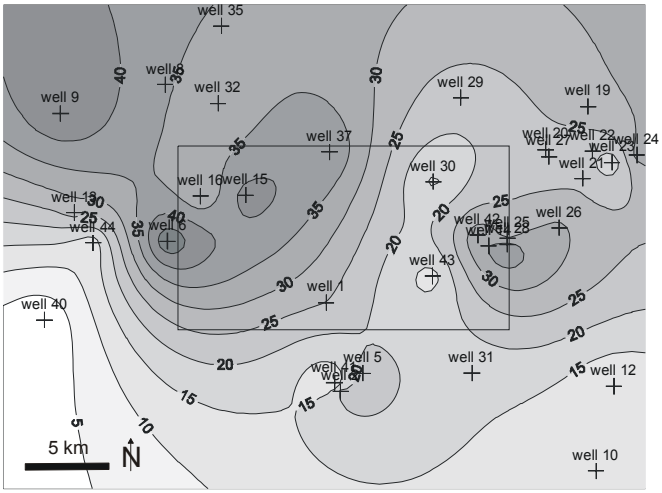

Fig. 4.2: Distribution of eolian damp intervals related to Wustrow member without top layers. Small rectangle delineates extension of seismic volume. The plot is based on lithofacies upscaling from 33 wells. Eolian dry influence increases generally from South with 5 % to North with 43 % due to the Northern playa lake.

The average sonic log speeds of the damp facies result higher due to the lower void volume of 7,2 % compared to those of the dry facies with 10,2 %. The average porosities were determined on 39 core samples and 238 core samples of the DGMK-database (appendix A-9), respectively. The velocities do not disclose pronounced differences in the ranges for the illitized and chloritized sections with mean values of 4700 and 4745 m/s respectively.

Table 4.2 includes the ranges of compressional velocities for the entire eolian interval. The severance in speed according to the diagenesis facies is still prominent and sustained after integrating sections of the dry and damp environment. A range for a segregating velocity ranges approximately from 4550 to 4650 m/s.
The increase and decline of velocity from well to well is identical to the change for the eolian dry sections. The analogy to the Wustrow member without top layers is still prominent. This indicates at least a co-determining effect from the reservoir part on the elastic properties of the Wustrow member without top layers.

4.1.4 Wustrow member without top layers

So far, the reservoir part of the Wustrow member demonstrates characteristic ranges in sonic travel times according to the diagenesis facies. The sonic velocities of the Wustrow member without top layers must evidence likewise distinct magnitudes in order to reflect the provinces of different diagenesis and permeability in the seismic slownesses.

Table 4.2 comprises the ranges of in-situ speed of Wustrow member without top layers. The sonic velocities exhibit a clear separation according to wells with different diagenesis types. Boreholes within illite altered regions feature comparatively minor ranges. A turning point could be constituted around 4600 m/s. Only well 43 deviates from this trend, probably due to its low reservoir rock porosity.
These findings demonstrate that the velocity contrasts for the incidences of the illite and chlorite morphotypes are prominent also in the seismic slownesses and could hence co-regulate the seismic facies classification for this horizon.

4.1.5 Non-reservoir section

The non-reservoir section comprises massive clay stones, silt- and clay stones with low till moderate sand content (<50%), sandstones in a muddy matrix and rarely occurring evaporitic layers (based on AppleCore files and GR-logs from DGMK-database, appendix A-7; and Gaupp & Solms 2005). These sediments formed principally at the shoreline of a perennial salt lake by periodical floodings and changes of the ground water table, and are confined by a horst and graben structure at the time of deposition (Gaupp et al. 2005, Gaupp et al. 1993, Budny 1991). Their abundances increase from the West with 4 volume %, to the East with 47 % and to the South with a maximum of 85 % (fig. 4.3).

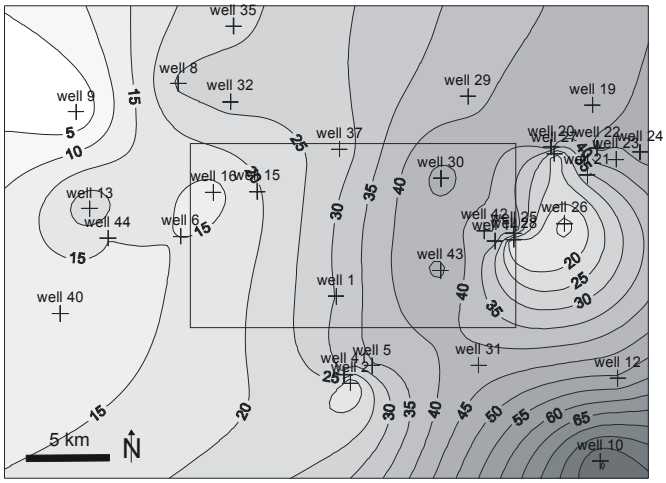

Fig. 4.3: Distribution of the non-reservoir unit as volume percentage of the Wustrow member without top layers. Smaller rectangle confines seismic volume. The plot is based on lithofacies upscaling from 32 wells. The abundances increase from West with 4 volume % to the East with 47 % and also to the South with a maximum magnitude of 85 %.

According to table 4.2 the non-reservoir sections exhibit average speeds from 4510 to 5050 m/s. The intervals belonging to wells of equal diagenesis types do not differ palpably by characteristic ranges as the variability is rather high in both intervals. However, the boreholes of chlorite alteration, on the average, feature a slightly higher in-situ speed for the non-reservoir units.
The comparison between the velocities of the Wustrow member without top layers and the non-reservoir volume unveils opposite, invariable and analogue changes from well to well. Thus the velocities of these sections appear not to entail the distinctions in overall field speeds.

Unfortunately, the diagenesis of non productive lithologies is not as thoroughly examined as for eolian Rotliegend units (Plein 1995 and based on own observations in DGMK-project). According to R. Gaupp (pers. comm., 2006, coordinator of DGMK-project) the silty and sandy sediments within the non-reservoir parts should be altered by similar diagenetic processes like the reservoir silt and sandstones. Therefore the micro textural distinctions for eolian dry sediments could be evident also in the sandy and silty non-reservoir deposit and provoke eventually its faint difference in sonic velocity for chloritized and illitized domains. Other possibilities related to the presence of shale beds are discussed in the following paragraphs.

4.1.6 Thin shale-reservoir rocks-interbeddings not resolved by GR-logs

GR-logs register natural radioactivity with a sampling rate of 2 and 6 inch (5 cm and 15,2 cm) depending on the used acquisition mode. Shale layers of minor dimension are hence not resolved. According to the activity contrasts of neighbouring strata interbeddings of such thin layers appear as vertical lines with constant gAPI. Such intercalations are not discriminable from massive shaly silt and sandstones.
The GR-records document elevated radioactivity between 20 and 80 gAPI for mostly all the damp and eolian drywell intervals. Some sandstone sections present only broad and low variances in GR-activity. Those readings could derive from thin intercalated shale as well as from authigenic and detrital clay minerals.
Shaly strata and clay stones occur especially in the eastern region of the large survey. This part was dominated by the sebkha environment and later altered by chlorite and hematite diagenesis types (Gaupp 2005).
It is thus conceivable that eventual proportionally high velocities for shale could induce the overall higher field speeds of the chloritized domains.

It must be noted that no exact attribute map of shale content can be generated for the large volume. The core files do cover shale strata only for a few wells. Hence, a calibration of GR-activity by mudstones for this horizon is not feasible. Furthermore, the GR-magnitudes for intervals of 100 % shale content vary strongly: thick beds interpreted as massive shale start at 120 as well as by 180 gAPI. Thus the standard benchmark of 80 gAPI or a characteristic limit for identifying and quantifying this lithology (e.g. Schlumberger 1991) can not be utilized unambiguously. The presented map of shale proportion (fig. 4.4) was produced by considering intervals exceeding 120 gAPI. It should thus be considered as an approximation to the real conditions within this horizon.
As additional aids to infer the distribution of shale strata please refer to the attribute maps of the non-reservoir sections (fig. 4.3), damp facies (fig. 4.2) and number of shale layers (fig. 4.7).

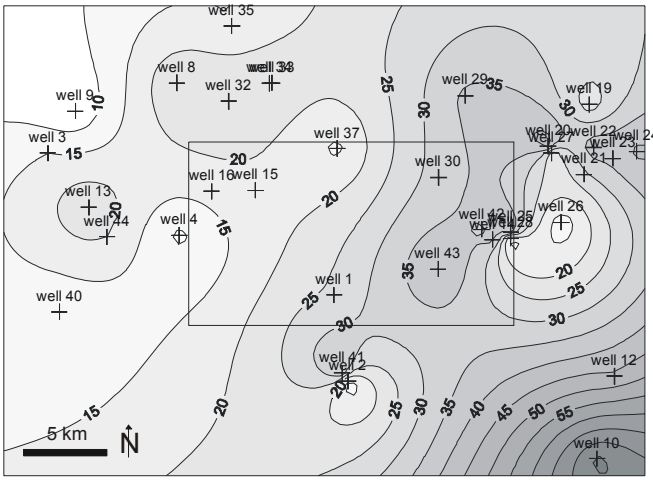

Fig. 4.4: Distribution of shale content in percentages. Smaller rectangle confines the seismic volume. The plot is based on lithofacies upscaling from 37 wells. The shale content augments from West with 8 % to the East with 40 % and to the South with a maximum of 75 %. The distribution is similar to the occurrence of non-reservoir intervals. The plotted shale content represents an approximation to real conditions as due to varying shale benchmarks of GR activity for this horizon.

Sonic speed analyses were conducted also for shale beds. Only those log intervals exceeding 180 gAPI were considered with the purpose to exclude assuredly any sand-shale interbeddings.
The ranges of velocities are presented in table 4.2. The average speeds vary largely from 4340 to 4944 m/s. The shale beds do not present a diverging representative travel time compared to the Wustrow member without top layers and to other reservoir units. This outcome evidences that the shale speeds can not produce the velocity contrasts for the illite and chlorite domains only by diverging abundances of clay stone.

4.1.7 Shale beds of different compressional velocity

Sonic velocity differences at the field scale could also be generated by dissimilar shale speeds originating from different depositional setting and burial history. Indeed, when evaluating the sonic shale speeds from wells of different diagenesis type, the maximum values are found in the chlorite designated boreholes. However, the low clay stone velocities are likewise frequent and resembling for regions of both clay mineral classes. This finding demonstrates that no clear characteristic difference is observable for the shale speeds from wells with chlorite and illite alteration.
The box-and-whisker plot evidence a strong influence of shale speeds on non-reservoir rock travel times. When comparing the increase and decline of velocity from well to well a similar change becomes apparent for both lithological intervals. This analogy is certifiable nearly throughout all wells in the plot. This finding evinces that the shale speeds and shale content suffice to govern the travel times of the non-reservoir parts.
However, the velocity changes from well to well of the shale beds manifest only a few analogue alterations to those of the Wustrow member without top layers. Hence, the elastic properties of the shale seem not to prevail the velocities of the eolian sections.

Summing up

In summary, shale beds appear to affect the velocities of the non-reservoir sections. This is strongly indicated by the analogue change in velocity from well to well for these sections. Additionally the similar diagenetic processes within the shaly silt- and sandstones of the non productive intervals could render the petrophysical properties comparable to those of the eolian part. This could provoke the faint distinction in velocity for the non-reservoir parts according to wells of different diagenesis type.
However, the sonic data of the Wustrow member without top layers exhibit no palpable evidence for a dominating effect of elastic properties from the non productive sections and the shale beds.
These facts strongly indicate that these lithologies should not constitute the basis for the correlation between seismic facies classes and the domains of diagenesis types and main permeability.
On the contrary, the interval velocities of the dry facies and the Wustrow member without top layers differ distinctly according to their clay mineral alteration. Further, the corresponding alterations in speed from well to well for these sections and the Wustrow member without top layers manifest a palpable analogy.
This implies that the petrophysical properties of the eolian dry and the reservoir at least co-determine the velocities at field dimensions and hence the facies classification for the seismic volume.
The porosities appear not to control decisively the severance in velocity for eolian intervals of distinct diagenetical alteration as high speeds are encountered in wells of elevated porosity.

Tab. 4.2: Sonic velocities integrated over the Wustrow member without top layers, the non-reservoir sections and the shale beds; the wells are differentiated according to the diagenesis types. Ranges of longitudinal speeds are presented by the mean magnitude as vertical line and by the 25 and 75 % percentiles as ends of the boxes. The integrated intervals do not comprise the upper shale beds of the Wustrow member. The interval from 4000 to 5000 m/s represents the typical range of compressional velocity for shale and shaly sandstones within these depths (Schön 1998). Porosities and permeabilities derive from core measurements.

Wustrow member without top layers - The velocities differ distinctly for wells of different diagenesis alteration. The highest speeds are encountered for wells with chlorite alteration. Only well 43 deviates from this trend, probably due to its low sandstone porosity. A vertical dotted line was set around a possible turning point of velocity to ease comparability and interpretation.

Eolian dry sections - The in-situ velocities result mostly lower than for the chloritized intervals. A turning interval could be set around 4500 till 4550 m/s (vertical dotted line). Wells 41 and 43 differ from this trend due to their minimum porosities. The rise and decline of velocities from well to well resemble for the Wustrow member without top layers and the eolian dry intervals.

Eolian dry and damp sections - The velocities are integrated over the dry and eolian dry intervals; these lithologies represent the complete reservoir of the Wustrow member. The separation in speed is still preserved. A turning point ranges around 4600 m/s. The change in velocity from well to well is identical to the trends in the eolian dry section and corresponds widely to the to the speed alteration of the Wustrow member without top layers. This fact strongly indicates a co-regulation of eolian intervals on the elastic properties of the Wustrow member without top layers.

Non-reservoir sections - The vertical dotted line delineates the maximum average speed within the wells with illite alteration. The velocities differ widely and not characteristically for the wells of different diagenesis facies. The wells of chlorite alteration demonstrate on the average only a slightly elevated speed.

Shale beds - The vertical dotted line delineates the maximum average speed within the wells with illite alteration. Highest magnitudes occur for clay stones from wells with chlorite morphotypes. These boreholes present also low velocities. The speeds vary largely and do not exhibit representative ranges for shale. The change of velocities from well to well is resembling for the shale and the non-reservoir sections. The speeds and content of shale thus suffice to codetermine the velocities of the non-reservoir rocks. A similar analogy between the travel times of the Wustrow member without top layers and the shale beds is absent. Thus a determining effect of clay stones on the overall elastic properties can be excluded.

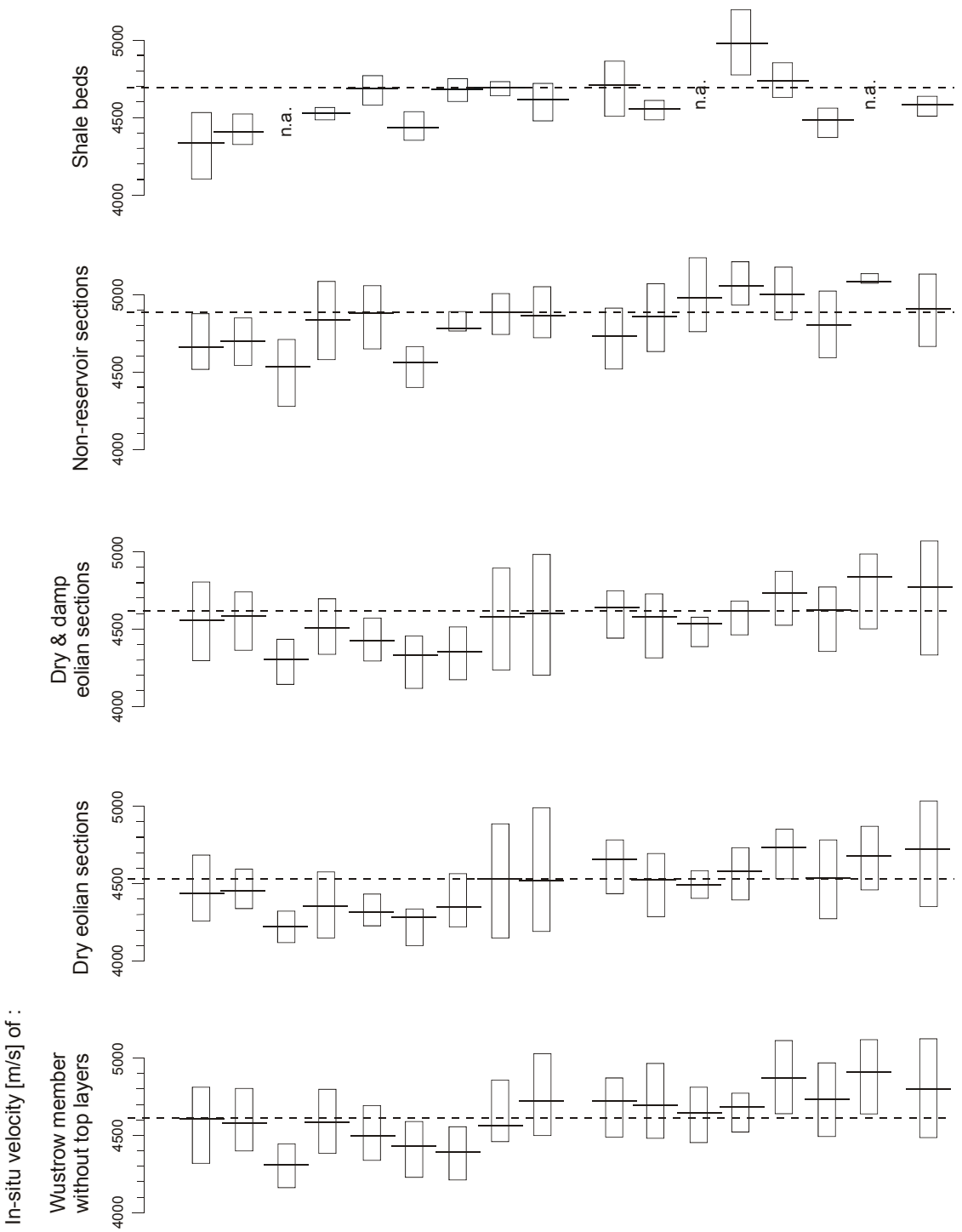

Well	Diagenesis type	Mean porosity [%]
Well 1	IC+IM	7,9
Well 5	IC+IM	7,4
Well 9	IC+IM	11,0
Well 15	IC+IM	8,2
Well 16	IC+IM	8,0
Well 26	IC+IM	12,7
Well 40	IC+IM	9,6
Well 41	IC+IM	7,8
Well 43	IC+IM	7,0
Well 20	CT	7,8
Well 25	CT	9,5
Well 27	CT	10,8
Well 28	CT	11,2
Well 30	CT	11,2
Well 42	CT	9,7
Well 32	CR,CS, CT	12,0
Well 35	CR,CS, CT	12,8

4.2 Relevance of velocity contrast for seismic signals

The average compressional velocity of the Wustrow intervals of illite and chlorite authigenesis constitute to 4510 and 4755 m/s respectively. The in-situ speeds for the two provinces of alteration differ hence by 245 m/s within the seismic volume and its surroundings.
According to Schön (1998) compressional velocities for shale and shaly sandstone reservoirs at depths around 4 km vary within 4000 and 5000 m/s. The difference in velocities for the illitized and chloritized regions amounts thus to remarkable 25 % of the possible range.

In order to verify whether these velocity contrasts suffice to cause characteristic distinctions in the seismic wavelets synthetic seismograms should be generated. Regrettably, this technique could not be applied due to time restrictions.

However, H. Yin (pers. comm., 2006, petrophysicist at URC research department ExxonMobil) regards the speed deviation to be assuredly large enough to generate pronounced dissimilarities in the wave traces, particularly in the height of the seismic deflections.

4.3 Influences of differences in stratigraphic structure on compressional velocity at the seismic scale

4.3.1 Introduction

This chapter investigates if differences in stratigraphic structure in the seismic volume co-regulate the seismic wave characteristics and hence the seismic facies classification.

The Wustrow member comprises locally constrained and continuous massive shale and shaly strata of variable thickness between 0,3 and 3 m (fig. 4.5). These lithologies of predominantly salt lake influence (e.g. Gast 1991, Behrendt 1993) accumulate in the northern and eastern region and intercalate mostly the upper Wustrow interval. The latter finding is based on 32 GR-logs in the large survey.

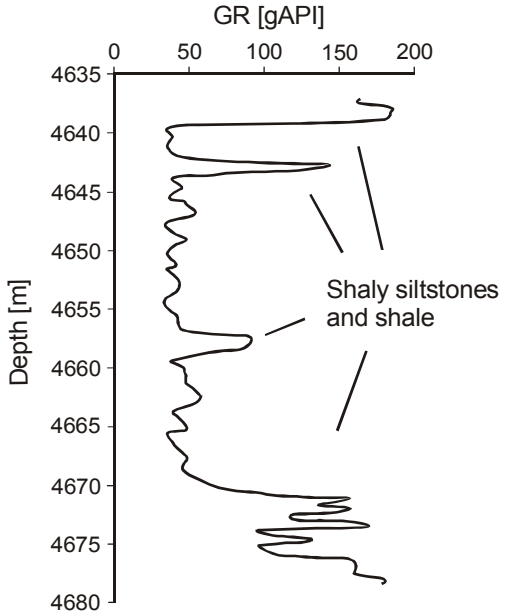

Fig. 4.5: Gamma ray - log of well 32 showing intervals of high GR activity deriving from shaly siltstones and shale beds.

4.3.2 Seismic resolution of intercalated shaly beds and shale

Seismic post processing is capable to vertically resolve beds with a minimum thickness of 1/4 and with appropriate deconvolution techniques under suitable conditions to 1/32 of the dominant wavelength (Brown 1996, Sheriff 1991).
Unfortunately, no information is obtainable from the petroleum companies and from associated geoconsultants on the acquisition parameters and processing methods used in the seismic survey due to proprietary reasons. However, a representative resolution can be calculated when applying potential minimum and maximum frequencies of 20 to 100 Hz for depths at 4500 m (Helbig & Treitel 2001) and a possible seismic velocity range of 4320 to 5340 m/s (from sonic logs for shale beds). Based on $\lambda = \frac{c}{f}$ with c as velocity, λ as wave length and f as frequency the minimum resolved layer thickness is 10,8 m and 1,4 m for maximum resolution.
The thicknesses of the discussed shaly beds and shale range thus within the limit of and below seismic separability and would hence not induce a deflection within the analyzed seismograms.

4.3.3 Interior reflections by shaly beds and shale

The shale and shaly layers could represent potential sources for re-echoing interior reflections (Parasnis 1997). For instance, the phenomenon of short-period internal reverberation (fig. 4.6) could attenuate elastic waves and diminish the modelled seismic velocities.

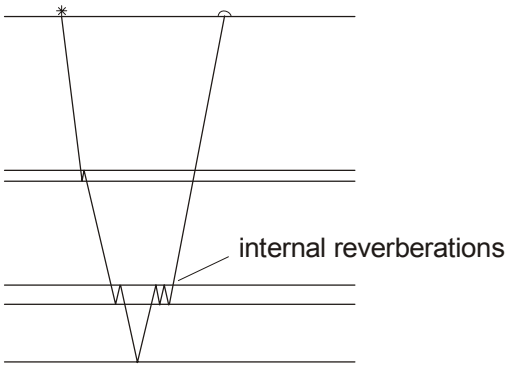

Fig. 4.6: Example for a short period internal reverberation within discontinuities of seismic impedances (after Parasnis 1997). Here illustrated is phenomena of short-period internal reflection potentially effective for the thin shale layers.

Figure 4.7 illustrates the distribution of shaly beds and shale intercalating the Wustrow reservoir.
Most of the intercalations occur in the northern and eastern region of the large survey due to the increasing influence of the playa lake incursions. The bulk part of the reservoir within the seismic survey barely embodies massive discontinuities. Only the GR-logs from well 37 and well 43 evidence each a 1 m thick clay stone layer.

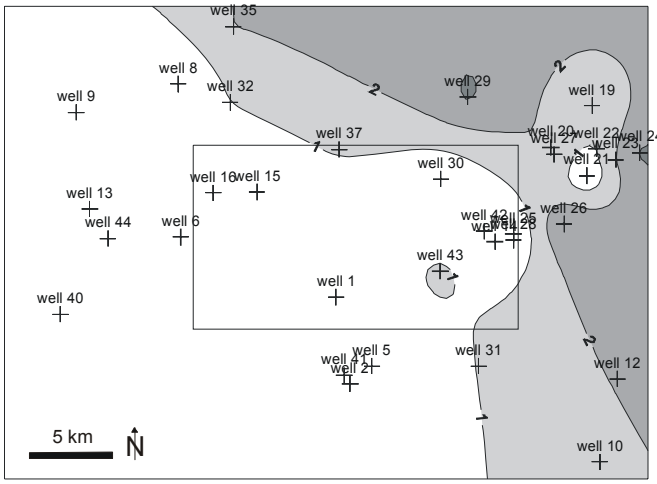

Fig. 4.7: Number of massive shale and shaly discontinuities visible by GR-logs and below the top layers of the Wustrow member. Small rectangle confines the seismic volume. The bulk part of the seismic volume barley comprises intercalations except for the locations of well 43 and 37.

The velocities and the bulk densities of the shale and shaly beds diverge substantially from the above and underlying silt and sandstones by approximately 300 till 1000 m/s and 0,5 g/cm^3. The intercalations represent thus locally constrained reflectors which could potentially affect seismic slowness and the configuration of wave traces through resonance effects.
Although the interface of the discontinuities within the reservoir represent a distinct impedance change its effect on the seismic facies classes by phenomena of reverberation is considered negligible as the discontinuities occupy merely a small part of the seismic volume.

4.4 Thicknesses of reservoir interval and relevance for seismic signals

The micro textural properties affecting compressional velocities, attenuation and reservoir properties at the plug scale are evidenced for the sand- and siltstones of the Wustrow horizon.
In order that the petrophysical properties of this lithology strike through at the seismic scale the reservoir section must comprise a considerable part of the seismic interval.
Based on the evaluation of GR-logs the reservoir proportions within the seismic volume range between 55 and 92 % (fig. 4.8). This unit thus represents the bulk of the Wustrow member without top layers and affects the seismic features volumetrically to the greatest extent.
Whether these proportions suffice can not be ascertained in this work. However, the thicknesses of the reservoir section are definitely resolved by seismic processing (see chapter 4.3.2).

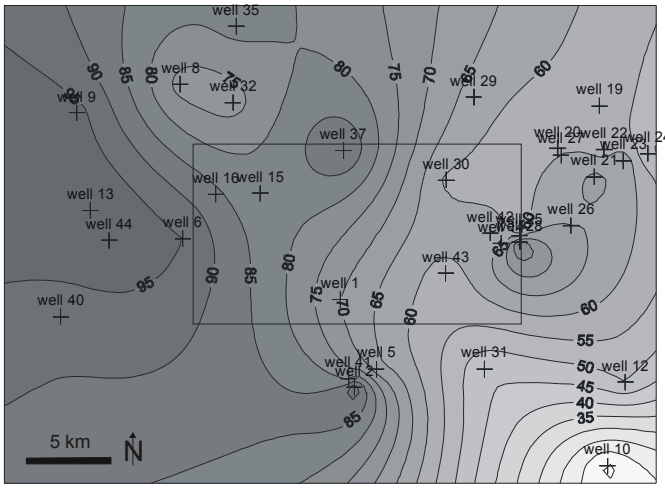

Fig. 4.8: Distribution of damp and dry facies. Small rectangle delineates extension of seismic volume. The plot is based on lithofacies upscaling from 33 wells. The reservoir interval comprises 57 till 92 % of the seismic volume and represents thus the volumetrically largest lithology which contributes to the seismic wavelets.

4.5 Comparability of ultrasonic, sonic and seismic velocities

This study utilizes ultrasonic waves for determining travel times in plugs and sonic logs as in-situ velocities and as substitution for seismic slownesses.
The sonic speeds of the horizon lie within the common range of compressional velocities of 3500-5000 m/s for water saturated sandstones with similar porosities and effective pressures of 40 MPa (based on Han et al. 1986 and Schön 1998). The used sonic data represent average magnitudes.
Sonic velocities are representative substitutes of seismic speeds (e.g. Fricke & Schön 1999, Helbig & Treitel 2001). This fact is largely utilized in standard techniques of petroleum exploration like Vertical Seismic Profiling (VSP). Furthermore, Gopa et al. (1994) compared compressional speeds from VSP and sonic log data of identical horizons and found small divergences of several percent due to different degrees of wave absorption. The effect on velocity deriving from different frequencies is insignificant according to basic theory (Reynolds 1997). In correspondence to common practice the used sonic data represent average magnitudes and integrate thus the seismic dimension.
The effect on velocity resulting from the different operating frequencies of the ultrasonic measurement at 80 kHz and the sonic tool at 20 kHz is negligible according to basic theory (Reynolds 1997) and the speed-frequency-saturation plots of Pham et al. (2002).
In general, the compressional speeds of a sonic tool result higher than the ultrasonic speeds of the dry plugs. The sonic speeds in the seismic volume range from 4000-5000 m/s and the plug speeds from 1650 to 3000 m/s. The reasons consist in the diverse thermodynamical conditions at the surface and the reservoir: the high reservoir pressure induces a closing of micro cracks (Schön 1998), which improves contact conditions and stiffness; the higher velocity of reservoir fluids compared to air (King 1966) provokes additionally a velocity increment. Ultrasonic plug velocities are widely applied for modelling seismic wave velocities (Wang 2001). However, potentially different travel time trends at surface and reservoir conditions are difficult to verify and should be generally not excluded in the reliability of interpretation.

4.6 Indications for distinct textural properties at the seismic scale

4.6.1 Introduction

It has been recognized that micro textural properties of solids and fluids could affect seismic wave characteristics (e.g. Dvorkin et al. 2002, Wang 2001). However, empirical evidences for such relations remain sparse, so far.
Avseth et al. (2000) investigated sandstone units which exhibited distinct seismic velocity ranges. The horizons differed mechanically only by their rigidity: the unit featuring lower speeds resulted unconsolidated and friable while the other turned out consolidated due to quartz cementation at the particle contacts. The authors could evidence the effect of this contact cement on the seismic velocity by means of high resolving vertical seismic profiling (VSP).
H. Yin (pers. comm., 2006, petrophysicist at URC research department, ExxonMobil), who investigates the petrophysical basis of elastic wave propagation, states that the micro textural features presented in this study should co-determine the seismic wave propagation.
The study of Avseth et al. (2000) and the frequent statements by authors (e.g. Bernard et al. 2003, Prasad et al. 2002, Batzle & Wang 1992, Dvorkin & Nur 1996, H. Yin) approve to utilize micro rock physics diagnostics in order to predict the seismic response at the field scale.

4.6.2 Particle contact conditions

As explained in chapter 3.2, particle contacts can condition both velocity and permeability of grain-clay-cement composites. Regions of distinct seismic velocity and fluid conductivity could hence be attributed to the bond conditions in the reservoir rocks. Avseth et al. (2000) evidenced that already a few percent of contact cement strongly affect the seismic wave traces for slightly cemented and friable reservoirs. Therefore differences in consolidation and cementation possibly existing at the field scale could provoke the velocity contrasts and the relation of seismic classes to reservoir quality.

4.6.2.1 Degree of compaction and cementation at the seismic scale

In the course of the DGMK-project no measurements on the grain arrangement in silt and sandstones could be accomplished nor was the compactional porosity loss was quantified, for example with packing indices (Taylor 1950, Wilson & McBride 1988).
The main blocky cements in the Wustrow interval constitute several generations of quartz, carbonates (calcite, anhydrite and siderite), sulphates (anhydrite and barite) and feldspars from different stages of diagenesis. According to Gaupp & Solms (2005) quartz precipitates are encountered mostly in the illitized parts, whereas carbonates and sulphates evolved chiefly in the northern and eastern part of the large survey, mostly due to the influence of the sebkha environment. These blocky precipitates can occlude pore space pervasively and therefore deteriorate reservoir qualities. Furthermore, R. Gaupp (pers. comm., 2006, coordinator of the DGMK-project) assumes a more intense consolidation for the southern and eastern part of the Wustrow interval due to indications of comparatively more severe pressure solution on thin sections. More information is covered in Gaupp et al. (1993), Gaupp (1996), Baunack (2002), Gaupp & Solms (2005) and in chapter 1.2.4.2.

Method

Hence the “intergranular volume-cement-porosity diagram” originally proposed by Houseknecht (1987) and modified by Ehrenberg (1989) was utilized in order to perceive any contingent variability in compaction and cementation for the seismic volume.
As this diagram functions only for sandstones of similar original porosity (porosity at deposition prior to compaction) and therefore similar sedimentary environment, the investigations were restricted to the eolian dry samples. Furthermore, packing conditions are highly dependent on grain sorting (Harrell 1981) and eolian dry sandstones exhibit a very well and better sorting than those of the damp dominated facies type.
The original porosity of eolian dry sandstones averages to 49-50 % according to studies on void volume and packing of unconsolidated eolian dune sands (Pryor 1973, Atkins & McBride 1992 based on active grain fall, grain flow and ripple sands). The intergranular volume-cement-porosity diagram presented by Houseknecht (1987) and Ehrenberg (1989) with an original porosity of 40 % was thus modified for this sedimentary facies with 50 % (fig. 4.9, 4.10).
The intergranular volume refers to the so called minus-porosity (Rosenfeld 1949), i.e. the percentage of intergranular cement and intergranular porosity. The porosity loss plotted at the right axis is based on the original void volume while the other parameters represent recent states of the compacted structure.
The required data on porosity, cementation and intergranular volume were derived from the petrographic database of the DGMK-project and own point counting records (appendix A-9). The cement refers to the sum of all authigenic minerals. Unfortunately, the porosity was infrequently differentiated into primary and secondary void volumes, which could lead to a downward shift in the following diagrams for several data points.
The data points in the diagram (figure 4.9) represent average values for the different wells. The corresponding mean sonic velocities are added to reveal eventual dependencies. The examined well sections are characterized by comparable porosities to minimize effects on velocity from different void volumes.

Results

Intergranular volume and intensity of cementation yield a similar spread for wells with lower and higher in-situ velocities.
According to Füchtbauer (1967) and McBride et al. (1991) particulate assemblies are compactable up to a porosity of 26 % by pure particle rearrangement. Void volumes below this benchmark were generated additionally by ductile component deformation and pressure dissolution.
The bulk part of the intergranular volume resides within a rather small range at and below 26% which indicates similar porosity decrease and similar extents of loss of solid volume.

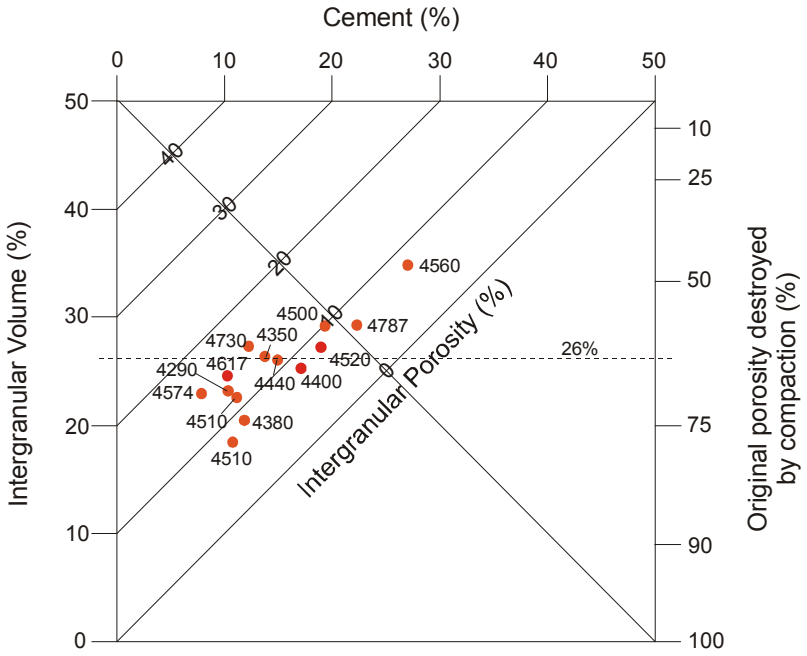

Fig. 4.9: IGV-cement-porosity diagram after Houseknecht (1987) and Ehrenberg (1989). Data points represent mean values for well sections of eolian dry facies. Mean sonic velocities of these intervals are added to test for eventual dependencies. Well intervals of comparatively high and low in-situ speeds do not exhibit preferred distributions. If relations were existent, data points with elevated velocities would plot in the lower section of more intense consolidation. A considerable part of the well sections featured porosity loss by secondary solution and particle deformation.

A few studies on Rotliegend diagenesis report characteristic amounts of intergranular volumes and authigenic minerals for different diagenesis types (Gaupp et al. 1993, Schöner 2006. Pervasive early sebkha cementation in the Wustrow silt and sandstones can preserve a minus porosity up to 40 % while some reservoir rocks especially from the eolian dry environment with illite coatings underwent intense consolidation due to the lack of framework sustaining precipitates (pers. comm., R. Gaupp, 2006, coordinator of the DGMK-project).
The IGV-cement-porosity diagram in figure 4.10 differentiates the eolian dry sections according to their type of diagenetic alteration. A similar independence on compaction and cementation is evident as the sonic velocity discriminates between the illitized and chloritized domains of comparable porosity. The data points in figure 4.10 coincide with the characteristic ranges presented by Gaupp et al. (1993) and Schöner (2006) for the chlorite and illite morphotypes and fall mostly into their overlapping regions.

Additionally well sections of similar porosity were differentiated according to their average permeability. In conformity to the above quoted diagrams, average permeability presents likewise no characteristic distinctions in consolidation and cementation at the field scale.

These findings indicate that the degrees of compaction and cementation and their impartiality towards the tested parameters should not induce the impedance contrasts and relations to reservoir properties at the field scale for the seismic volume.

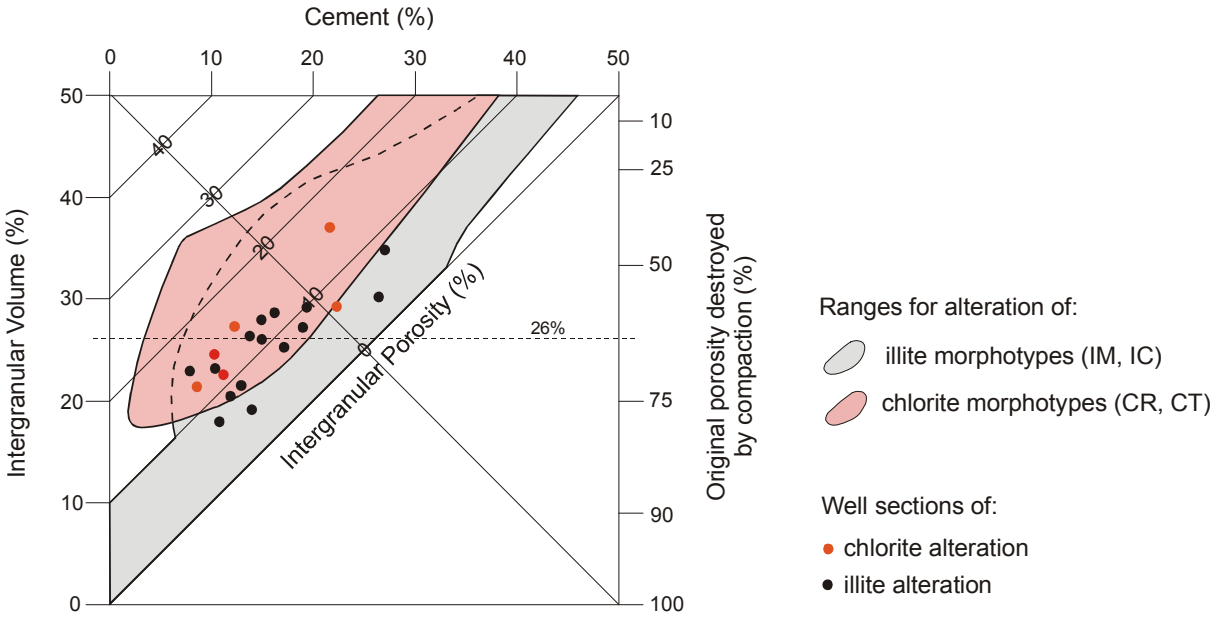

Fig. 4.10: IGV-cement-porosity diagram after Houseknecht (1987) and Ehrenberg (1989). Data points represent mean values for well sections of eolian dry facies. Coloured regions delineate characteristic IGV-porosity-cement proportions for illite and chlorite altered sandstones after Gaupp et al. (1993) and Schöner (2006). The data points fall mostly within the overlapping fields.

4.6.2.2 Packing indices by different sedimentary facies

The particle contact conditions of the Wustrow silt and sandstones could be co-determined by the original packing conditions of the dry and eolian dry sediments.
However, according to Atkins & McBride (1992), packing configurations of sands demonstrate as much variation within as in between the sedimentary environments (determined for river point and braid bar, beach, eolian ripple, grain fall and grain slide sands). Furthermore, diagenetic processes like cementation and secondary solution, (and age, tectonic stress or overpressure; remark of the author) control ultimately the bond properties of deeply buried sandstones (Atkins & McBride 1992). This conclusion is also evidenced by the large scatter of packing indices and porosity with depth for sandstones from similar depositional environment (e.g. Schön 1998, Wilson & McBride 1988, Moore 1975).
An eventual specific distribution of particle contacts related to the eolian dry and damp facies is therefore regarded rather unlikely for this deeply buried and diagenetically altered reservoir.

4.6.2.3 Packing indices by different grain sorting

In poorly sorted sands small grains occupy the intergranular voids and increase the average number of particle contacts per grain. Therefore packing indices are highly dependent on grain sorting (Harrell 1981).
The grain sorting of eolian dry and damp silt and sandstones turns out strongly varying in the seismic volume and does not demonstrate any relation to porosity, density, permeability or velocity at the plug or the field scale.

4.6.2.4 Blocky cements

The intensity of cementation has a strong impact on the rigidity and velocity of rocks (Avseth et al. 2000, Dvorkin & Nur 1996). Already small amounts seem to increase the hardness and

speeds of porous media severely (Liu et al. 1991, Dvorkin et al. 1994). This is also observable for the three investigated samples A-C where the grain structure with the largest contact area to blocky precipitates exhibits the lowest travel times.

The average proportions of blocky cements were therefore compared to mean sonic velocities from the reservoir sections of several wells (fig. 4.11).
The percentage of cement in the void volume is represented as the ratio of blocky precipitates to the sum of porosity and cement. The parameter comprises the amounts of secondary quartz, carbonates, sulphates and feldspars.
Although Trappe et al. (2005) exclude a relation between the distribution of seismic classes and the sum of all authigenic minerals, a slight graphical trend is observable between mean field velocities and mean abundance of blocky cements for both provinces of alteration. These investigations included less boreholes as for the previously discussed analyses due to restrictions in the available database.

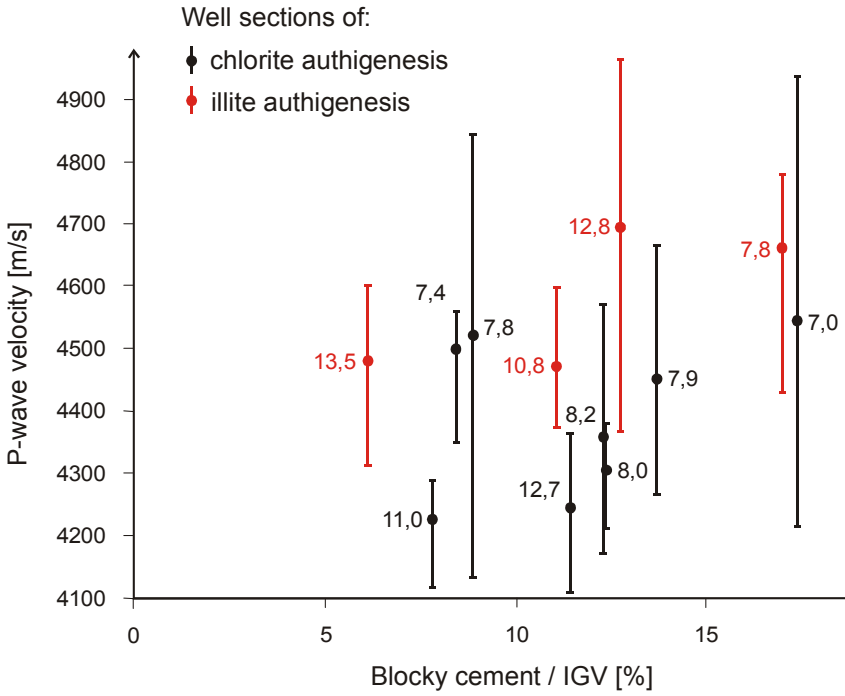

Fig. 4.11: Average compressional velocities of sonic logs versus mean proportions of blocky cement related to the intergranular volume. The parameters refer to well sections of the eolian dry facies. The 25 and 75 %-quantiles of the sonic velocities are illustrated as the end of the vertical lines. Mean porosities added next to the data points. The average values for eolian sections within both provinces of alteration exhibit a fair positive trend for velocity and cementation; however when including the average porosities the "dependence" results plurivalent.

However the here presented trend in the diagram is also a function of porosity. The impairing effect of void volume on velocity becomes evident when including the average void volumes into the examinations. This approach delivers thus a plurivalent outcome as in section 3.2.4.1, when examining the apparent relation between the proportion of blocky cements and velocities at the plug scale.

Summing up

The sonic velocities do not reveal any relevant dependencies on the IGV-cement-porosity proportions. The provinces of different diagenetic alteration exhibit likewise no distinct

correlation on consolidation and cementation. An eventual effect on reservoir permeability is also not discernible. Only the proportion of cementation appears to increase with sonic velocities. However this tendency is codetermined by the average porosities and evident for well sections of both diagenesis types.
The explicated effects of particle contact conditions on compressional velocities and permeability evident at the plug scale can thus not be verified for field dimensions in the seismic volume with the presented methods. However effects, also if not sweeping on the field velocities and permeabilities, remain continuing plausible.

4.6.3 Proportions of load bearing clay minerals and of not load bearing components - Consistency of petrological and micro textural features

In order that the properties ‘proportion of clay minerals between particle contacts’ and ‘volume of not load bearing components’ are effective also at the seismic scale, the reservoir section must be consistent regarding these textural characteristics:

- In the illite altered and chlorite altered provinces of the seismic volume the morphotypes of the other regions are barely documented within the reservoir interval. So, for instance, the region of chlorite authigenesis features locally fibres of IM-morphotype but at evanescent small quantities (well 37 with 0,2 %).
- All thin sections of the reservoir section of the seismic volume feature corresponding clay mineral morphotypes. This fact indicates a laterally and vertically consistent occurrence of specific diagenesis types.
- The occurrence of IM-fibres is restricted within the seismic volume to IC-altered silt and sandstones.
- The load bearing clay mineral (IC) evolved at a synsedimentary and early diagenetic stage by infiltration of clay bearing suspension currents and pedogenetic processes. Hence, during the consolidation, it resided between particle contacts at a future weight supporting position. Envelopes of tangential chlorite (CT) formed at a later and intermediate phase of diagenesis when already some mechanical compaction occurred. In contrast to the IC-morphotype, this precipitate results thus less abundant between particle bonds.
- The Wustrow reservoir was subject to different diagenetic processes, which could have dissolved minerals to various extents. However, according to the DGMK-petrographic database and own investigations (appendix A-9), illite morphotypes turn out much more abundant in the illitized reservoir samples than chlorite precipitates in chloritized specimens. The relative difference constitutes with 3,8 point counted % and 0,4 %, respectively, to a factor of 7,5. The determination on thin sections from 33 wells (DGMK-database, appendix A-9) permits to extend this difference to the overall reservoir interval.
These findings support to extend the characteristic differences in the ‘proportion for clay minerals between particle contacts’ and for ‘volume of not-load bearing components’ to the whole reservoir unit.

4.6.4 Pore geometry

Pore geometries are generally a strong function of particle contact conditions. The lack of evidences for different cementation and consolidation at the field scale is already explicated in chapter 4.6.2.1. Distinct degrees of packing in the eolian dry and damp sections are likewise not evident as the packing configurations within and between a sedimentary environment demonstrate similar large variations (Atkins & McBride 1992). Furthermore, grain sizes and grain sorting result likewise strongly varying in the seismic volume.

These features affected definitely the pore geometry of the reservoir section. However, distinctions in particle contact conditions and hence pore geometry could not be verified for the provinces of different permeability and clay mineral authigenesis.
Pore geometry is also determined by dissolution processes. According to R. Gaupp (pers. comm. 2006, coordinator of DGMK-project) and the diagenesis model, the eastern sections of the large survey and of the seismic volume featuring chlorite authigenesis and sebkha-type cementation were subject to extensive dissolution processes. These processes assuredly affected the characteristics of the pore geometries at the reservoir scale to relevant extents as they enhanced reservoir qualities in these regions substantially. Hence, the pore geometrical characteristics pore throats, pore size and interconnectedness, could, on the average, turn out considerably elevated for this region compared to the province of low fluid conductivity and illite alteration.

4.7 General arguments against or hampering the extension to seismic dimensions

The ultrasonic velocity measurement and the rigidity and permeability examinations were not conducted on probes under in-situ conditions.
So, for instance, the investigated plugs could contain micro fractures, which are formed, when the core is released from reservoir conditions. Under elevated pressure compliant voids are closed and the increase in particle contact area renders the rocks geomechanically harder. This textural difference would result in minor porosities and permeabilities and higher compressional velocities than actually measured for the analyzed samples.
Jones & Owens (1980) studied the rates of alteration for porosities and permeabilities with pressure for tight consolidated sandstones. Porosities decrease under elevated pressure to a maximum of 5-10 relative % in a linear relationship. The rate of reduction resulted comparable for his specimens and could thus be ignored for the present work.
However, pressure reduces the fluid conductivity more severely by two to more than ten times and in a more complex manner (Jones & Owens 1980). Furthermore, other rock features, like the presence of water and intra pore clays, affect permeability of low permeability sandstones too.
These facts could signify that distinctions of permeability at surface conditions are not existent or present to different degrees at reservoir conditions.
Compressional velocities exhibit a positive correlation with differential pressure and rise particularly for lower stress regimes depending on the proportion and stiffness of compliant micro fractures (Wyllie et al. 1958, Schön 1983). Distinctions in wave speed at surface and at reservoir conditions could arise also from the fact that the modules of air and brine are different and temperature dependent (Batzle & Wang 1992). Furthermore, extensional velocity exhibits an intricate relation to pore fluid distribution, pore geometry, and viscous and inertial effects of the pore fluid.
These circumstances could hamper the comparability of distinct velocities at surface and in-situ conditions.

As explicated in chapters 3.2.1, 3.2.4.1 and 3.7.2, p-wave velocity and attenuation depend on particle contact conditions which could vary for instance by sedimentological structures. In deed, the plug velocity measurements demonstrate that compressional waves crossing the bedding are slower than the waves parallel to the bedding plane. This anisotropy could be

relevant for the seismic velocities if the reservoir section of the seismic volume is diverse by distinct sedimentological features.
The degree of influence from tectonic lineaments on the configuration of wavelets is not assuredly quantifiable. Trappe & Schubarth-Engelschall (2005) tracked large scale faults and fractures in the seismic volume by means of coherency processing. However, the effects of small scale tectonic discontinuities on the seismic wave characteristics are not determinable.

Up to now no sound investigations exist which identify the geological features affecting seismic attributes like amplitude, shape and lateral coherency of seismic traces. This lack of knowledge supports the general criticism on the geological sense of seismic attribute interpretation (e.g. Brown 1996) and of neural network outputs. Statements from the auditorium during presentations of this study often claimed that “the neural network can not explain its results”.

5 Conclusions

This study tried to find the petrophysical basis for significant correlations between processed seismic signals and reservoir properties ascertained for the Wustrow member in the Rotliegend of NW-Germany. A secondary objective consisted in explaining the large scatter of permeability for reservoir rocks of comparable porosity and equal diagenesis type in the investigated horizon.

The predictability of seismic classes for various reservoir properties reported by the DGMK-project 593-8 was revised. Consequently the reliability for forecasting the occurrence of clay morphotypes, reservoir performance and bituminisation was particularly set in seismic classes representing less favourable reservoir qualities.

The compressional velocities and attenuation processes are the only petrophysical factors affecting the seismic facies classification as bulk density is barely varying. The provinces of illite and chlorite alteration feature different average compressional in-situ velocities. The divergence in velocity represents a relevant contrast to provoke distinct configurations in the analyzed seismic wavelets.

The following facts strongly indicate that the relevant petrophysical properties provoking the characteristic velocity contrasts are existent in the reservoir intervals of the Wustrow horizon:
The distinctive velocities are verifiable in the reservoir sections of different diagenesis. The non-reservoir sections exhibit only a slightly elevated average travel time for regions of illite alteration. The speeds of the shale beds determine those of the non-reservoir unit but do not govern the slownesses of the overall horizon. Seismic signal modifications generated by internal reverberations or reflections on thin shaly or saline strata intercalating the reservoir are demonstrably not relevant due to their marginal occurrence within the seismic volume. Shale layers not resolved by GR-logs do not affect overall velocities distinctly due to the wide span of slownesses for shale beds, ascertained also in identical wells. Furthermore, the seismic wavelets analyzed in the neural network classification integrate the reservoir sections and the underlying non-reservoir interval of the Wustrow member. Its shale and saline hanging wall is thus not comprised in the seismic signal classification. The reservoir unit affects thus volumetrically with 55-92 % the result of the seismic classification to the largest extent.

Generally compressional velocities are believed to be primarily dependent on porosity. However, the average void volumes of the reservoir rocks appear not to control field speeds solely as elevated porosities are encountered in the sandstones of higher velocity.
This outcome is observable for rocks at both the field and the plug scale.
The quoted fact portends that the following textural rock features should determine the rigidities of the Wustrow reservoir. These properties represent, affect or indicate also reservoir characteristics.

Load bearing clay minerals strongly reduce the velocity of rocks. Quantitative studies on selected samples of comparable properties but largely varying compressional velocity feature highly distinct abundances of clay minerals between particle contacts according to the occurring diagenesis type. The distinct amounts depending on the clay mineral authigenesis were palpably evident in all available samples.
The observed thicknesses and abundances of the clay mineral coatings within particle bonds appear to suffice to alter the overall elastic properties. The envelopes feature similar and larger diameters than those of shale layers, for which strong decelerating effects on

compressional velocities were proven. Furthermore, the occurring proportions of illite coatings resemble total clay contents reported in studies which demonstrated a substantial decline of velocity by augmenting clay quantity. The sparse bare contacts in the illitized specimens appear thus not to bear the whole compressional load of the transmigrating wave. This micro textural distinction for reservoir rocks of different alteration is existent throughout the whole seismic volume due to the subsequent findings:
- Coatings of illite (IC) evolved syndepositionally and at an early stage of diagenesis. Hence, in the compacted framework, they resided between particle contacts at a weight supporting position. Coatings of chlorite (CT) formed at a later and intermediate stage of diagenesis when already some mechanical consolidation took place. In contrast to the IC-morphotype, this precipitate is less abundant at this micro textural position and should reduce velocity to a minor degree (or not at all, in case the bare particle bonds suffice to transmit the whole deformation).
- The reservoir section was exposed to different diagenetic processes which could have dissolved these clay minerals to dissimilar extents. However, according to the DGMK-database and own observations (appendix A-9), illite coatings are 3-7 times more abundant in the illitized reservoir than the sum of all chlorite precipitates in the chloritized sections. Comparable quantitative differences are documented also for other Rotliegend reservoirs.
- The Wustrow reservoir appears to be laterally and vertically consistent regarding the distinct occurrence of clay morphotypes in the seismic volume. According to the DGMK-database and own investigations (appendix A-9) a paragenesis of illite and chlorite minerals is barely present in the investigated horizon. The occurrence of IM-fibres within the seismic sector is restricted to reservoir rocks of IC-alteration. Furthermore, all samples of the DGMK-project and of this study deriving from the seismic volume feature corresponding clay morphotypes.

The conspicuously lower compressional speeds for rocks of illite authigenesis could also be attributable to their comparatively larger abundance of authigenic minerals in pore space. The bulk of such particles represents illite precipitates (IM) which build loose meshwork structures in voids. These components reduce the porosity of the sandstones but do not affect the overall rigidity. Sandstones of chlorite authigenesis in the seismic volume comprise likewise non-weight supporting minerals like CR, CS-chlorite but at insignificant abundances.

The distinctions in particle bonds could also provoke the largely diverging velocities of Wustrow reservoir rocks. Chloritized samples of comparable properties but largely diverging velocity present characteristic distinctions in particle contact configuration. Those specimens with low velocity feature the most isolated grains, while the grains in the samples of high velocity present the largest contacts to blocky cement and bonds formed by pressure solution. However, characteristic differences in chemical and mechanical compaction could not be ascertained at the field scale.

Variations in pore geometry could likewise regulate the speeds of the reservoir rocks. Chloritized samples of comparable properties but largely diverging velocity differ accordingly in average magnitudes and ranges of specific attributes inducing distinct rigidities and enabling squirting phenomena in the water bearing case. However, except for an indication of a more intense secondary mineral dissolution in the chloritized province, characteristic pore geometrical dissimilarities, could not be identified for the field scale.

Elastic properties of the load bearing illite and chlorite minerals appear not to induce the velocity contrasts as the micro impedances differ only slightly. Their difference to the impedances of main minerals results by far more significant. Unfortunately the SAM-

measurements featured high standard deviations and could not be repeated due to instrumental problems.

The characteristic distinctions in the amount of load bearing clay minerals between particle contacts and in the proportions of not load bearing minerals for the regions of illite and chlorite authigenesis could be responsible for their dissimilar field velocities. The relevant divergence in field speeds could provoke dissimilar wave traces and co-regulate the classification of the seismic signals. The correlation of seismic classes to the occurrence of illite minerals is thus attributable to the micro textural distinctions of the illitized sandstones.
The permeability is severely reduced by the presence of IM-fibres. This precipitate occurs predominantly in the province of illite authigenesis and is barely documented for the province of chlorite authigenesis. The correlation of seismic facies classes to major permeability trends could thus be a result of the textural properties in the illitized sandstones affecting velocity and the restricted occurrence of the IM-morphotype. Likewise, the predictability of seismic facies classes for intense bituminisation results to be a product of the correlation to illite provinces as the organic matter impregnation is widely restricted to these regions.
The effects of particle contact conditions and pore geometrical attributes could determine both velocities and permeabilities of the Wustrow rocks. Although evidences for characteristic distinctions at the field scale are lacking, their codetermining influence, also if possibly not prevailing, remains still plausible.

The pore geometrical studies and the modelling of permeability demonstrates that the largely diverging permeability for eolian samples of similar porosity and diagenesis type is relatable to distinct variations in pore throat size and -distribution, degree of interconnectivity, fractions of intragranular porosity and pore wall roughness. The pronounced void geometrical distinctions are evidently a result of dissimilar intensities in secondary dissolution and mechanical and chemical consolidation, apparent at the micro scale.

The influence of anelastic processes on seismic wavelets could not be quantified due to the lack of data. Seismic energy loss could be caused by eventual characteristic variations in reservoir temperature, particle contact conditions and the relative motion of pore fluids and intrapore illite fibres. The calculated maximal modification of the seismic amplitude by potential distinct gas saturations within the regions of blue/green and red/yellow classes appears to be negligible.
Characteristic fluid saturations could also have provoked the ascertained velocity contrasts for regions of different clay mineral authigenesis. Depending on the saturation conditions divergences in field speeds are either intensified or attenuated. An influence of this parameter on the classification outcome is possible, but unfortunately is not quantifiable in this study due to the lack of data.
Additional reservoir properties which could mask the velocity and attenuation effects by the cited micro textural features represent eventual characteristic distinctions in sedimentological structures and small-scale tectonic fractures. Furthermore, compressional velocity and permeability exhibit generally a complex dependence on p/T- conditions and magnitudes ascertained at atmospheric conditions are hence not easily extendable to the reservoir situation.

Several arguments complicate the extension of relations ascertained at the plug scale to field dimensions, particularly the possibly distinct behaviour of permeability and velocity under reservoir conditions and the general criticism on the geological background of seismic attributes. It must be noted that, in the light of the explicated arguments impairing the

extension, the proposed petrophysical basis is regarded as a potentially co-regulating basis for the correlations between seismic facies classes and trends of reservoir properties.

Several approaches in this study illustrated the impediments encountered when inspecting multi-dependent databases for two-dimensional trends. In order to identify unambiguously rock properties co-regulating compressional speed and/or permeability it is necessary to reduce the sum of the relevant factors. In this study, some investigations are hence conducted on samples which resemble as much as possible but diverge largely in compressional velocity and permeability. This approach enabled to direct the focus of the investigations on a single or two parameters. As the necessary restriction limited the analyses to a reduced set of appropriate specimens, the identified features most probably affecting the rigidity and permeability, could not be tested on a wider range of samples. However, the characteristic distinctions in the abundance of clay mineral coatings within particle contacts, the volume of not load bearing components, the particle contact conditions and the depending pore geometries represent the only plausible reasons for the divergences in velocity between the samples of chlorite and illite authigenesis, and the distinctions of velocity and permeability within the specimens of solely chlorite alteration.

Generally the effect of texture on seismic properties is poorly understood as structures of sedimentary rocks in wells are difficult to qualify and quantify. Literature does not report any studies on textural properties affecting the elastic and anelastic behaviour of rocks except for pore geometry, cementation, clay content, intra pore precipitates and grain size sorting, so far. The here presented outcome represents thus partly new knowledge derived with specially developed parameters.

Petroleum exploration industry is keenly pushing the development of techniques which enable the forecast of reservoir quality from seismic signals calibrated with geological information. This study contributed to this need by identifying significant dependencies between reservoir properties and the elastic features of rocks, and testing their relevance for wave characteristics at the seismic scale.
Furthermore, the here conducted rock physics diagnostics demonstrate that textural differences can explain velocity contrasts in rocks of comparable porosity and lithology. Such investigations are thus indispensable when for instance improving the accuracy of porosity prediction from sonic log data or modelling depths from seismic slownesses.

6 References

Abram P., Bechtel A., Gawlick H.-J., Gratzer R., 2001: Sedimentologische und organo-geochemische Aspekte des Oberen organisch-reichen Hauptdolomites in den Gailtaler Alpen - Untersuchungen anhand eines Aufschlusses NE des Witzalas (Windische Höhe, Kärnten, Österreich).- diploma thesis, University of Mining, Leoben, 103 p.

Akbar N., Dvorkin J., Nur A., 1993: Relating p-wave attenuation to permeability.- Geophysics, v. 58, p. 20-29.

Akbar N., Mavko G., Nur A, Dvorkin J., 1994: Seismic signatures of reservoir transport properties and pore fluid distribution.- Geopphysics, v.9, p.1222–1236.

Alexandrov K.S., Ryzhova T.V., 1961: Elastic properties of rock-forming minerals, II. Layered silicates.- Bull. (Izv) USSR Acad. Sci. Geophys. Ser., v. 9, p. 1165-1168.

Alexandrov K.S., Eisenberg L.A., Rysova T.V., 1966: Vycislenie uprugich parametrov gornich porod po mineralnomu sostavu.- Izv. A. N. USSR, Ser. Geol. Moskva, v. 2, p. 3-19.

Amyx J.W., Bass D.M. Jr., Whiting R.L., 1960: Petroleum reservoir engineering, physical properties.- McGraw-Hill, New York, 610 p.

Anselmetti F.S., Eberli G.P., 1993: Controls on sonic velocity in carbonates.- Pure and Applied Geophysics, v. 141, p. 287-323.

Anselmetti F.S., Eberli G.P., 1997: Sonic velocity in carbonate sediments and rocks: in: Palaz I., Marfurt K.J., eds., Carbonate Seismology.- SEG Geophysical Developments Series, v. 6, p. 53-74.

Appel M., Freeman J.J., Gardner J.S., Hirasaki G.H., Zhang Q.G., Shafer J.L., 2001: Interpretation of restricted diffusion in sandstones with internal field gradients.- Magnetic Resonance Imaging, v. 19, p. 535-537.

Arastoopout H., Chen S.T., 1987: Analysis of flow of gas and water in a fractured and non-fractured low-permeability reservoir under production.- SPE Annual Technical Conference, Dallas, September 27-30, 1987, abs.

Arbib M.A., 1995: The handbook of brain theory and Neural Network.- MIT Press, Cambridge, 697 p.

Arns C.H., Sakellariou A., Senden T.J., Sheppard A.P., Sok R., Pincewski W.V., Knackstedt M.A., 2005: Digital core laboratory, Reservoir core analysis from 3D images.- Petrophysics, v. 46, n. 3, in preparation.

Atkins J.E., McBride E.F., 1992: Porosity and packing of Holocene river, dune, and beach sands.- AAPG Bulletin, v. 76, p. 339-355.

Avcan, G.M., Matveenko A.A., Stefankiewicz Z.B., 1968: Vlijanie vsestoronnego davlenija na fiziceskie svojstva pescanikov.- Prikladn. Geofiz. Moskva, v. 55, p. 149-164.

Avseth P., Dvorkin J., Mavko G., Rykkje J., 2000: Rock physics diagnostic of North Sea sands - Link between microstructure and seismic properties.- Geophys. Res. Lett., v. 27, p. 2761-2764.

Baldschuhn R., Frisch U., Kockel F., 1997: Geotektonischer Atlas von NW-Deutschland 1: 300000.- Bundesanstalt für Geowissenschaften und Rohstoffe (BGR), Hannover.

Banik N.C., 1984: Velocity anisotropy of shales and depth estimation in the North Sea basin.- Geophysics, v. 49, p. 1411-1419.

Barucci E., Landi L., 1998: Nonlinear Versus Linear Learning Devices - A Procedural Perspective.- Computational Economics, Springer-Verlag, Berlin, v. 12, n. 2, p. 171-191.

Barnes A., 2001: Seismic Attributes in your Facies.- Canadian Society of Exploration Geophysicists Recorder, p. 41-47.

Basan P.B., Lowden B.D., Whattler P.R., Attard J.J., 1997: Pore-size data in petrophysics - a perspective on the measurement of pore geometry.- in: Lovell M.A., Harvey P.K., Development in Petrophysics.- Geol. Soc. Spec. Publ., n. 122, p. 47–67.

Basan P.B., Lowden B.D., Strobel J., 2003: Maximising NMR-log interpretations in thinly bedded reservoirs - an example from offshore Egypt.- AAPG International Conference Barcelona, Spain, September 21-24, 2003, abs.

Batzle M., Wang Z., 1992: Seismic properties of pore fluids.- Geophysics, v. 57, p. 1396-1408.

Baunack C., 2002: Petrographische Untersuchungen und Modellierung der Quarzdiagenese in Rotliegend-Sandsteinen des Norddeutschen Beckens.- diploma thesis, Friedrich-Schiller-University, Jena, 85 p.

Bear J., 1972: Dynamics of fluids in porous media.- Elsevier Science and Technology, Amsterdam, 764 p.

Behrendt L., 1993: Die sedimentologischen Leithorizonte im Saxon im Nordteil der DDR.- Z. angew. Geol., v. 39, p. 70-78.

Berge P.A., Berryman J.G., 1995: Realizability of negative pore compressibility in poroelastic composites.- J. Appl. Mech., v. 62, p. 1053-1062.

Bernard Du X., Prasad M., Reinstaedtler M., 2003: The effect of cementation on the seismic properties of sandstones.- in: Arnold W., Hirsekorn S., eds., Proc. Int. Symp. Acoustical Imaging, v. 27, p. 399-405.

Best A.I., McCann C., Sothcott J., 1994: The relationships between the velocities, attenuations and petrophysical properties of reservoir sedimentary rocks.- Geophysical Prospecting, v. 42, p. 151-178.

Best A.I., McCann C., 1995: Seismic attenuation and pore-fluid viscosity in clay-rich reservoir sandstones.- Geophysics, v. 60, p. 1386-1397.

Best A.I., Sams M.S., 1997: Compressional wave velocity and attenuation at ultrasonic and sonic frequencies in near surface sedimentary rocks.- Geophysical Prospecting, v. 45, p. 327-344.

Biot M.A., 1956 (a): Theory of propagation of elastic waves in a fluid saturated porous solid, I Low frequency range.- J. Acous. Soc., v. 28, p. 168-178.

Biot M.A., 1956 (b): Theory of propagation of elastic waves in a fluid saturated porous solid, II Higher frequency range.- J. Acous. Soc., v. 28, p. 179-191.

Blenkinsop T., 2000: Deformation microstructures and mechanisms in minerals and rocks.- Kluwer Academic Publishers, Dordrecht, 150 p.

Blum H., 1967: A transformation for extracting new descriptors of shape - Models of the perception of speech and visual form.- MIT Press, Cambridge, p. 362-380.

Bourbie T., Coussy O., Zinszner B., 1987: Acoustics of porous media.- Gulf Publishing Company, Houston, 331 p.

Bradley J.J., Fort A.N., 1966: Internal friction in rocks.- in: Clark, SP. Jr., ed., Handbook of Physical Constants, Memoir 97.- Geol. Soc., p. 175-193.

Briggs A., 1992: Acoustic Microscopy.- Clarendon Press, Oxford, 325 p.

Brown A.R., 1996: Interpretation of three-dimensional seismic data.- AAPG memoir 42, AAPG, Tulsa, 341 p.

Brunauer S., Emmett P.H., Teller E., 1938: Adsorption of gases in multimolecular layers.- J. Am. Chem. Soc., v. 60, p. 309-319.

Budny M.. 1991: Seismic reservoir interpretation of deep Permian carbonates and sandstones (NW-German gas province).- First Break, v. 9, p. 55-64.

Burkhardt H., Mörig R., Schütt R., 1990: Experimental and theoretical investigations of seismic wave absorption mechanisms in sedimentary rocks: Application of absorption of seismic waves in hydrocarbon exploration.- DGMK-report 386, DGMK, Hamburg, p. 141-199.

Burri P., Faupel J., Koopmann B., 1993: The Rotliegend in Northwest Germany, from frontier to fairway.- in: Parker J.R., ed., Petroleum Geology of Northwest Europe.- Proceedings of the 4th Conference, Geol. Soc., p. 741-748.

Byerlee J.D., 1990: Friction, overpressure and fault normal compression.- Geophys. Res. Lett., v. 17, p. 2109–2112.

Byrnes A.P., 1997: Reservoir characteristics of low-permeability sandstones in the Rocky Mountains.- The Mount. Geol., v. 34, p. 39–48.

Cadoret T., Marion D., Zinszner B., 1995: Influence of frequency and fluid distribution on elastic wave velocities in partially saturated limestones.- J. Geophys. Res., v. 100, p. 9789-9803.

Calabi L., Hartnett W.E., 1968: Shape recognition, prairie fires, convex deficiencies and skeletons.- Amer. Math. Monthly, v. 75, p. 335-342.

Callan R., 1999: The Essence of Neural Networks.- Prentice Hall Europe, New Jersey, p. 1-200.

Carman P.C., 1937: Fluid flow through a granular bed.- Trans. Inst. Chem. Eng., v. 15, p. 150–156.

Carman P.C., 1956: Flow of gases through porous media.- Butterworths Scientific Publications, London, 182 p.

Castagna J.P., Batzle M.L., Eastwood R.L., 1985: Relationships between compressional-wave and shear-wave velocities in clastic silicate rocks.- Geophysics, v. 50, p. 571-581.

Castagna J.P., Batzle M.L., Han D.H., 1995: Issues in rock physics and implications for DHI interpretation.- The Leading Edge, v. 14, p. 883-885.

Chilingarian G.V., Torabzadeh J., Riecke H.H., Metghalchi M., Mazzullo S.J., 1992: Interrelationships among Surface Area, Permeability, Porosity, Pore Size and Residual Water Saturation.- Developments in Petroleum Science, v. 30, p. 379-397.

Cluff R.M., Shanley K.W., Byrnes A.P., 2005: Permeability Jail and Implications for “Basin Centered Gas” Production and Resource Assessment.- AAPG Hedberg Conference Understanding, Exploring and Developing Tight Gas Sands, Vail, April 24-29, 2005, abs.

Collins R.E., 1961: Flow of fluids through porous materials.- The Petroleum Publishing Company, Tulsa, 270 p., abs.

Committee on Fracture Characterization and Fluid Flow, 1996: Rock Fractures and Fluid Flow, Contemporary Understanding and Applications.- National Academies Press, Committee on Fracture Characterization and Fluid Flow, National Research Council, 568 p.

Crain E.R., 2000: Crain's Petrophysical Handbook - Petrophysical Well Log Analysis.- Spectrum 2000-Mindware, http.- //www.spec2000.net/.

De G.S., Winterstein D.F., Meadows M.A., 1994: Comparison of P- and S-wave velocities and Q's from VSP and sonic log data.- Geophysics, v. 59, p. 1512-1529.

Deutrich T., 1993: Illitbildung in Rotliegendsandsteinen des Nordwestdeutschen Beckens.- doct. thesis, Johannes Gutenberg University, Mainz, 179 p.

Diaz E., Prasad M., Mavko G., Dvorkin J., 2003: Effect of glauconite on the elastic properties, porosity, and permeability of reservoir rocks.- The Leading Edge, v. 22, p. 42-45.

Dillon C.G., Worden R.H., Barclay S.A., 2004: Simulations of the effects of diagenesis on the evolution of sandstone porosity.- J. Sed. Res., v. 74, p. 877-888.

Doyen P.M., 1988: Permeability, conductivity and pore geometry of sandstone.- J. Geophys. Res., v. 95, p. 6993-7005.

Dullien F.A.L., 1992: Porous Media, Fluid Transport and Pore Structure.- Academic Press, Inc., San Diego, 574 p.

Dunn K.-J., Bergmann D.J., Latorraca G.A., 2002: Nuclear Magnetic Resonance, Petrophysical and Logging Applications.- Pergamon Press, Amsterdam, 293 p.

Dutton S.P., Clift S.J., Hamilton D.S., Hamlin H.S., Hentz T.F., Howard W.E., Akhter M.S., Laubach S.E., 1993: Major low-permeability-sandstone gas reservoirs in the continental United States.- Bureau of Economic Geology, Report of Investigations, University of TX, Austin, n. 211, 221 p.

Dvorkin J., Mavko G., Nur A., 1991: The effect of cementation on the elastic properties of granular material.- Mechanics of Materials, v. 12, p. 207-217.

Dvorkin J., Nur A., Yin H., 1994: Effective properties of cemented granular materials.- Mechanics of materials, v. 18., p. 351-366.

Dvorkin J., Nur A., 1996: Elasticity of high-porosity sandstones - Theory for two North Sea Datasets.- Geophysics, v. 61, p. 1363-1370.

Dvorkin J., Brevik I., 1999: Diagnosing high-porosity sandstones - Strength and permeability from porosity and velocity.- Geophysics, v. 64, p. 795-799.

Dvorkin J., Gutierrez M., Nur A., 2002: On the universality of diagenetic trends.- The Leading Edge, v. 21, p. 40-43.

Eberhardt-Phillips D., Han D.-H., Zoback M.D., 1989: Empirical relationships among seismic velocity, effective pressure, porosity and clay content in sandstones.- Geophysics, v. 54, p. 82-89.

Edmundson H.N., Raymer, L.L., 1979: Radioactive logging parameters of common minerals.- 20th SPWLA Annual Logging Symposium, Tulsa, 1979, p. 1-20.

Ehrenberg N., 1989: Assessing the relative importance of compaction, processes and cementation to reduction of porosity in sandstones - discussion; compaction and porosity evolution of Pliocene sandstones, Ventura Basin, California - discussion.- AAPG Bull., v. 73, p. 1274-1276.

Ehrlich R., Kennedy S.K., Crabtree S.J., Cannon R.L., 1984: Petrographic image analysis 1. Analysis of reservoir pore complexes.- J. Sed. Petrol., v. 54, p. 1365-1378.

Endres A.L., Knight R., 1991: The effects of pore-scale fluid distribution on the physical properties of partially saturated tight sandstones.- J. Applied Phys., v. 9, p. 1091-1098.

Engelhardt W.V., 1960: Der Porenraum der Sedimente.- Springer-Verlag, Berlin, 207 p.

Fauzi U., 1997: Untersuchungen zur Charakterisierung der Porengeometrie von Gesteinen zur Abschätzung der hydraulischen Permeabilität und des Formationsfaktors mit Hilfe von Bildanalysen.- Mitteilungen aus dem Institut für Geophysik und Meteorologie der Universität zu Köln, v. 113, 174 p.

Fisher Q.J., Casey M., Clennell M.B., Knipe R.J., 1999: Mechanical compaction of deeply buried sandstones of the North Sea.- Marine and Petroleum Geology, v. 16, p. 605-618.

Folk R.L., Ward W.C., 1957: Brazos river bar - a study of significant grain size parameters.- J. Sediment. Petrol., v. 27, p. 3-26.

Fricke S., Schön J., 1999: Praktische Bohrlochgeophysik.- Enke im Georg Thieme Verlag, Stuttgart, 267 p.

Füchtbauer H., 1967: Der Einfluß des Ablagerungsmilieus auf die Sandstein-Diagenese im Mittleren Buntsandstein.- Sediment. Geol., v. 1, p. 159-179.

Füchtbauer H., 1988: Sedimente und Sedimentgesteine.- Schweizerbart'sche Verlagsbuchhandlung, Stuttgart, 1141 p.

Fukushima E., Roeder S.B.W., 1981: Experimental Pulse NMR - A Nuts and Bolts Approach.- Addison-Wesley Publishing Company, Reading, New Jersey, 539 p.

Gast R., 1988: Rifting im Rotliegend Niedersachsens.- Die Geowissenschaften, v. 6, p. 115-122.

Gast R., 1991: The Perennial Rotliegend Saline Lake in NW-Germany.- Geol. Jb., A 119, p. 25-59.

Gaupp R., Liermann N., Pusch G., 2004: Adding value through Integrated Research to Unlock the Tight Gas Potential in the Rotliegendes Formation of North-Germany.- 14th Europec Biennal Conference, Spain, Madrid, 13-16 June, 2004, 9 p., abs.

Gaupp R., Matter A., Platt J., Ramseyer K., Walzebuck J.P., 1993: Diagenesis and Fluid Evolution of Deeply Buried Permian (Rotliegend) Gas Reservoirs, Northwest Germany.- AAPG Bull., v. 77, n. 7, p. 1111-1128.

Gaupp R., 1996: Diagenesis types and their application in diagenesis mapping.- Zbl. Geol. Paläont., Teil 1, 1994, 11/12, p. 1183-1199.

Gaupp R., 2005: Model conclusions.- in: Gaupp et al. (2005), eds., Paleo Oil- and Gasfields in the Rotliegend of the North German Basin - Effects upon Hydrocarbon Reservoir Quality.- DGMK Forschungsbericht 593-8, DGMK, Hamburg, 212 p., p. 5.1-5.17.

Gaupp R., Solms M., 2005: Sedimentological and Petrological Investigations.- in: Gaupp et al. (2005), eds., Paleo Oil- and Gasfields in the Rotliegend of the North German Basin - Effects upon Hydrocarbon Reservoir Quality.- DGMK Forschungsbericht 593-8, DGMK, Hamburg, 212 p.: p. 1.1 -1.44.

Gaupp R., Solms M., Baunack C., Pudlo D., Trappe H., Schubarth-Engelschall J., Littke R., Schwarzer D., Oncken O., Krawczyck C., Tanner D., 2005: Paleo Oil- and Gasfields in the Rotliegend of the North German Basin - Effects upon Hydrocarbon Reservoir Quality.- DGMK Forschungsbericht 593-8, DGMK, Hamburg, 212 p.

Gebrande H., Kern H., Rummel F., 1982: Elasticity and inelasticity.- in: K.-H. Hellwege, Landolt-Börnstein F., eds., Numerical Data and Functional Relationships in Science and Technology, New Series, Group V.- Physical Properties of Rocks, Springer-Verlag, Berlin, 233 p.

Georgi D.T., Menger S.K., 1994: Reservoir quality, porosity and permeability relationships.- Trans. 14, Mintrop Seminar, DGMK and Ruhr Universität Bochum, p. 163/1-163/35, abs.

German Stratigraphic Commission, 2002: Stratigraphic Table of 2002.- German Stratigraphic Commission, Potsdam, p. 16.

Gist G.A., 1994: Interpreting laboratory velocity measurements in partially gas-saturated rocks.- Geophysics, v. 59, p. 1100-1109.

Gopa S., Winterstein D.F., Meadows M.A., 1994: Comparison of P- and S-wave velocities and Q's from VSP and sonic log data.- Geophysics, v. 59, p. 1512–1529.

Gordon R.B., Davis L.A., 1968: Velocity and attenuation of seismic waves in imperfectly elastic rock.- J. Geophys. Res., v. 73, p. 3917-3935.

Gralla P., 1988: Das Oberrotliegende in NW-Deutschland - Lithostratigraphie und Faziesanalyse.- Geol. Jb., A 106, 56 p.

Gregory A.R., 1976: Fluid saturation effects on dynamic elastic properties of sedimentary rocks.- Geophysics, v. 41, p. 895-921.

Grill W., Hillmann K., Würz K.U., Wesner J., 1996: Scanning Ultrasonic Microscopy with Phase Contrast.- in: Briggs A., Arnold W., Advances in Acoustic Microscopy.- Plenum Press, New York, p. 167-218.

Guéguen Y., Dienes J., 1989: Transport properties of rocks from statistics and percolation.- Mathematical Geology, v. 21, n. 1, p. 1-13.

Guéguen Y., Bouteca M., 2004: Mechanics of fluid saturated rocks.- Elsevier Science and Technology, New York, 450 p.

Hamilton E.L., 1970: Sound velocity and related properties of marine sediments, North Pacific.- J. Geophys. Res., v. 75, n. 23, p. 4423-4446.

Han D.-H, Nur A., Morgan F.D., 1986: The effects of porosity and clay content on wave velocities in sandstones.- Geophysics, v. 51, p. 2093-2107.

Harrell J.A., 1981: Measurement errors in thin-section analysis of grain packing.- Jour. Sed. Petrology, v. 51, p. 674-676.

Harris D., Pan G., 1999: Mineral Favourability Mapping - A Comparison of Artificial Neural Networks, Logistic Regression, and Discriminant Analysis.- Nat. Resour. Res., Springer-Verlag, Berlin, v. 8, n. 2, p. 93-109.

Hart B.S., Engler T., Pearson R., Robinson R.L., 2003: 3-D Seismic Horizon - Based Approaches to Fracture-Swarm Sweet Spot.- AAPG International Conference Barcelona, September 21-24, 2003, abs.

Hartung M., Heinke J., Reichel B., 1993: Evaluating gas in-place from 3D seismic data - Rotliegend formation, North-Germany.- First Break, v. 11, p. 241-245.

Hearst J.R., Nelson P.H., Paillet F.L., 1985: Well Logging for Physical Properties.- A handbook for Geophysists, Geologists, and Engineers.- John Wiley and Sons, New York, 483 p.

Helbig K., Treitel S.,2001: Handbook of geophysical exploration: Seismic exploration.- Pergamon Press, Amsterdam, p. 436.

Helle H.B., Bhatt A., 2002: Fluid saturation from well logs using committee neural networks Source-Petroleum Geosciences.- Geol. Soc., v. 8, n. 2, p. 109-118.

Helmuth H.-J., Süssmuth S., 1993: Die lithostratigraphische Gliederung des jüngeren Oberrotliegenden (Oberrotliegendes II) in Nordostdeutschland.- Geol. Jb., A 131, p. 31-55.

Hillmann K., Grill W., Bereiter-Hahn J., 1994: Determination of ultrasonic attenuation in small samples of solid material by scanning acoustic microscopy with phase contrast.- J. of Alloys and Compounds, v. 211-212, p. 625-627.

Hirsekorn S., Pangraz S., 1994: Materials characterization with the acoustic microscope.- Appl. Phys. Lett., v. 64, p. 1632 – 1634.

Hoffmann N., Kamps H.-J., Schneider J., 1989: Neuerkenntnisse zur Biostratigraphie und Paläodynamik des Perms in der Nordostdeutschen Senke - ein Diskussionsbeitrag.- Z. angew. Geol., v. 35, p. 198-207.

Houseknecht D.W., 1987: Assessing the relative importance of compaction processes and cementation to reduction of porosity in sandstones.- AAPG Bull., v. 71, p. 633–642.

Howard J.J., Kenyon W.E, Straley C., 1991: Proton-magnetic-resonance and pore-size variations in reservoir sandstones.- SPE Formation Evaluation, v. 8, n. 3, p. 194-200.

Howarth R.J., 1998: Improved estimators of uncertainty in proportions, point counting, and pass-fail test results.- Am. J. Sc., v. 298, p. 594-607.

Hower J., Mowatt T.C., 1966: The mineralogy of illites and mixed-layer illite / montmorillonites.- American Mineralogist, v. 51, p. 825-854.

Hughes E.R., Leighton T.G., Petley G.W., White P.R., Chivers R.C., 2003: Estimation of critical and viscous frequencies for Biot theory in cancellous bone.- Ultrasonics, 41, n. 5, p. 365-368.

Hürlimann M.D., 1998: Effective gradients in porous media due to susceptibility differences.- J. Magn. Reson., v. 131, p. 232-240.

Hyne N.J., 1991: Dictionary of Petroleum Exploration, Drilling and Production.- PennWell Publish. Corp., Tulsa, 625 p.

James N.P., Choquette P.W., 1986: Diagenesis 6, Limestones - The sea floor diagenetic environment.- Geoscience Canada, v. 10, p. 162-178.

Jennings J.B., 1987: Capillary pressure techniques - application to exploration and development geology.- AAPG Bulletin, v. 71, p. 1196-1209.

Jones F.O., Owens W.W., 1980: A Laboratory Study of Low-Permeability Gas Sands.- J. Petr. Techn., v. 32, n. 9, p. 1631-1640.

Johnston D.H., Toksöz M.N., Timur A., 1979: Attenuation of seismic waves in dry and saturated rocks, II mechanisms.- Geophysics, v. 44, p. 691-711.

Johnston D.H., Toksöz M.N., 1981: Definitions and terminology.- in: Toksöz M.N., Johnston D.H., eds., Seismic Wave Attenuation.- SEG, Geophysics Reprint Series, n. 2, p. 1-5.

Katahara K., 1996: Clay mineral elastic properties, 66th SEG Annual Meeting and International Exhibition, Denver, Expanded technical programme, abs.

Kendall M.G., Moran P.A.P., 1963: Geometrical propability.- Hafner Publishing Company, New York, 125 p.

Kenyon W.E., 1992: Nuclear magnetic resonance as a petrophysical measurement.- Nuclear Geophysics, v. 6, n. 2, p. 153–171.

Killops S.D., Killops V.J., 1993: An Introduction to Organic Geochemistry.- John Wiley and Sons, New York, 265 p.

King M.S., 1966: Wave velocities as a function of overburden pressure and pore fluids.- Geophysics, v. 21, p. 739-754.

Kleinberg R.L., Horsfield M.A., 1990: Transverse relaxation progresses in porous sedimentary rock.- J. Magn. Reson., v. 88, p. 9-19.

Klimentos T., McCann C., 1990: Relationships between compressional wave attenuation, porosity, clay content, and permeability of sandstone.- Geophysics, v. 55, p. 998-1014.

Klimentos T., 1991: The effects of porosity-permeability-clay content on the velocity of compressional waves.- Geophysics, v. 56, p. 1930-1939.

Knight R., Dvorkin J., Nur A., 1998: Acoustic signatures of partial saturation.- Geophysics, v. 63, p. 132-138.

Knopoff L., 1964: Q.- Rev. Geophysics, v. 2, p. 625-660.

Knopoff L., 1965: Attenuation of elastic waves in the Earth,.- in: Mason, W.S., ed., Physical Acoustics.- Academic Press, New York, p. 287-324.

Kocurek G., Havholm K.G., 1993: Eolian sequence stratigraphy - a conceptual framework.- in: Weimer P., Possamentier H.W., eds., Siciliclastic Sequence Stratigraphy.- AAPG Mem., Tulsa, v. 58, p. 393-409.

Kohonen T., 1988: Self-Organization and Associative Memory.- Springer-Verlag, Heidelberg, 312 p.

Kowallis B.J., Jones L.E.A., Wang H.F., 1984: Velocity-porosity-clay content systematics of poorly consolidated sandstones.- J. Geophys. Res., v. 89, p. 10355-10364.

Kozeny J., 1927: Über kapillare Leitung des Wassers im Boden.- Sitzungsber. Akad. Wiss. Wien, v. 136, p. 271–306.

Kuster G.T., Toksöz M.N., 1974: Velocity and attenuation of seismic waves in two-phase media - part 1. Theoretical formulations.- Geophysics, v. 39, p. 587-606.

Lemmons R.A., Quate C.F., 1974: Acoustic microscope - scanning version.- Appl. Phys. Lett., v. 24, p. 163.

Liewig N., Clauer N., 2000: K-Ar dating of varied microtextural illite in Permian gas reservoirs, northern Germany.- Clay Minerals, v. 35, n. 1, p. 271-281.

Lindseth R.O., 1982: Digital processing of geophysical data - a review.- Continuing Education Program, SEG, Yale, 282 p.

Liu X., Dvorkin J., Nur A., 1991: The effect of intergranular cementation on rock properties - experimental study.- AGU Annual Meeting San Francisco, December, 1991, abs.

Lockner D.A., Walsh J.B., Byerlee J.D, 1977: Changes in seismic velocity and attenuation during deformation of granite.- J. Geophys. Res., v. 82, n. 33, p. 5374-5378.

Lokhorst A., 1998: NW-European Gas Atlas - Composition and Isotope ratios of Natural Gas-NITG-TNO.- National Geological Survey, Haarlem, CD.

Lucet N., 1989: Vitesse et attenuation des ondes elastiques, soniques et ultrasoniques dans les roches sous pression de confinement, Ph.D. thesis, University of Paris.

Malischewsky P.G., Schnapp J.-D., 2004: Oberflächenwellen und Materialprüfung aus seismologischer Sicht.- DGZfP Jahrestagung 2004, Salzburg, Berichtsband BB89, CD 1-7.

Marks S.G., McCann C., Oliver J.S., Sothcott J., 1992: Compressional wave quality factors of reservoir sandstone at 50 Hz and 1 MHz, 54th Meeting EAEG, Paris 1992, p. 338-339, abs.

Matheron G., 1975: Random sets and integral geometry.- John Wiley and Sons, New York, 261 p.

Mathisen M.E., Budny M., 1990: Seismic lithostratigraphy of deep subsalt Permo-Carboniferous gas reservoirs, NW-German Basin.- Geophysics, v. 55, p. 1357-1365.

Mavko G., Nur A., 1975: Melt squirt in the asthenosphere.- J. Geophys. Res., v. 80, p. 1444-1448.

Mavko G., Nur A., 1979: Wave attenuation in partially saturated rocks.- Geophysics, v. 44, p. 161-178.

Mavko G., Nolen-Hoeksema R., 1994: Estimating seismic velocities at ultrasonic frequencies in partially saturated rocks.- Geophysics, v. 59, p. 252-258.

McBride E.F., Diggs T.N., Wilson J.C., 1991: Compaction of Wilcox and Carrizo sandstones (Paleocen-Eocene) to 4420 m, TX Gulf coast, Jour. Sed. Petrology, v. 61, p. 73-85.

McCann C., McCann D.M., 1985: A theory of compressional wave attenuation in non cohesive sediments.- Geophysics, v. 50, p. 1311-1317.

McNally G.H., 1987: Estimation of coal measures rock strength using sonic and neutron logs.- Geoexploration, v. 24, p. 381-395.

Melas F.F., Friedman G.M., 1992: Petrophysical characteristics of the Jurassic Smackover Formation, Jay Field.- AAPG Bulletin, v. 76; n. 1, p. 81-100.

Minear J.W., 1982: Clay models and acoustic velocities.- SPE 57th Annual Tech. Conf. and Exhib., New Orleans, September 27-29, 1982, abs.

Moore W.R., 1975: Grain packing-porosity relationships of Minnelusa sandstones, Powder River Basin, Wyoming.- The Mount. Geol., v. 12, n. 2, p. 45-53.

Mountney N.P., Thompson D.B., 2002: Aeolian dune and damp/wet interdune sedimentation - an example from the Triassic Helsby Sandstone Formation, Cheshire Basin.- Sedimentology, v. 49, p. 805-833.

Mowers T.T., Budd D.A., 1996: Quantification of porosity and permeability reduction due to calcite cementation using computer-assisted petrographic image analysis techniques.- AAPG Bulletin, v. 80, p. 309-322.

Murphy W.F., 1982: Effects of partial water saturation on attenuation in Massilon sandstones and Vycor porous glass.- J. Acous. Soc. Am., v. 71, n. 6, p. 1458-1468.

Murphy W.F., 1984: Acoustic measures of partial gas saturation in tight sandstones.- J. Geophys. Res., v. 89, p. 11549-11559.

Murphy W.F., Winkler K.W., Kleinberg R.L., 1984: Frame modulus reduction in sedimentary rocks - The effect of adsorption at grain contacts.- Geophys. Res. Lett., v. 11, p. 805-808.

Murphy W.F., Winkler K.W., Kleinberg R.L., 1986: Acoustic relaxation in sedimentary rocks - Dependence on grain contacts and fluid saturation.- Geophysics, v. 51, p. 757–766.

O'Brien J.J., Lerche I., 1988: Impact of heat flux anomalies around salt diapirs and salt sheets in the Gulf Coast on hydrocarbon maturity.- Gulf Coast Association of Geologic Societies, v. 58, p. 231-243.

O'Connell R.J., Budiansky B., 1974: Seismic velocities in dry and saturated cracked solids.- J. Geophys. Res., v. 79, p. 5412-5426.

O'Connell R.J., Budiansky B., 1977, Viscoelastic properties of fluid-saturated cracked solids.- J. Geophys. Res., v. 82, p. 5719-5736.

O'Connell R., Budiansky B., 1978: Measures of dissipation in viscoelastic media.- Geoph. Res. Lett., p. 1-8.

O'Connell R.J, 1984: A Viscoelastic Model of Anelasticity of Fluid Saturated Porous Rocks - Physics and Chemistry of Porous Media.- Amer. Inst. Phys., Spec. Publ., p. 166-175.

Øren P.E., Antonsen F., Rueslåtten H.G., Bakke S., 2002: Numerical simulations of NMR-responses for improved interpretations of NMR-measurements in reservoir rocks.- 77th Annual Technical Meeting, San Antonio, 30 September-3 October, 2002, abs.

Palmer I.D., Traviola M.L, 1981: Attenuation by squirt flow in under-saturated gas sands.- Geophysics, v.45, p. 1780-1792.

Panda M.N., Lake L.W., 1994: Estimation of single-phase permeability from the parameters of a particle-size distribution.- AAPG Bulletin, v. 78, n. 7, p. 1028-1039.

Pandit B., Savage J.C., 1973: Experimental test of Lomnitz's theory of internal friction in rocks.- J. Geophys. Res., v. 78, p. 6097– 6099.

Pape H., Riepe L., Schopper J.R., 1985: Permeability from Porous Rocks Derived from Internal Surface.- 47th EAEG-Meeting 1985, Budapest, abs.

Pape H., Riepe L., Schopper J.R., 1987: Theory of self-similar network structures in sedimentary and igneous rocks and their investigation with microscopical and physical methods.- J. Micros., v. 148, p. 121-147.

Pape H., Clauser C., Iffland J., 1999: Permeability prediction for reservoir sandstones based on fractal pore space geometry.- Geophysics, v. 64, p. 1447-1460.

Parasnis D.S., 1997: Principles of Applied Geophysics.- Chapman and Hall, London, 429 p.

Pasternak M., Kosinowski M., Lösch J., 2001: Petroleum and Natural Gas in the Federal Republic of Germany - Geological Survey of Lower Saxony, Schweizerbart'sche Verlagsbuchhandlung, Hannover, 53 p.

Pettijohn F.J., Potter P.E., Siever R., 1972: Sand and Sandstone.- Springer-Verlag, Berlin, 618 p.

Pettijohn F.J., 1975: Sedimentary rocks.- Harper and Row, New York, 628 p.

Pham N., Carcione J.M., Helle H., Ursin B., 2002: Wave velocities and attenuation of shaly sandstones as a function of pore pressure and partial saturation.- Geophysical Prospecting, v. 50, p. 615-627.

Philipp W., Reinicke K.M., 1982: Zur Entstehung und Erschließung der Gasprovinz Osthannover.- Erdöl-Erdgas, v. 98, p. 85–90.

Pittman E.D., 1971, Microporosity in carbonate rocks.- AAPG Bull., v. 55, p. 1873–1881.

Pittman E.D., 1992: Relationship of porosity and permeability to various parameters derived from mercury injection - capillary pressure curves for sandstones.- AAPG Bulletin, v. 51, p. 191-198.

Platt J., 1991: The diagenesis of early Permian Rotliegend deposits from Northwest-Germany.- doctoral thesis, University of Bern, 367 p.

Platt J., 1993: Controls on clay mineral distribution and chemistry in the early Permian Rotliegend of Germany.- Clay Min., v. 28, p. 393-416.

Plein E., 1994: Deutschland / Germany.- in: Kulke H., ed., Regional Erdöl- und Erdgasgeologie der Erde, Teil I: Europa und Asien.- Gebrüder Bornträger, Berlin, p. 139-191.

Plein E., 1995: Norddeutsches Rotliegendbecken, Rotliegend-Monographie, Teil II.- Courier Forschungs Institut Senckenberg, Frankfurt a. M., 193 p.

Pointer T., Liu E., Hudson J.A., 2000: Seismic wave propagation in cracked porous media.- Geophys. J. Int., v. 142, p. 199-231.

Porwal A., Carranza E.J.M., Hale M., 2003: Artificial Neural Networks for Mineral-Potential Mapping - A Case Study from Aravalli Province, Western India.- Nat. Resour. Res., Springer-Verlag, Berlin, v. 12, n. 3, p. 155-171.

Post J.L., Plummer C.C., 1972: Chlorite series of the Flagstaff Hillarea, California - a preliminary investigation.- Clays and Clay Minerals, v. 20, p. 271-283.

Prasad M., Manghnani M. H., Siegesmund S., 1994: Velocity and attenuation characteristics of selected KTB core samples.- Scientific Drilling, v. 4, p. 221-231.

Prasad M., Manghnani H., 1997: Effects of pore and differential pressure on compressional wave velocity and quality factor in Berea and Michigan sandstones.- Geophysics, v. 62, p. 1163-1176.

Prasad M., Palafox G., Nur A., 1999: Velocity and attenuation characteristics of Daqing sandstones - Effects of permeability on velocity and attenuation anisotropy.- EOS, v. 80, F963.

Prasad M., 2001: Mapping impedance microstructure in rocks with acoustic microscopy.- The Leading Edge, v. 20, n. 2, p. 172-179.

Prasad M., 2003: Correlating Permeability with Velocity using Flow Zone Indicators.- Geophysics, v. 68, p. 108-117.

Prasad M., Kopycinska M., Rabe U., Arnold W., 2002: Measurement of Young's modulus of clay minerals using Atomic Force Acoustic Microscopy.- Geophys. Res. Lett., v. 29, n. 8, p. 1-4.

Pride S.R., Harris J., Johnson D.L., Mateeva A., Nihei K., Nowack R.L., Rector J., Spetzler H., Wu R., Yamomoto T., Berryman J., Fehler M., 2003: Permeability dependence of seismic amplitudes.- The Leading Edge, v. 22, n. 6, p. 518-525.

Pryor W.A., 1973: Permeability-Porosity Patterns and Variations in some Holocene Sand Bodies.- AAPG Bulletin, v. 57, p. 162-189.

Purcell W.R., 1949: Capilary pressures - their measurements using mercury and the calculation of permeability therefrom.- AIME, Petroleum transactions, p. 39-48.

Raymer L.L., Hunt E.R., Gardner J.S., 1980: An improved sonic transit time - to - porosity transform.- SPWLA, 21st Ann. Logg. Symp., July 1980, p. 1-12, abs.l

Reynolds J.M., 1997: An introduction to applied and environmental geophysics.- John Wiley and Sons, Chichester, London, 806 p.

Rifai H., Kappes R., Wonik T., 2005: Beschreibung und Bedienung des Kernmagnetischen Resonanzspektrometers 'Maran Ultra 5'.- Institut GGA, Hannover, Bericht, Archiv-Nr. 125640, 35 p.

Rink M., 1976: A computerized quantitative image analysis procedure for investigating features and an adaptive image process.- J. Microsc., v. 107, n. 3, p. 267–286.

Ritter H., Martinetz T., Schulten K., 1991: Neuronale Netze.- Addison-Wesley, Bonn, 325 p.

Rosenfeld M.A., 1949: Some aspects of porosity and cementation.- Prod. Month., v. 13, p. 39-42.

Rossel N.C., 1982: Clay mineral diagenesis in Rotliegend aeolian sandstones of the southern North sea.- Clay. Min., v. 17, p. 69-77.

Rowe J., Burley S.D., 1997: Faulting and porosity modification in the Sherwood Sandstone at Alderely Edge, northeastern Cheshire - an exhumed example of fault-related diagenesis.- in: Meadows N.S., Trueblood S.P., Hardman M., Cowan G., eds., Petroleum geology of the Irish Sea and adjacent areas.- Geol. Soc. Spec. Publ., v. 124, p. 325-352.

Rummerfield N.F., 1954: Reflection quality, a fourth dimension.- Geophysics, v. 29, p. 684-694.

Russell B., Hampson D., Todorov T., Lines L., 2002: Combining geostatistics and multi-attribute transforms - a channel sand case study, Blackfoot oilfield (Alberta).- J. Petr. Geol., v. 25, n. 1, p. 97-117.

Ruzyla K., 1986: Characterization of pore space by quantitative image analysis.- Formation Evaluation, v. 1, p. 389-398.

Schoder L., Plein E., Bachmann G.H., Gast R.E., Gebhardt U., Graf R., Helmuth H.-J., Pa-. sternak M., Porth H., Süssmuth S., 1995: Stratigraphische Neugliederung des Rotliegend im Norddeutschen Becken.- Geol. Jb., A 148, 21 p.

Scheidegger A.E., 1974: The physics of flow through porous media.- Univ. of Toronto Press, 313 p.

Schlumberger Educational Services, 1991: Log Interpretation Principles/Applications, Schlumberger manual.- Schlumberger Educational Services, 171 p.

Schön J.H., 1983: Petrophysik.- Enke Verlag, Stuttgart, p. 405.

Schön J.H., 1998: Physical Properties of Rocks.- in: Helbig K., Treitel S., eds., Handbook of Geophysical Exploration.- Elsevier Science and Technology, Oxford, v. 18, 583 p.

Schöner R., 2006: Comparison of Rotliegend sandstone diagenesis from the northern and southern margin of the North German Basin, and implications for the importance of organic maturation and migration.- doctoral thesis, Friedrich-Schiller-University, Jena, 160 p.

Schopper, J.R., 1972: Theoretische Untersuchung elektrischer, hydraulischer und anderer physikalischer Eigenschaften poröser Gesteine mit Hilfe statistischer Netzwerkmodelle.- post doctoral lecture qualification, Technische Universität, Clausthal.

Schopper J.R., 1982: Porosity and permeability.- in: Physical Properties of Rocks, G. Angenheister, ed., Springer-Verlag, Berlin, v. 1a, p. 184-193.

Schowalter T.T., 1979: Mechanics of secondary hydrocarbon migration and entrapment.- AAPG Bulletin, v. 63, p. 723-760.

Schwarzer D., Littke R., 2005: Petroleum Systems Modelling.- in: Gaupp et al. (2005), eds., Paleo Oil- and Gasfields in the Rotliegend of the North German Basin - Effects upon Hydrocarbon Reservoir Quality.- DGMK Forschungsbericht 593-8, DGMK, Hamburg, 212, p. 3.1-3.58.

Serra O., 1984 a: Fundamentals of well-log interpretation.- Elsevier Science and Technology, Amsterdam, v. 1, 340 p.

Serra O., 1984 b: Fundamentals of well-log interpretation.- Elsevier Science and Technology, Amsterdam, v. 2, 337p.

Shanley K.W., Cluff R.M., Robinson J.W., 2004: Factors controlling prolific gas production from low-permeability sandstone reservoirs - Implications for resource assessment, prospect development, and risk analysis.- AAPG Bulletin, v. 88, n. 8, p. 1083-1121.

Sheriff R.E., 1991: Encyclopedic Dictionary of Exploration Geophysics.- SEG, Yale, 384 p.

Slawinski M.A., 2002: Seismic Waves and Rays in Elastic Media (Seismic Exploration Series).- in: Treitel S., Helbig K., eds., Handbook of Geophysical Exploration.- Pergamon Press, Oxford, v. 34.

Smith D.A., 1966: Theoretical considerations of sealing and non-sealing faults.- AAPG Bulletin, v. 50, p. 363-374.

Soeder D.J., Randolph P.L., 1987: Porosity, permeability, and pore structure of the tight Mesaverde Sandstone, Piceance Basin, Colorado.- SPE Formation Evaluation, v. 2, n. 6, p. 129–136.

Soeder D.J., Chowdiah P., 1990: Pore Geometry in High and Low Permeability Sandstones, Travis Peak Formation, East TX.- SPE Formation Evaluation, v. 5, p. 421-430.

Spetzler H.A.W., Anderson D.L., 1968: The effect of temperature and partial melting on velocity and attenuation in a simple binary system.- J. Geophys. Res., v. 73, n. 18, p. 6051-6060.

Stapf S., Han S.I., 2005: Nuclear Magnetic Resonance Imaging in Chemical Engineering.- Wiley-VCH, Weinheim, 610 p.

Straley C., Morris C.E., Kenyon W.E., Howard J.J., 1991: NMR in partially saturated rocks - Laboratory insights on free fluid index and comparison with borehole logs.- 32nd Ann. Logging Symp. Trans, Soc. Prof. Log Analysts, 25 p, abs.

Strauß C., Solms M., 2000: Reservoir Quality Prediction in the Northwest German Rotliegend.- DGMK Tagungsbericht 2000-2, DGMK-Frühjahrstagung des Fachbereichs Aufsuchung und Gewinnung, April 2000, Celle, p. 69-79.

Sun Y.F., 2004: Pore structure effects on elastic wave propagation in rocks - AVO modelling.- J. Geophys. Eng., v. 1, p. 268-276.

Swingler K., 2001: Applying neural networks: a practical guide.- Kaufman, San Francisco, p. 303.

Taner M.T., Sheriff R.E., 1977: Application of amplitude, frequency, and other attributes to stratigraphic and hydrocarbon determination.- in: Payton, C.E., ed., Applications to hydrocarbon exploration.- AAPG Memoir 26, Tulsa, p. 301-327.

Taner M.T., Köhler F., Sheriff R.E., 1979: Complex seismic trace analysis.- Geophysics, v. 44, p. 1041-1063.

Tanner D.C., Krawczyk C.M., Oncken O., 2005: Three-dimensional Structural Modelling.- in: Gaupp et al. (2005), eds., Paleo Oil- and Gasfields in the Rotliegend of the North German Basin - Effects upon Hydrocarbon Reservoir Quality.- DGMK Forschungsbericht 593-8, DGMK, Hamburg, 212 p., p. 2.1 -2.17.

Taylor J.M., 1950: Pore space reduction in sandstones.- AAPG Bulletin, v. 34, p. 701-716.

Tebo J.M., Hart B.S., 2005: Use of volume-based 3-D seismic attribute analysis to characterize physical property distribution - a case study to delineate reservoir heterogeneity at the Appleton Field, SW Alabama.- J. Sed. Res., v. 75, p. 723-735.

Terzaghi K., 1955: Influence of geological factors on the engineering properties of sediments.- Economic Geology, 50th Anniversary Volume, II, p. 557-618.

Theng B.K.G., 1974: The chemistry of clay-organic reactions.- John Wiley and Sons, Chichester, London, 343 p.

Thomeer J.H.M., 1960: Introduction of a pore geometrical factor defined by the capillary pressure curve.- J. Petr. Techn., v. 219, p. 73-77.

Tiab D., Erle D., 2004: Petrophysics - Theory and Practice of Measuring Reservoir Rock and Fluid Transport Properties.- Elsevier Science and Technology, Amsterdam, 880 p.

Timur A., 1977: Temperature dependence of compressional and shear wave velocities in rocks.- Geophysics, v. 42, p. 950–956.

Toksöz M.N., Cheng C.H., Timur A., 1976: Velocities of seismic waves in porous rocks.- Geophysics, v. 41, p. 621–645.

Toksöz M.N., Johnston D.H., Timur A., 1979: Attenuation of seismic waves in dry and saturated rock - I. Laboratory measurements.- Geophysics, v. 44, p. 681-690.

Toksöz M.N., Johnston D.H., 1981: Attenuation Mechanisms.- SEG, Geophysics Reprint Series, SEG Tulsa, p. 459.

Tosaya C., Nur A., 1982: Effects of diagenesis and clays on compressional velocities in rocks.- Geophys. Res. Lett., v. 9. p. 5-8.

Trappe H., Hellmich C., 1998: Seismic Characterization of Rotliegend Reservoirs - From Bright Spot to Stochastic Simulation.- First Break, v. 16, p. 79-87.

Trappe H., Hellmich C., 2000: Using neural network techniques to predict porosity thickness from 3D seismic.- First break, v. 18, p. 377-384.

Trappe H., Schubarth-Engelschall J., 2005: Three dimensional Seismic Special Processing and Interpretation.- in: Gaupp et al. (2005), eds., Paleo Oil- and Gasfields in the Rotliegend of the North German Basin - Effects upon Hydrocarbon Reservoir Quality.- DGMK Forschungsbericht 593-8, DGMK, Hamburg, 212 p., p. 4.1 -4.62.

Trappe H., Schubarth-Engelschall J., Laggiard E., technical note 14: Seismic Facies Classification of Deep Rotliegend Sandstones by Neural Network Technique.- http://www.teec.de/tech_note/Technical_Note_14/technical_note_14.html .

Trent B.C., 1991: Numerical simulation of wave propagation through cemented granular material.- in: Karamanlidis D., Stout R.B., eds., Wave propagation in granular media.- ASME, New York, p. 9-15.

Trent B.C., Margolin L.G., 1992: A numerical laboratory for granular solids.- Eng. Comp., v. 9, p. 191-197.

Tröger W.E., 1969: Optische Bestimmung der gesteinsbildenden Minerale, Teil 2.- Schweizerbart'sche Verlagsbuchhandlung, Stuttgart, 822 p.

Trusheim F., 1971: Zur Bildung der Salzlager im Rotliegenden und Mesozoikum Mitteleuropas.- Beiheft Geol. Jb, v. 112, p. 51.

Tucker M., 1993: The field description of sedimentary rocks.- John Wiley and Sons, Chichester, London, 112 p.

Tutuncu A.N., Podio A.L., Sharma M.M., 1994: An experimental investigation of factors influencing compressional- and shear wave velocities and attenuations in tight gas sandstones.- Geophysics, v. 59, p. 77-86.

Van Der Plas L., Tobi A.C., 1965: A chart for judging the reliability of point counting results.- Am. J. Sci., v. 263, p. 87–90.

Vanorio T., Prasad M., Nur A., 2003: Elastic properties of dry clay mineral aggregates, suspensions and sandstones.- Geophys. J. Int., v. 155, p. 319-326.

Vavra C.L., Kaldi J.G., Sneider R.M., 1992: Geological Applications of Capillary Pressure - A Review.- AAPG Bulletin, v. 76, p. 840-850.

Verdier J.P., 1996: The Rotliegend sedimentation history of the southern North Sea and adjacent countries. - In: Rondeel H.E., Batjes D.A.J., Nieuwenhuijs W.H., eds., Geology of gas and oil under the Netherlands.- Kluwer Academic Publishers, p. 45-56.

Wardlaw N.C., Taylor R.P., 1976: Mercury capillary pressure curves and the interpretation of pore structures and capillary behaviour in reservoir rocks.- Bulletin of Canadian Petroleum Geology, v. 24, p. 225-262.

Wang Z., Nur A., 1990: Wave velocities in hydrocarbon saturated rocks - Experimental results.- Geophysics, v. 55, p. 723-733.

Wang Z., Hirsche W.K., Sedgwick G., 1991: Seismic velocities in carbonate rocks.- J. Can. Pet. Tech., v. 30, n. 2, p. 112–22.

Wang Z., 2001: Fundamentals of seismic rock physics.- Geophysics, v. 66, p. 398-412.

Wang Z., Wang H., Cates M.E., 2001: Effective elastic properties of solid clays.- Geophysics, v. 66, p. 428-440.

Wardlaw N.C., 1976: Pore geometry of carbonates as revealed by pore casts and capillary pressure data.- AAPG Bulletin, v. 60, n. 2, p. 245-257.

Wardlaw N.C., Taylor R.P., 1976: Mercury capillary pressure curves and the interpretation of pore structure and capillary behaviour in reservoir rocks.- Bulletin of Canadian Petroleum Geology, v. 24, n. 2, p. 225-262.

Washburn E.W., 1921: Note on a method of determining the distribution of pore sizes in a porous material.- Proceedings of the National Academy of Science of the USA, Washington, v. 7, p. 115-116.

Waxman M.H., Smits L.J.M., 1968: Electrical conductivities in oil-bearing shaly sands.- SPE Journal, v. 8, p. 107-122.

Weaver C.E., Pollard L.D., 1975: The Chemistry of Clay Minerals.- Elsevier Scientific Publication Co., New York, 213 p.

White J.E., 1975: Computed seismic speeds and attenuation in rocks with partial gas saturation.- Geophysics, v. 40, p. 224-232.

Wilsom J.M., 2000: An introduction to applied and environmental geophysics.- John Wiley and Sons, Chichester, London, 796 p.

Wilson J.C., McBride E.F., 1988: Compaction and porosity evolution of Pliocene sandstones, Ventura Basin, California.- AAPG Bulletin, v. 72, n. 6, p. 664-681.

Winkler K., Nur A., 1978: Attenuation and velocity in dry and saturated Massilon sandstone.- 48th Annual Int. SEG Meeting, San Francisco, abs.

Winkler K., Nur A., 1979: Pore fluids and seismic attenuation in rocks.- Geophys. Res. Lett., v. 6. p. 1-4.

Winkler K, Nur A., 1982: Seismic attenuation - effects of pore fluids and frictional sliding.- Geophysics, v. 47, p. 1-15.

Winkler K., 1986: Estimates of velocity dispersion between seismic and ultrasonic frequencies.- Geophysics, v. 51, p. 183-189.

Wohlenberg J., 1982: Density.- in: Numerical data and functional relationships in science and technology, New Series;Group V.- Physical Properties of Rocks, subv. a, Springer-Verlag, Berlin.

Worden R.H., Heasley E.C., Barclay S.A., 1999: The effects of petroleum emplacement on diagenesis - a comparison between sandstone and carbonate reservoirs.- in: Transfert dans les systèmes sédimentaires de l'échelle du pore a celle du basin.- Sciences Géologiques, Strasbourg, Mémoire No. 100, p. 149-154.

Würz K.U., Wesner J., Hillmann K., Grill W., 1995: Determination of elastic constants using a Scanning Acoustic Microscope.- Z. Phys. B 97, 487.

Wyllie M.R.J., Gregory A.R., Gardner L.W., 1956: Elastic wave velocities in heterogeneous and porous media.- Geophysics, v. 21, p. 41-70.

Wyllie M.R.J., Gregory A.R., Gardner G.H.F., 1958: An experimental investigation of factors affecting elastic wave velocities in porous media.- Geophysics, v. 23, p. 459-493.

Wyllie M.R.J., Gregory A.R., Gardner G.H.F., 1962: Studies of elastic wave attenuation in porous media.- Geophysics, v. 27, p. 569–589.

Yilmaz Ö., 1987: Seismic data processing.- SEG, Investigations in Geophysics, Tulsa, n. 2, p. 526.

Yin C.S., Batzle M.L., Smith B.J., 1992: Effects of partial liquid/gas saturation on extensional wave attenuation in Berea Sandstone.- Geophys. Res. Lett., v. 19, p. 1399-1402.

Yin H., Dvorkin J., 1994: Strength of cemented grains.- Geophys. Res. Lett., v. 21, p. 903-906.

Yuan H.H., Swanson B.F., 1989: Resolving pore-space characteristics by rate-controlled porosimetry.- SPE Formation Evaluation, v. 4, p. 17-24.

Ziegler P., 1990: Geological Atlas of Western and Central Europe.- Geol. Soc. and Shell International Petroleum Maatschappij B.V., London, 239 p.

Ziegler K., Turner P., Daines S., eds., 1997, Petroleum geology of the Southern North Sea–Future potential: London, The Geological Society, Special Publication 123, 209 p.

Zinin p., Weise W., Lobkis O., Boseck S., 1997: The theory of three-dimensional imaging of strong scatterers in scanning acoustic microscopy.- Wave Motion, v. 25, n. 3, p. 213-236.

Appendix

Due to the large quantity of acquired data the bulk part of the information is adjoined in digital form. The written appendix comprises figures for explanation of the files and, whenever possible, some contents are also given in written format in order to ease rapid accessibility of the files. The CD's contain raw and processed data differentiated in folders according to the main chapters of the study. The appendix on the CD is structured as follows (fig. 1):

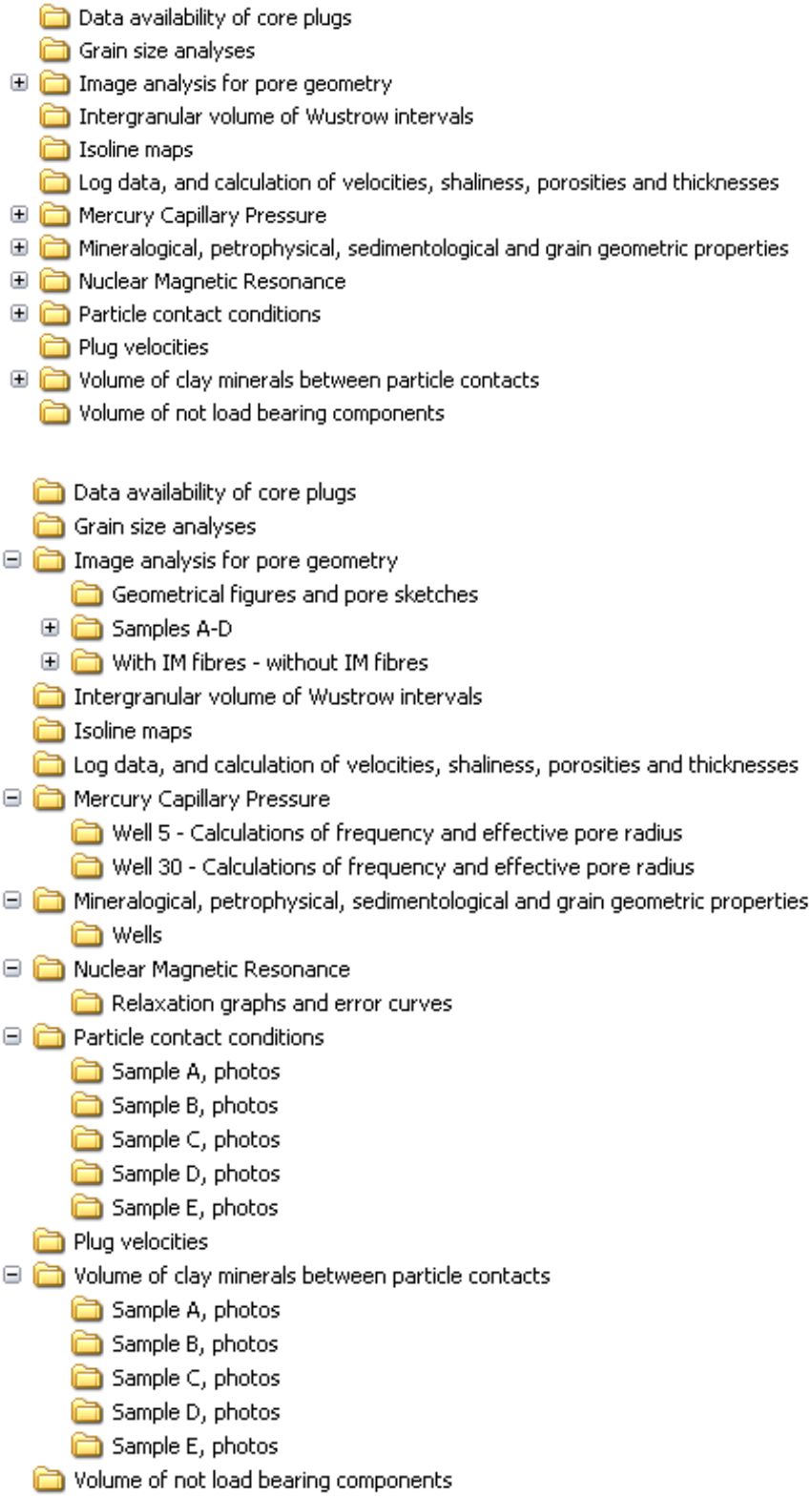

Fig. 1: Structure of digital appendix: above with main folders, below with sub- folders.

A-1: Data availability of core plugs

The following tables (tab. 1-5) list the type of data present of the available Wustrow core plugs. The plugs represent sand and siltstones from the dry and damp eolian and the mudflat/lake facies. The specimens derive from three wells of chlorite and illite authigenesis and red/yellow and blue/green facies classes respectively. The data on quantitative mineralogy and sedimentological characterisation are attained from the DGMK-database.

Label	Por., Perm. & Dens.	P-wave Vel.	Capillary Press.	Nucl. Magn. Res.	Rigidity & Perm. examinations	Quant. Mineral. & Sediment.
1010	x	x		x		
1019	x	x		x		
1020	x	x		x		
sample B / 1030	x	x			x	x
1040	x	x				
1050	x		x		x	
sample A / 1051	x	x			x	x
1060	x	x		x		
sample C / 1070	x	x			x	x
1080	x		x		x	
1089	x	x		x		
1090	x	x		x		x
1100	x		x		x	
1110	x		x		x	
1120	x	x		x		
1121	x	x				
1130	x	x		x		
1140	x		x		x	
2010	x	x		x		
2020	x	x		x		
2030	x		x		x	
2040	x		x		x	
2050	x		x		x	
2060	x		x		x	

Tab. 1: Data availability of core plugs from Well 30 of chlorite authigenesis

Label	Por., Perm. & Dens.	P-wave Vel.	Capillary Press.	Nucl. Magn. Res.	Rigidity & Perm. examinations	Quant. Mineral. & Sediment.
400	x					x
410	x					x
440	x				x	x
490		x				
500		x				
510	x	x				x
520		x				
530		x				
540		x			x	
541		x				
550		x				
560		x				
570	x	x		x	x	x
571		x				
580		x				
590		x				
591		x				

Tab. 2: Data availability of core plugs from Well 43 of illite authigenesis

Label	Por., Perm. & Dens.	P-wave Vel.	Capillary Press.	Nucl. Magn. Res.	Rigidity & Perm. examinations	Quant. Mineral. & Sediment.
610		x				
620		x				
621		x				
630		x				
640	x	x		x		x
650		x				
660		x				
661		x				
670		x				
710		x				
sample D / 720	x	x		x	x	x
721		x				
730		x			x	
740		x				
760		x				
761		x				
770	x	x		x	x	x
780		x				
790		x			x	
791		x				
800		x				
810		x				
821		x				
830		x				
850		x			x	
sample E / 860	x	x		x	x	x
880		x				
890	x	x		x		x
891		x				
900		x			x	
910		x				
911		x				
920		x				
930		x				
941		x				
950	x	x		x		x
1020		x			x	
1021		x				
1050	x					x
1091		x				
1100		x				
1160		x			x	
1181		x				
1210		x				
1240		x				
1250		x				
1280	x	x		x		x
1320	x			x		x
1350	x					x
1321		x				

Tab. 3: Data availability of core plugs from Well 43 of illite authigenesis – continuation

Label	Por., Perm. & Dens.	P-wave Vel.	Capillary Press.	Nucl. Magn. Res.	Rigidity & Perm. examinations	Quant. Mineral. & Sediment.
1020		x				
1021		x				
1030		x		x		
1040	x	x		x		x
1050		x				
1060		x				
1061		x				
1069	x		x		x	
1070	x	x		x		x
1079		x				
1080		x				
1090		x				
1099		x				
1100	x	x		x		x
1110		x				
1120		x				
1130	x	x		x		x
1140	x		x		x	
1141		x				
1150		x				
1160	x	x		x		x
1170		x		x		
1171		x				
1180		x				
1190	x	x		x		x
1200		x		x		
1201		x				
1210		x				
1220	x	x		x		x
1230		x				
1239		x				
1240		x				
1250	x	x				x
1259		x				
1260		x				
1270		x				
1280	x	x		x		x
1281	x		x		x	
1290		x				
1291		x				
1300		x				
1310	x	x		x		x
1320		x				
1321		x				
1330		x				
1340	x		x		x	x
1350		x				
1351		x				
1360		x		x		
1370	x		x		x	x
1380		x				
1381	x		x		x	
1390	x	x				x
1400		x				
1410	x		x		x	
1411	x		x		x	

Tab. 4: Data availability of core plugs from Well 5 of illite authigenesis.

Label	Por., Perm. & Dens.	P-wave Vel.	Capillary Press.	Nucl. Magn. Res.	Rigidity & Perm. examinations	Quant. Mineral. & Sediment.
1420		x				
1429	x		x		x	
1430	x	x		x		x
1440	x		x		x	
1441		x				
1450		x				
1459		x				
1460	x	x		x		x
1470		x				
1480		x				
1490	x		x		x	x
1500		x				
1510		x				
1520	x	x				x
1530	x		x		x	

Tab. 5: Data availability of core plugs from Well 5 of illite authigenesis - continuation

A-2: Clay minerals between particle contacts

The file ‘Clay minerals between particle contacts’ lists the raw data for the five samples.
The raw data represent the proportional lengths of particle contacts without clay minerals on the whole length of particle contacts.
The calculated amounts of load bearing clay minerals are given as average magnitudes and standard deviations.
The micro photographs and their image composites are listed in the folders ‘Sample A’, ‘Sample B’ etc. The long side length of a single microphotograph corresponds to 0,32 mm.
These microphotographs were also utilized for the analysis of the volume of not load bearing clay minerals.

A-3: Grain size analyses

The files ‘Sample A’, ‘Sample B’ etc. comprise the raw data and their average and standard deviations for grain sizes and aspect ratios for each sample. The calculations of sorting skewness and the graphs of all specimens are contained in the file ‘Sample C & parameters of all samples’.
The lengths of the grains are given as maximum extension of the particle and its perpendicular minimum dimension. The mean grain size represents the maximum length. The aspect ratio is calculated by the quotient of minimum to maximum extension.

A-4: Image analysis for pore geometry

The folder ’Micro photos’ comprises the microscopic images and the elaborated products of the samples. The bulk part of the file names have not been translated into English. Therefore some explanations are given:
The elaborated images are denoted as (tab. 6):

File name	Corresponds to picture after:
“sample name”, farben geändert “sample name”, verändert “sample name”, verändert-2 “sample name”, farben ersetzen	isolating the voids and correcting wrong processing
“sample name”, farben geändert, markiert “sample name”, verändert-2, markiert, binarisiert “sample name”, farben ersetzen, markiert	coding the voids and correcting wrong digitization

Tab. 6: Explanation of the file names.

Some file names contain the original labels of the samples: Sample A corresponds to ‘1051’, sample B to ‘1030’, sample C to ‘1070’, sample D to ‘720’, sample E to ‘860’.

The folder ‘photo composite’ comprises the compilation of the microphotographs as CorelDraw© and exported image files. In order to ease the image analysis for the software the composites were sectioned in photo stretches and denoted accordingly: ‘720, horizontal below’ corresponds to the lower photo stretch of the compilation (fig. 2).

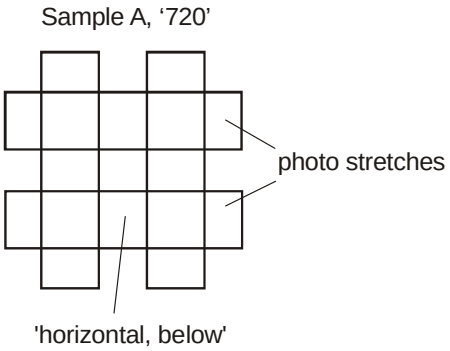

Fig. 2: Sketch of photo compilation for sample A. The compilation was sectioned into stretches for the software. The input files were denoted according to their position in the composite.

The folder ‘Raw data’ comprises the unprocessed data from ImageC© software as Excel files. As the data quantity for sample A exceeds the limiting capacity for the Excel-spreadsheet analysis the raw data file were partitioned and denoted with the extensions ‘a’, ‘b’, etc.

The folder ‘Spread sheet analysis’ comprises the calculation of parameters shown as tables and diagrams, and the frequency scales and final tables.
The files contain several attributes and graphical comparisons which were not covered in the written study. The files contain only relevant data of the corresponding parameter.
If not clearly specified, the files in the folders ‘Sample A’, ‘Sample B’, etc contain magnitudes which are not in measure. The correct values are presented in the folder ‘Frequency scales and final tables’.
The processing of the pore geometrical data derived by image analysis resulted labour intensive and complex. It was tried to render the adjoined files as comprehensible as possible for the reader. However a full understanding of the analysis is only feasible by long-time examination.
The following tables (tab. 7-9) exemplify the principal procedure of data elaboration.
The presented data were determined on sample B.

1030, 1, horizontal Area$	1030, 2, vertical, left Area$	1030, 3, vertical, right Area$
45,39	22,69	68,08
22,69	45,39	68,08
68,08	22,69	68,08
22,69	90,77	68,08
68,08	45,39	68,08
45,39	22,69	22,69
22,69	181,55	90,77
45,39	45,39	68,08
45,39	22,69	22,69
68,08	45,39	90,77
22,69	45,39	181,55
22,69	45,39	45,39
...	...	...

Amount of object	
57454	total
8626	>=3 dots
15,01	%

Table 7: Raw data of pore sizes from the 3 photo stretches. The data are not in measure. Relative proportion of objects of a size equal and larger three dots.

Pivot table				Average				
45,39	Anzahl von 45,39				Amount of obj k*l		% of all area	
22,69	45,39	Summe	68,080786	7122	23,45	484871,358	1,58	**1013**
68,08	22,693595	14304	90,774381	4544	14,96	412478,787	1,34	
22,69	45,387191	12774	113,467977	2392	7,87	271415,401	0,88	
68,08	68,080786	7122	136,16157	1716	5,65	233653,254	0,76	
45,39	90,774381	4544	158,85517	1238	4,08	196662,7	0,64	
22,69	113,467977	2392	181,54876	967	3,18	175557,651	0,57	
45,39	136,16157	1716	204,24236	738	2,43	150730,862	0,49	
45,39	158,85517	1238	226,93595	640	2,11	145239,008	0,47	
68,08	181,54876	967	249,62955	511	1,68	127560,7	0,41	
22,69	204,24236	738	272,32314	442	1,46	120366,828	0,39	
22,69	226,93595	640	295,24368	335	1,10	98906,6328	0,32	
...	...	...	...	...	...	...	...	

Table 8: Pivot table for sorting the objects by size and their amount and consequent calculation of average for objects equal and larger three dots.

Pivot table			Amount			Size classes
68,080786	7122	484871,358	19868	2198169,72	7,15	250
90,774381	4544	412478,787	2828	1032646,19	3,36	500
113,467977	2392	271415,401	2248	1636096,35	5,32	1000
136,16157	1716	233653,254	2038	2909642,76	9,46	2000
158,85517	1238	196662,7	987	2439062,7	7,93	3000
181,54876	967	175557,651	645	2238796,03	7,28	4000
204,24236	738	150730,862	350	1562327,64	5,08	5000
226,93595	640	145239,008	559	3420343,29	11,12	7500
249,62955	511	127560,7	271	2380912,86	7,74	10000
272,32314	442	120366,828	169	1865976,8	6,07	12500
295,24368	335	98906,6328	108	1488866,66	4,84	15000
317,93727	324	103011,675	73	1183088,84	3,85	17500
...	...	...	...	...	...	...

Tab. 9: Pivot table for sorting the objects by size and their amount and consequent calculation of frequency for pore size classes.

The folder ‘With and Without IM-fibres’ contains the data regarding the comparison of pore geometrical results for images, where the IM-fibres are coded as voids or as solid constituents. The files are ordered in the same structure as the files for samples A-D.

The folder ‘Geometrical figures and pore sketches’ comprises the raw data and analysis regarding the geometrical figures and the schematics of pores.

In case of an elaboration of the pore geometrical database the files should not be renamed as they are often interlinked.

A-5: Intergranular volume of Wustrow intervals

The file ‘Average intergranular volume of wells’ contains a list of average IGV’s for each well determined on thin sections of the Wustrow reservoir interval. The data derive from the DGMK database. The coordinates of the wells were not released from industry for public use.

A-6: Isoline maps

The folder ‘Isoline maps’ contains the data quantified by means of ‘Lithofacies Upscaling’ (Gaupp & Solms 2005) for:

Relative proportions in Wustrow horizon without upper shale beds of:
- Dry eolian facies
- Damp eolian facies
- The sum of dry and damp eolian facies corresponding to the reservoir unit
- Shale content
- Non reservoir unit

Non reservoir unit with upper shale beds
Number of shale beds within the reservoir unit
True vertical thickness of
- Wustrow reservoir
- Wustrow member

Average magnitude in reservoir unit of
- Porosity calculated from sonic logs
- Core permeability

The coordinates are not added as the locations of the wells are not released for public use.

A-7: Log data and calculation of velocity, shaliness, porosities and thicknesses

The log files contain raw data from Gamma Ray (GR), Sonic, density, neutron and caliper services for the whole stratigraphic Wustrow section. The logs were utilized to calculate shaliness, total and shale corrected porosities, compressional velocities and impedances, compressional velocities for dry, damp, non reservoir and shale lithologies, and relative thicknesses. The parameters were represented by average, minimum and maximum magnitudes and standard deviations. Shaliness was quantified by standard techniques presented in Schlumberger (1989). Total and shale corrected porosities were determined by means of the Raymer and Hunt equation (Raymer et al. 1980) and Wyllie (1956) for water saturated samples.
The data presentation in the digital files is exemplified on well 15 (tab. 10-13).

Depth	GR	Compr. slown.	Density	Caliper	Compr. velocity	Comp. impedance	Shaliness	Porosity
[m]	[gAPI]	[µs/m]	g/cm³	inch	[m/s]	[Rayl]	decimal	[%]
4640,51	168,581	217,099	2,63032	7,16023	4606	12115763	0,929	
4640,52	168,848	216,734	2,62892	7,16053	4614	12129707	0,930	
4640,53	169,114	216,37	2,62753	7,16083	4622	12143689	0,932	
4640,54	169,38	216,005	2,62614	7,16113	4630	12157774	0,934	
4640,55	169,646	215,64	2,62475	7,16143	4637	12171907	0,936	
4640,56	169,912	215,275	2,62336	7,16174	4645	12186088	0,938	
4640,57	170,178	214,911	2,62197	7,16204	4653	12200260	0,940	
...	...	...	...	...	...	...	...	...

Tab. 10: Raw data of wireline logs and calculated velocities, impedances and total porosities.

Porosity, shale corrected [%]	Compr. velocity GR < 49 [m/s]	Compr. velocity 49>GR<100 [m/s]	Compr. velocity GR<100 [m/s]	Compr. velocity 49>GR>100 [m/s]	Compr. velocity 49>GR>130 [m/s]	Compr. velocity 49>GR>150 [m/s]
				4606	4606	4606
				4614	4614	4614
				4622	4622	4622
				4630	4630	4630
				4637	4637	4637
				4645	4645	4645
				4653	4653	4653
...	...	...	...	...	...	...

Tab. 11: Calculated shale corrected porosities, and compressional velocities for well sections of different GR-intervals which correspond to specific lithologies.

	Density g/cm³	Velocity total [m/s]	Impedance total [Rayl]	Porosity [%]	Porosity, sh. corr. [%]	Velocity GR < 49	Velocity 49>GR<100 [m/s]	Velocity GR<100 [m/s]	Velocity 49>GR>100 [m/s]	Velocity 49>GR>130 [m/s]	Velocity 49>GR>150 [m/s]
Min.	2,36	3706	8780519	-0,337	-0,006	0	4107	0	4415	4415	4415
Max.	2,76	5313	14259248	0,192	0,187	4813	5313	5313	5288	5079	4729
Average	2,55	4578	11694179	0,104	0,075	4318	4670	4500	4883	4707	4545
St. dev.	0,10	341	1257135	0,033	0,046	344	261	351	252	208	60

Tab. 12: Statistic features for well log parameters.

GR-limit [gAPI]	Thickness total [m]	Thickness sand/siltsone [m]	Thickness shale+shaly [m]	Thickness sand/siltsone [%]	Thickness shale+shaly [%]
100	33,99	27,37	6,62	0,19	0,81
172					
35					

Tab. 13: Thickness in absolute and relative magnitudes for the shaly reservoir section and the non-reservoir unit and GR limits for the shale-free and shale layers.

A-8: Mercury Capillary Pressure

The file “Effective pore radius and Pore Throat Sorting (PTS)” comprises the raw data for the quantification of the parameters and their average, minimum and maximum magnitudes.
The file “Frequency scales of effective pore radius” contains the graphs for the proportions of the effective pore radius.
The file “Effective porosity, most frequent radius and effective pore radius” lists the average, minimum and maximum magnitudes of the parameters differentiated for the two wells and low and high porosity plugs.
The file “Effective pore radius and porosity & permeability” illustrates the relations of average pore throat to permeability and porosity.
The folder “Calculation of effective pore radius and capillary pressure curves” includes the whole raw data, the calculation of effective pore radius and the capillary pressure curves.
Some of the tables (tab. 14, 15) and graphs (fig. 3, 4) are presented below. The data were quantified on the chloritized sample 1050 from well 30.

Pressure [bar]	Eff. radius [µm]	S (Hg) [ ]	Pressure [bar]	Eff. radius [µm]	S (Hg) [ ]
1,56	4,714	0	12,631	0,582	0,01669
1,759	4,181	0,02051	15,251	0,482	0,01689
1,953	3,765	0,10732	18,421	0,399	0,01595
2,144	3,430	0,0985	22,131	0,332	0,01858
2,336	3,148	0,10232	26,231	0,280	0,01865
2,527	2,910	0,077	30,281	0,243	0,01616
2,714	2,710	0,04808	35,551	0,207	0,01668
2,898	2,537	0,04566	40,721	0,181	0,01468
3,08	2,388	0,0284	47,011	0,156	0,01623
3,262	2,254	0,02287	54,721	0,134	0,01317
3,619	2,032	0,03215	64,041	0,115	0,0142
3,963	1,856	0,02267	73,991	0,099	0,01167
4,467	1,646	0,02353	84,921	0,087	0,01117
4,942	1,488	0,01918	96,191	0,076	0,00965
5,643	1,303	0,0211	110,531	0,067	0,00812
6,729	1,093	0,01944	124,921	0,059	0,00711
8,242	0,892	0,0195	138,091	0,053	0,00457
10,121	0,727	0,01914			

Tab. 14: Data on pressure, effective pore radius and mercury volume; pressure range from 1,56 to 138,09 bar. Effective pore radius is derived by means of the Washburn equation (Washburn 1921) and the material properties for mercury (Pittman 1992) presented in chapter 3.3.5. S (Hg) quantifies the volume of mercury penetrated in pore space within a certain pressure interval. The table is present in folder “Calculation of effective pore radius and capillary pressure curves of well 30”.

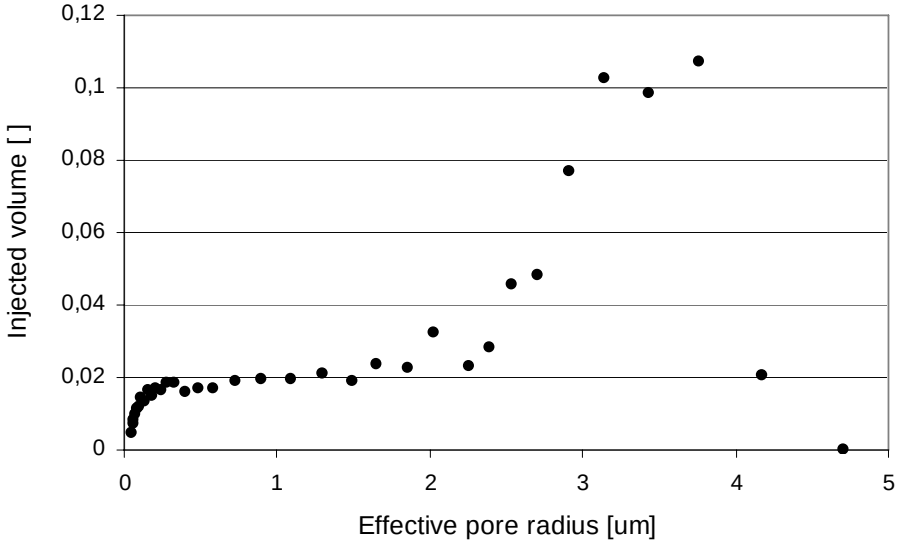

Fig. 3: Proportion of effective pore throat as a function of injected mercury volume. The table is present in folder "Calculation of effective pore radius and capillary pressure curves of well 30".

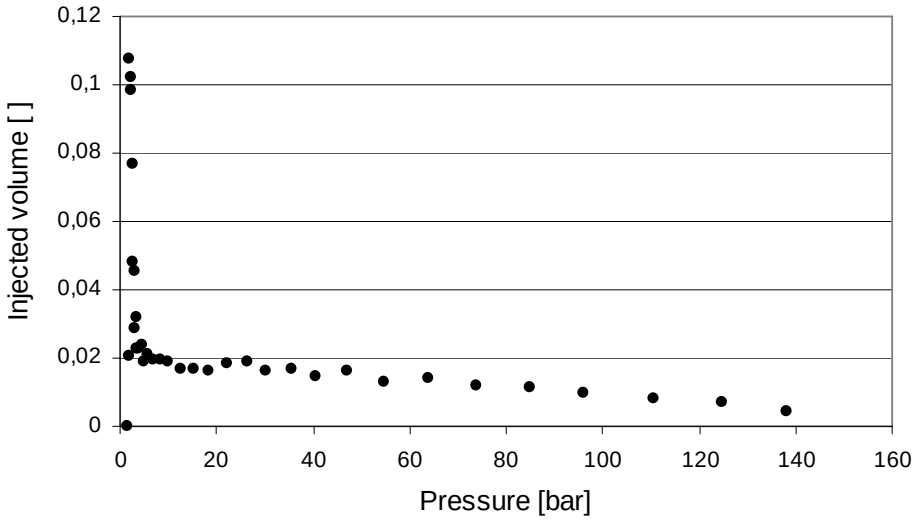

Fig. 4: Injected mercury volume in dependence to applied confining pressure. Mercury volume in proportion to total porosity. The curve is present in folder "Calculation of effective pore radius and capillary pressure curves of well 30".

r (um) [µm]	S (Hg) [ ]	r*s [µm]	r (um) [µm]	S (Hg) [ ]	r*s [µm]	r (um) [µm]	S (Hg) [ ]	r*s [µm]	r (um) [µm]	S (Hg) [ ]	r*s [µm]
4,714			2,254	0,023	0,052	0,582	0,017	0,010	0,134	0,013	0,002
4,181	0,021	0,086	2,032	0,032	0,065	0,482	0,017	0,008	0,115	0,014	0,002
3,765	0,107	0,404	1,856	0,023	0,042	0,399	0,016	0,006	0,099	0,012	0,001
3,430	0,099	0,338	1,646	0,024	0,039	0,332	0,019	0,006	0,087	0,011	0,001
3,148	0,102	0,322	1,488	0,019	0,029	0,280	0,019	0,005	0,076	0,010	0,001
2,910	0,077	0,224	1,303	0,021	0,027	0,243	0,016	0,004	0,067	0,008	0,001
2,710	0,048	0,130	1,093	0,019	0,021	0,207	0,017	0,003	0,059	0,007	0,000
2,537	0,046	0,116	0,892	0,020	0,017	0,181	0,015	0,003	0,053	0,005	0,000
2,388	0,028	0,068	0,727	0,019	0,014	0,156	0,016	0,003			
									2,04971	0,95754	5,891

	Eff. p.ra. [µm]	**PTS** [ ]
average	**2,14**	**2,427**

Tab. 15: Table for quantification of average magnitudes for effective pore radius and pore throat sorting (PTS). The curve present in folder "Effective pore radius and Pore Throat Sorting (PTS)"

A-9: Mineralogical, petrophysical, sedimentological and grain geometrical properties

This folder lists tabellary the mineralogical, petrophysical, sedimentological and grain geometrical data of plugs. The information derives from cores from members of the Hannover and Dethlingen formation and is differentiated according to the wells.
The bulk part of the data is attained from the DGMK-dataset. The files contain additionally many graphs and calculations which were produced in this study to test for interdependencies.
For some thin sections the DGMK-database lacks proportions of clay minerals. Please refer to the column 'diagenesis type' in order to retrieve information on the type of occurring authigenesis.
The mineralogical composition of the samples A-E was determined by pointcounting (400 counts) on thin sections (tab. 16).

Samples in [%]	Qtz, mono.	Qtz, poly.	Fsp	Ltcl	Qtz	Cc	IC	IM	Por	CT	Hmt	Fsp	Anh
A	48,2	6,2	10,0	6,0	10,2	2,0	0,0	0,0	10,2	1,2	0,0	2,0	4,0
B	46,8	6,3	9,0	4,5	8,0	7,2	0,0	0,0	9,6	1,0	0,0	1,8	6,0
C	45,0	6,4	5,6	7,3	6,5	4,6	0,0	0,0	10,1	1,7	0,0	2,2	7,1
D	43,0	4,4	2,9	8,7	6,1	8,5	5,0	11,2	9,7	0,0	0,4	0,0	0,9
E	44,1	4,6	4,6	8,3	6,3	5,2	5,2	12,6	9,2	0,0	0,0	0,0	0,0

Etched Ltcl.	Non etched Ltcl.	Intragran. Porosity
24	76	16
24	76	13
41	59	20
17	83	4
14	86	3

Tab. 16: Mineralogical composition and pores. The amount of secondary solution expressed in the proportions of etched lithoclasts and intragranular porosity.

A-10: Nuclear Magnetic Resonance

The folder ‘Relaxation graphs and error curves’ in the CD comprises the curves of radio signal decay and determination of error. An example is shown below (fig. 4); these curves were determined on sample C.

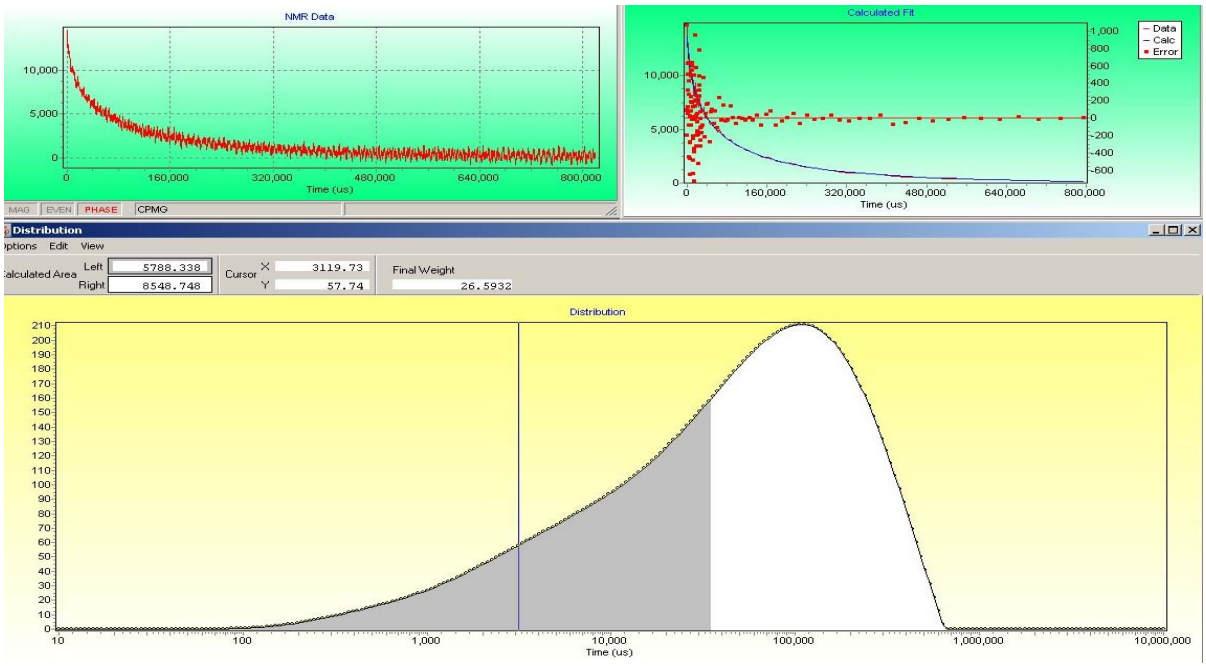

Fig. 4: The lower graph represents the relaxation curve for sample C (below). The curve in the upper left represents the decay of radio signal with time, the curve in the right depicts the signal to noise ratio and the interpolation for the decay. For more information see Rifai et al. (2005) and chapter 3.3.4.

The raw data of Nuclear Magnetic Resonance (NMR) measurements is shown tabellary below (tab. 17-19).
The water proportions were defined according to the standard limits given in literature (e.g. Howard et al. 1990) for clay bearing sandstones. The amounts for clay bound, capillary and free water are given in absolute and relative magnitudes. The porosity & permeability data derive from DGMK-database.
The samples represent Wustrow sand- and siltstones from dry and damp eolian environment. The plugs derive from wells 5 and 43 of illite authigenesis and well 30 of chlorite authigenesis which correspond to the blue/ green and red/yellow seismic classes respectively.

Label	Weight saturated	Area saturated	**Bound water** < 4µs		**Capillary water** > 4µs & < 33µs		**Mobile water** > 33 µs		Porosity	Permeability
	[g]	[ ]	absolute	[%]	absolute	[%]	absolute	[%]	[%]	[mD]
1030	54,52	160820,717	111158,3	**69,12**	42469,607	**26,41**	7192,81	**4,47**	4,5	0,043
		156350,409	116147,392	**74,29**	33185,197	**21,22**	7017,82	**4,49**		
1070	53,71	170145,205	104907,213	**61,66**	50534,039	**29,70**	14703,953	**8,64**	5,4	0,038
		161557,506	105983,379	**65,60**	41088,594	**25,43**	14485,533	**8,97**		
1100	49,49	138827,384	58827,443	**42,37**	46671,379	**33,62**	33328,562	**24,01**	7,6	0,388
		128672,384	50480,815	**39,23**	47759,668	**37,12**	30431,901	**23,65**		
1130	52,21	160729,296	61773,609	**38,43**	52932,051	**32,93**	46023,636	**28,63**	10,4	0,211
		155848,158	62102,097	**39,85**	51484,375	**33,03**	42261,686	**27,12**		
1170	53,67	135686,626	70217,184	**51,75**	46883,574	**34,55**	18585,868	**13,70**	8,8	0,075
		122434,698	65099,642	**53,17**	42126,225	**34,41**	15208,831	**12,42**		
1200	53,09	156320,612	77929,771	**49,85**	52767,077	**33,76**	25623,764	**16,39**	8,8	0,070
		144449,117	71989,781	**49,84**	51657,749	**35,76**	20801,587	**14,40**		
1220	53,24	175978,858	111588,974	**63,41**	50250,93	**28,56**	14138,954	**8,03**	7,6	0,050
		168022,907	114755,712	**68,30**	42162,557	**25,09**	11104,638	**6,61**		
1310	54,89	151953,157	74389,131	**48,96**	64139,894	**42,21**	13424,132	**8,83**	4,9	0,045
		143237,586	65707,297	**45,87**	66620,978	**46,51**	10909,311	**7,62**		
1360	54,7	169103,688	92673,543	**54,80**	59230,385	**35,03**	17199,76	**10,17**	6,0	0,032
		158546,547	92982,655	**58,65**	53644,641	**33,84**	11919,251	**7,52**		
1430	51,68	194669,413	56480,244	**29,01**	64906,534	**33,34**	73282,635	**37,64**	12,3	0,312
		187757,239	56098,598	**29,88**	65767,597	**35,03**	65891,044	**35,09**		
1460	53,16	176144,434	65001,959	**36,90**	74068,732	**42,05**	37073,743	**21,05**	8,0	0,090
		172934,23	67104,373	**38,80**	74751,186	**43,23**	31078,671	**17,97**		

Tab. 17: Raw data of NMR for well 5.

Label	Weight saturated	Area saturated	**Bound water** < 4µs		**Capillary water** > 4µs & < 33µs		**Mobile water** > 33 µs		Porosity	Permeability
	[g]	[ ]	absolute	[%]	absolute	[%]	absolute	[%]	[%]	[mD]
640	n.a.	32763,63	9041	**27,59**	18146,9063	**55,39**	5575,727	**17,02**	12,6	0,182
		33508,96	9710,447	**28,98**	18807,2051	**56,13**	4991,305	**14,90**		
720	n.a.	30483,46	11913,8	**39,08**	13726,5518	**45,03**	4843,11	**15,89**	11,3	0,213
sam. D		26035,69	7091,316	**27,24**	14162,2129	**54,40**	4782,162	**18,37**		
860	n.a.	39826,68	14668,77	**36,83**	19254,7051	**48,35**	5903,204	**14,82**	9,8	0,053
sam. E		34279,36	8924,571	**26,03**	19748,0156	**57,61**	5606,771	**16,36**		
890	n.a.	39182,86	12190,15	**31,11**	21327,9395	**54,43**	5664,771	**14,46**	10,4	0,096
		35370,61	8582,817	**24,27**	21192,9414	**59,92**	5594,85	**15,82**		
1040	55,85	48174,8	40464,2	**83,99**	6314,30078	**13,11**	1396,3	**2,90**	4	0,0001
		43119	36413,7	**84,45**	5755,10156	**13,35**	950,2	**2,20**		
570	51,31	37953,7	7883,8	**20,77**	12649,999	**33,33**	17419,9	**45,90**	14,9	0,345
		38486,3	7897,7	**20,52**	13879,4697	**36,06**	16709,13	**43,42**		
600	53,38	40641,8	12047	**29,64**	14826,9004	**36,48**	13767,9	**33,88**	10,9	0,305
		n.a.	n.a.		n.a.		n.a.			
1160	52,52	37729,6	18017,8	**47,76**	12784,1016	**33,88**	6927,7	**18,36**	9,7	0,129
		33722,1	15689,1	**46,52**	12109,8027	**35,91**	5923,2	**17,56**		
1320	56,52	37879,83	28875,7	**76,23**	7007,91797	**18,50**	1996,21	**5,27**	3	0,02
		32848,92	23923,9	**72,83**	6713,71094	**20,44**	2211,31	**6,73**		
1280	48,58	36083,93	9144,72	**25,34**	9110,39941	**25,25**	17828,81	**49,41**	14,8	2,66
		33440,66	6915,2	**20,68**	9334,43066	**27,91**	17191,03	**51,41**		
950	56,14	44231,59	36190,16	**81,82**	6843,76953	**15,47**	1197,66	**2,71**	2,7	0,011
		34772,6	27284,5	**78,47**	6022,87109	**17,32**	1465,23	**4,21**		
1010	54,78	39485,95	30897,46	**78,25**	7660,35938	**19,40**	928,13	**2,35**	3,6	0,0036
		32173,25	24654,2	**76,63**	6505,85156	**20,22**	1013,2	**3,15**		
770	54,05	33496,15	10228,37	**30,54**	14347,2471	**42,83**	8920,53	**26,63**	9,8	0,114
		30792,39	7351,47	**23,87**	14842,6797	**48,20**	8598,24	**27,92**		

Tab. 18: Raw data of NMR for well 43.

Label	Weight saturated	Area saturated	**Bound water** < 4µs		**Capillary water** > 4µs & < 33µs		**Mobile water** > 33 µs		Porosity	Permeability
	[g]	[ ]	absolute	[%]	absolute	[%]	absolute	[%]	[%]	[mD]
1010 O	n.a.	36803,623	8156,216	**22,17**	5714,97998	**15,68**	22811,94	**62,60**	12,29	10,7518
		35853,783	7919,389	**22,09**	6250,233398	**16,73**	21728,51	**58,17**		
1019 O	n.a.	41208,34	11113,31	**26,97**	7978,033203	**19,36**	22116,99	**53,67**	12,01	12,5764
		37444,54	7925,815	**21,17**	8976,005859	**23,97**	20542,71	**54,86**		
1060 O	n.a.	43520,07	10982,36	**25,24**	6669,945313	**15,33**	25867,76	**59,44**	12,61	38,7694
		41755,18	9497,379	**22,75**	7822,787109	**18,73**	24435,01	**58,52**		
1020 O	n.a.	40278,58	9682,255	**24,04**	8646,813477	**21,47**	21949,51	**54,49**	12,33	15,8535
		37320,26	7502,098	**20,10**	10280,07227	**27,55**	19538,09	**52,35**		
2020 O	n.a.	39143,48	18470,033	**47,19**	11588,55469	**29,81**	9085,529	**23,37**	10,62	3,852
		36520,14	17922,867	**49,08**	11432,76172	**30,81**	7235,665	**19,50**		
1040 O	n.a.	48174,8	40464,24	**83,99**	6314,285156	**13,11**	1396,271	**2,90**	9,79	3,6101
		43004,7	36308,11	**84,43**	5749,511719	**13,37**	947,083	**2,20**		
1090 O	n.a.	37464,55	12841,53	**34,28**	7871,318359	**21,01**	16751,71	**44,71**	10,51	14,6689
		33081,38	9338,903	**28,23**	9006,338867	**27,22**	14736,14	**44,55**		
2010 O	n.a.	31803,27	15825,09	**49,76**	8233,097656	**25,89**	7745,073	**24,35**	8,15	1,9774
		n.a.	n.a.		n.a.		n.a.			
1089	52,2	41792,57	15322,45	**36,66**	13985,22949	**33,46**	12484,89	**29,87**	11,3	0,3599
		39461,34	15204,57	**38,53**	14482,43945	**36,70**	9774,33	**24,77**		
1120	52,8	39997,06	15348,35	**38,37**	13261,18945	**33,16**	11387,52	**28,47**	10,62	6,1503
		34432,55	11213,85	**32,57**	14400,89258	**41,82**	8817,81	**25,61**		
1130	53,64	38896,79	23504,68	**60,43**	10276,37891	**26,42**	5115,73	**13,15**	8,29	0,4634
		35399,25	21847,57	**61,72**	9584,746094	**27,08**	3966,934	**11,21**		
1070	33,75	40334,74	14009,06	**34,73**	6921,948242	**17,16**	19403,73	**48,11**	11,52	118,8035
sam. C		37032,46	9396,2	**25,37**	8105,110352	**21,89**	19531,15	**52,74**		
1030	33,9	35443,93	12735,28	**35,93**	7253,618164	**20,47**	15455,03	**43,60**	11,56	16,4709
sam. B		29820,68	8341,73	**27,97**	8546,054688	**28,66**	12932,89	**43,37**		

Tab. 19: Raw data of NMR for well 30.

A-11: Particle contact conditions

The folder ‘Particle contact conditions’ contains the raw data of the proportions of particle contacts: differentiated are interfaces of sutured & concavo/convex, tangential point and tangential point shape, and contacts to blocky cement and open pore space.
The three files of a single specimen denoted with the extension 1, 2, 3 correspond to the two to three lines crossing the photo composite (chapter 3.2).
The folders ‘Sample A’, ‘Sample B’ etc. contain the microphotographs of each sample and the image composites. The long side length of a single microphotograph corresponds to 1,28 mm. These photos were utilized also for the grain geometrical analyses.

A-12: Plug velocities

The following tables (tab. 20, 21) list the ultrasonic plug speeds differentiated into velocities measured parallel and perpendicular to the lamination. Only those data are shown which were used for the analyses.

Well	Plug label	Utilized velocities parallel to lamination	perpendicular to lamination	Well	Plug label	Utilized velocities parallel to lamination	perpendicular to lamination
Well 5	1020	2665	2573	Well 30	1019	2750	2488
	1040	2926	2640		1020	2920	2489
	1050	2955	2196		sam. B / 1030	2562	2448
	1060	2765	1991		1040	2795	2530
	1061	2869	2339		sam. A / 1051	2928	2814
	1070	2817	1991		1060	2371	2667
	1079	2550	1919		sam. C / 1070	2240	2164
	1080	2926	2427		1089	2409	2720
	1090	2350	2043		1120	2730	2263
	1110	2046	1678		1130	2621	2531
	1120	2134	1800		2020	2650	2298
	1130	2164	1868	Well 43	560	2100	1757
	1141	2060	1710		570	2100	1717
	1150	2128	1860		600	2180	1641
	1160	2200	1914		620	2147	1674
	1170	2400	1820		640	n.a.	2000
	1180	2344	1891		sam. D / 720	2004	1950
	1200	2200	1952		721	2320	1975
	1201	2020	2200		730	2260	1970
	1230	2374	2073		760	2380	2046
	1250	2588	2132		761	2220	1761
	1259	2300	1880		770	2438	1965
	1290	2210	1778		780	2290	1756
	1350	2300	2263		791	2300	1867
	1351	2489	2086		850	2290	1759
	1380	2451	2296		851	2219	1606
	1390	2439	2102		sam. E / 860	2015	1990
	1400	2378	2196		870	2250	1875
	1420	2175	1778		891	2107	1750
	1430	2263	2150		950	2720	2120
	1450	2060	1799		1091	2745	2203
	1459	1766	1980		1121	2490	2141
	1460	2250	1940		1320	2685	2118
	1500	3052	1777				

Tab. 20: Selected plug velocities from wells 5, 30 and 43; these plugs of mostly dry eolian facies were chosen as they feature clearly visible laminations and lack fissures. The remnant plug speeds are adjoined in the folder 'Plug velocities'.

1010	Velocity [m/] Different positions on plug					1259	Velocity [m/] Different positions on plug					
3381	3450	3448	3373	3413		1901	1885	1930	1879	1907	
3375	3455	3447	3379	3415		1879	1887	1927	1879	1903	
3379	3458	3455	3383	3413		1893	1881	1933	1865	1915	
3375	3461	3451	3391	3413		1884	1885	1920	1855	1907	
3372	3456	3458	3374	3417		1889	1877	1933	1888	1912	
3372	3453	3453	3373	3407		1883	1877	1931	1884	1907	
3379	3453	3457	3375	3417		1889	1879	1936	1876	1903	
3375	3450	3455	3378	3413		1884	1874	1927	1878	1904	
3365	3450	3450	3375	3410		1889	1879	1928	1882	1904	
3383	3451	3455	3370	3418		1887	1881	1925	1885	1908	
3377	3447	3455	3360	3418		1893	1884	1928	1875	1911	
3376	**3453**	**3453**	**3376**	**3414**	Average	**1888**	**1881**	**1929**	**1877**	**1907**	Average
5,0	**4,1**	**3,6**	**7,8**	**3,5**	Abs. stand. dev.	**6,0**	**4,1**	**4,4**	**9,5**	**3,9**	Abs. stand. dev.
0,15	**0,12**	**0,10**	**0,23**	**0,10**	Rel. stand. dev. [%]	**0,32**	**0,22**	**0,23**	**0,51**	**0,21**	Rel. stand. dev. [%]
				3414	Average					**1896**	Average
				35	Abs. stand. dev.					**20**	Abs. stand. dev.
				1,03	Rel. stand. dev. [%]					**1,07**	Rel. stand. dev. [%]

1050	Velocity [m/] Different positions on plug					
2179	2205	2220	2209	2164	
2182	2207	2225	2213	2162	
2182	2203	2217	2216	2173	
2179	2208	2217	2208	2166	
2184	2201	2223	2219	2171	
2174	2203	2220	2221	2174	
2186	2198	2209	2223	2161	
2192	2208	2226	2225	2167	
2172	2205	2229	2216	2169	
2176	2198	2220	2204	2169	
2166	2195	2227	2216	2167	
2179	**2203**	**2221**	**2215**	**2168**	Average
7,2	**4,4**	**5,7**	**6,5**	**4,2**	Abs. stand. dev.
0,33	**0,20**	**0,26**	**0,29**	**0,19**	Rel. stand. dev. [%]
				2197	Average
				22	Abs. stand. dev.
				0,98	Rel. stand. dev. [%]

Tab. 21: Standard deviation of plug velocities. The speeds were determined on three samples of varying porosity at five different positions. The velocity was measured 10 times at each position (corresponds to column). The relative and absolute standard deviations are derived for each location and for the single plugs. The specimen derive from well 5.

A-13 Description of main sedimentary facies associations in the seismic volume

The following table (tab. 22) is taken from Gaupp & Solms (2005).

Facies Association	Depositional Environment	Lithofacies
Aeolian dry	Aeolian Dune	Axh, Axg, Al, Am, (Axhe, Axge, Ale, Ame)
	Dry Sandflat	Al, Axg, Am, Al, (Axge, Ale, Ame)
Aeolian damp	Damp Sandsheet	Aw, Awe, Aweb
	Damp Sandflat	SAp, (SApe, SApb, SApeb, Sapc)
Mudflat / Lake	Mudflat	Mp, Mm, (Mpeb, Mmeb, Mpb, Mmb, Mme, Mpe)
	Lake (Ephemeral)	Mld (Mldb)
	Lake (Perennial)	Ml (Mlb)
	Lake (Chemical)	Egyp, Ehal, Eanh, Elim, Edol

Lithofacies	Description	Interpretation
Ml	Siltstones/claystones with low-moderate sand content (<50%); planar laminated and possible cross-laminated with or without desiccation cracks, absence of wavy bedding.	Predominantly subaqueous suspension deposits with indications of periodic introduction of sandy traction currents; local indications of subaerial exposure.
Mm	Massive red-brown siltstone/claystone (<10% sandstone)	Subaqueous suspension deposits perhaps modified by evaporitic processes.
Mp	Wavy, irregular laminated sandy siltstone/claystone with 20-50 % sandstone often dispersed in muddy matrix.	Muddy wet sandflat with admixed aeolian sand; structures dominated by “adhesion” and “evaporative” features. The result is a mudstone rich sand patch texture.
Sap	Wavy laminated sandstone with 20-50% clay /silt content; generally irregular thinly bedded (mm- to cm scale) (wavy discontimuous and continous lamination common) character with common disrupted bedding associated with evaporites, rare desiccationcracks. Often interbedded with Mp facies.	Damp sandflat deposit dominated by adhesion and disrupted or deformed waterlain structures and “evaporative” structureless; the result is a distinctive sand patch sedimentary texture similar to that present in Mp.
Aw	Wavy bedded sandstone with <20% clay content; greater sand content than in Sap; low clay content (<20%). Often interbedded with Ax facies.	Wavy bedded damp sandsheet dominated by “adhesion” structures and occasional thin (mm- to cm-scale) horizons of wind ripple lamination/ cross-lamination.
Am	Apparently massive sandstone with zero clay content and possibly (relict) bimodal sorting.	Massive aeolian sandstone, possibly disrupted by post-depositional processes (e.g. fluidisation, liquefaction or dissolution)
Al	Subhorizontally and horizontally laminated, generally with bimodal translacent strata (’pin-stripe’-lamination) and granule ripple lamination; low clay/silt content (typically <10%).	Wind ripple/proto-dune sandsheet deposits
Axh	Cross-bedded with angle of foresets greater than 15 degrees. Sandstone dominated by grain-flow cross-strata, grain fall laminae, and/or translatent strata.	Aeolian dune deposits
Axg	Cross-bedded sandstone with angle of foresets less than 15 degrees. Dominated by grain fall laminae, ‘pin-stripe’ lamination present in places.	Low amplitude aeolian dunes
Egyp, Ehal, Eanh, Edol, Elim	Gypsum (Egyp), halite (Ehal), anhydrite (Eanh), dolomite (Edol) and limestone (Elim) deposits may be laminated or massive.	Evaporites and subaqueous salts and carbonates

Tab. 22: Description of dominant facies association in seismic volume (after Gaupp & Solms 2005)

A-14: Volume of clay minerals between particle contacts

The file ‘Clay minerals between particle contacts’ lists the raw data for the five samples.
The raw data represent the proportional lengths of particle contacts without clay minerals on the whole length of particle contacts.
The calculated amounts of load bearing clay minerals are given as average magnitudes and standard deviations.
The micro photographs and their image composites are listed in the folders ‘Sample A’, ‘Sample B’ etc. The long side length of a single microphotograph corresponds to 0,32 mm.
These microphotographs were also utilized for ‘Volume of not load bearing clay minerals’.

A-15: Volume of not load bearing components

The file ‘Volume of not load bearing components’ contains the raw data for each sample with average magnitudes and standard deviations, and the calculated parameters V_{p+c} and deviation of V_{p+c} from core porosity.
The utilized microphotographs are contained in the folder ‘Clay minerals between particle contacts’.

CURRICULUM VITAE
Peter Abram

E-mail: peter.abram@uni-jena.de

PERSONAL DATA

Nationality:	Italian
Date & place of birth:	28th december 1974 in Bozen (Northern Italy)
Native language:	German

PROFESSIONAL & PRACTICAL EXPERIENCE

October 2006 - presence	QI-Rock Physicist in Centres of Expertise - EPT Solutions in Shell Exploration and Production International
May 2003 – October 2006	Scientific employee at the **Institute of Geosciences** in Jena Investigating "Relations between seismic signals and reservoir properties of Gas Reservoirs", doctoral thesis, started in October 2003, lecturer for "Petrophysics of sediments" and "Geological interpretation of wireline data"
August 2001- March 2003	**Schlumberger Oilfield Services** Trained to become Field Engineer for Reservoir Evaluation Wireline in Medan (Sumatra) Worked for Exxon Mobil, AGIP, Shell, on/offshore, to acquire logging data in Nigeria (till begin of January 2003)
July - August 2000	**Preussag Energie Lingen, Germany** (now Gaz de France) Assistant to the production geology department Geological modelling of a petroleum reservoir in Tunisia
July - September 1999	**Joanneum Geophysical Research, Austria** Geophysical measurements and interpretations to trace water horizons between national borders
July - August 1998	**GKB Mining, Austria** Collaborator of the engineering department Development of a mining programme to guarantee an economic production of raw material for three years
April 1998	**Salinen Austria AG, Austria** Drilling operations in underground mines, interpretation of core samples to explore salt layers
1999 - 2000	**Institute of sedimentology, University Leoben** Part time lecturer in petroleum geology and sedimentology

EDUCATION

2001-2002	Training for wireline logging and safety courses for on/offshore
2001	Graduated as Petroleum Geologist, M. Eng. (mont.) with distinction
1997	Start major subject Petroleum Geology
1994	Enrolment at the University of Mining, Leoben (Austria)
1994	Abitur at the scientific high school in Bozen

Publications

Abram P., Gaupp R. (2006): Relations between seismic signals and reservoir properties of Tight Gas Reservoirs in Northwest-Germany (Permian Rotliegend sandstones). - DGMK Tagungsbericht 2006-1, p. 81-90.

Abram P., Gaupp R. (2005): Relations between seismic signals and reservoir properties of Tight Gas Reservoirs in Northwest-Germany (Permian Rotliegend sandstones).- AAPG International Conference and Exhibition, Paris, Abstracts, p. A1.

Abram P., Gaupp R. (2005): Relations between seismic signals and reservoir properties of Tight Gas Reservoirs in Northwest-Germany (Permian Rotliegend sandstones). - DGMK Tagungsbericht 2005-1, p. 153-162.

Abram P., Gaupp R. (2004): Relations between seismic signals and reservoir properties of Tight Gas Reservoirs in Northwest-Germany (Permian Rotliegend sandstones).- AAPG European Region Conference with GSA, Prague, Abstracts, p. 56.

Abram P., Gaupp R. (2004): Beziehungen zwischen seismischen Signalen und Lagerstätten-Eigenschaften im Wustrow-Member (Rotliegend) der Tight Gas Reservoirs in Nordwestdeutschland.- Schriftenreihe der Deutschen Geologischen Gesellschaft, GeoLeipzig 2004 'Geowissenschaften sichern Zukunft', Abstracts, p. 360.

Abram P., Gaupp R. (2004): Beziehungen zwischen seismischen Signalen und Lagerstätten-Eigenschaften im Wustrow-Member (Rotliegend) der Tight Gas Reservoirs in Nordwestdeutschland.- Schriftenreihe der Deutschen Geologischen Gesellschaft, Sediment 2004 in Aachen, Abstracts, p.11, 33.

Abram P., Gratzer R., Bechtel A., Gawlick H.-J. (2001): Geochemistry, sedimentology and stratigraphy of the bituminous 'Seefelder Schichten' in Carinthia, Austria.- Mitteilungen der Bergbau und Geologiestudenten.

Prices: "Ozan Sungurlu Award for best poster presentation", bei AAPG-Confex, Paris 2005
"2nd place for best oral presentation", bei AAPG-Confex, Paris 2005

INTERESTS

Founder and former president of "ISUL-International Students Union Leoben" Backpacker in Vietnam, Chile, Bolivia
Member of a diving and a climbing club, cyclist and hobby-carpenter
Exploring old mines in the surroundings of my hometown

Languages:	German: native
	Dutch, Italian, English: fluent
	French, Russian: basic knowledge

Jena, 20. September 2006 Peter Abram

Selbständigkeitserklärung

Ich erkläre hiermit, dass ich die vorliegende Arbeit selbständig und unter der Verwendung der angegebenen Hilfsmittel, persönlichen Mitteilungen und Quellen angefertigt habe.

Jena, 20. September 2006 Peter Abram